The Development of a High Speed 3D 2-photon Microscope for Neuroscience

Paul Anthony Kirkby

UCL

Doctor of Philosophy

Declaration

I, Paul Anthony Kirkby, confirm that the work presented in this thesis is my own. Where information has been derived from other sources, I confirm that this has been indicated in the thesis.

Abstract

The progress of neuroscience is limited by the instrumentation available to it for studying the brain. At present, there is a serious instrumentation gap between functional Magnetic Resonance Imaging (fMRI) of whole brains and the microscopic scale functional imaging possible with today's optical microscopes and electrophysiology techniques, such as patch clamping of individual neurons. This thesis describes the development of a new extension to optical microscopy that enables refocusing within 25 microseconds rather than the large fraction of a second possible by moving the sample or objective. The system is capable of refocusing a laser beam that is monitoring activity in 3D samples of live brain tissue 300 times faster than previously possible. This will make practical a new type of optical functional imaging for studying small sub-networks of neurons containing up to about 30,000 neurons at up to 30,000 sub micrometre sized monitored points of interest per second. The thesis describes the development of a detailed design for a new type of 3D scanner that uses Acousto-Optic Deflectors (AODs) to diffractively deflect and focus an intense laser beam beneath a conventional microscope objective. The fluorescence of calcium sensitive dyes in live neurons is used to monitor action potentials conveying signals between neurons. The optical and systems engineering problems and design trade-offs involved are discussed in detail. The results of extensive computer modelling are described and innovative solutions to several key optical physics based engineering problems are explained. The practical problems found in building a prototype machine incorporating these innovations are described and the encouraging first operational results from the machine reported.

Acknowledgements

I am very grateful for the opportunity that this PhD and preceeding MRes has given me to retrain from optoelectonics research engineering into neuroscience instrumentation. I am indebted to the EPSRC/BBSRC funded UCL Centre for Mathematics Physics Life Sciences and Experimental biology (CoMPLEX, http://www.ucl.ac.uk/complex/) and in particular to Andrew Pomianowski, Guy Moss and Alan Johnstone three of its directors for agreeing to take a chance on such a 'mature' student at the beginning and for supporting and encouraging me throughout.

This project was conceived by Angus Silver in 2004 and a pilot project was funded by EPSRC starting in 2005 (Silver 2004). It has been a great pleasure to be part of the Silver Lab that Angus leads so effectively. This project has been carried out predominantly by K M N Srinivas Nadella, a Research Fellow and myself, with very regular discussion and leadership from Angus. During the 4 years of the thesis I have also had funding support from The Worshipful Company of Scientific Instrument Makers since I won their 'Beloe Fellowship' in 2008. Angus Silver has also used part of his Welcome Trust, Medical Research Council Fellowships to support the overall project and extend my student grant.

There are many different skills and attributes required to progress the development of such a complex instrument as described in this Thesis. At each stage, I have done the initial conceptual work and Matlab modeling for all the aspects of the work described in the thesis (except the temporal compensator). I have developed the concepts and implemented all the Matlab code described here for controlling the AOL laser spot position vs. time. Srinivas has done the majority of the experimental implementation, such as optical train assembly and alignment and the development and implementation of all the LabView code that provides the user interface.

The results presented in Chapter 5 include our first demonstrations of the feasibility of the microscope for 3D biological functional imaging at kHz rates. This work was carried out by Tomas Fernandez-Alfonso and Srinivas. Srinivas also designed and carried out the experimental measurements of temporal dispersion compensation. All the other experimental work described in this thesis was carried out jointly by myself

and Srinivas. We are very grateful to Alan Hogben and Duncan Farqueharson for the high quality mechanical work that has been carried out by the UCL Biosciences Engineering workshop and to Bruno Pichler for much help with software development.

I would like to thank Warren Seale and Mike Draper of Gouch and Housego (www.goochandhousego.com) for their advice and help with AOD design and analysis of performance and Mike Hillier of Isomet (www.isomet.com) for his enthusiastic development of improved versions of the iDDS for this project. Particularly at the beginning of the project, Bill Vogt and Todd Keifer of Prairie Technologies (www.prairie-technologies.com) were very helpful in training us in microscope engineering and throughout the project Mike Szulczewski CEO of Prairie has provided enthusiastic support and strategic advice in a business context. Abigail Watts of UCL Business has been our guardian in UCL business and overseen the project from the perspective of its commercial exploitation. Mark Roberts of JA Kemp Patent Attourneys has been a pleasure to work with and suggested the clarification I used on the way the ramp rate equations in chapter 3 were presented.

Finally I would like to thank John Mitchell of UCL Electrical Engineering, and my other colleagues in the Silver Lab and the wider UCL community for many inspiring useful and enjoyable conversations. At home I would like to thank my wife Geraldine for her support and encouragement throughout the course of this PhD and Geraldine, Valerie Shephard and my sister Margaret Kirkby for enthusiastic style advice and proof reading. I take responsibility for the remaining errors.

Glossary

AFL Absolute Frequency Limit; the first miniscan drive algorithm described graphically in Figure 2.24 for setting miniscan start and stop drive frequencies based on predefined absolute frequency limits.

AOD acousto-optic deflector

AOL acousto-optic lens

AOLM acousto-optic lens microscope

DOE diffractive optical element

FOV field of view

FWHM full width half maximum

neuronal processes the dendrites or axons of a neuron

HWP half wave plate

PMT photomultiplier tube

psf point spread function: the 3D distribution of optical energy (or 2-photon excitation) at the focus of a lens

OFL Optimised Frequency Limit: an algorithm of optimising the pairs of drive frequencies for the AODs on each axis to maximise efficiency and minimise efficiency variation during a miniscan

RF radio frequency

ROI region of interest

telecentric relay an optical system, usually a pair of lenses that relay an input image to an output field .It has the property of constant magnification independent of z position.

voxel the 3D equivalent of a 2D pixel , a ‘volume pixel’

Table of Contents

Chapter 1 Introduction and background

The slowness of mechanical refocusing of conventional optical microscopes severely limits the speed at which they can form images of 3D objects. This thesis describes the design, development and testing of a prototype 'Acousto-Optic Lens Microscope' (AOLM) aimed at overcoming some of these longstanding limitations. The motivation for developing the AOLM system was the desire to extend the use of laser microscopy in order to fill the 'instrumentation gap' in neuroscience in available techniques for functional imaging of the brain in three dimensions at high speed.

There are approximately 10^{11} neurons in the brain. They communicate by sending electrical signals known as action potentials along the complex branching axons. These are short pulses about 1ms in duration and typically have an amplitude of up to 100mV. They occur at rates from 0-1 kHz. There is currently no instrument capable of both imaging and identifying individual neurons from a 3 dimensional volume of brain tissue and recording activity from many neurons in parallel at sufficiently high speed to detect the millisecond timing of individual action potentials. Partly as a result of this, we are far from understanding how cortical networks carry out the information processing that presumably allows an animal to form its ongoing impression of the outside world and pursue its goals in the environment. Such an instrument is therefore highly desirable for neuroscience to make more progress in understanding how the neural networks forming the brain encode and process information.

In the longer term, it is highly likely that understanding the spatio-temporal coding and processing mechanisms of the brain will open up entirely new ways of understanding disorders of the brain and lead to new treatment for a wide range of mental disorders.

This chapter discusses the biological objectives for developing the AOLM , describes the principle of operation of 2-photon microscopy, introduces acousto-optic scanning and the concepts that allow scanning and focusing to be extended into the third

dimension, outlines the target specification for the AOLM and summarises the state of the art of 3D AOD deflection systems at the start of the project.

Biological objective – Understanding how the brain process information in its neural networks

The mammalian brain is by far the most complex information processing and decision making system in the known universe. Neuroscience has been attempting to understand the structure and functional mechanisms of the brain for over 100 years (Cajal 1911). Tremendous progress has been made, first in identifying that individual cells (neurons) are the key unit of processing, classifying the structure and form of many different types of neurons and more recently in understanding the remarkable biochemical complexity of even the smallest parts of individual neurons (Nicholls 2001).The direction and pace of neuroscience is, to a large extent, determined by the instruments available for monitoring and imaging the brain at the relevant physical scale. Many of the key improvements in understanding have been made by using instrumentation with higher capabilities than previously available. Before discussing improved instrumentation, consider first the instruments available today to study the various levels of the hierarchical structure of the brain.

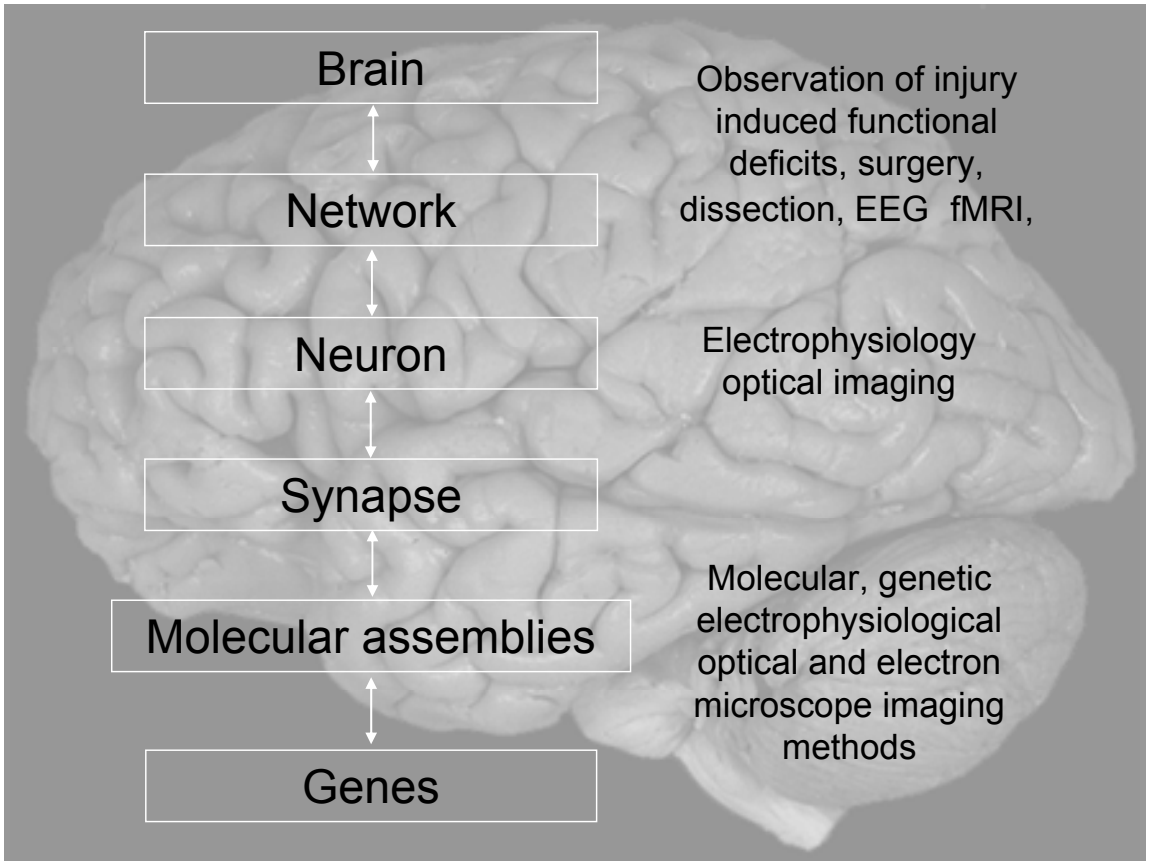

Figure 1.1 Summary of the hierarchical view of brain structure as it is understood today indicating the main techniques used for their study at each level. EEG is electroencephalography, the use of sensitive electrodes distributed across the scalp, fMRI is functional Magnetic Resonance Imaging.

Figure 1.1 summarises the hierarchical view of brain structure as it is understood today and indicates the main techniques used for their study. At the scale of whole brains, studies of loss of function from brain injury or surgery and anatomical dissection are used to determine structure and its relationship to function. The functioning of live whole brains can be best studied today using the electroencephalograph (EEG) and functional Magnetic Resonance Imaging (fMRI) instruments (Jezzard 2001). Such instrumentation, using computerised tests on humans have been invaluable for identifying (or confirming) the function of the different regions of the brain. It has, at a very high level, even provided some evidence as to what algorithms are being used by the brain for the decision making process involved (Daw and Doya 2006).

At the ‘network of neurons’ hierarchical level, electrophysiological techniques involving sensitive amplification of extracellular electric potentials and currents are often used. These use fine metallic electrode tips to record signals up to a few mV at bandwidths up to 10 kHz. Multi-electrode arrays have been inserted into the brains of awake behaving animals and have yielded important information (Huxter, Burgess et al. 2003). A disadvantage of such techniques is, however, that it is difficult to be sure which neurons are generating the signals being measured and how they are interconnected (Buzsaki 2004).

At the ‘neuron’ hierarchical level, the most precise electrophysiological technique in widespread use today uses glass tipped pipette electrodes with tips of the order of 1 μm diameter. Using optical microscopy and precision micromanipulators, these can be used to record electrical potentials and currents from individual neurons using a technique known as ‘patch clamping’ (Hamill, Marty et al. 1981). These techniques have progressed from being used on cultured neurons to *in-vitro* use on acute slices of live brain tissue from animals such as mice that have been killed up to a few hours previously (Edwards, Konnerth et al. 1989). More recently the use of patch clamping has been extended to *in-vivo* use on live animals, under anaesthetic (Margrie, Brecht et al. 2002).

Signal Processing in the neural networks of the brain

The way in which information is represented, processed and stored in the brain is very far from being understood, however many generic details are known. For instance, the features of sensory inputs can be encoded as distinct spatiotemporal patterns of firing neurons in the cortex. *In vivo* recordings from different areas of the cortex show that only a small fraction of the neurons in a network are active in response to a particular sensory stimulus feature, implying that the ‘population code’ representing the stimulus is ‘sparse’(Vinje and Gallant 2000; Margrie, Brecht et al. 2002; Brecht, Roth et al. 2003; Olshausen and Field 2004; Kerr, de Kock et al. 2007). This temporal sparseness is believed, in part at least, to be because sparse population codes are the most energy efficient (Levy and Baxter 1996; Attwell and Laughlin 2001).

Temporal and spatial sparseness of action potentials and the regions of interest on neurons where the signal can be monitored

From the perspective of monitoring the action potentials in the neural tissue the temporal sparseness of action potentials is a considerable problem, with individual neurons firing at rates from very small fractions of 1 Hz up to about 1 kHz, often in an unpredictable and very 'bursty' manner. In the worst case therefore, in order to monitor every action potential in every neuron in a volume of tissue, it is necessary that every neuron is monitored at least every millisecond.

Naturally, as a result of the temporal sparseness, at any particular time only the order of 1% to 10% of neurons are firing action potentials. From the perspective of monitoring the action potentials in the brain, the parts of neurons that can be monitored are also spatially very sparse. This is particularly true if it is desired to monitor the action potentials at high bandwidth (>kHz sampling rates). This is because the action potentials themselves are confined to the 10nm thick membranes of the neuron cell walls. For electrical monitoring, part of the cell wall must be contacted by a probe or patch clamp and the part of the cell that is in practice usually easiest to contact is the neuron cell body. These are in the range of 5-30 μm in diameter and usually separated by several cell diameters. The rest of the space is filled with other types of non neuronal cells and tissue and a high density of the sub micron diameter branching tree like 'axons' (output fibres from the neuron bodies) and 'dendrites' (input fibres to the cell bodies). Dendrites and axons form the complex networks that link the cell bodies to each other via electrochemical 'synapses' between them. They can be any length from a few μm up to many mm. Thus in general, it is necessary to use optical microscopy with the order of 1 μm precision micromanipulators for adjusting position of electrical monitoring probes for >1 kHz monitoring speed of individual neurons.

If optical techniques are used for monitoring (see Chapter 2) then again, for high speed 100 Hz -1 kHz monitoring rates, the monitoring position needs to be chosen for each neuron with the order of 1 to 5 μm precision. For slower speeds, 10s to 100s of

ms, whole cell bodies can be optically monitored which may be up to 20-30 μm across.

In conclusion, the high speed monitoring of the signals that propagate between neurons in live brain tissue and as such represent a key aspect of how neurons process information can only be monitored with instrumentation capable of high precision in time and 3D space. The signals themselves are temporally very sparse (typically 1ms long separated 1ms to 10s of seconds). The regions of interest on the neurons for monitoring the signals at high speed are spatially very sparse, being sub micron up to a few μm in dimension separated by up to many 10s of μm.

Functional Imaging of neurons in networks: current limitations and why this is an important problem to solve

The main limitation of current cellular level electrophysiological instrumentation techniques is that it is very difficult indeed to patch more than a few cells at a time in parallel, thus it is currently very difficult to determine, in parallel, the millisecond timing of action potentials of more than three or four identified cells of the cortex. This is important because there is increasing evidence that in different parts of the brain not only the rate, but also that the precise timing (Huxter, Burgess et al. 2003; Montemurro, Rasch et al. 2008) of action potentials within bursts of action potentials from distributed groups of neurons, convey more information than the average burst rate. There is already widespread evidence that network oscillations at a wide variety of frequencies play a significant role in synchronizing signalling of information from one part of the brain to another (Buzsaki 2006). There are also examples where the evidence strongly suggests that the phase of an action potential, that is its time within the cycle of some larger scale network oscillation, carries significant information.

Perhaps the most well known example of the importance of precise timing or phase within an oscillation carrying significant information is the evidence from electrodes in awake behaving rats. Extra cellular electrodes placed in the hippocampus show that certain cells, referred to as ‘place cells’, fire with a rate that reaches a maximum at certain unique positions within a 2D environment. Other place cells have maxima elsewhere in the environment forming a type of map. The phase of firing of these ‘place cells’ within the 10Hz theta oscillations of the hippocampus varies

progressively as the rat moves through the spatial position that causes the cell to fire fastest (Huxter, Burgess et al. 2003). The theta oscillation is an oscillation of the hippocampus network and is measured using an electro-encephalogram. They showed that the time of firing with respect to this oscillation and the firing rate are dissociable and can represent variables such as the animal's location within the 'place field' and its speed of movement through the field. The firing of place cells must be a necessary part of the rat's internal cognitive map of the outside world. Other detailed studies (Jeffery 2007) show that the so called 'place cells' that the tips of the multi-electrode array happen to be close to, not only fire as a result of place but also apparently in response to other modalities of input and even 'internal brain state' so that the evidence suggests that the brain's representation of external reality is not coded into the firing of individual neurons, but into spatio-temporal patterns of firing of neurons distributed across a region of, or perhaps indeed across the whole, brain.

Some recent additional evidence from multi-electrode arrays, monitoring the precise timing of action potentials of the detached retina of a salamander whilst controlled sequences of images are projected onto the retina, show that the relative timing of action potentials from nearby ganglion cells carries significantly more information than can be carried by rate alone.(Gollisch and Meister 2008). There is also evidence from multi-unit recording in the primary visual cortex of anaesthetised macaques, that shows that that spike timing with respect to local field potential (LFP) conveys 50% more information than the spikes themselves.(Montemurro, Rasch et al. 2008)

A key issue is whether there is some general principle or pattern to the 'population codes' or 'spatio-temporal patterns of action potentials' that communicate information from one part of the brain to another. Is there a generic code for the precise spatio-temporal patterns of action potentials propagating in bundles of axons between one part of the brain and another? The alternative, that it is that the precise timing is random and it is only the overall rate of action potentials that is significant, is looking less likely as more accurate evidence is gathered from different parts of the brain.

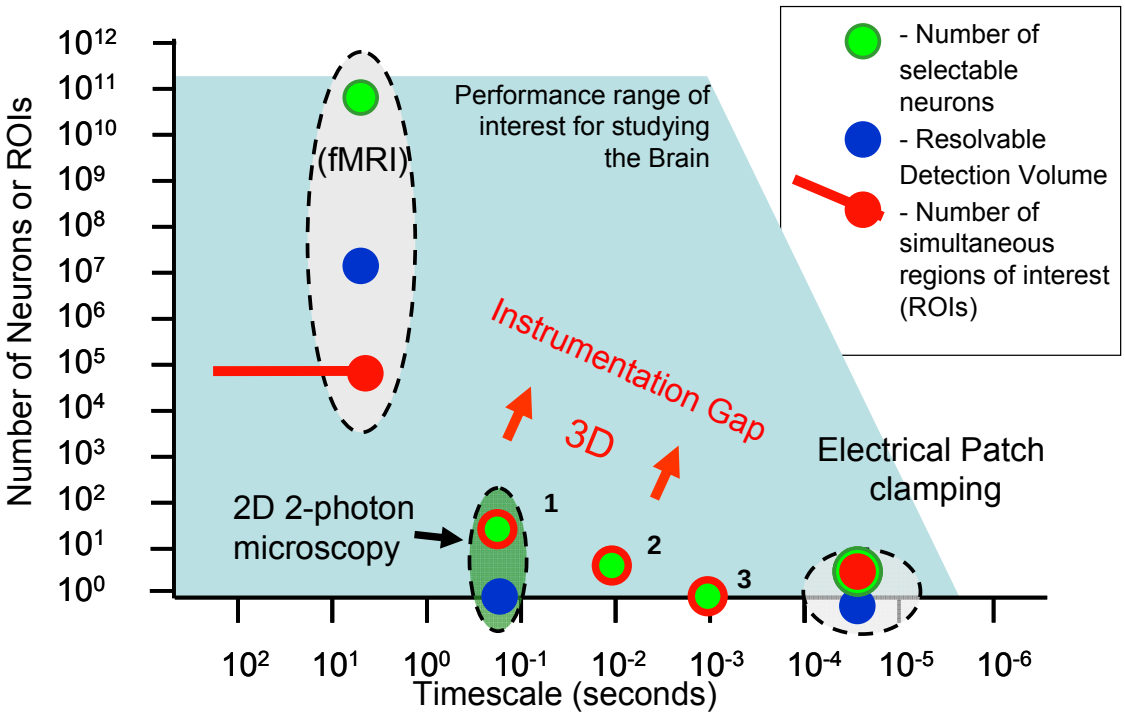

Figure 1.2 Schematic diagram to illustrate the regions of operation of different types of functional imaging of the brain available or demonstrated in 2005/6. The vertical scale is the number of selectable neurons the instrument can study (green), the number of neurons in the finest resolution 'voxel' of the instrument (blue), and the number of separate regions of interest it can monitor (red). The horizontal axis represents the fastest timescale that the instrument can work at. The experimental performance of 3 examples of 2D optical functional imaging systems based on 2-photon microscopy are also plotted.1)(Kerr and Denk 2008), 2) (Salome, Kremer et al. 2006),3) (Sabatini and Regehr 1996) (DiGregorio and Silver 2001)

Unfortunately, there is at present an 'instrumentation gap' in equipment capable of measuring the millisecond timing precision of multiple neurons. The instrumentation gap can perhaps be best visualised using the large range logarithmic-scale schematic diagram illustrated in Figure 1.2. The vertical scale shows numbers representing the important performance parameters of the instrument i.e.; the maximum total number of neurons it can image, the number of neurons in a maximum spatial resolution 'voxel' and the number of separate regions of interest it can monitor in parallel in its functional mode, a voxel is the 3D equivalent of a 2D pixel, a 'volume pixel'. The horizontal axis represents the maximum speed at which the functional information can be gathered. At the network of neurons level, the ideal neuroscientists 'cerebroscope', (the instrument hypothesised by philosophers and psychologists for measuring brain state) would be able to monitor the action potentials over the whole range of scales up to the whole human brain (10^{11} neurons) firing at 0 Hz to 1 kHz as indicated by the

pale blue shaded region of interest. Present day instruments fall many orders of magnitude short of this goal. The fMRI machine can indeed measure whole brains, but its finest spatial resolution of a few cubic mm corresponds to at least 10^6 neurons and its fastest time resolution is a few seconds. The maximum number of separate regions of interest it can monitor in parallel is thus at most 10^5. The horizontal red line on Figure 1.2 indicates that there is no advantage in slowing the response of the fMRI machine below a few seconds, the maximum number of regions of interest is still limited by the spatial resolution to 10^5 voxels. For fast measurements, patch clamping can monitor at up to 10 kHz (or more), but to date it has only been used to record from single neurons in vivo.

As will be described in the next section of the introduction in more detail, the development of 2-photon laser scanning microscopy (Denk, Strickler et al. 1990) has partially filled this instrumentation gap by allowing imaging of calcium in neuronal populations *in vivo* at sub-micrometer resolution deep within tissue (Zipfel, Williams et al. 2003; Helmchen and Denk 2005). The rapid rise (1ms – 100ms) and slow decay 20ms to seconds) of fluorescent dyes that monitor calcium concentration near the cell membrane after each action potential, can be used to monitor action potential timing in neurons with precisions ranging from ms to seconds depending on experimental conditions.

The conventional 2-photon microscopes mostly used to date have provided high spatial but low temporal resolution maps of cortical activity, allowing receptive fields to be mapped with cellular resolution (Ohki, Chung et al. 2005; Kerr, de Kock et al. 2007; Sato, Gray et al. 2007). Although current methods can detect a single action potential evoked calcium transient (Kerr, Greenberg et al. 2005; Yaksi and Friedrich 2006), and can therefore reliably identify cells that respond to a particular sensory stimulus, they currently do not have the temporal resolution to determine how such sensory information flows through networks or is encoded in the spike times of neuronal assemblies. These microscopes use galvanometer mirrors for XY scanning. The momentum and limited frequency response of the mechanical movement of the mirrors is not well suited to collecting signals from the spatially sparse regions of interest on particular neurons in the tissue, so there is a practical limit on the number of neurons that can be imaged. The point by point serial nature of 2-photon imaging

leads to the number of neurons that can be imaged that is approximately inversely related to the speed at which each neuron is monitored. The experimental limits in 2005/6 for such 2-photon 2D scanning 2-photon microscopes are shown by the numbered data points on Figure 1.2. Typically galvanometer scanning microscopes can monitor up to 30 neurons in a frame at 10Hz (Kerr and Denk 2008). The number of neurons is primarily limited because the 2D scanning only sections a single plane of neurons. For 300 μm square scan area, this is unlikely to contain more than 30-50 active neurons that can be monitored in the L2/3 cortex often studied (Ohki, Chung et al. 2005). Furthermore, because of the repetitive raster scanning, and the sparsity of the points of interest in the 2D plane, a large fraction of time is spent mapping regions where nothing of interest is happening. The frame rate is limited to about 10Hz. (Imaging time 100ms). Faster monitoring can obtained by reducing the scan area of a galvanometer scanning system, until at 1kHz rates it is only possible to scan along one line, maybe straight or a 2D Lissajous figure, typically only 1-3 neurons (Sabatini and Regehr 1996; DiGregorio and Silver 2001).

Also indicated on the schematic diagram is a point (2) showing the approximate performance of 2D 2-photon microscopes that use acousto-optic deflector (AOD) based deflection systems (Iyer, Losavio et al. 2003; Iyer, Hoogland et al. 2006; Salome, Kremer et al. 2006). As described in more detail in the next section, these deflect the laser beam using diffraction from an acoustic travelling wave. AOD deflectors enable the focused laser point to jump discontinuously from one region of interest to another in a particular 2D plane and gather light from the most active parts of particular neurons at a much higher duty cycle than is possible with the continuous movement of the galvanometer based scanning. These experimental results were for sampling points on one neuron with 5 regions of interest and 5 separate neurons respectively. There are, however, considerable practical difficulties in using AODs to their best advantage which will be discussed in more detail in chapter 3.

In summary therefore, at the start of the PhD, three properties of neural networks posed a considerable, and unsolved, technical challenge: (1) neurons are spatially distributed in 3D space, (2) signalling events are brief (action potentials ~ 1ms) and flow through networks rapidly and (3) only a small fraction of neurons (typically ~1-

10%) are usually active at once. As indicated in Figure 1.2, in 2005 there were no demonstrated techniques capable of imaging, identifying and monitoring the functionality of 3D networks of neurons in the large region of spatial and temporal resolution between fMRI and patch clamping of individual neurons. The objective of this PhD was thus to develop an instrument with this capability.

2-photon Microscopy – principles, and limits to speed and duty cycle.

Basic principles

Figure 1.3 illustrates the basic principle of 2-photon fluorescence microscope. (Denk, Piston et al. 1995; Zipfel, Williams et al. 2003; Helmchen and Denk 2005). Unlike conventional fluorescence, where the energy of the single excitatory photon must be greater than the energy of the emission photon, two photon fluorophores can absorb 2 photons at a time of half the energy normally required in order to excite an internal state of higher energy than the emission wavelength. The excited state then decays both non-radiatively and radiatively, giving off a photon of fluorescence at the fluorophore emission wavelength Figure 1.3 a). Thus the emission wavelength, typically in the red or green depending on the type of fluorophore molecule, is shorter wavelength than the excitation wavelength. The primary advantage of using this type of fluorescence for microscopy of brain tissue is that this allows the excitation wavelength to be in the near infrared, typically 700-1000nm wavelength. At these wavelengths absorption, damage and optical scattering are many times less than if the excitation is in the blue or ultra violet range Figure 1.3 b). This enables 2-photon microscopy to be used for imaging up to 1mm deep in brain tissue, about an order of magnitude greater than with blue excitation.

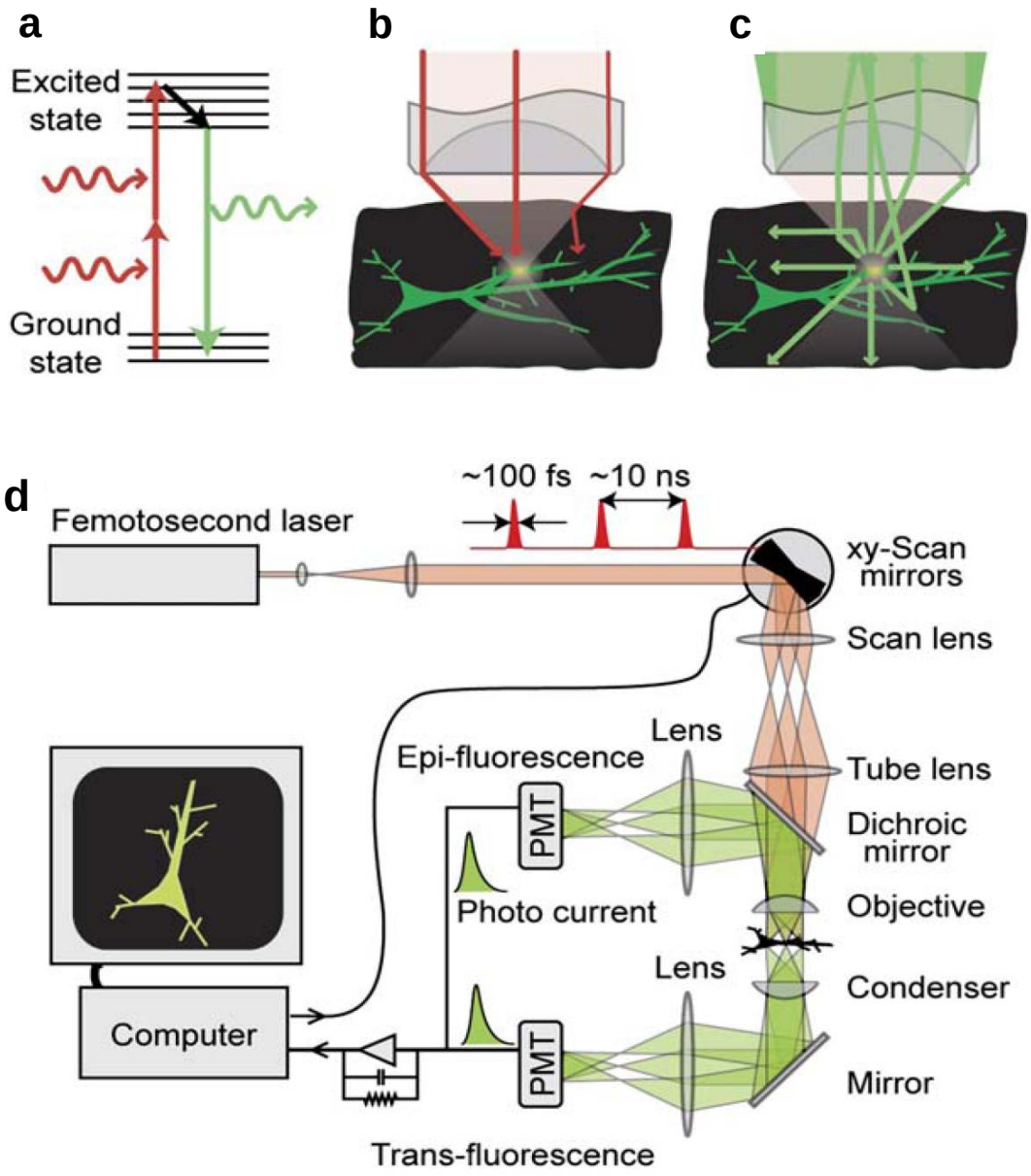

Figure 1.3 Diagrams from Zipfel (Zipfel, Williams et al. 2003) to illustrate the principles of operation, a-c) and system layout d) of the 2-photon microscope. a) Two photon excitation of a fluorophore occurs when the incoming long wavelength light intensity is so high that it absorbs two photons to excite an energy level in the molecule that normally would require a single photon of half the wavelength. The fluorescence emission is then at a shorter wavelength than the excitation wavelength. b) The near infra red excitation laser light is focused down through the tissue to form high intensity at the focus despite some scattering shown. c) The green emitted fluorescence is collected and projected onto sensitive detectors by the objective (and maybe condenser lens). d) As the focused spot is scanned in a raster pattern by the computer controlled galvanometer mirrors, the faint detected signal is amplified by photomultiplier tubes (PMTs) and plotted at the correct position on a computer screen to form the image.

Two photon excitation requires two photons to arrive at the same time at the fluorescent molecule. This only occurs with any significant probability under extremely intense illumination. The Titanium-Sapphire laser is the widely preferred source for such systems. This laser can emit 1-3 W average power in the wavelength range 700-1000 nm. By using mode locking of the laser cavity, all the output energy is concentrated into a stream of ultra short pulses of light in the range 70-140 fs long, at a rate of around 80 MHz (1femto-second = 10^{-15} s = one millionth of a nanosecond). This time compression concentrates the light intensity by a factor of about 10^5 thus increasing the probability of 2 photons arriving together at the fluorophore by 10^{10}. At the speed of light, these Ti-sapphire laser output pulses are only about 30 μm (or 35 wavelengths) long. Such short pulses therefore also have a relatively broad spectral width because of Heisenberg's uncertainty principle. The typical spectral width for 800 nm Gaussian laser pulses of 100 fs FWHM (full width half maximum) is 10.6 nm. As will be discussed in chapter 3, this broad spectral width has significant consequences for the use of diffractive optical devices such as acousto-optic deflectors. In the 2-photon microscope, the intensity of the laser light is further enhanced by the spatial convergence as it approaches the focus of the objective in the specimen (Figure 1.3c). Photons can arrive at the focus at over 10^{24} photons/s. This is a high enough rate to elicit sufficient 2-photon fluorescence, that sensitive photo detectors can monitor the signal and reconstruct the 3D image of fluorophore emission (Figure 1.3 d).

A typical 2-photon microscope layout is shown in Figure 1.3d). Galvanometer mirrors scan the beam, usually in a raster pattern. The sensitive photomultiplier tubes (PMTs) pick up a light signal that is proportional to the photon detection rate of the fluorescence (shown as green). A master computer that controls the drive signals to the galvanometer mirrors, and therefore knows microsecond by microsecond where the focal spot is focused is therefore able to reconstruct the 2D image of the object being scanned beneath the objective. For imaging in 3D after each 2D frame in the XY plane, either the objective or the specimen is moved along the Z axis and a new XY plane scanned. An important aspect of 2-photon microscopy is the fact that as emission is proportional to light intensity squared, the 2-photon emission is only

emitted for a very small region around the focal point in all three XYZ directions. Because emission rate falls off as the square of intensity, very little 2-photon light is emitted from the unwanted region of the incoming laser beam above the focus. This 'self sectioning' ability of 2-photon systems means that the extra complexity and light loss of confocal light detection systems (Wilson and Carlini 1984; White, Amos et al. 1987; Wilson and Carlini 1987; Wilson 1990; Amos and White 2003) is not necessarily needed for 2-photon system, except if the very highest spatial resolution is a dominant requirement.

At the focus of the Ti sapphire laser beam a sub micron volume of the neural tissue is thus excited by the intense laser light. The amount of short wavelength 2-photon fluorescence then depends on the density of fluorescent dye molecules in this excited volume and the 2-photon conversion efficiency of these molecules.

Fluorescent dyes for functional optical imaging

Different fluorescent dyes are used for different applications. For instance, for showing the structure of individual neurons by infusion of dye from a patch clamp, one of the common dyes to use is Alexa594. For functional optical imaging, there is choice of using membrane voltage sensitive dyes and Calcium sensitive dyes. The action potentials of neurons are usually measured by measuring the electrical potential across the cell membrane. Voltage sensitive dyes (Antic and Zecevic 1995; Nelson and Katz 1995; Tsutsui, Karasawa et al. 2008) are lipophylic dyes that dissolve in the membrane of a cell and respond rapidly (less than 10 μs) to the membrane potential. However voltage sensitive dyes in practice have a poor signal to noise ratio resulting from the small change in fluorescence with voltage ($\Delta F/F <$ a few %). This necessitates wide field monitoring of the signal of large numbers of neurons (Petersen, Hahn et al. 2003; Ferezou, Bolea et al. 2006). Also, unfortunately to date no one has succeeded in developing a satisfactory voltage sensitive dye that operates with 2-photon excitation so that it can be used at high speed in deep tissue.

Calcium sensitive dyes (Lev-Ram, Miyakawa et al. 1992; Stosiek, Garaschuk et al. 2003) change fluorescence intensity in response to changes in calcium concentrations inside the cells. One of the important biochemical changes that occur as part of the

complex sequence of events at the membrane is a sudden increase in calcium concentration. This is a result of the influx of calcium at voltage gated calcium ion channels (Hille 2001). Calcium, which is toxic to cells at high concentration and hence actively pumped out of cells, is widely used at very low concentrations for internal biochemical signalling on a wide range of timescales. Particular dyes have been developed which monitor calcium concentration, becoming more efficient 2-photon fluorophores as calcium concentration increases. By injecting or diffusing such dyes into neurons it is possible to monitor action potentials indirectly by monitoring the fluorescence.It has been shown (Sabatini and Regehr 1999) (DiGregorio, Negrete et al. 2000; Higley and Sabatini 2008) that, with care to collect fluorescent photons efficiently, and for total collection times of the order of 8-20 μs per voxel, it is possible to obtain sufficiently high signal to noise ratio to reliably monitor the timing of action potentials down to millisecond resolution.

To date, the calcium sensitive dyes are proving more practical for optical functional imaging of small networks of neurons than voltage sensitive dyes. One significant factor is that the calcium sensitive dyes invariably have a slow decay response (tens to hundreds of ms) compared to the rise in fluorescence immediately after the action potential (approximately 1ms with optimised dyes). This gives the calcium response an integrating or ‘memory’ response which aids the detection of action potentials as soon as the system sampling interval at a ROI is greater than the approximately 1 ms time of one action potential.

The fluorescent signal increases as the square of laser intensity, so it is also necessary to have sufficient laser power at the point of focus. Typically, at least 2.5 mW average power would be necessary at the focus in the specimen; this corresponds to the order of 1 MW/cm^2 at the focus. These figures are important to bear in mind when designing the overall system.

2D vs. 3D – number of addressable neurons that can be chosen for optical functional imaging

Perhaps the most important limitation of nearly all conventional optical microscopes, including laser scanning 2-photon microscopes, is that they are designed to image in a single focal plane(X-Y).

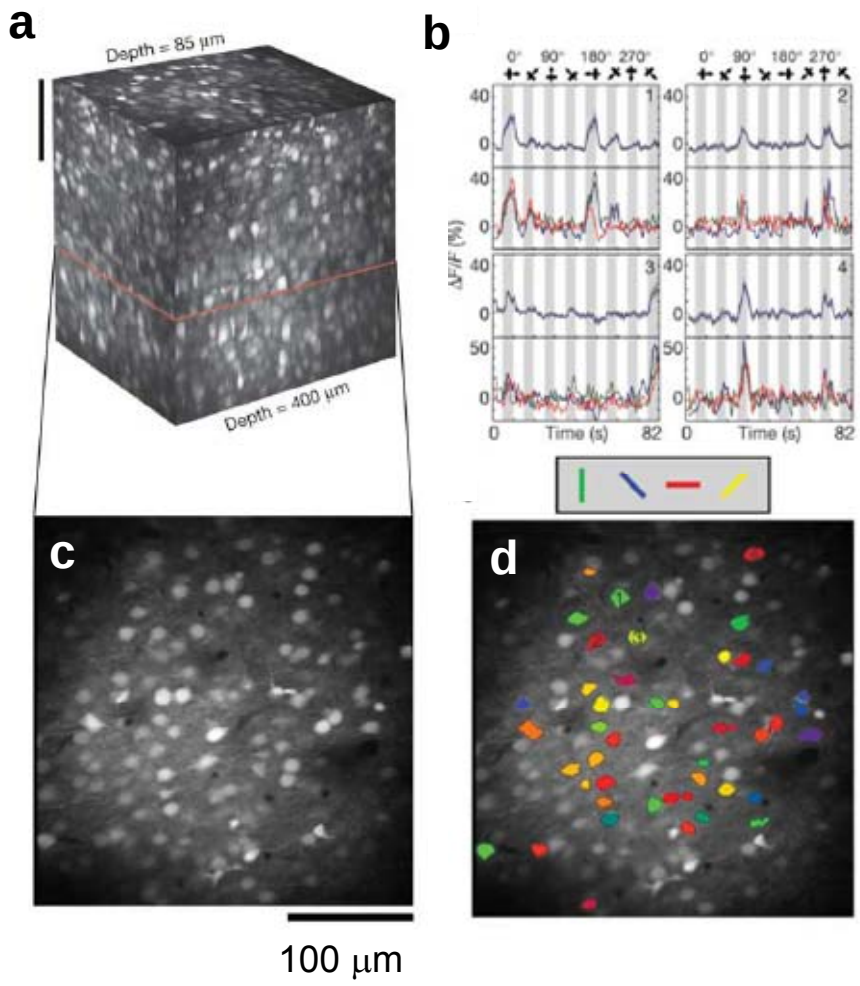

Figure 1.4 functional optical imaging of the brain using conventional two photon microscopy. The images show a) a 400×400×400 µm region of the visual cortex of a rat. b) Measured calcium sensitive fluorescence images from particular neurons showing how the calcium level over many 10s of seconds is affected by the excitation on the rats retina. In the cortex, particular neurons are sensitive to image edges orientated in particular directions as indicated by the different colours. c) A typical 2D section that took the order of 1 second to collect. d) Regions of interest, particular neuron bodies sensitive to particular orientations as indicated by their colour. Modified from (Ohki, Chung et al. 2005).

One of the limitations this causes are illustrated by Figure 1.4 (Ohki, Chung et al. 2005) which shows how 2-photon calcium imaging was used to analyse the structure of the orientation sensitivity of neurons in the visual cortex of a rat in 3D. Typically, high resolution 2D raster scanning takes at least the order of 1 second for each 2D plane, leading to minutes of elapsed time for full 3D scans. The 3D block of rat cortex imaged in the figure has 300 μm sides and contains the order of 1000- 3000 neurons that can be imaged. A single 2D plane on the other hand contains only 30 to 50 neurons that are bright enough (well enough aligned with the 2D plane) for functional imaging as shown in the 2D sections. It is therefore clearly desirable that a machine for optical functional imaging should not only be able to point in 2D, but also in 3D. It is also extremely likely that it will be difficult, if not impossible, to correctly interpret the nature population coding in neural tissue from purely two dimensional data. The networks themselves are 3D and it is very likely that population codes themselves are 3D spatial plus temporal codes.

Options for high speed 3D focusing

Several approaches have been proposed that allow rapid functional imaging in 3D and higher speed random access point measurements. These include sinusoidal displacement of the objective lens with a piezoelectric driver (Gobel, Kampa et al. 2007), the use of deformable mirrors (Zhu, Sun et al. 1999) and lenses (Oku, Hashimoto et al. 2004), two conjugate objective lenses with a piston mirror (Botcherby, Juskaitis et al. 2007), the use of many fixed optical fibres in 3D (Rózsa, Katona et al. 2007) and AODs for focusing and scanning (Reddy and Saggau 2005; Reddy, Kelleher et al. 2008).

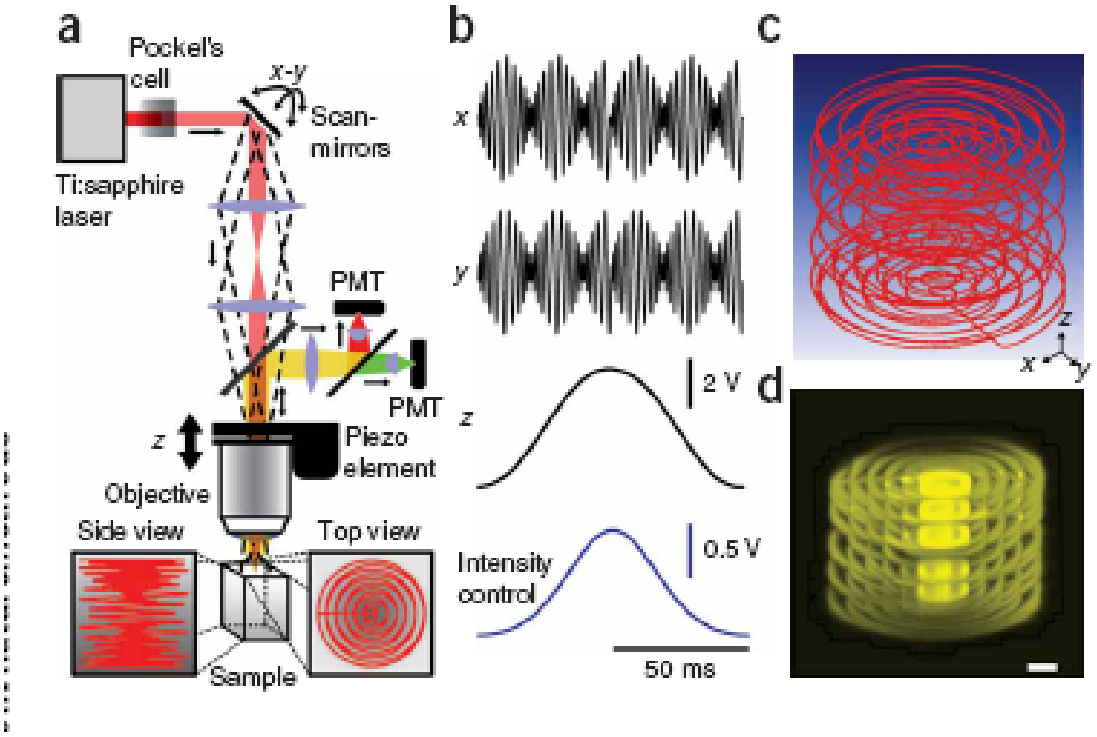

Figure 1.5 3D 2-photon microscope using an oscillating microscope objective driven by a piezo-electric actuators to scan up to 250μm along the Z axis at up to 10Hz. (Gobel, Kampa et al. 2007). a) conventional 2 photon microscope with b) approximately sinusoidally driven XY deflection mirrors and a 10Hz Z oscillating objective lens. Note c) the 3D spiral path carefully computed to pass through the maximum number of cell bodies in the minimum time and d) image of one complete cycle of laser spot movement in a fluorescent dye solution.

One of the first to be successfully demonstrated was (Gobel, Kampa et al. 2007). In addition to rapidly scanned XY plane galvanometer mirrors, the system uses an oscillating microscope objective driven by a piezo-electric actuators to scan up to 250 μm along the Z axis at up to 10Hz. Illustrations from (Gobel, Kampa et al. 2007) showing the apparatus and results are reproduced here in Figure 1.5. Note that after initial raster scanning of the whole volume of tissue, the path of the laser spot is pre-calculated to cross as many of the cell bodies forming the ROIs in the tissue as possible. The complex 3D spiral closed loop motion enabled them to monitor up to 90% of the target cells in a 250 μm cube of tissue with an overall imaging time per 3D 'frame'of 100ms. As the neuronal bodies being studied were quite large, despite the long path the laser spot was programmed to take through 3D space, the laser spot was in cell bodies of interest for about 5% of the total scan time. Experimentally the paper reports results for functional imaging of up to 500 neurons within the 250μm

cube of tissue at 10Hz this is about a factor of 10 higher than possible with a 2D scanner.

An interesting recently reported system with the potential for much more rapid refocusing in Z is the piston mirror system (Botcherby, Juskaitis et al. 2007). Although this is still a mechanical system it has the potential for operation at speeds up to around 1kHz cycle time as it uses a light weight piston mirror that sits in air at the focus of an auxiliary objective. There is thus no need to move the objective. By matching the angular convergence of the auxiliary objective so that it matches the sine and the Hershel conditions with the main water immersion objective, a high degree of correction of the spherical aberration that would otherwise limit the Z displacement of a high NA remotely focused objective has been demonstrated. I include further discussion on the prospects for such 3D scanning systems in the discussion of chapter six.

In the final part of the introduction I introduce the basic concepts for pointing scanning and focusing in 3D using AODs and how such a system can be optically coupled into a microscope.

Introduction to AODs for scanning, pointing and focusing

Principle of operation of AODs

An acousto-optic deflector is a transparent crystal made of a material with a refractive index that varies rapidly with mechanical stress such as compression or tension. If a sound wave propagates through such a crystal, the peaks and troughs of the wave produce a moving optical refractive index grating. A diagram of such a device is shown in Figure 1.6. A piezo-electric transducer converts an electrical signal to a travelling ‘curtain’ of sound waves in the crystal. The curtain propagates across the crystal locally modulating the refractive index in a pattern that mimics the electrical input. The modulated refractive index in turn modulates the phase of the incident laser beam propagating approximately at right angles to the sound wave through the crystal. This causes diffraction of the laser beam. For a simple sine wave input signal at a frequency f_{ac}, the total angular deflection of the beam is given by (Xu and Stroud 1992):-

$$\phi = \frac{\lambda_0 f_{ac}}{V_{ac}}$$ equation 1.1

Where λ_o = optical wavelength in free space

V_{ac} = acoustic velocity in the crystal

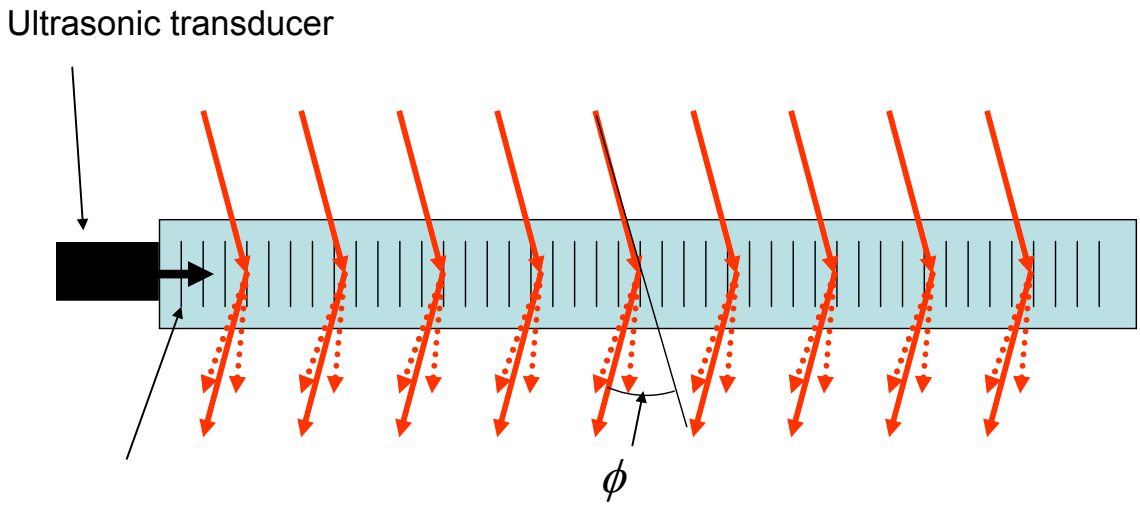

Figure 1.6 Bragg diffraction from a travelling ultrasonic sound wave in an Acousto-Optic Deflector (AOD). The red incoming arrows represent the laser light. The transducer on the left converts the incoming radio frequency electrical signal into a shear mode sound wave in the transparent tellurium dioxide (TeO_2) crystal. This travels at about 600m/s across the 15mm aperture crystal in only 25μs. The laser light is diffracted off the refractive index variations indicated by the vertical black lines which represent regions of higher compression from the sound wave peaks. Changing the drive frequency changes the angle of diffraction ϕ.

For near infrared and visible operation the crystal is often made of Tellurium Dioxide (TeO_2), an unusual anisotropic crystal with one of the highest known efficiencies for coupling light and sound waves. The structural anisotropy of the crystal causes unusual but useful variations in the speed of both light and sound as a function of 3D direction of propagation in the crystal.

There are two possible modes of operation of AODs, the first, known as Raman–Nath (Xu and Stroud 1992) has a thin curtain of sound and operates like a 2D surface relief grating. This diffracts light into a whole series of diffraction orders (-n...-1 0 1 ...+n). The angle of incidence of the light is not critical, but the efficiency in any particular

diffraction order is low because of the multiple orders of diffraction. The second mode of diffraction is known as the Bragg mode, shown in Figure 1.6. The sound wave has significant thickness in the direction of propagation of the light wave (the thickness is approximately equal to the length of the acoustic transducer in this direction and is illustrated by the vertical length of the black line sound wave peaks in the diagram). This means that the diffraction is from a 3D stack of high or low index sheets i.e. diffracting from a 3D structure like X rays diffracting off the planes of a crystal. This also means that for the optimum laser input direction the diffraction is concentrated into one particular diffractive order, usually the first (-1) order at a very high efficiency, theoretically approaching 100% at particular acoustic drive powers. Note that undiffracted light that propagates straight through the crystal is referred to as zero order light and may need to be suppressed to avoid unwanted interference. Note also from this equation that, in contrast to a galvanometer mirror used as an angular deflector that the deflection of the laser beam is directly proportional to its wavelength. Thus, higher wavelength components of light will be deflected by more than lower wavelength components. This causes a serious chromatic aberration effect to be discussed in chapter 3.

Forming a spherical lens with AODs

It is well known (Xu and Stroud 1992) that if the drive frequency of an AOD is ramped rapidly, the delaying effect of the acoustic wave propagating across the crystal causes divergence or convergence (‘focusing’) of the laser beam.

Assume the acoustic wave is ramped such that its frequency increases or decreases with time linearly, by giving it the form:

$$f_{ac}(t) = f_{ac}(0) + at \qquad \text{equation 1.2}$$

Where a is the ramp rate and is measured in MHz per second.

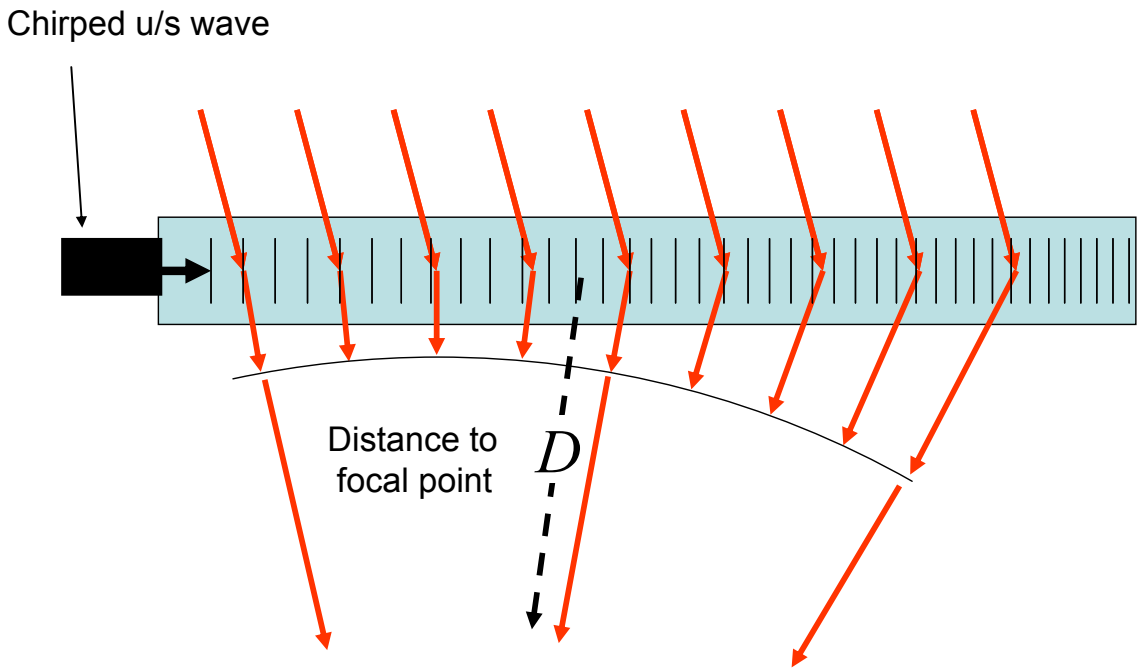

Figure 1.7 Diffraction from a chirped RF drive waveform which produces the ultrasonic (u/s) wave propagating to the right across the crystal, note acoustic wavelength (distance between vertical black lines) is smaller on the right of the crystal because the RF drive frequency in this case is decreasing with time. Chirping the drive frequency at a linear chirp rate produces a perfectly circular wavefront with a radius of curvature *D*. Note that in 3D, the lens formed is cylindrical bringing light to a line focus at the focal point with line perpendicular to the page in this diagram

Figure 1.7. shows the situation where the chirp rate a is negative. As the angle of diffraction is proportional to the frequency of the acoustic wave, those parts of the laser beam that are deflected by the high-frequency portion of the acoustic wave will be deflected more than those parts which are diffracted by the low frequency portion. It can be seen that the effect is to focus the laser beam at a position in the direction of the dotted arrow in the figure. The distance D to the focal position in the vertical direction is given by (Xu and Stroud 1992):

$$D = \frac{V_{ac}^2}{\lambda_0 a} \qquad \text{equation 1.3}$$

As is also illustrated in Figure 1.7 and Figure 1.8a, the acoustic wave moves to the right at the acoustic wave velocity V_{ac}. The focus created by the converging laser beam will therefore also move to the right at the acoustic velocity. Therefore single

AODs can be only used to focus a laser to a position that moves at the acoustic velocity V_{ac} and the focal distance is strictly determined by the chirp rate. For this reason, the focusing effect of AODs was usually regarded (Xu and Stroud 1992) as an unwanted side effect in most practical applications. The fact that the focusing only occurs in one direction means that it introduces astigmatism into the laser beam which then can only be optically corrected for one particular scan rate.

The range of acoustic frequencies that may usefully be propagated through the crystal is limited because the diffraction efficiency drops rapidly outside the design range of the AOD. Figure 1.8b shows the frequency of the acoustic wave as it varies with time and Figure 1.8c shows the frequency of the acoustic wave as it varies with distance.

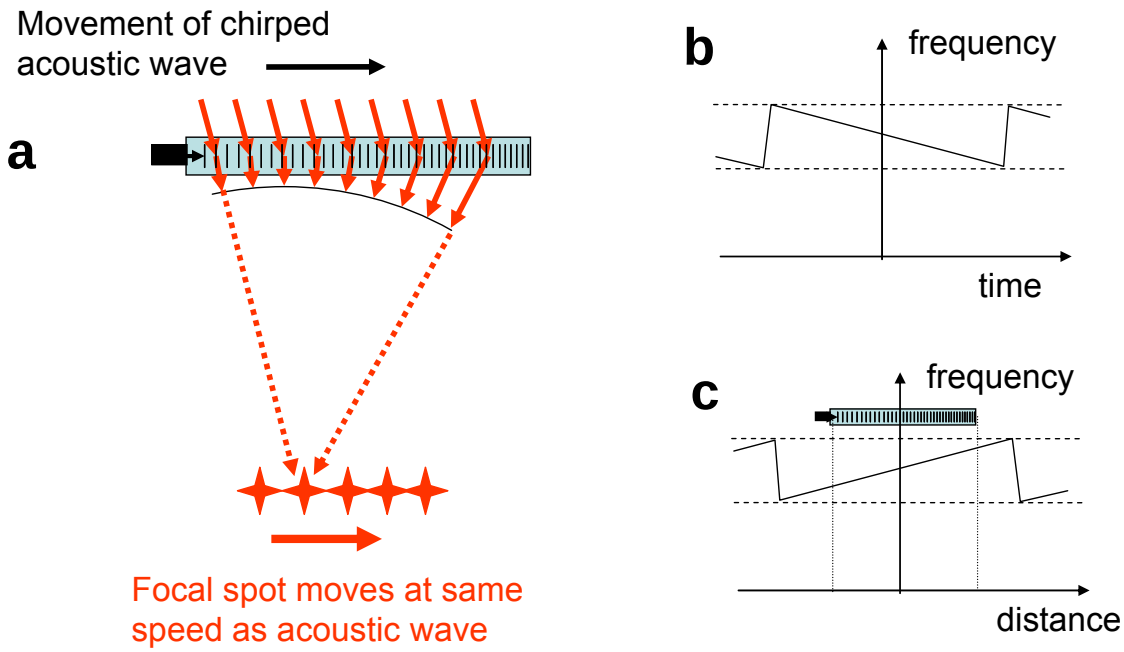

Figure 1.8 a) Cylindrical lens with the focal point is moving at the speed of sound to the right. b&c) two diagrams plotting drive frequency vs. time b) against time at fixed spatial position , c)against space at a fixed time. Note the drive frequencies have to be kept within the high efficiency drive bandwidth of the AOD.

As can be see from Figure 1.8b, it is necessary to keep the frequency of the acoustic wave between the limits f_{min} and f_{max}. It is therefore not possible to indefinitely chirp the frequency of the acoustic wave and, once the frequency reaches f_{min}, it is necessary

to reset the frequency to f_{max} such that the chirping can continue. This creates a "saw-tooth" graph in Figure 1.8b. A similar saw-tooth pattern occurs in Figure 1.8c, but it is reversed because the frequencies present in the acoustic wave on the right-hand side of the crystal represent frequencies at an earlier time point than the frequencies present in the acoustic wave at the left-hand side of the crystal. For commercial TeO_2 AODs, typical values for f_{min} are 50-60 MHz and typical values for f_{max} are 90-100 MHz. These frequency limits cause the maximum continuous total scan time to be limited to $Tsmax = (f_{max} - f_{min})/a$. Because it is necessary to wait one AOD fill time for the reset discontinuity to propagate right across the crystal before gathering data from the focused laser spot, there is a limited duty cycle:

$$MaxDutyCycle = (Ts\max - AODfill)/Ts\max \qquad \text{equation 1.4}$$

This reduces as the absolute value of ramp rate a increases becoming zero when $Tsmax$ reduces to the AOD fill time. Thus there is a maximum ramp rate and resultant shortest focal length determined by the AOD physical parameters.

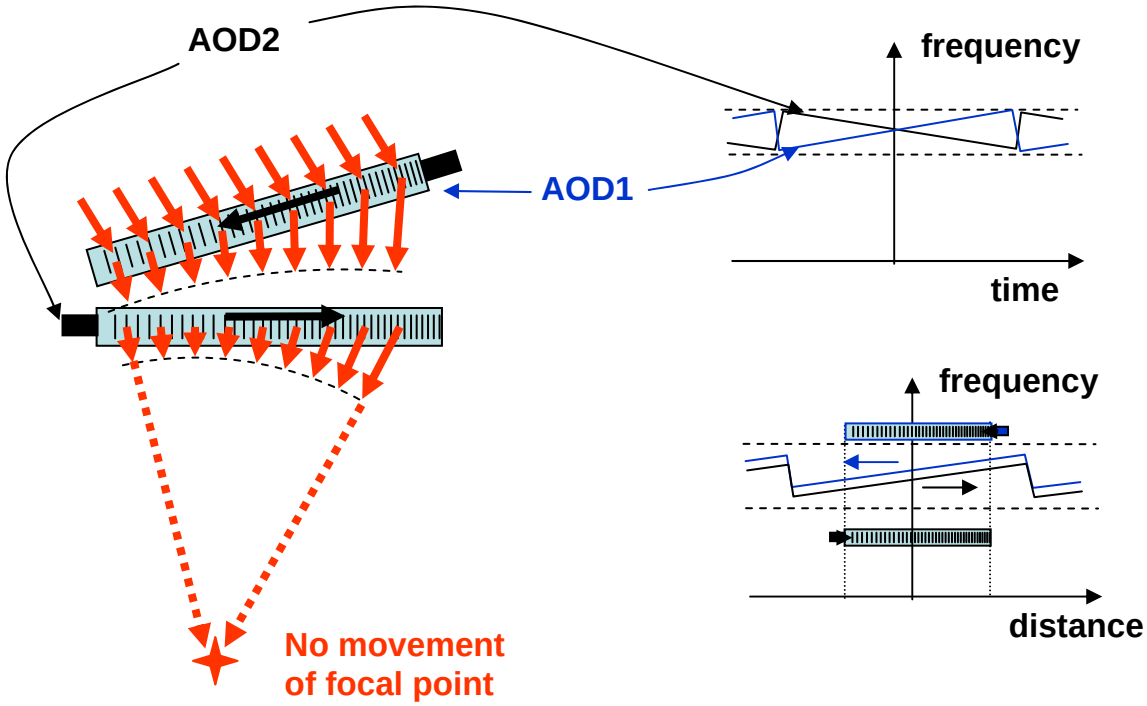

Figure 1.9 Dynamic cylindrical lens with stationary focus. This is the first proposed and demonstrated system for producing a stationary focus beneath a pair of AODs with counter propagating sound waves (Kaplan, Friedman et al. 2001). Note that for a stationary focus the wave front curvature induced by the two AODs must be equal so that the lensing effect is split equally between the two AODs.

Kaplan (Kaplan, Friedman et al. 2001) showed for the first time how to make use of two AODs in series to cancel out the lateral movement of the focal spot and dynamically control the Z focus of the laser beam. The basic principle is illustrated in Figure 1.9. In this configuration, a second AOD crystal and ultrasonic transducer is utilised and the ultrasonic waves in the AODs propagate in opposite directions. In Figure 1.9 the upper AOD has an ultrasonic wave propagating from the right to the left and the lower AOD has an ultrasonic wave propagating from the left to the right. The first AOD deflects the input laser beam to become a converging laser beam with the (virtual) focal spot moving from the right to the left. The chirp on the second AOD is such that it doubles the convergence of the beam and exactly compensates for the movement of the focal point of the laser beam so that the resultant (real) focus is stationary.

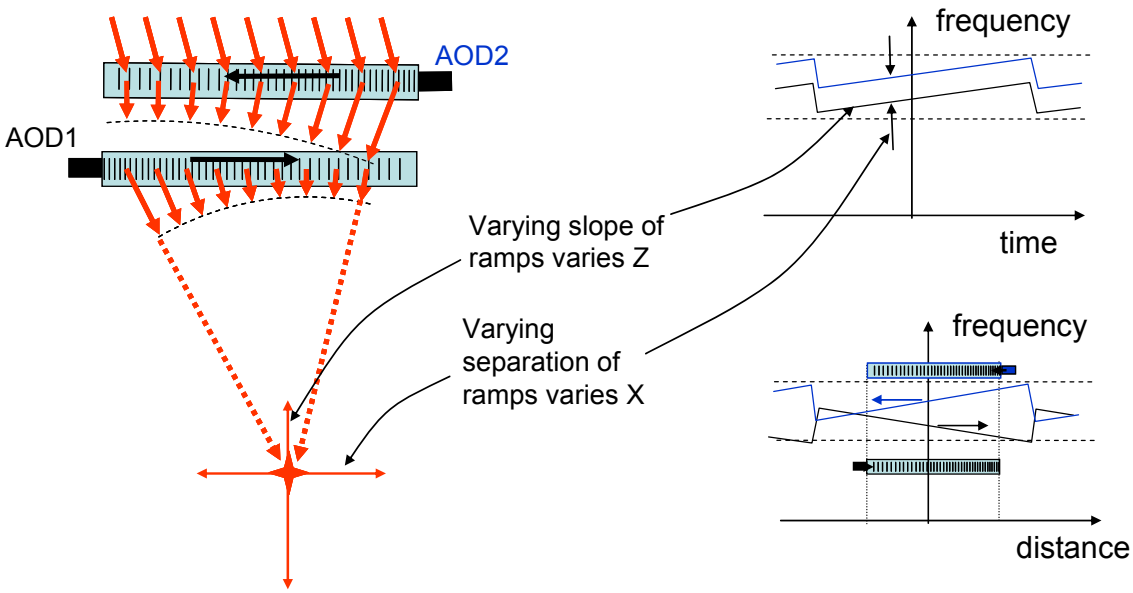

Figure 1.10 An AOD pair acting as a cylindrical lens that can focused over an XZ field of view as indicated by the red arrows. This is called the Inverted Bragg Configuration (IBC). It not only produces a stationary focal spot, but also cancels out the chromatic aberration at the centre of the field of view. This is so called because unlike in the Kaplan configuration of the previous figure, the Bragg diffraction of the counter-propagating waves is inverted in the two AODs.

Neglecting the separation between the AODs, the distance to the stationary focus is therefore half the distance to the focus of a single AOD and is given by:

$$D = \frac{V_{ac}^2}{2\lambda_0 a} \qquad \text{equation 1.5}$$

By modulating the ramp rate *a* at high speed, Kaplan was able to demonstrate the shifting of a focus along the Z axis at up to 400 kHz without any X displacement. He pointed out that by shifting the frequency separation of the ramps as illustrated in Figure 1.10 [1] that the X position could be controlled at will. Finally, as these AODs only focus in one 2D plane (the XZ plane) they produce a line focus perpendicular to the plane of the page (in the Y direction). To solve this, he suggested that two more AODs should be added, rotated 90 degrees about the Z axis, so that the input laser beam could be focused independently in the YZ plane to a point in 3D as illustrated in Figure 1.11. The four AODs can equally well produce diverging wavefronts.

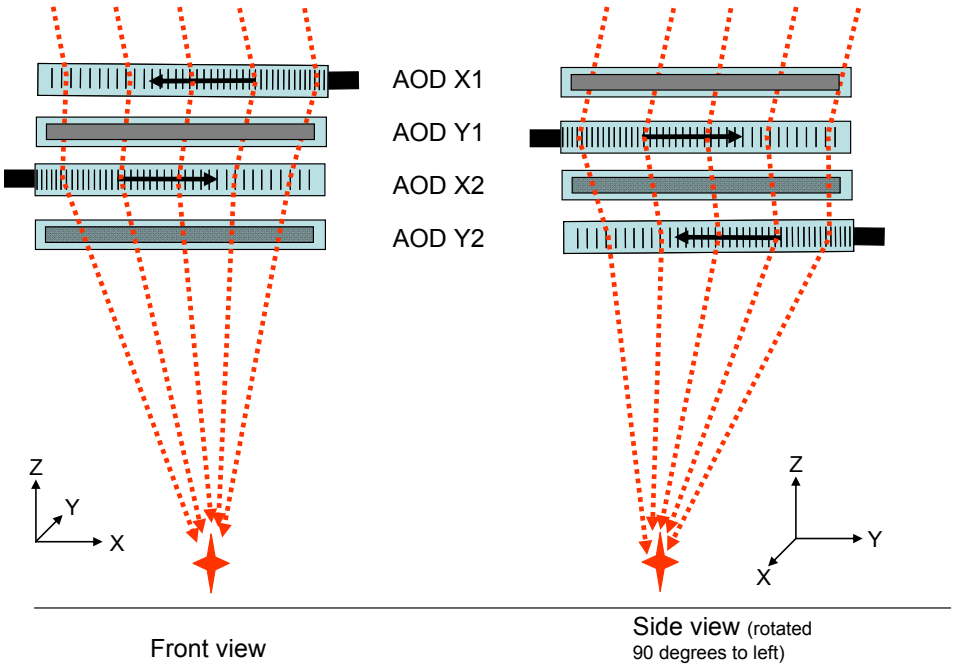

Figure 1.11 Spherical acousto-optic lens with stationary focus. It uses four AODs interleaved as shown here to convert the two cylindrical lenses formed by the XZ and YZ pairs of AODs to form a dynamic spherical lens that can bring light to a focus anywhere within its 3D field of view.

[1] Note the slightly different configuration of AODs used by Kaplan in figure 1.9 and by us in subsequent figures, this will be discussed in more detail in chapter 2.

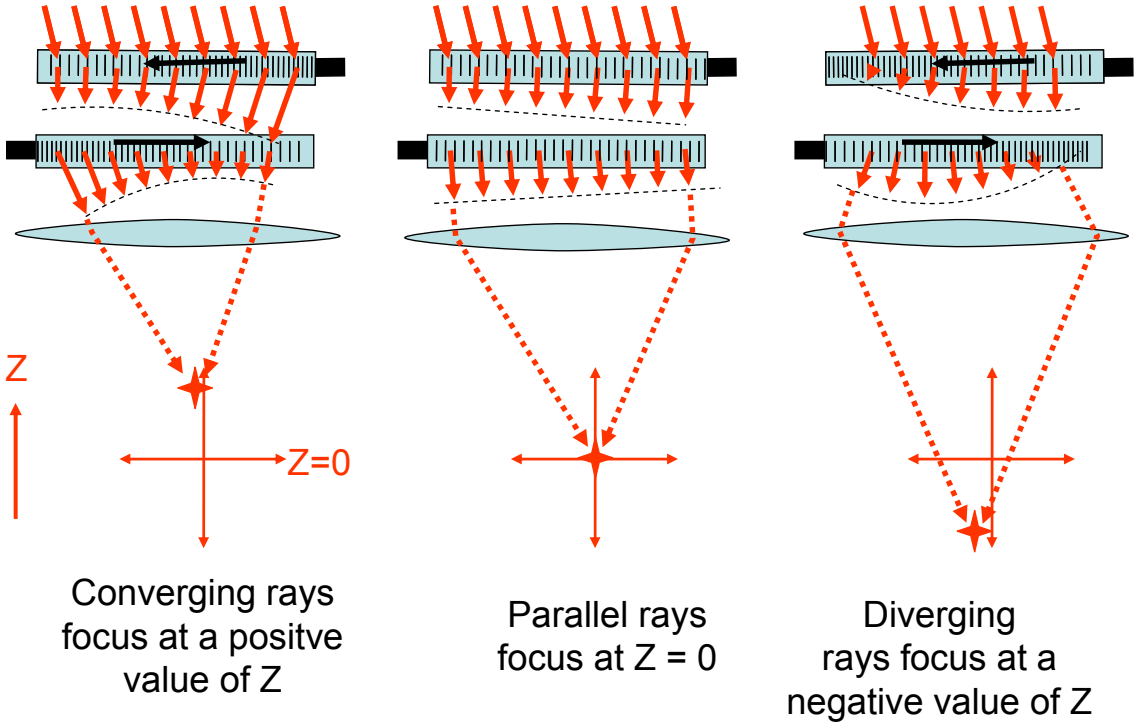

Figure 1.12 a subsequent lens system can be used to bring the converging or diverging light from an Acousto Optic Lens (AOL) to a real focus either above or below the natural focus of the lens.

To use these capabilities in a real system, a subsequent lens system (Figure 1.12) is used to bring converging, plane or diverging wavefronts to a real focus at different Z positions. The four AODs thus form an Acousto-Optic Lens (AOL) that enables a stationary focused point to be produced anywhere in a 3D volume of space limited by the field of view of the system and that can jump from any position to any other position at speeds only limited by the AOD fill time.

Proposed overall system layout

To couple the AOL into a two photon microscope, the image formed by the first lens after the AODs is relayed using a sequence of telecentric relays that include the tube lens and objective of the microscope as the final telecentric pair. This is illustrated in Figure 1.13. A telecentric relay is an optical system, usually a pair of lenses that relay an input image to an output field. It has the property of constant magnification independent of the Z position of the object and image. I discovered this was important in my first Matlab geometric optic models (not shown) of AODs coupled to lens systems which showed that unless the relays were telecentric the X, Y and Z

magnification varied with the Z focus of the AODs. Referring to Figure 1.13, if there was only one relay made with two lenses of focal length *f1* and *f2*, then if the first image is a distance *f1+Z1* from lens 1, the lenses are separated by *f1+f2* and the image 2 is at a distance f2-Z2 as shown, then the demagnification in the XY plane of the focal position within the field of view of image 1 is *f1/f2* and demagnification in the Z direction is $(f1/f2)^2$. So, as an example, if *f1/f2* = 20, the field of view of the image 1 focus might be 5mm in X and Y and 120 mm in Z. This would be demagnified to 250 μm in X and Y and 300 μm in Z. In a real system there are several telecentric relays whose magnification is multiplicative.

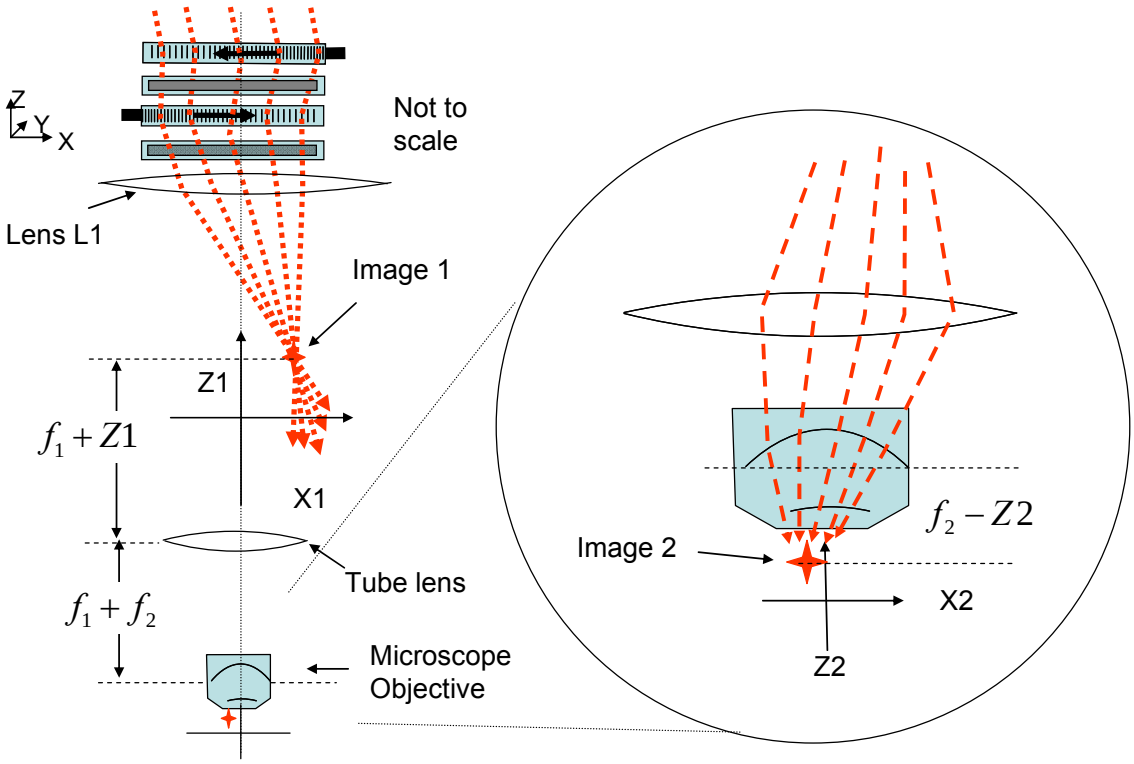

Figure 1.13 Microscope relay optics. The first image after the AOL is a real focal spot focused a distance Z1 above the natural focal plane of the tube lens by the converging action of the AOL as illustrated. This focused spot can be anywhere in the field of view of the AOL plus its first lens. This spot is then relayed through optics to a high numerical aperture but much demagnified field of view beneath the objective lens. Shown here for illustration the tube lens and objective are treated as a telecentric relay. Telecentric relays relay the field of view without Z axis changes in magnification as explained in the text.

Summary of objectives and challenges

Target specification

In conclusion to this introduction, it is useful to summarise the target specification of the system agreed at the start of the PhD after initial consideration of the neuro-scientific requirements, the basic properties of AODs, and feasible system layouts:

- Image with better than

  1×1×2 μm XYZ resolution

  in a 250×250×250 μm volume of tissue

  corresponding to 7.8 million voxels

- Focus laser beam to 30 different randomly chosen XYZ locations per millisecond
- To be able to image with sufficient signal to noise ratio for the detection of the millisecond range timing of individual action potentials monitored by Calcium sensitive dye.
- Note the Ti:Sapphire typical maximum operating range is 700 to 1000 nm. It should be possible to use the system at any chosen wavelength in order to match particular dyes.

Summary of the state of the art for 3D AOD deflectors at the start of the PhD and primary challenges

In 2001, (Kaplan, Friedman et al. 2001) had demonstrated that 2AODs could be used to scan a 2D line focus in the XZ plane at up to 400 kHz and proposed that the principle could be extended to focusing a 3D point focus anywhere in a 3D volume. In 2004 (Silver 2004) proposed combining such a scan system with a 2-photon microscope to make a 3D optical functional imaging system as described above. In 2005 (Reddy and Saggau 2005) independently published a proposal for a similar 3D system and demonstrated 2D AOD focusing in the XZ plane (not 3D focusing as implied in the abstract).

Some of the challenges that needed to be overcome in order to use AODs as the primary deflection system in a 2-photon microscope are discussed in (Reddy and Saggau 2005). These, and others, are described in detail in the following chapters, in abbreviated summary however they are:

- AODs cause chromatic aberration because, unlike galvanometer mirrors, the deflection angle is function of wavelength (equation 1.1). Since the ultra short (100fs) pulses of Ti-Sapphire lasers inherently have a broad spectrum as a result of Heisenberg's uncertainly principle, deflected focused spots have increasing chromatic aberration as deflection angle increases.
- AODs also introduce a high temporal dispersion so that, unless pre-compensated, temporal dispersion spreads the 100fs pulses necessary for high 2-photon efficiency into pulses many times longer and greatly reduces 2-photon efficiency.
- AOD efficiency is a strong function of incident and diffracted angle and hence modulates light efficiency as a function of scan position in the field of view. In particular the acceptance angle of standard commercial AODs is very narrow. This needs controlling and compensating.
- The use of telecentric relays between AODs proposed in (Reddy and Saggau 2005) makes the AOL sub-system very spread out (>1m optical path length) and makes it impractical to change wavelength of the laser source easily.
- When remotely focusing a high numerical aperture microscope objective by adjusting the convergence or divergence of the back aperture light beam, as proposed here using the AOL, spherical aberration is introduced that will limit the focusing range. This effect increases rapidly at high NA.

Summary of chapter 1

This chapter starts by describing the ‘instrumentation gap’ in neuroscience that the AOLM is aimed at reducing, it then describes the current state of the art of 2-photon microscopy for biology and in particular why it is so suitable for neuroscience. Today’s 2-photon microscopes however suffer from the same slow mechanical Z axis refocusing problem as all previous microscopes. The chapter then describes the state of the art of high speed acousto-optic lensing in 2005/6, introduces the layout of the proposed high speed 3D 2-photon microscope. It concludes by outlining the target specification for the AOLM agreed early in the PhD and outlines the primary challenges in using acousto optic lenses in a 2-photon microscope.

Chapter 2 Initial design considerations

AODs are not widely used in 2-photon microscopes for good practical reasons. Despite their high speed and high precision of deflection angle, the problems of chromatic aberration, temporal pulse dispersion and variable diffraction efficiency, to name but three, have discouraged their use. Throughout the period of the work this thesis describes we have had numerous discussions on the relative merits of different approaches. Most papers describing the various types of deflection system have a qualitative justification of the choice of deflector /focusing technology.

Before considering the design options for an AOD based system, the first section of this chapter is intended to semi-quantitatively analyse the differing deflection bandwidth requirements of **scanning** and **pointing** mode systems. This makes the benefits of the choice of a **pointing** mode system very clear for high resolution optical functional imaging with small 'sparse' regions of interest in comparison to the total scan dimensions. It also shows that in comparison with presently available mechanical alternatives, AOD based deflection systems are much better suited to pointing mode deflection applications.

The topics covered in the remainder of this chapter are the derivation of the field of view of the microscope from the physical properties of the AOD, a description of the problems caused by using telecentric relays between AODs and a novel solution based on a compact configuration of AOL and the derivation of the equations for pointing and scanning using the compact AOL configuration.

Choice of deflection system: Scanning, pointing and the sparsity problem

The problem and defining the limiting factors

It is often difficult to compare the relative merits of different techniques for optical functional imaging based on 2-photon microscopy. For instance, for 2D systems, how do you compare a resonant galvanometer deflection system that might be able to scan at 10 or even 20 kHz with an AOD deflection system with a 25 μs fill time that can point at 30 kHz to different regions of interest? This section aims to clarify the

problem by defining the separate factors that limit the speed at which two photon functional imaging can be performed and deriving the relationships between them. These limiting factors are, the minimum data collection time per ROI (region of interest), T_{ROI} , the bandwidth of the deflection system B_D and the spatial sparsity of the regions of interest within the scan volume S_S. The following section defines these terms in more detail and discusses the specification of different systems:-

Minimum data collection time per region of interest T_{ROI}. For each neuron or part of a neuron that is being monitored it is necessary to collect a certain number of photons in the brighter fluorescent state of fluorophores in order to obtain a high enough signal to noise ratio to measure the timing with a specified degree of precision (Gobel, Kampa et al. 2007). Evidence from our own experiments (unpublished) on calcium dyes in solution and from observations of the results of many others on different 2-photon microscope rigs suggests that the rule of thumb is that T_{ROI} needs to be 10 to 20 μs to get adequate signal to noise ratio for single shot monitoring of action potentials. This obviously limits the maximum number of regions of interest that can be monitored per unit time to 1/ T_{ROI} = 50-100,000 ROIs per second = 50-100 ROIs/ms. Since 2-photon fluorescence increases as the square of illumination intensity, you might expect that T_{ROI} could be reduced by a factor of 4 by doubling the illumination power, however in practice there are saturation and photo-damage effects that limit how far T_{ROI} can be reduced.

Bandwidth of the deflection system B_D. If you plot the displacement in space of the focal point of the laser microscope system vs. time you get a time series or continuous signal that can be analysed in terms of its bandwidth. This bandwidth is the deflection bandwidth required to make the laser spot follow that path.

Spatial sparsity of the regions of interest within the scan volume S_S. This is defined as the width of the linear scan dimension of the instrument's scan volume W_S divided by the average width W_{ROI} of each region of interest i.e. how many average ROIs fit across the scan frame. By definition therefore $S_S = W_S / W_{ROI}$

The duty cycle of a functional optical imaging system

We have classified two modes of deflection vs. time: scanning mode and pointing mode. In the **scanning mode** the laser spot moves through the regions of interest at a rate close to the average scanning speed of the spot through each scanning cycle. The spot displacement in a particular spatial dimension vs. time can be saw tooth as in raster scanning, or approximately sinusoidal as in spiral or Lissajous figure scanning. In **pointing mode** the laser spot is caused to dwell approximately stationary in each region of interest before transiting as rapidly as possible to the next region of interest.

The duty cycle of a functional optical imaging system is the percentage of time it spends in regions of interest compared to the total elapsed time. This is clarified in Figure 2.1 for the scanning mode. The displacement vs. time plotted here is roughly sinusoidal so that the bandwidth required of the deflection system is only $B_D = 1/T_C$ where T_C = cycle time.

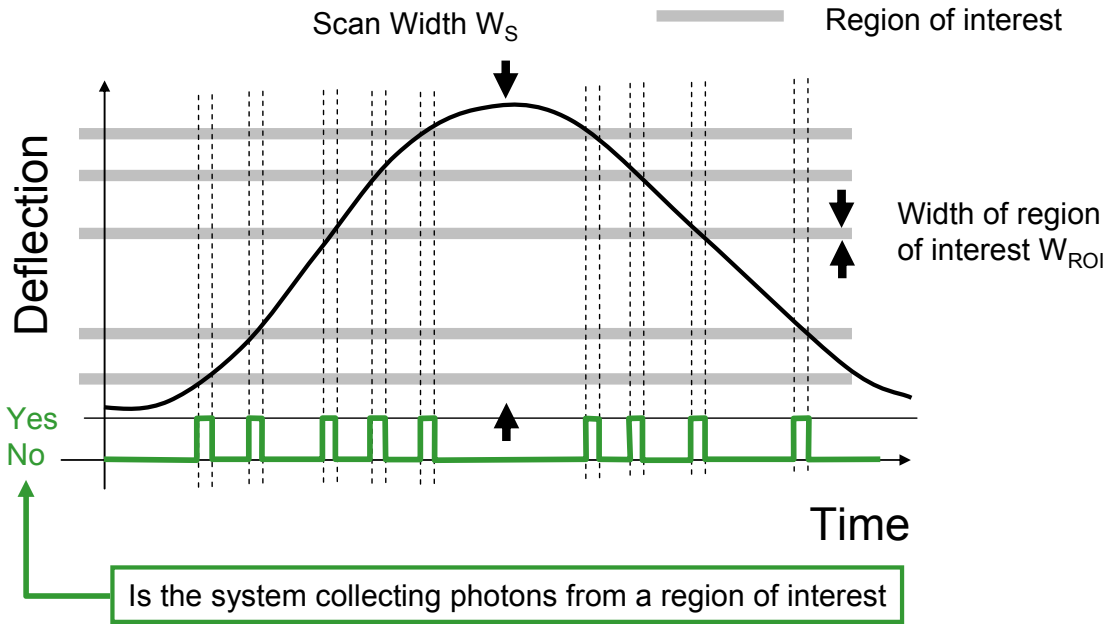

Figure 2.1 Schematic diagram showing one cycle of a one dimensional scanning system that is scanning a focused laser spot along a line and back again. There are five short regions of interest along this line indicated in grey. When the laser spot is in a region of interest it is collecting photons of interest from any luminescence there. Marked in green is whether the photons are from a region of interest or not. The duty cycle is the percentage of 'Yes' time compared to total time.

For randomly positioned regions of interest the approximate average scanning mode duty cycle $D_{Sp} = N_{ROI} / S_S$ where N_{ROI} is the number of regions of interest (to check

this equation consider if $N_{ROI} = S_S$ then the all the scan area would be full of regions of interest and the duty cycle would be 100%). The key point to note here is that as the sparsity increases, so the duty cycle reduces in proportion.

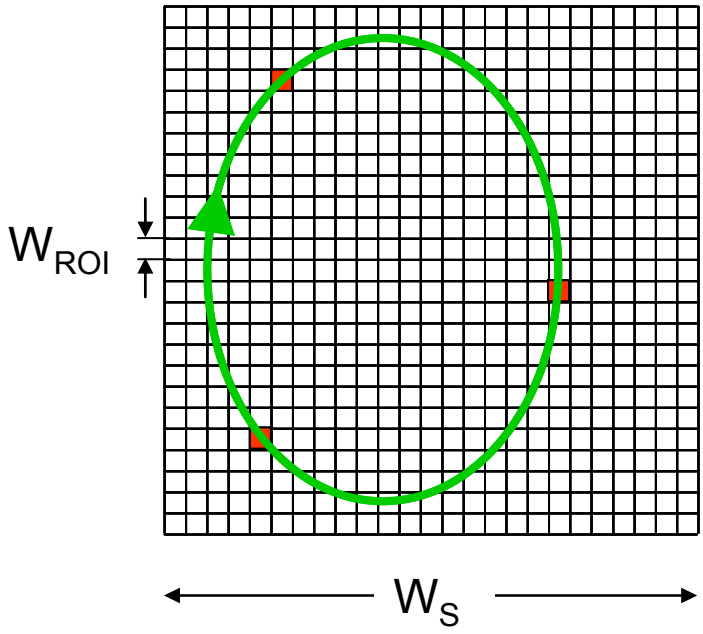

Figure 2.2 Schematic diagram showing how in two dimensions approximately sinusoidal displacement vs. time on each axis results in approximately elliptical paths being traced in space. The precise dimensions of the green elliptical path were chosen to pass through the 3 target regions of interest (ROI)s shown in red. An ellipse can be always be found to pass through any 3 randomly positioned ROIs. This is not possible for 4 or more ROIs.

It is slightly more complicated to understand the effect of sparsity on duty cycle for approximately sinusoidal displacement in 2 or 3 dimensions. (Gobel, Kampa et al. 2007) have developed fast algorithms for computing fastest possible approximately sinusoidal spatial paths vs. time through randomly placed ROIs in 3D space given defined displacement bandwidths in each dimension. They point out that for randomly positioned ROIs it is always possible to calculate the dimensions of an ellipse that passes through each of 3 points. For more than 3 points this is not possible, although occasionally it will happen that 4 or more do lie on the same ellipse. This is illustrated for two dimensions in Figure 2.2. This means that algorithms for passing through the largest possible number of randomly positioned ROIs in the minimum time can only average slightly more than 3 ROIs per cycle where the cycle time is the inverse of the highest frequency within the displacement bandwidth.

To estimate how duty cycle varies with the number of points in the target area, consider a square of side W_S containing 3 ROIs. The ROIs are on a grid of $Ss \times Ss$. Note that $Ss = W_S/W_{ROI}$. The 3 ROIs are randomly positioned as illustrated in Figure 2.2 (red squares) with the approximately elliptical path going through all three ROIs. Consider a circle of diameter 0.7 × length of the side of the square. This is approximately the same circumference as the average path length of an ellipse through any three randomly chosen ROIs, averaged over many ellipses. It is clear that the size of the ROI is inversely proportional to S_S. Simple geometry shows that the duty cycle in this scanning mode D_{Sc} is given by:

$$D_{Sc} = 3 / 0.7 \pi S_s \cdot \qquad \text{equation 2.1}$$

If you now assume that for each region of interest you wish to collect data for the minimum time required to obtain a good signal to noise ratio T_{ROI} then the duty cycle has a direct effect on the imaging time it takes to collect one data point from each region of interest and form one spatial image for one time point. The imaging time T_{img} is

$$T_{img} = N_{ROI}\, T_{ROI} / D_{Sc} = 0.73\, N_{ROI}\, T_{ROI}\, S_S \qquad \text{equation 2.2}$$

Where N_{ROI} is the number of regions of interest being scanned.

Similarly the sinusoidal scan frequency F_S, which is approximately one third of the average ROI sampling rate of the system R_S is given by:

$$F_s = R_s / 3 = 1 / (0.73\, T_{ROI}\, S_s) \qquad \text{equation 2.3}$$

Since the dimensions of neuron bodies range from 5-30 μm and the dimensions of neuronal processes range from say 0.3 to 3 μm an optical functional imaging system with a 300 μm field of view width has a spatial sparsity ranging from 10 to 1000

corresponding to duty cycles from 13% down to 0.13%. and imaging times per ROI varying from 73 μs to 7.3ms. (based on T_{ROI} = 10 μs)

Note that this derivation shows, that in the scanning mode, beyond a certain minimum, the scanning speed of a scanning mode system is not an important parameter. The system is not 'scan speed' limited, it is 'photon collection rate' limited. It is now the spatial sparsity that is important. Here, in this 'photon limited' case I have assumed that the scanning speed is reduced so that it takes T_{ROI} to pass through each ROI so that sufficient photons are collected that the signal to noise ratio is obtained in a single pass through all the ROIs. The system could be driven faster, but then it would have to make multiple passes through each ROI to build up the signal to noise ratio and the total imaging time T_{img} would be the same.

For high speed optical functional imaging with Calcium sensitive dyes it is important to note that the smaller parts of the neuron show much the fastest response. This is because as calcium diffuses away from its source (the membrane in this case) its time response slows down as in any diffusion process. The calcium can also often cause secondary calcium release from stores within the cell body. For the fastest response therefore it is important for the imaging system to be able to select the smallest possible regions of interest and therefore operate at high sparsity. This is therefore clearly a serious problem for any scanning mode optical functional imaging system that is aimed at imaging many neurons in millisecond imaging times.

Pointing Mode rather than scanning mode solves the sparsity – duty cycle problem

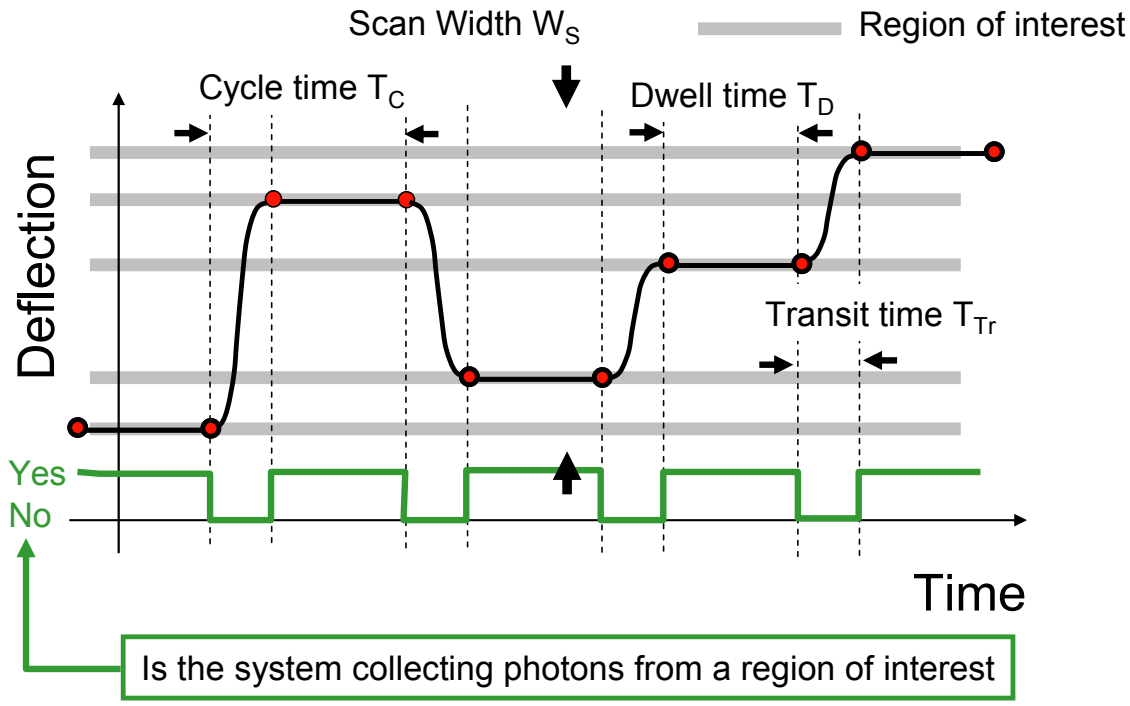

Figure 2.3 Schematic diagram of a pointing mode deflection system which accurately controls displacement vs. time to jump from one region of interest to another. The green line indicates whether the system is collecting photons from a region of interest or not. The red dots are inserted to illustrate the minimum set of sample points that would be necessary for defining deflection vs. time and hence calculating the bandwidth requirement of the deflection system.

To solve the sparsity-duty cycle problem the obvious solution is to 'stare' (i.e. focus the laser spot) at a particular ROI for a time preferably greater than or equal to T_{ROI} with a stationary spot, then jump to the next region of interest as rapidly as possible. This however requires a much higher deflection bandwidth. This is illustrated in Figure 2.3 which shows deflection vs. time for a pointing mode system monitoring the same set of ROIs as Figure 2.1. The laser spot dwells in each ROI for a time T_D and then jumps in a transit time $T_{Tr} = T_C - T_D$ to the next ROI.

The duty cycle in the pointing mode $D_{Pt} = T_D/T_C = T_D/(T_D+T_{Tr})$ and is not dependent on sparsity. This gives the pointing mode a very large advantage over scanning mode as sparsity increases. This is illustrated in Figure 2.4. In this case, for the pointing mode the parameters chosen are T_D = 16μs, T_{Tr} = 24 μs resulting in a 40% duty cycle

irrespective of sparsity. These figures are typical of those we expected to use for an AOD in pointing mode.

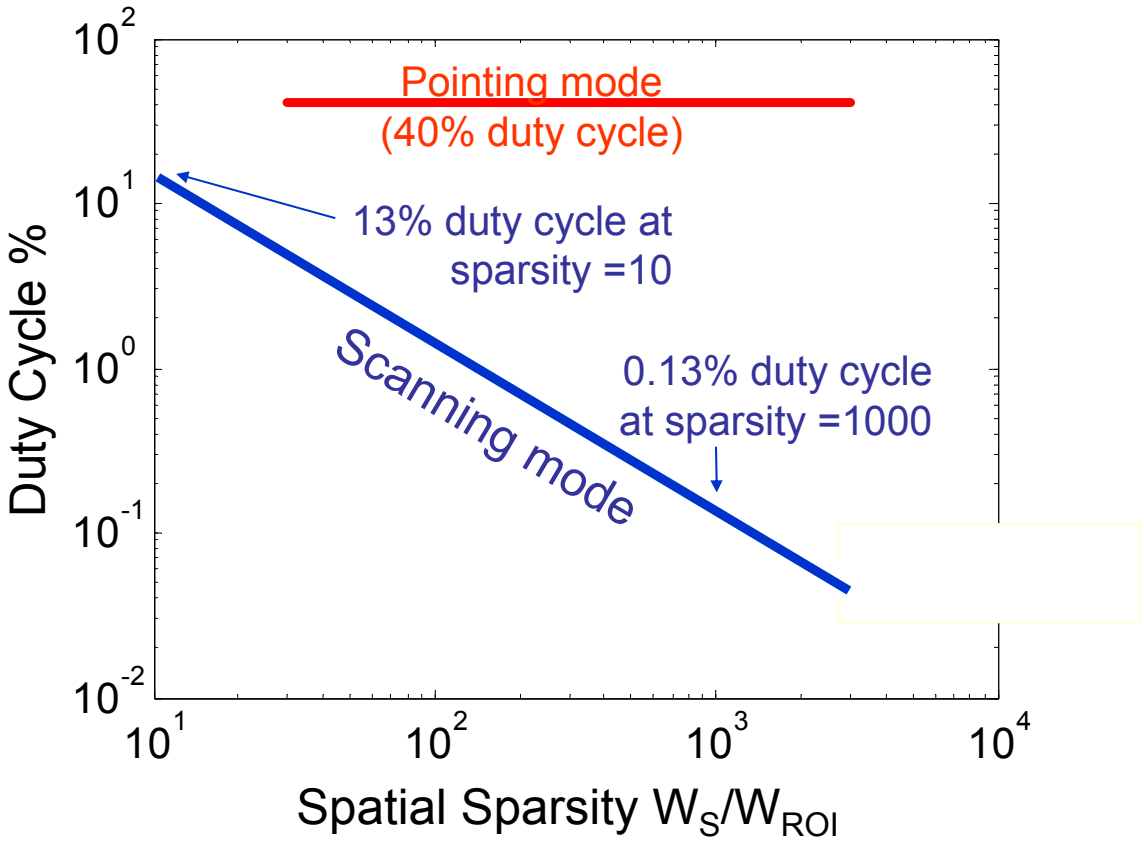

Figure 2.4 A comparison of the duty cycle vs. spatial sparsity for the scanning mode (blue) and the pointing mode (red). For the pointing mode T_D = 16μs , T_{Tr} = 24 μs.

For the fastest possible sampling rate in the pointing mode, without reducing the photon collection time below T_{ROI}, $T_D = T_{ROI}$. Therefore The optimum sampling rate Rs:

$$R_s = D_{Pt} / T_{ROI} = 1 / (T_{ROI} + T_{Tr}) \qquad \text{equation 2.4}$$

This sets the optimum sampling rate for a pointing system with a given transit time.

The total imaging time T_{img} in the pointing mode is therefore:

$$T_{img} = N_{ROI}(T_{ROI} + T_{Tr}) \qquad \text{equation 2.5}$$

To calculate the bandwidth requirement of the deflection trace in Figure 2.3 it is necessary to take the Fourier Transform of the deflection vs. time curve. Nyquist's sampling theorem (Landau 1967) states that to sample a perfectly bandwidth limited signal it is necessary to sample at twice the frequency of the limiting bandwidth. The corollary to this is that the pointing mode deflection signal must have frequency components up to half the frequency defined by the closest sampling points on either side of the transit shown in red dots $1/(2T_{Tr})$.This is easy to understand intuitively from the figure as I have shown each pointing region linked by a half sine wave to the next. The frequency of the full sine wave would thus be $1/(2T_{Tr})$. Thus the minimum bandwidth requirement for a deflection system operating in the pointing mode is approximately given by:

$$B_D = 1/2T_{Tr} \qquad \text{equation 2.6}$$

Furthermore the fact that the spot must stay pointing within the ROI and not drift implies that the frequency response of the deflection system must be flat down to low enough frequencies that there is no sag during the duration of the spot within the ROI. It also must not oscillate in position, this implies that the upper part of the frequency response above B_D must be well damped, i.e. decaying gently with no resonance.

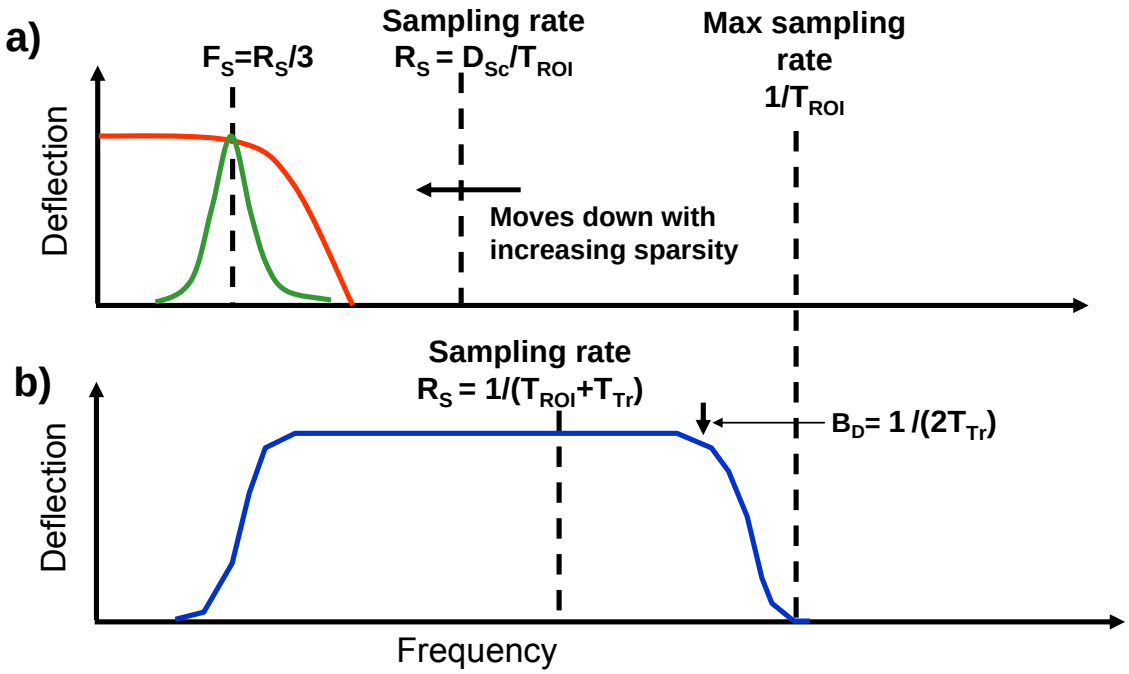

Figure 2.5 The required deflection frequency response for a) the scanning mode and b) the pointing mode. In order to reproduce the required approximately sinusoidal deflection vs. time curves in the scanning mode either the red or green frequency responses would be satisfactory. The green curve corresponds to a resonant scanner. The pointing mode shown in b) for the same ROI sampling rate R_S requires the wide flat frequency response shown in blue

The required frequency response of scanners for the pointing mode and scanning mode are compared in Figure 2.5. Figure 2.5a shows the required scanning mode frequency response for the scanning mode. For T_{ROI} of 10μs, the maximum possible sampling rate with a sparsity of 1 (corresponding to all points being of interest) is 100 kHz. The duty cycle reduces this rate to 13 to 0.13 kHz for sparsities of 10 to 1000 respectively. The required sinusoidal scanning frequency is therefore reduced to the range between 4.3 kHz to 43 Hz. If the deflection waveform is sinusoidal, then a resonant scanner can be used with a frequency response as indicated in green. If the waveform is saw tooth as in raster scanning then a carefully designed control system is needed to give the required linearity and a frequency response greater than F_S with smoothly damped higher frequencies to suppress any mechanical resonance of the deflector (Brown 2009), as shown in the red curve.

As shown in Figure 2.5b the required frequency response for the pointing mode is much more demanding. Taking for example a region of interest pointing time T_{ROI} of

10μs and a transit time between ROIs T_{Tr} of 10μs -25μs , the duty cycle is 50% to 28% and the cycle time T_c = 20μs to 35 μs. The bandwidth B_D required of the deflection system is B_D =1/2 T_{Tr} which is 50 kHz to 20 kHz.

Suitability of galvanometer and AOD deflectors for pointing and scanning

The fastest resonant galvanometer mirror scanners operate at up to 10 kHz, (exceptionally 20 kHz) (Brown 2008) whereas the fastest well controlled galvanometer mirrors for raster scanning have a 4 kHz mechanical resonance but are electronically linearised and damped to have about 1 kHz damped overall frequency response (Brown 2009) similar to the red line in Figure 2.5a).

Acousto-Optic scanners on the other hand have a typical transit time (AOD fill time) of 4 to 25 μs (Xu and Stroud 1992) and are naturally suited to precise steady, drift free, pointing simply by keeping the deflection frequency constant.

Given these facts and the analysis I have just derived it is clear that unless non resonant wide bandwidth precision controlled mechanical deflectors can be developed with bandwidths of 20 kHz or more, 20 times those available today, there is little chance of using mechanical galvanometer based scanners for pointing mode deflection for high speed 2-photon calcium fluorescence optical functional imaging of multiple neurons with sparse regions of interest at kHz rates. Galvanometers are best suited for scanning mode.

From a deflection bandwidth and stability of pointing perspective AODs, on the other hand, are well suited to both scanning and pointing. They do however have other drawbacks such as chromatic aberration and a lower transmission efficiency which varies with deflection angle. These drawbacks have restricted their use to niche applications where the characteristics of AODs are of paramount importance.

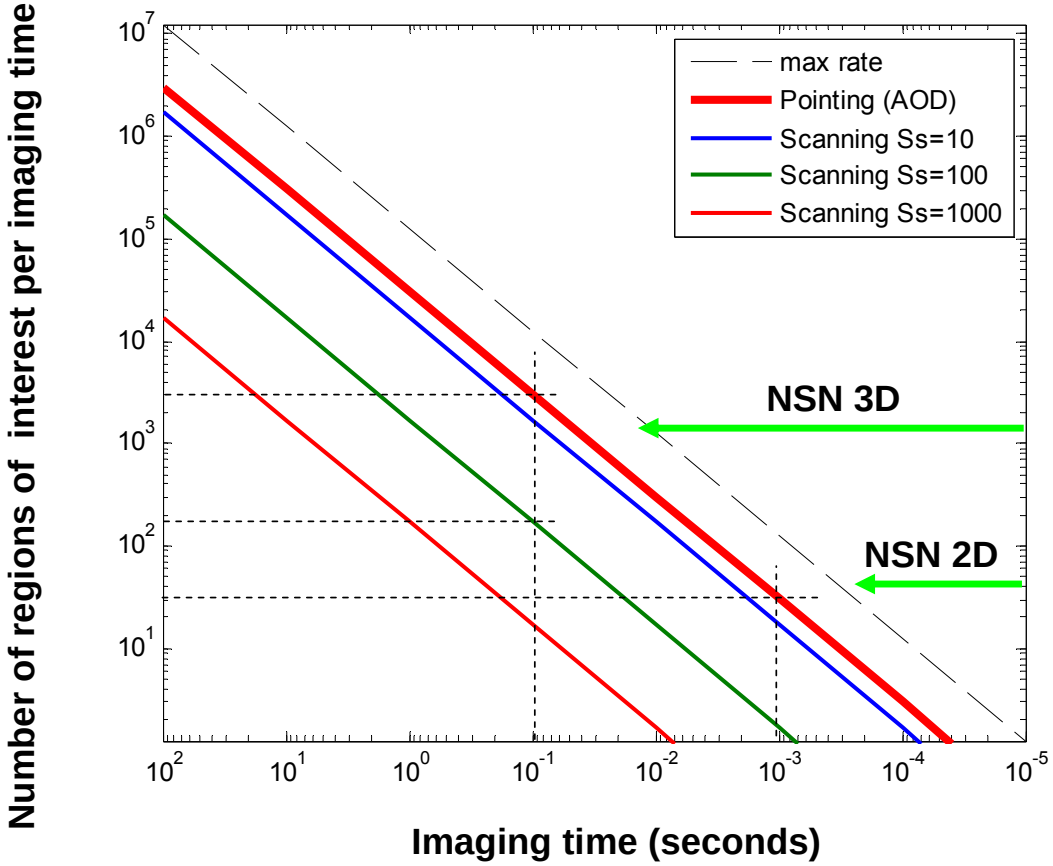

Figure 2.6 Relationship between the number of regions of interest that can be monitored by an optical functional imaging system using the pointing mode or the scanning mode and the time taken to image all those ROIs. In all cases the total dwell time in each region of interest T_{ROI} is 8µs. Note this assumes laser power is adjusted with imaging depth to compensate for tissue scattering loss, pointing mode transit time is 25µs. The sloping black dashed line shows the maximum number of ROIs that could be monitored with infinite deflection bandwidth (zero transit time between ROIs).The vertical and horizontal dashed black lines pick out particular imaging rates for comparison. The scanning mode results are for 3 different spatial sparsities *Ss*. The horizontal green arrows indicate the approximate number of neurons that are selectable (NSN) for high speed imaging in a volume of rat cortex 250×250×250µm (3D) and 250×250µm (2D). (Ohki, Chung et al. 2005)

The results of this section are summarised in the plot of Figure 2.6 which compares the number of regions of interest that can be chosen for monitoring by an optical functional imaging system in either the pointing mode or the scanning mode as a function of the total imaging time. (i.e. the time for the laser spot to monitor all the ROIs once and return to the first ROI). So for 1ms imaging time (vertical dashed line) the pointing mode is able to monitor 30 ROIs, whereas the scanning mode with a sparsity of 100 is only able to monitor 1.8 ROIs. At the 100ms imaging time (vertical

dashed line) these figures are 100 times greater at 3000 and 180 respectively. Thus AOD based pointing mode systems are much better for optical functional imaging of brain regions where the spatial sparsity of the regions of interest necessary to obtain millisecond response times is high. Any mechanical deflection system would need 20 kHz bandwidth and a wide flat frequency response with no resonances to compete with an AOD of 25 μs AOD fill time for the pointing mode application.

How scanning and pointing will be used in practice to maximise the performance

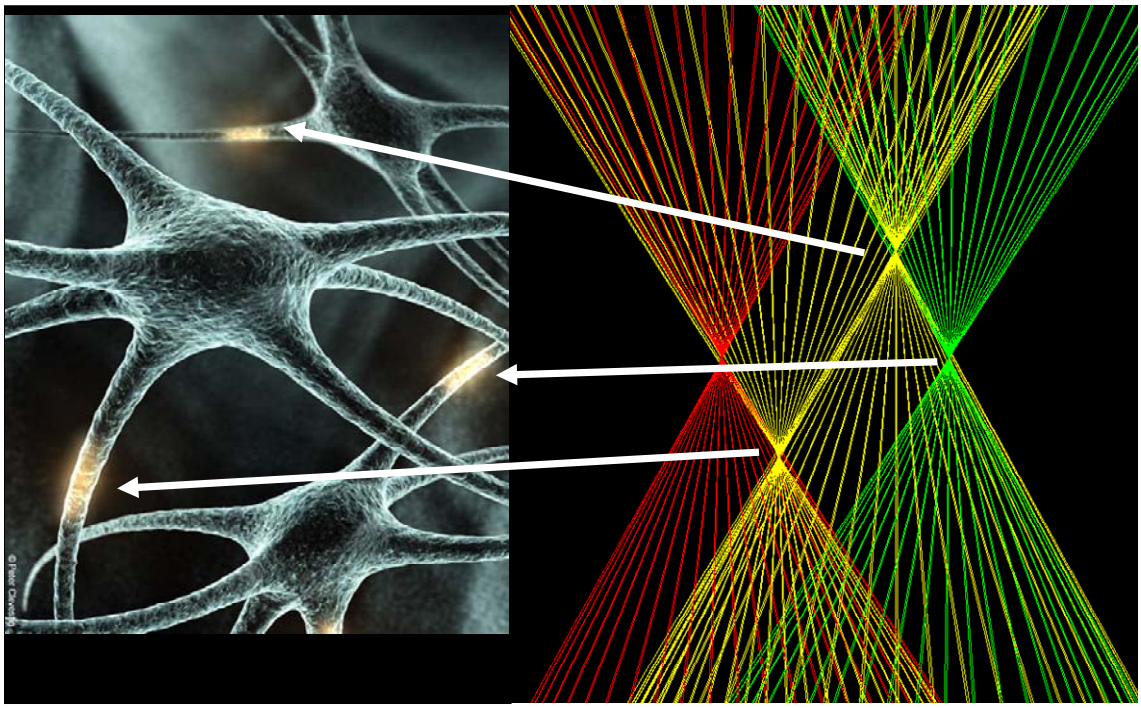

Figure 2.7 Diagram to illustrate the pointing mode in 3D. On the left is a computer graphic of neurons in 3D with bright regions to indicate the chosen regions of interest. On the right, part of a Zemax (http://www.zemax.com) diagram of light rays coming to different foci in 3D beneath a microscope objective. Image of neurons with permission (Peter Clevestig)

In order to use such a 2-photon functional optical imaging machine to it maximum advantage it is envisaged, as illustrated in Figure 2.7 that the tissue to be imaged is first imaged slowly in 3D with a full raster scan to understand the anatomy. Regions of interest are then selected for functional imaging with the pointing mode so that the functional imaging can take place at the fastest possible rate for the number of ROIs chosen. The system therefore needs a deflection and focusing system capable of both scanning the full 3D volume of tissue in the minimum possible time and subsequently pointing to the chosen regions of interest at high speed in 3D. Because of proposed

capability for a 4 AODs to point scan and deflect in 3 dimensions (Kaplan, Friedman et al. 2001), and the requirement to monitor small regions of interest with a sparsity S_S = 250μm/1μm = 250 , AOD technology was chosen for this application.

Choice of Acousto Optic Lens configuration

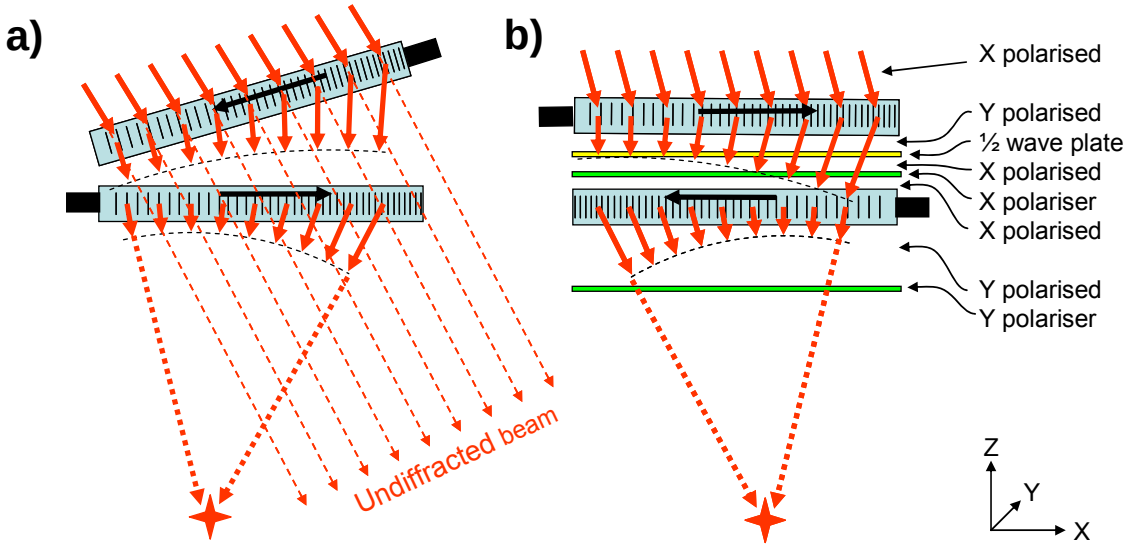

Figure 2.8 comparison of the a) Kaplan configuration (Kaplan, Friedman et al. 2001) and b) Inverted Bragg Configuration (IBC). Note in both cases the sound waves of each AOD pair are propagating in opposite directions (black arrows) AODs with the light diffracting towards the transducer (black rectangle) are in the -1 Bragg diffraction order, those diffracting away from the transducer are in the +1order. In a) the undiffracted zero order beam is at a considerable angle to the diffracted bem and is absorbed by baffles. In b) each AOD rotates the diffracted plane of polarization 90 degrees. This makes it possible to remove the unwanted zero order undiffracted light with a polarizer. The half wave plate is to ensure the polarization of the diffracted light from the first AOD is rotated 90 degrees so that it will couple into the second AOD. Wanted light beams are labled X or Y 'polarised'.

In Kaplan's published design(Kaplan, Friedman et al. 2001) (Figure 2.8a.) The upper AOD diffracts light in the +1 diffractive order (defined as the 1st order diffracted wave diffracted AWAY from the transducer), and the lower AOD is thus -1 diffractive order (diffracts towards the transducer). In general because of the different diffractive order, for high performance, a different detailed design of AOD may be necessary for AOD2 and AOD 1.

An alternative configuration is shown in Figure 2.8b. We call this the Inverted Bragg Configuration (IBC) because the Bragg gratings that form the active element of the AODs are inverted with respect to one another, with both gratings diffracting in the -1 order. The IBC is most simply implemented with identical AODs by rotating AOD2 180 degrees about the Z axis with respect to AOD1 .The following table summarises the relative merits of these two configurations.

• **Kaplan Configuration**	• **Inverted Bragg Configuration (IBC)**
• Requires an extra component (grating or prism) to compensate for spatial chromatic dispersion at mid point of field of view.	• self compensating at mid point
• Works with any AOD	• Requires AODs that rotate polarisation 90 degrees
• Unwanted undiffracted (zero order) light must be geometrically arranged to hit baffles	• Polarisers required to cut out unwanted zero order undiffracted light.

Table 2.1 Comparison of Kaplan (Kaplan, Friedman et al. 2001)and IBC configuration of AODs

As has pointed out in the literature (Reddy and Saggau 2005) (subsequent to our independent understanding) the IBC is naturally self compensating to spatial chromatic aberration caused by the AODs. When the drive frequencies to the two AODs are equal and the focal spot is at the centre of its field of view both the deflection and the chromatic aberration caused by the AOD diffraction (equation 1.1) are naturally cancelled out to zero irrespective of the spectral width of the laser. As will be discussed in chapter 3, the residual ‘magnification chromatic aberration’ becomes proportionately larger as net deflection of the spot from the centre of the field of view increases. The chromatic aberration of the Kaplan configuration is cumulative because the deflection angles add rather than subtract and hence there is large aberration that must be pre-compensated with another prism or grating. It is however easy to suppress the residual zero order mode light in this configuration with a simple baffle. The IBC only works with AODs that rotate the plane of polarisation by approximately 90 degrees so that polarising sheets can be used to absorb the

unwanted zero order mode light and transmit the wanted diffracted light. This is not a problem because the highest efficiency AODs are anisotropic TeO_2 devices which rotate the diffracted plane of polarisation. For these reasons we chose to develop our AOL based in the inverted Bragg configuration. (Note, In Figure 2.8b a ½ wave plate is also included because, with two AODs both deflecting in the same plane as shown, the polarisation of the diffracted wave must be returned to the input polarisation of the next AOD. For the X1, Y1, X2, Y2 configuration we are implementing, ½ wave plates would not be necessary if the polarisation was exactly rotated by 90 degrees by diffraction. (See chapter 3- Design of AODs for more detail on this.)

Design of the complete AOLM: the starting point

Our starting point for the design of the overall acousto-optic lens microscope was simply to combine 4AODs in series to form an acousto optic lens following the principles described (Kaplan, Friedman et al. 2001) and relay the beam into a microscope as shown in Figure 1.13 .

The first problem this poses became obvious once I tried to design the AOL using simple geometric optics. Because of the significant thickness of the AODs it is impossible in practice to put the diffractive gratings of the AODs sufficiently close together along the Z axis that the equation given by (Kaplan, Friedman et al. 2001) and reproduced in equation 1.5 results in a stationary laser spot. This is because these equations assume zero optical distance between the AODs. An initial search for suitable AODs revealed that all high performance AODs are several cm thick with the curtain of sound waves bisecting the crystal at a steep angle. They are not at all like the idealised thin devices shown in the diagrams of chapter 1. (Their detailed design is described in Chapter 3). If spaces of several centimetres are introduced between the AOD gratings the wavefront curvature changes between the AODs and the cancelation of sideways movement of the focal spot would not be accurate.

Initially, to solve this problem, I designed 1:1 telecentric relays that project the image of one AOD onto the next AOD. This means that three relays are needed between the

four AODs as well as subsequent relays into and through the microscope. We have also made the decision to project the image from the AOL via the galvanometer mirrors of the microscope in order to test whether the AOL can be an additional feature to an otherwise standard commercial microscope. In order to achieve this it is necessary to design optics that relays the image of the output face of the last AOD of the AOL to form a conjugate image on the galvanometer mirrors with the correct demagnification to just fill the galvanometer mirrors. (4:1 demagnification in our case).

In a commercial 2-photon microscope the subsequent field lens and tube lens form a conjugate image of the galvanometer mirrors on the back aperture of the microscope objective. This relay is usually magnifying so that for instance the 3mm aperture of the galvanometers is expanded up to the 8 or 9 mm back aperture entrance pupil of a water immersion microscope objective. The complete optical train of this first design is shown in Figure 2.9.

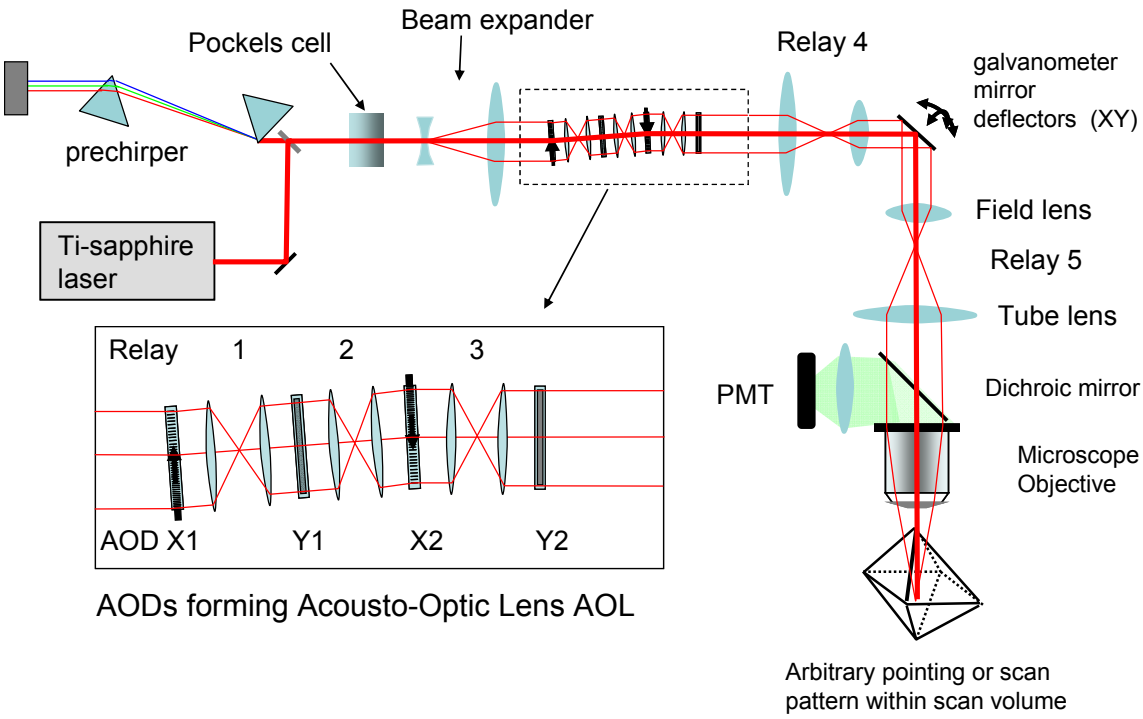

Figure 2.9 Initial design for the overall optical system layout of the microscope. The additional telecentric relays numbered 1,2,3 between the AODs forming the AOL are to ensure zero effective optical distance between one AOD grating and the next as assumed by Kaplan in deriving equations 1.3 to 1.5 for a stationary focal point. Relay 4 and 5 demagnify the conjugate image of the last AOD onto the galvanometer mirrors and then magnify the image onto the back aperture of the microscope objective lens. By varying the drive to the AOL, the focal point can be focused or scanned through any point within the octahedral field of view.

Note that I have labelled the telecentric relays as 1-5 with a pair of lenses for each relaying the output aperture of one element on to the input aperture of the next. Equally well I could have labelled the pairs of lenses starting with the last lens of relay 4 and the first of relay 5 and the last lens of relay 5 and the microscope objective as two telecentric relays relaying the first real focused image formed by the AOL, via a second after the microscope field lens to the final focus spot beneath the objective. The design of the relay optics is thus a sequence of interwoven telecentric relays. The final field of view of the microscope is shown as the octahedral shape beneath the objective. This octahedral shaped field of view is what you expect for AODs with all four frequency drive bandwidths equal. This is because in the natural focal plane of the objective lens (Z2=0 in Figure 1.13) the bandwidth limits can be used entirely for X or Y displacement. As the AOL focus increases or decreases above or below the natural focal plane so more and more of the available bandwidth is used up by the

ramps applied to the AODs. When the maximum ramp rate (and Z displacement) is reached, there is no bandwidth left for X or Y displacement.

Derivation of field of view of microscope from AOD RF frequency limits and AOD physical parameters

Whilst designing the microscope, particularly when discussing the design with end users, the issue often came up of what microscope objective to use with what NA and subsequently what is the optimum relay lens magnification on to the back aperture. These discussions can get quite confusing and there is often a tendency for the end user to assume for instance that it is the objective magnification that determines the field of view and that NA can be independently adjusted by adjusting relay magnification. Of course geometric optics is not like that; you can deduce from the optical sine theorem(Hecht 2001) that as you vary the magnification of an image the NA is inversely related to the magnification. This applies equally to field of view, which is the image of all the possible points the laser can be deflected to focus upon. In view of this, I decided to derive the equations for the 3D field of view of the AOLM purely in terms of the AOD physical characteristics (maximum scan angle and aperture) and the effective NA the final focused point. Providing there are no apertures limiting the NA between the last AOD and this focus then the details of all the intervening optics are irrelevant. The design trade off between *NA* and field of view is then clear and can be made independently of all the degrees of freedom for the design of the intervening optical train.

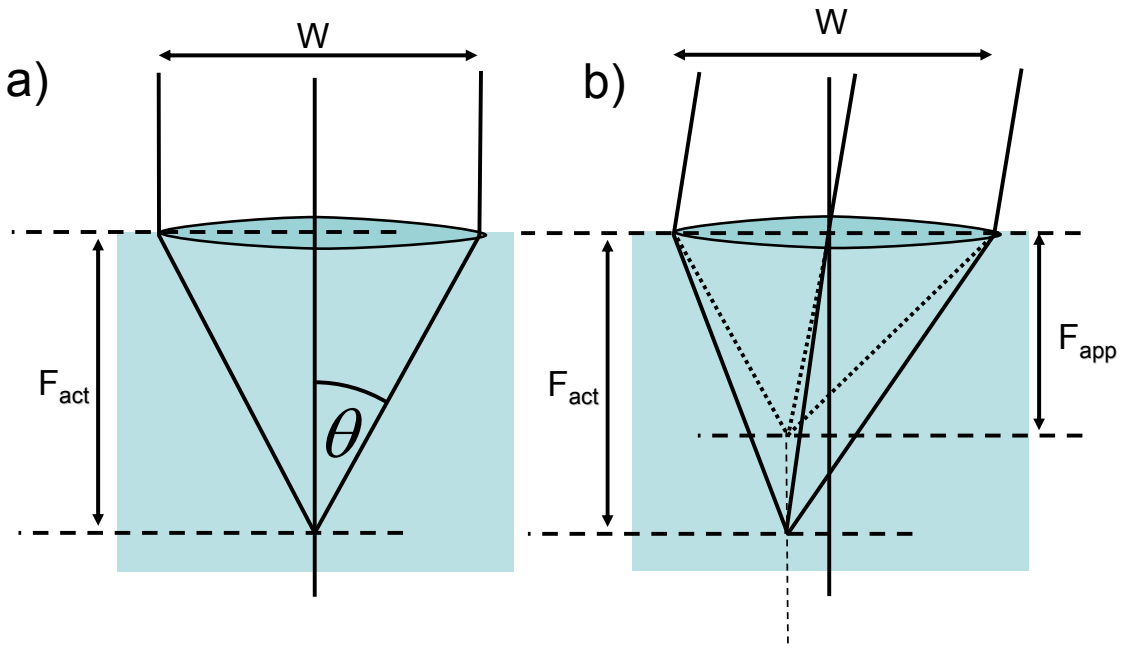

Figure 2.10 a) Parameters relating the actual focal length of a water immersion lens F_{act} to aperture width W and its numerical aperture $NA=n \sin \theta$. The refractive index of water, shown in blue is n =1.33. b) Diagram to show how the apparent focal length which determines the lens magnification is 1/n times the actual focal length in water. The dotted lines represent the externally apparent path of the rays.

Derivation of 3D field of view of AOLM

Referring to Figure 2.10 a) and starting from the basic definition of numerical aperture beneath a water immersion lens $NA = n \sin \theta$ and Pythagoras' theorem it is straight forward to deduce that:

$$F_{act} = \frac{Wn}{2NA}\left(1 - \frac{NA^2}{n^2}\right)^{1/2} \qquad \text{equation 2.7}$$

Where:

F_{act} = Actual focal length in water of the focusing lens

W = full width of lens aperture fill by incoming laser light from AODs

n = refractive index of water = 1.33

NA = effective numerical aperture of final focal spot

Because of the transition from water beneath the final objective to air above, the apparent magnification of the lens is increased by n, the refractive index of water, and its externally apparent focal length F_{app} is 1/n times F_{act} the actual focal length in

water. This is illustrated in Figure 2.10 b). It is the apparent focal length that is calculated if the tube length of a microscope is divided by its magnification on the barrel of the objective.

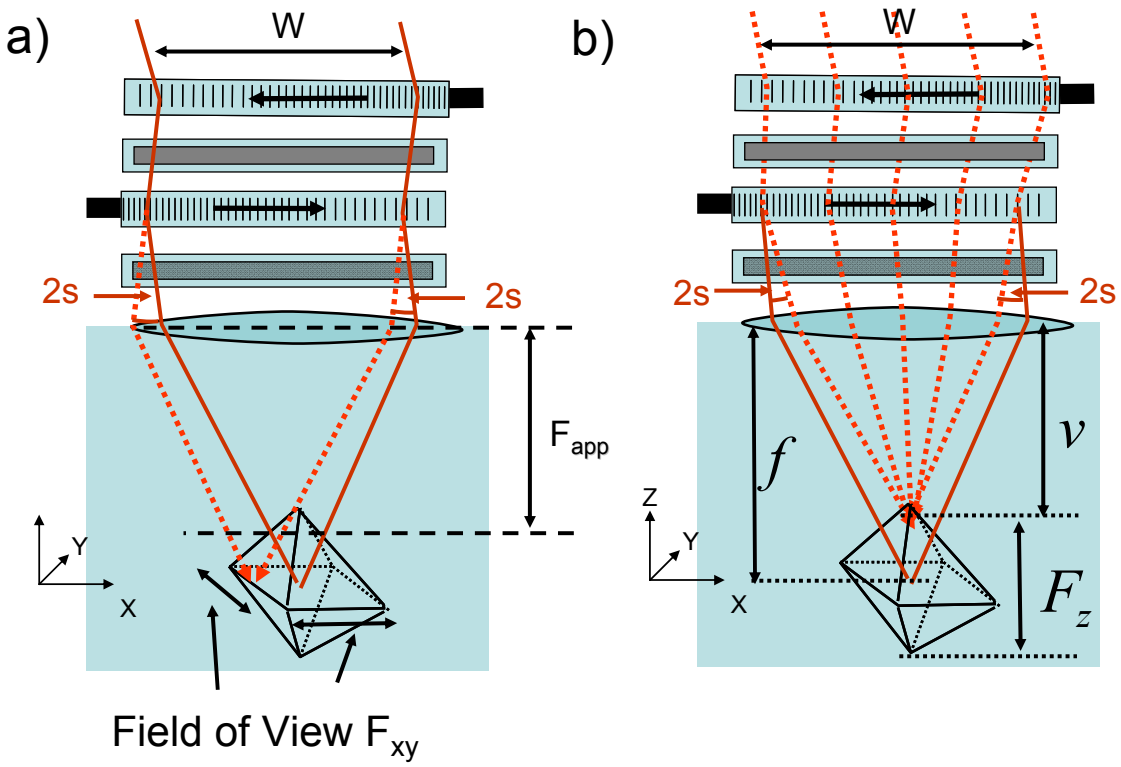

Figure 2.11a) Diagram to illustrate how the X or Y field of view is calculated from the fact that the maximum total angle of scan of the beam is 4s where s is the semiscan angle of the AODs. Note that now the input beam width defines the effective NA of the lens. It does not matter if the objective has a larger aperture with a higher NA written on the barrel. The dotted lines represent the path of the rays with the AOL set at Z=0 and maximum deflection in X. b) Diagram to show how the equations for the axial field of view are calculated by considering that the maximum convergence (or divergence) between the extreme edges of the AODs is 2s+2s as shown focusing on the upper point of the octahedral field of view. The dotted lines in this figure show the paths of the incoming rays focusing on the very top of the octahedral scan volume.

The simplest combination of the four AODs of an AOL with such a water immersion lens is shown in Figure 2.11. The maximum scan angle of either of the 2 pairs of AODs in the X or Y direction is 4*s* where *s* is the maximum semiscan angle of one of the AODs. To be clear, 2s is the angle one AOD deflects light through if its drive frequency is changed from f_{min} to f_{max}. Inspection of the diagram Figure 2.11 b) shows the input rays on both sides of the lens maximally deflected to the left by an angle 2s. Combining this with equation (2.7) results in :

$$F_{xy} = 4sF_{app} = \frac{2Ws}{NA}\left(1-\frac{NA^2}{n^2}\right)^{1/2}$$ equation 2.8

Where F_{xy} = the X or Y direction field of view that the laser spot can scan over beneath the lens in its natural focal plane.

Figure 2.11b) shows how the maximum displacement of the focal spot along the Z axis can be deduced from the difference between the axial focal position at Z=0 for zero chirp diffractive gratings and the axial position when the gratings are maximally chirped, with converging deflection at the edges of the AOD aperture of 2*s*. The basic paraxial equation relating object to image distance for a lens with the image in a medium of refractive index *n* is(Hecht 2001):

$$\frac{1}{u}+\frac{n}{v}=\frac{n}{f}$$ equation 2.9

Where $u = -W/4s$ is the distance of the object from the lens (with the correct sign convention), *v* is the distance of the image from the lens (in water) and *f* is focal length of the lens (in water).

Combining this equation with equation (2.7) and rearranging gives;

$$F_z = \frac{8F_{act}^2 s}{nW} = \frac{2Wsn}{NA^2}\left(1-\frac{NA^2}{n^2}\right)$$ equation 2.10

Where F_z is the maximum distance it is possible to scan in along the Z axis.

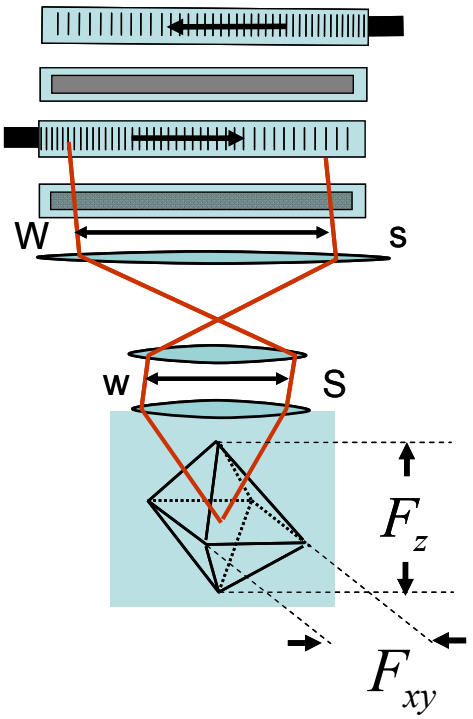

Figure 2.12 Diagram that demonstrates that the field of view is independent of the intermediate optics because the equations are all in terms of the product Ws, the AOD aperture times the semiscan angle. This product is constant.

The final Figure 2.12 relating to this derivation illustrates why this expression is independent of how the light is relayed from the AODs to the final objective. It shows an additional telecentric relay between the AOD and the objective. This is marked with different values of W and s, w and S. However, providing there are no restricting apertures, the optical sine theorem (Hecht 2001) determines that $Ws = sW$. Since the equations (2.8) and (2.10) for the field of view only contain the product Ws it is clear that the expressions are indeed independent of the intermediate optics.

NA vs. field of view

Equations (2.8) and (2.10) can now be used to study the design trade offs of the system. Figure 2.13 shows how the X and Y field of view varies as a function of the NA for s = 3, 6 and 9 mrad semiscan angles and W=15 mm AOD aperture width. This AOD width was chosen to be as large as reasonably practical given that we did not want it too large for commercial manufacture or for its AOD fill time is to exceed 24 μs so that it still enables data collection time $T_{ROI} = 9\ \mu s$ at 30 kHz sampling rate.

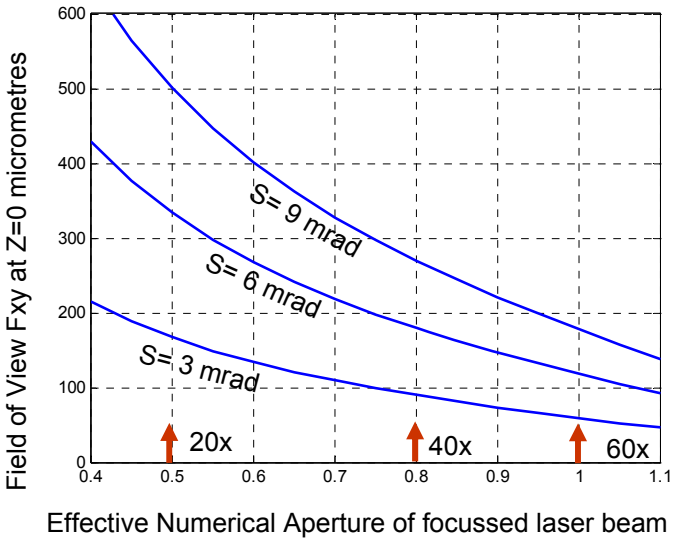

Figure 2.13 Theoretical plot of the field of view in the X orY plane from an AOD of width W=15mm and semiscan angles 's' as marked. Also shown on the diagram is the magnification of an Olympus objective lens that would have that particular effective NA with the 8mm diameter back aperture projected image of the last AOD.

Marked along the NA axis are the magnifications of three different objective lenses that would give that NA for a projected image of the AODs on their back aperture of 8mm diameter. Note that although it is easy to get a greater than the target 250 μm XY field of view with these scan angles this is only at low NAs(e.g. beneath a 20X objective with 8mm back aperture fill). Since 2-photon fluorescence intensity increases rapidly as NA increases (because of the smaller point-spread function at the focus), the optimum overall design is likely to be at least 0.7 NA, maybe more. We therefore need large aperture acousto-optic devices capable of giving high efficiency over a large scan angle. To achieve 250 μm octahedral field of view (FOV) beneath a NA = 0.8 objective (a normal NA for galvanometer based 2-photon imaging) would require AODs that remained high efficiency over an angular range of approximately +/-9mrad per AOD (9 mrad semi-scan angle). This is very challenging as discussed in the next chapter.

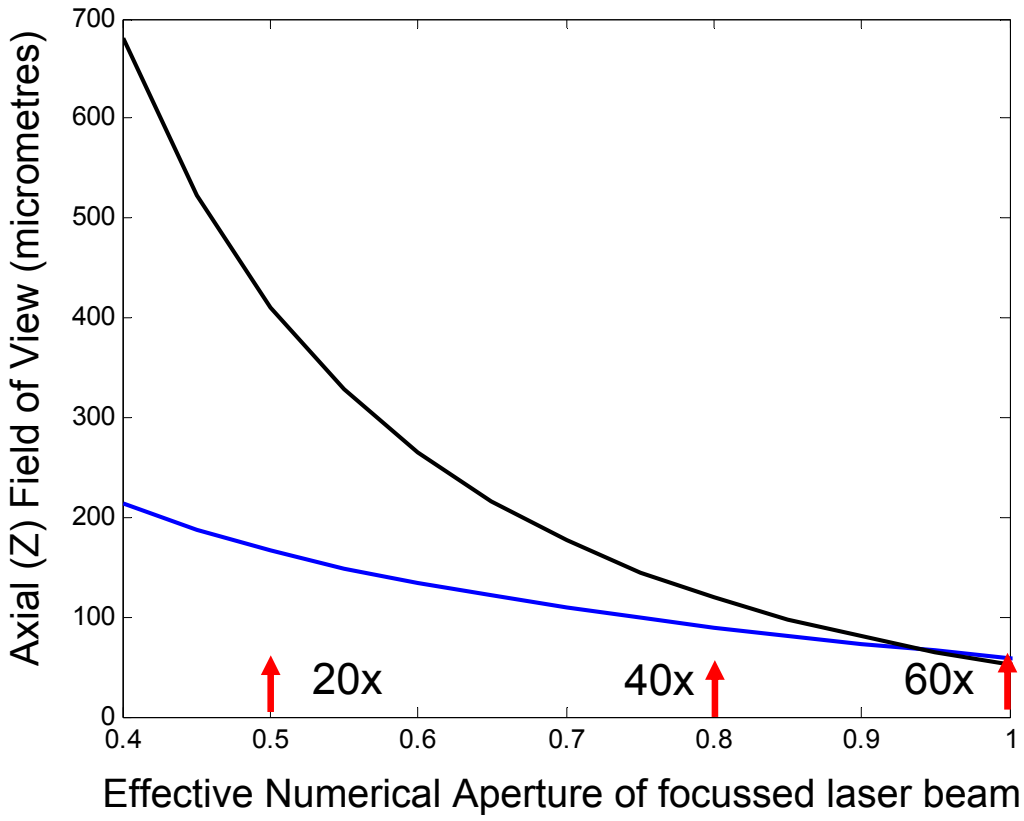

Figure 2.14 Comparison the way in which axial field of view and XY field of view vary with NA. The black line shows the axial (Z) field of view has an approximately inverse square relationship of axial field of view. The blue line is F_{XY}, the XY plane field of view. W= 15mm s= 4.35mrad.

In the Z direction, the field of view is an even more dramatic function of NA as shown in Figure 2.14 which compares the Z field of view with the XY field of view as NA varies. In this case the semi-scan angle is fixed at s = 4.35 mrad and W = 15mm. In this case it requires NA be reduced to about 0.7 to obtain a 250 μm FOV to the tips of the octahedral FOV. Reducing the NA to about 0.55 doubles the FOV to 500 μm because of the approximately inverse square law relationship. For NA= 0.8 the octahedral Z field of view is 180 μm, therefore to achieve 250 μm the semi-scan angle needs to be increased to at least 6 mrad. To cover a 250 μm cube, rather than octahedron (as implied by the target specification), at NA = 0.8, would require the maximum angular scans were increased outside this range, to about 12 mrad. However, even if the AOL can deflect high optical power across this large Z field of view, 2- photon performance may be limited by aberrations to the point spread function as discussed in the following chapters. This and several other relevant other factors all need to be understood to optimise the overall design. The conclusion of this

section is that for a large (15mm) aperture AOL to achieve a 250 × 250 × 250 μm cubic FOV at NA= 0.5 requires a semi-scan angle of just less than 6 mrad, however, the required semiscan angle is a strong function of the NA of the final beam so that for instance to achieve this FOV at NA= 0.8 requires a semi-scan angle of more than 12 mrad.

Problems caused by using telecentric relays in the AOL

As mentioned earlier in this section, in order to produce stationary spot at a large value of the Z axial focus using Kaplan's equation (equation 1.5) it is necessary for the optical separation between the gratings forming the AOL to be zero. To achieve this, in the initially proposed system layout shown in Figure 2.9 the AODs forming the AOL are each linked by telecentric relays.

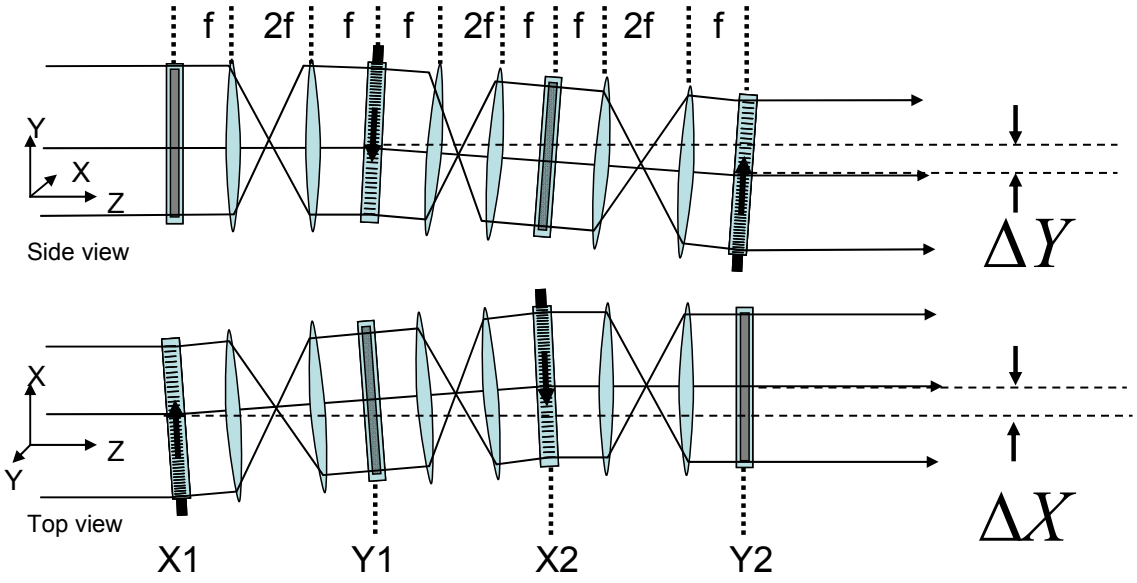

Figure 2.15 Top and side view of the first design of AOL showing the transverse deflection of the beam as it propagates. The drive on all four is AODs at the centre frequency. The vertical and horizontal displacement ΔX and ΔY of the last AOD with respect to the first alters by 8mm for a wavelength range of 700 to 900nm.

Early in the project it was realised that this arrangement of telecentric relays would make it very difficult to change the system wavelength without several hours of careful realignment of the optical train linking the AODs. The reason for this is illustrated in Figure 2.15 which shows the optical train of the AOL in more detail in both side view and plan view. Each AOD is separated by a '4*f*' telecentric relay. The

total length of each relay is four times the lens focal length which for 15mm aperture AODs would probably be chosen to be at least f = 100 mm. This is in order to keep the lens NA sufficiently low for readily available lenses to be adequate quality for diffraction limited imaging. The total length of the AOL is thus 1200mm. The AODs must be aligned so that the input and output beams of each AOD are at the optimum efficiency when the AODs are driven at their centre frequencies. The configuration is such that when all AODs are driven at their centre frequencies the light beam is deflected sideways and then upwards in the first two AODs. The deflection is then cancelled out exactly in the next two AODs so that there is no net deflection and the output beam is parallel to the input beam. This output beam is then carefully aligned and launched into the relays leading to the microscope. The problem arises when you wish to change the laser wavelength. It is straight forward to show by repeated use of equation 1.1 for the deflection angle of the AOD that the total sideways or vertical displacement of the input beam is given by:

$$\Delta X = \Delta Y \cong 8f \times \frac{\lambda \nu_{ac}}{V_{ac}} \qquad \text{equation 2.11}$$

where ν_{ac} in this case is the acoustic drive frequency

Despite the fact that the AODs we finally chose had centre frequencies as low as ν_{ac} = 35MHz, the wavelength dependence of equation 2.11 means that both the sideways and vertical alignment of the output beam with respect to the input beam changes by 8mm even for a restricted range of wavelengths 700 to 900 nm. We could not see a practical mechanical solution to this problem. On adjusting the laser wavelength, not only would the Bragg angle of each AOD have to be fine tuned, (not too difficult to automate), but the lateral and vertical displacement of the AODs would need to be altered by up to 8 mm and some arrangement made to either the input or output beam positions to accommodate the changes in displacement. This is clearly a serious practical issue which we believed if not solved would probably cause this type of microscope to be impractical or very expensive for commercial production.

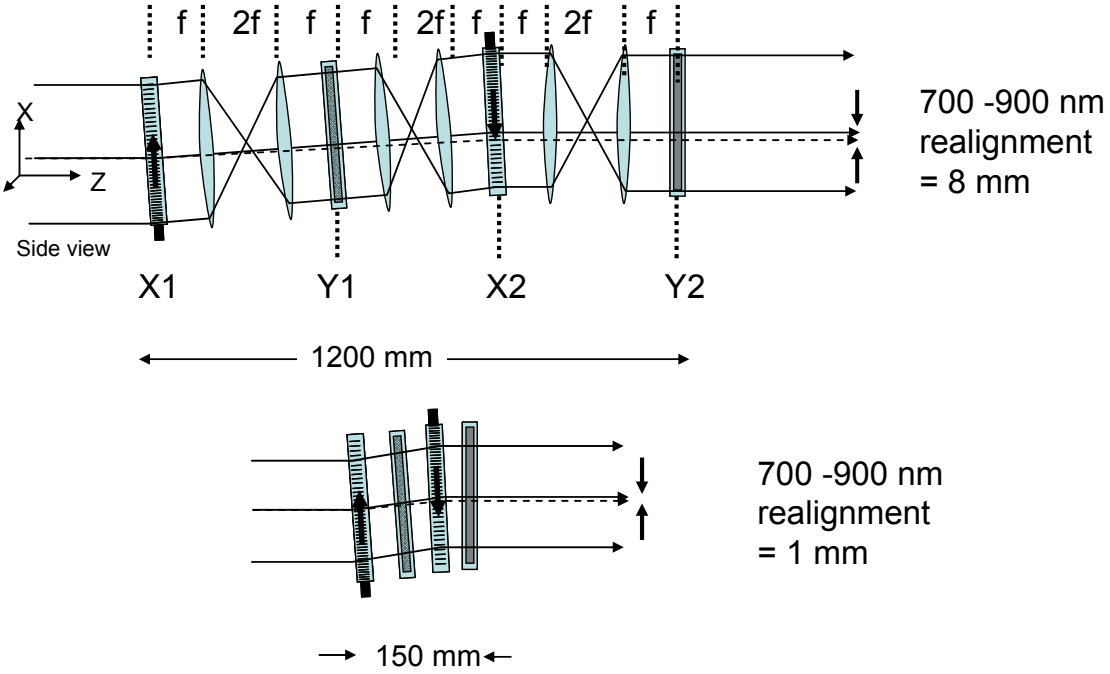

Figure 2.16 Diagram to illustrate the advantage of the proposed compact configuration of AODs reducing wavelength realignment to a much more manageable 1mm. The dashed line represents the deflection of the central ray of the AOL at the extreme short wavelength end of the range and the solid line the axis at the long wavelength extreme.

Novel and practical compact configuration for the AOL

In order to solve the problem of large lateral shift with wavelength, I decided to explore the feasibility of a compact design of AOL. This simply aligns the AODs axially with no intermediate lenses so that the overall length of the AOL is reduced to the thickness of 4 AODs plus any air gaps, intermediate polarisers etc. The compact configuration of AODs is compared with the original relay design in Figure 2.16. If the total length of the AOL between the first and last AOD grating could be kept below about 150 mm it seemed plausible that no lateral movement of the >15mm aperture AODs would in practice be necessary to compensate the now less than 1mm displacement of the beam axis over the wavelength operating range. Changing wavelength would involve only very small computer controlled adjustments of AOD Bragg angle. This mechanically simple solution of course causes complication in the opto-electronic drive system. The equations that Kaplan derived are no longer accurate.

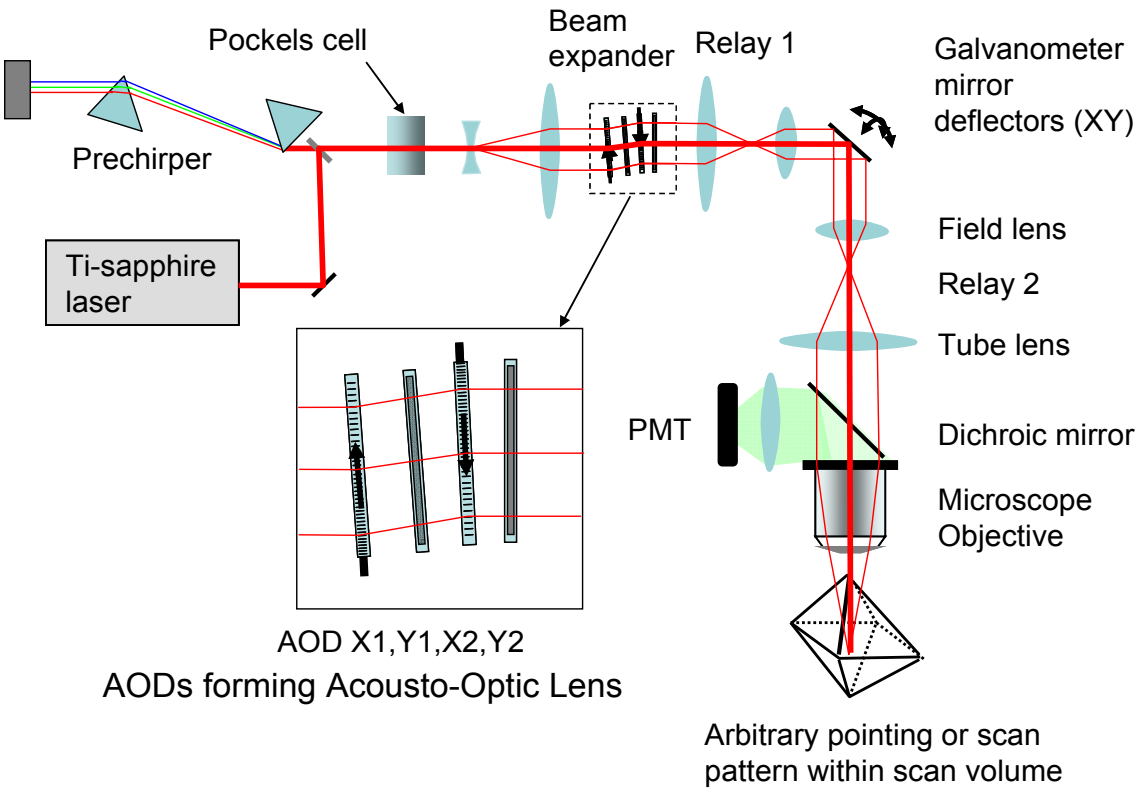

Figure 2.17 Diagram of the complete optical layout of the system as we implemented in the first prototype. This uses the compact configuration of Acousto-Optic Lens so there are no telecentric relays between each AOD and the next. PMT stands for photomultiplier tube.

Figure 2.17 shows a diagram of the complete system with the telecentric relay replaced by the AODs in the compact configuration. Apart form the greater practicality for wavelength changing, the optical train is over a metre shorter than the original design and uses six less lenses.

Derivation of equations for pointing and scanning in the 'compact configuration' AOL

To derive the correct equations for driving the compact configuration of AOL, it is necessary to understand its properties in some detail. I used a diagrammatic geometric optics approach as this gave me the best understanding of how the multi stage dynamic lens system works and the resulting physical intuition to solve the problems that arose at each stage of the design. At a later stage I have made extensive use of Zemax (http://www.zemax.com/), the well known computer software for modelling optical systems. This is better for modelling physical reality in more detail and gaining understanding and minimising the optical aberrations in the system. In the following sections I derive the new equations for driving the AOL, not just for

pointing at a particular point in 3D space (which we refer to as the pointing mode), but also for scanning at the highest possible speed in 3D space by the 3D equivalent of the conventional TV raster scan. This later mode of operation we refer to as the 'miniscan mode' for reasons that will become obvious.

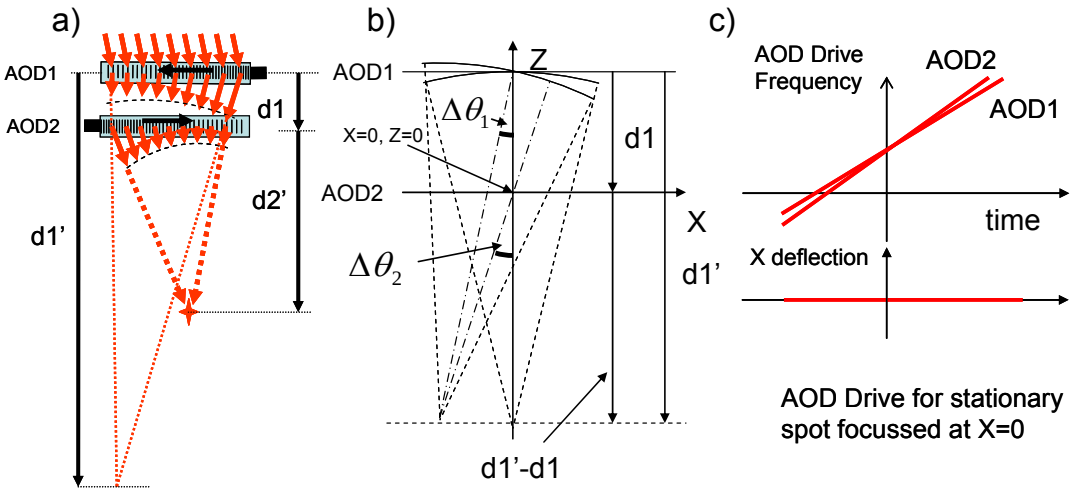

Figure 2.18 Geometric arrangement of optical wavefronts and the drive parameters required for use with the compact configuration of AOL. a) definition of distances and focal lengths of converging waves from AODs, b) showing how as the sound wave in the top AOD progresses to the left it causes the deflection angle at X=0 to increase. However the angle of deflection at X=0 on AOD2 is greater according to the geometrically derived equations in the text. c) shows how the ramp rates of AOD 1 must be less than the ramp rate of AOD2 if the resulting focused spot is to be stationary.

Deriving equations for the Pointing mode

Consider first the case of AOD1 and AOD2 as shown in Figure 2.18a). These are being driven respectively with chirped waveforms:

$$f_1 = f_c + a_1 t \qquad \text{equation 2.12}$$

$$f_2 = f_c + a_2 t \qquad \text{equation 2.13}$$

Frequency drive f_1 is causing a curvature on the wavefront because its drive is chirped. The distance between the AODs is d_1 and the distance to the focus of the converging wave of AOD1 is $d_1^{'}$. Now, referring to Figure 2.18b consider a time t = 0 when the diffracted wave from a position x = 0 on AOD1 is precisely vertical down the Z axis, passing through position x=0 on AOD2. Now consider a time Δt later when the frequency of the ramp is shifted by $\Delta f_1 = a_1 \Delta t$ so that the angle of diffraction changes by a fixed amount $\Delta\theta_1$ then the focus of the converging beam is

displaced in the – X direction as shown. At the fixed point X=0 on AOD2, the angle of the ray passing through that point on its way to the focus shifts by $\Delta\theta_2$ as shown. It is clear by simple geometry that:

$$\frac{\Delta\theta_2}{\Delta\theta_1} \cong \frac{d_1^{'}}{d_1^{'} - d_1} \qquad \text{equation 2.14}$$

Thus if you wish to cancel the rotation of the incoming wave from AOD1 at AOD2 in order to keep the diffracted wave from AOD pointing at the same focal position the rate frequency shift of AOD2, a_2 needs to be greater than a_1. (For this IBC configuration, increasing the frequency of both AODs causes cancellation not addition of the angular deflection). The ratio of the frequency shift rates is the same as the ratio of the angles of deflection in the diagram. Therefore:

$$\frac{a_2}{a_1} \cong \frac{d_1^{'}}{d_1^{'} - d_1} \qquad \text{equation 2.15}$$

These ramp rates are illustrated in Figure 2.18c which shows frequency vs. time for the two AODs driven to produce a stationary focal spot plotted as X deflection vs. time underneath. In order to calculate the specific drive equations for a particular desired focal spot distance $d_2^{'}$, we use equation 1.3 defining the distance to the focus for a given ramp rate and the fact the curvature of the wavefront entering AOD2 is doubled by the additional curvature induced to keep the direction of focus stationary simple rearrangement of the equations shows that:

$$d_2^{'} = \frac{d_1^{'} - d_1}{2} \qquad \text{equation 2.16}$$

And

$$a_2 = \frac{V^2}{2\lambda d_2^{'}} \qquad \text{equation 2.17}$$

$$a_1 = \frac{V^2}{\lambda\left(2d_2^{'} + d_1\right)} \qquad \text{equation 2.18}$$

$$\frac{a_1}{a_2} = \frac{2d_2'}{2d_2' + d_1}$$ equation 2.19

These equations are those needed for setting up and controlling the microscope as they give the drive parameters in terms of the distance d_2' from the final face of the final AOD to the point of focus of the AOL. In these equations, d_1 is always a positive value. The values of d_2', a_1 and a_2 are positive for converging rays for the +1 diffraction order shown in Figure 1.12 a and negative for diverging rays as shown in Figure 1.12 c.

It is apparent that if d_1 is made to be zero then a_1 equals a_2. This is the assumption used in Kaplan's equations. Note that in the equations and analysis above, the distances are apparent optical thicknesses. If further optical components are interposed between the AODs, such as half wave plates and polarisers, then the apparent optical separation needs to be calculated by taking into account the refractive index of such additional components. Also, the refractive index of the AODs themselves needs to be taken into account. This can be done by assuming that the acoustic wave enters and leaves the AOD at its thickness-midpoint such that the apparent optical distance d_1 is equal to the distance in air between the AODs plus half the thickness of AOD1 divided by its refractive index plus half the thickness of AOD2 divided by its refractive index. When the two AODs are identical, then the value d_1 equals the distance in air plus the thickness of the AOD divided by its refractive index.

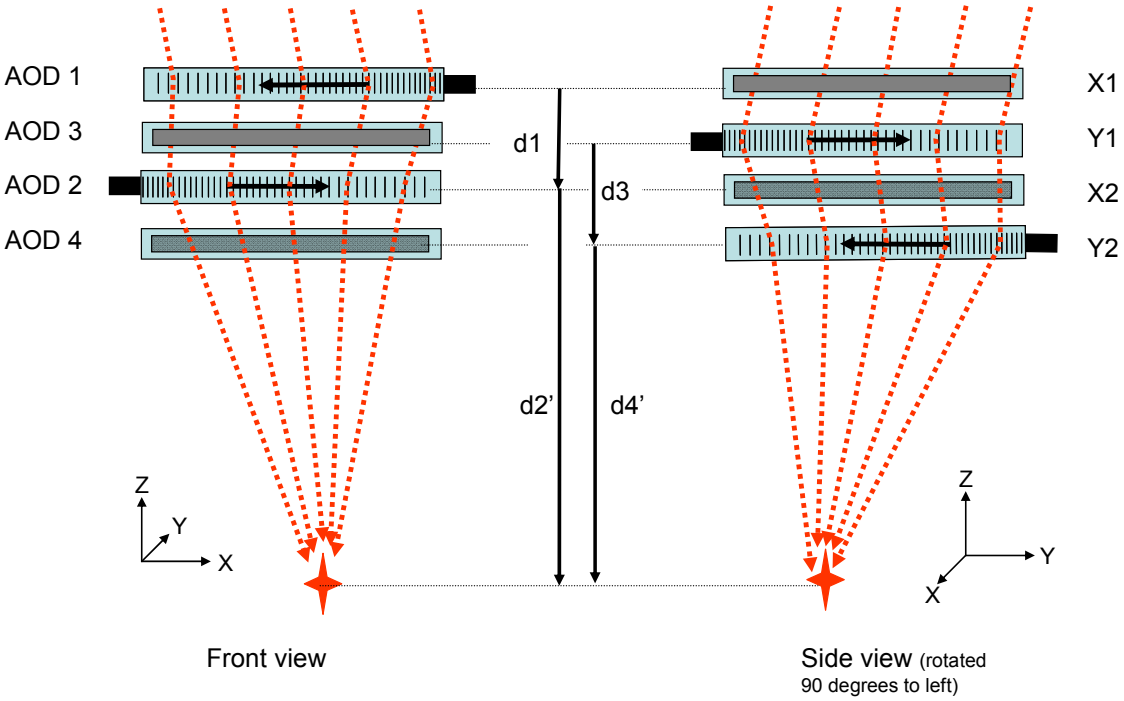

Figure 2.19 Sequence and orientation of four AODs forming an AOL. They are labeled, and distances are defined for the equations of the compact configuration. Note the interleaved numbering of AODs 1 and 2 and 3 and 4 so that it is clear from the equations that the equations for the XZ plane and YZ plane are essentially the same.

These principles can be extended to a system which uses four AODs to focus in the X,Y and Z dimensions. Figure 2.19a) and b) show two orthogonal views of a four AOD system. The third and fourth AOD3 and AOD4 are interleaved with AODs 1 and 2 as shown, the distance between AOD3 and AOD4 being d_3 and the distance from AOD4 to the focal point being $d_4^{'}$. The ramp rates for the third and fourth AODs can be calculated in a similar way as for the first and second AODs. Very similar equations apply:-

$$a_4 = \frac{V^2}{2\lambda d_4^{'}}$$ equation 2.20

$$a_3 = \frac{V^2}{\lambda\left(2d_4^{'} + d_3\right)}$$ equation 2.21

$$\frac{a_3}{a_4} = \frac{2d_4^{'}}{2d_4^{'} + d_3}$$ equation 2.22

AOD1 and AOD2 focus in the chosen X-Z plane whilst AOD3 and AOD4 focus in the Y-Z plane. The distances $d_2^{'}$ and $d_4^{'}$ are such as to ensure that the final focus is the same in both planes. Any error will cause astigmatism. As noted earlier the actual distances between the AODs and the optical thickness of any intervening components, as well as the AODs themselves, needs to be taken into account when determining $d_1, d_2, d_3, d_2^{'}$ and $d_4^{'}$.

Depending on the exact configuration used, further fine tuning may be applied to achieve an exactly stationary spot. The equations above are based on the simplified assumption of AOD crystals having surfaces that are perpendicular to the direction of propagation of the light. It is possible to manufacture the AODs with slightly angled faces (and there are practical reasons to do exactly this) and this can cause errors that result in a small residual movement of the focal position. These residual movements can be corrected by small adjustments to the ratio of ramp rates a_1/a_2, a_2/a_4. These corrections can either be found experimentally or by building a more accurate optical model using a commercial programme like Zemax. When such angled faces are used, typical corrections are much less than +/-2% to the ramp rate of each AOD.

Similarly, small corrections may be applied to the ratio of the X ramp rate to the Y ramp rate to fine tune the astigmatism of the focus. This is equivalent to adjusting the ratio of $d_2^{'}$ to $d_4^{'}$ so that the Z value of the focal position in the X-Z and X-Y planes is the same. These fine tuning corrections may be a function of the Z position of the focal spot and can readily be built into the algorithms that compute the ramp rate of the AODs before each scan.

It is clear from the derivation that in theory the compact configuration of AOL can be used to achieve a stationary focal point at any chosen value of Z within the field of view. The control equations need now to be extended to calculate the precise start and stop frequencies of each frequency ramp, how to adjust these to cause particular X and Y deflection and how to adjust the frequency ramp rates to not only point at a particular spot but also to scan in the XY plane to build up a raster image at the fastest possible rate. This requires precise control of X and Y plane scan rate at a fixed Z

plane. The fact that the AODs have a limited operating frequency range and the frequency ramp rates for Z focusing are high, also means that it is often necessary to reset the drive frequencies to the other side of the operating frequency range. It is therefore necessary to understand how to offset the drive frequencies without causing any X or Y movement of the focused spot and restart an interrupted scan.

I have found these issues quite complex during the development and have had to correct implemented control software more than once because of my initial lack of clarity on the issue of resetting pairs of AOD drive frequencies to maintain precise knowledge of the pointing position vs. time of the focused laser spot. Recently I have developed a graphical way of understanding this very multidimensional problem. This is illustrated in Figure 2.20.

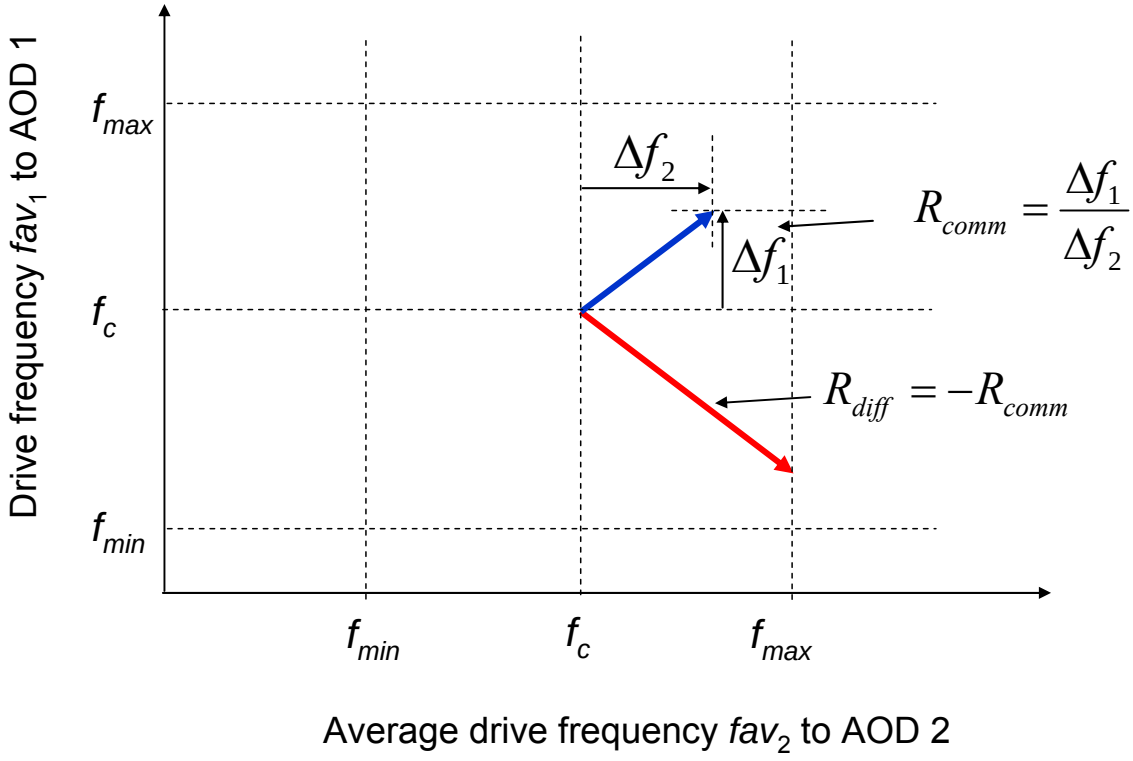

Figure 2.20 A graphical way to analyse drive frequencies applied to the XZ pair of AODs. The common mode ratio (or gradient) shown blue is the gradient in frequency space that produces no movement of the focal spot. The orthogonal differential mode gradient (shown in red) produces only X deflection of the spot with no common mode deflection.

For the case of XZ deflection and focusing with AOD1 and AOD2 as discussed above, the drive frequencies fav_2 and fav_1 can be plotted on the X and Y axes of a graph as illustrated. These '*f* average' symbols represent the frequency at the centre of the AOD at the particular time being considered. As the ramp rates a_1 and a_2 are

linear in both time and space, the frequencies at the centre are the spatial averages of the frequencies currently in the AOD aperture and in turn determine the average deflection angle of the AOD. Referring to Figure 2.20, any pair of average frequencies can be represented on this plot by a point in the fav_2 , fav_1 plane. A gradual or step change in the pair of drive centre frequencies can be represented by a vector lying in the plane. Its direction determines what happens to the focal spot position. If fav_2 and fav_1 are changed with a differential gradient marked as common mode drive gradient R_{comm}, there is no change in the position of the spot. Common mode drive frequency change is defined as change where the ratio of the frequency changes is :

$$R_{comm} = \frac{\Delta fav_1}{\Delta fav_2} = \frac{2d_2^{'}}{2d_2^{'} + d_1} \qquad \text{equation 2.23}$$

Notice that this ratio of frequency change is exactly the ratio of ramp rates that gives a stationary focal spot at a distance $d_2^{'}$ from the last AOD. It has a fixed value for any particular chosen Z focal plane. For a stationary focal spot, if you plotted the two frequencies at the centre of the two AODs as they varied with time, they would move along a line parallel to the vector shown. It also implies that it does not matter what pair of frequencies you start the ramp at as long as they are on this common mode deflection line, the focal spot will always be at the same position.

The converse applies to the differential mode line on this plot defined by:

$$R_{diff} = \frac{\Delta fav_1}{\Delta fav_2} = \frac{-2d_2^{'}}{2d_2^{'} + d_1} \qquad \text{equation 2.24}$$

Changes in this direction produce changes in X position of the focal spot with no changes in common mode frequency difference. Its gradient is by definition -1 times the common mode gradient. Referring to Figure 2.20 and Figure 2.21 , in fav_2,fav_1 frequency space the vectors $\boldsymbol{R_{comm}}$ = [1, R_{comm}] and $\boldsymbol{R_{diff}}$ = [1, R_{diff}] (where vectors are shown in bold and scalars in normal type face) can be used as the unit vectors of a 2D basis. Any vector in this plane can be analysed in terms of its common mode and differential mode basis vector components.

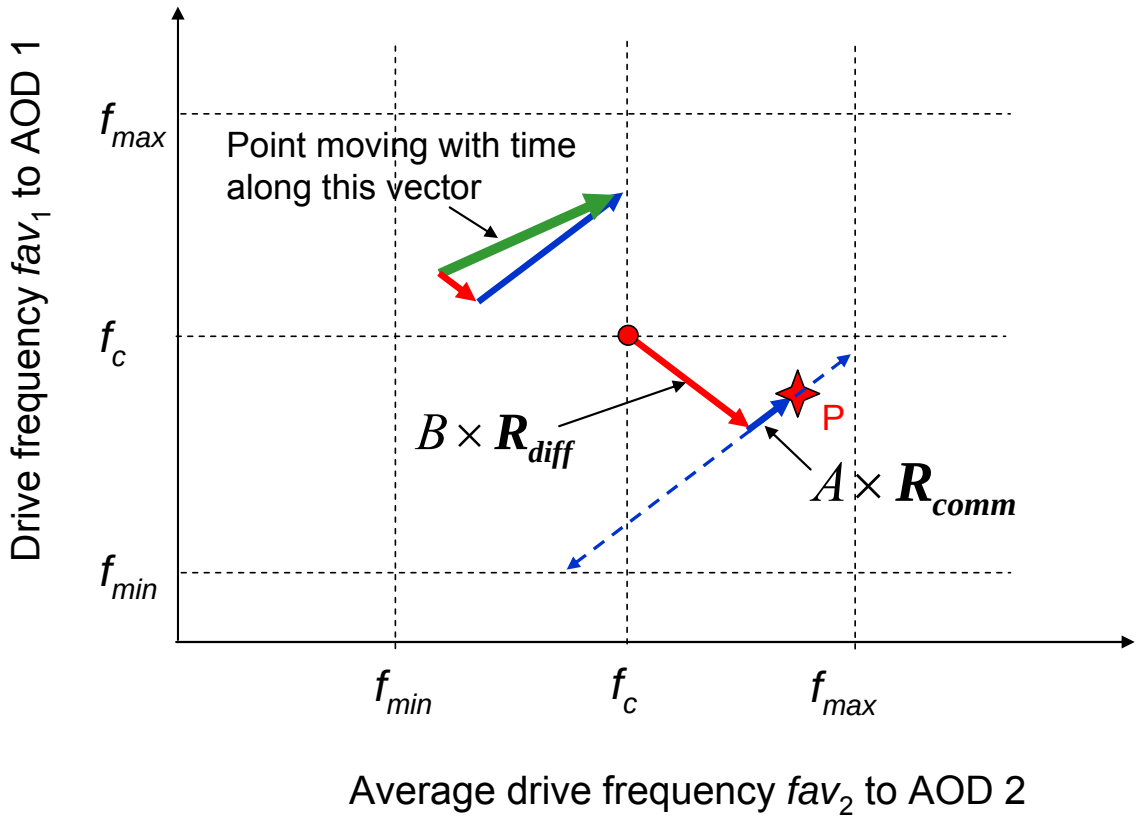

Figure 2.21 Showing how any pair of frequencies (P red star) or difference in pair of frequencies vector can be analysed into common mode (blue) and differential mode components (red). Bold text refers to a vector, normal text to a scalar. The dotted blue line represents all pairs of frequencies between the AOD drive limit frequencies that point in the same direction as the point P. Driving the AODs repetitively up this line and jumping back to the lower position corresponds to the sawtooth of frequencies required to focus on a spot in the same lateral offset (X) that static frequency pair at P would point. The rate of shift along the line determines the focus (Z). The Green vector direction combines a large common mode with a small differential mode and steady movement along this line produces fixed Z focusing and relatively slow X translation of the focal point.

The red point 'P' represents a particular fav_2, fav_1 coordinate. This can equally well be represented by the vector equation

$$[fav_1, fav_2] = [f_c, f_c] + A \times \boldsymbol{R}_{comm} + B \times \boldsymbol{R}_{diff} \qquad \text{equation 2.25}$$

Where f_c is the centre frequency of the AOD drive range and A and B are the scalar multipliers for the unit vectors pointing in the $\boldsymbol{R}_{comm}$ and $\boldsymbol{R}_{diff}$ directions as illustrated by the red and blue arrows on the figure. The blue dotted line through the point 'P' with a gradient R_{comm} (scalar) is the line of all the other points that equally well would

point at the same position. Using this plot it is now obvious that for repeated pointing at the same position in 3D space that point P points at, without the drive frequencies going outside the high efficiency regions of the AODs, the ramps must repeatedly start at the pair of frequencies defined by the lower left end of the dotted blue line and stop at the top right end. In jumping back to the start, there is no shift in the position the AODs are pointing at.

Figure 2.21 also shows a green line representing a time sequence of [fav_2, fav_1] coordinates. These can also be analysed into their $A \times \boldsymbol{R}_{comm} + B \times \boldsymbol{R}_{diff}$ pairs as shown in red and blue. In this case the green line is the drive to produce a focused beam with a small differential component that means the spot is slowly moving in the X direction (shown in red). The common mode scan rate in time determines the Z focal plane (and the precise direction of the $\boldsymbol{R}_{comm}$ and $\boldsymbol{R}_{diff}$ unit vectors on this plot.) as shown in blue and red.

Deriving algorithms for the scanning mode

To build up a three-dimensional image of a semi transparent sample (such as brain tissue), it is useful to be able to follow a raster scan with the focal point along a predetermined path through the sample. The most commonly used raster scan is to move the focal point in the X direction, keeping the Y and Z values constant, to then increment the Y position by some small amount, to perform another scan in the X direction and so on until a two-dimensional grid of scans is achieved. The Z direction is then incremented and another two-dimensional grid is scanned until a three dimensional volume has been built up. This type of raster scanning, illustrated in Figure 2.22, is much faster than building up an image by using the pointing mode to sequentially address every point. The pointing mode takes one AOD fill time plus one data collection time (dwell time) to take data from each point. With 25 μs AOD fill time and a typical 4 μs dwell time this process takes nearly 4 minutes in the pointing mode for the 7.8 million voxels[2] that our target system is capable of resolving. With raster scanning many data points are gathered for each AOD fill time by moving the focused spot over sequential voxels at a rate of 1 dwell time per voxel. As the raster scans increase in length so the total scan time reduces asymptotically towards the

[2]Number of voxels in a 250μm cube divided by a 1×1×2 μm voxel: 250×250×250/2= 7.8125 million voxels,

limit of one dwell time per voxel which is about 30 seconds for 4 μs dwell time scanning the full 3D volume.

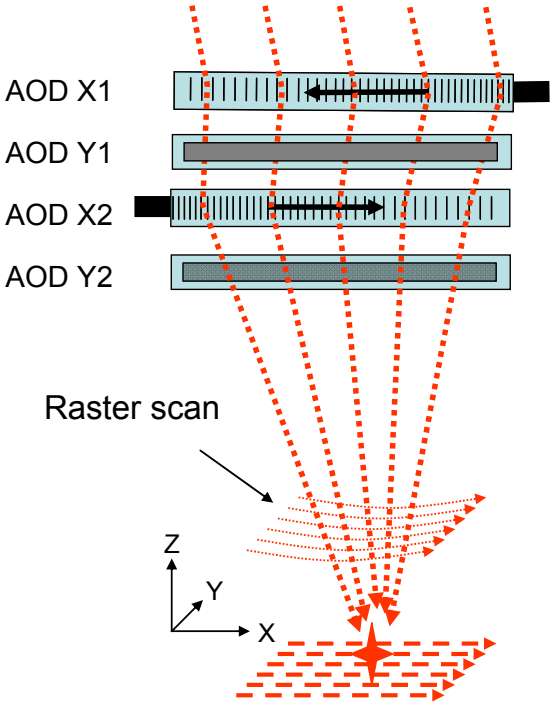

Figure 2.22 An acousto-optic lens forming a raster scan of a 2D plane. The bold converging red lines represent the laser beam converging towards a focus. The straight dashed red lines indicate the path traced by the focal point (red star). The curved dotted red lines show the spot scanning with time from left to right starting with the furthest line.

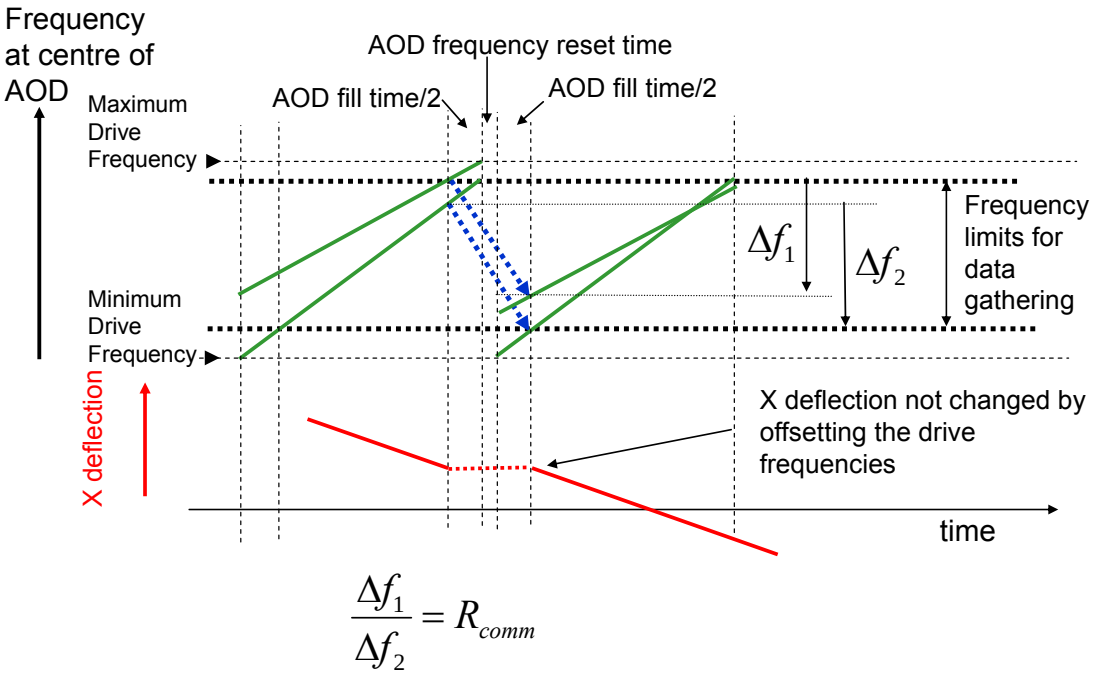

Figure 2.23 Diagram to illustrate AOD X1 and AOD X2 drive frequencies vs. time for part of a sequence of miniscans deflecting in X and focusing a focal spot at a constant Z plane across one line of a raster at fixed Y value. The pair of green lines corresponds to a single vector in the frequency space diagram (next figure). The red line shows that there is no X deflection in the fly-back period between the end of one data gathering sequence and the beginning of the next.

Consider now the drive frequency sequence necessary to scan a focal spot along the maximum possible distance in the X direction without exceeding the drive frequency limits of the AODs. Figure 2.23 shows the AOD centre frequencies plotted against time whilst scanning in the X direction. In order to produce the required focusing in Z the ramp rates on both AODs are high. Since there is a limited frequency range, it is not possible to do a single scan right across the maximum possible X scan range. The scanning process therefore has to be broken up into a sequence of ‘miniscans’. Two of these miniscan frequency traces are plotted in the figure showing the transition between them. The maximum and minimum drive frequencies for the AODs are defined by the limiting frequencies where the efficiency drops below say 80% of the peak efficiency.

It takes one AOD fill time for the sound wave to fill the AOD aperture so that data recording can begin, and the time at which a particular frequency reaches the mid point of the AOD is half the AOD fill time after it was transmitted by the transducer. Recording of fluorescence data from a full AOD is therefore only possible for

frequencies sent by the transducer more than half an AOD fill time from either the beginning or end of the frequency ramp. This further reduces the available frequency range as shown by the inset bold dotted lines on the figure. The total time from the end of data gathering of one miniscan to the start of data gathering of the next is thus the AOD fill time plus any 'flyback' time for electronically resetting the drive frequencies.

The key point in developing an algorithm for calculating the precise start and stop frequencies of each miniscan is that the position of the focal spot at the start of the first voxel of a new miniscan must be in exactly in the same position as the it was at the trailing edge of the last voxel of the previous miniscan. This is illustrated in the lower part of the figure in red. The frequency offsets Δf_1 and Δf_2 must therefore be in the exact ratio R_{comm}.

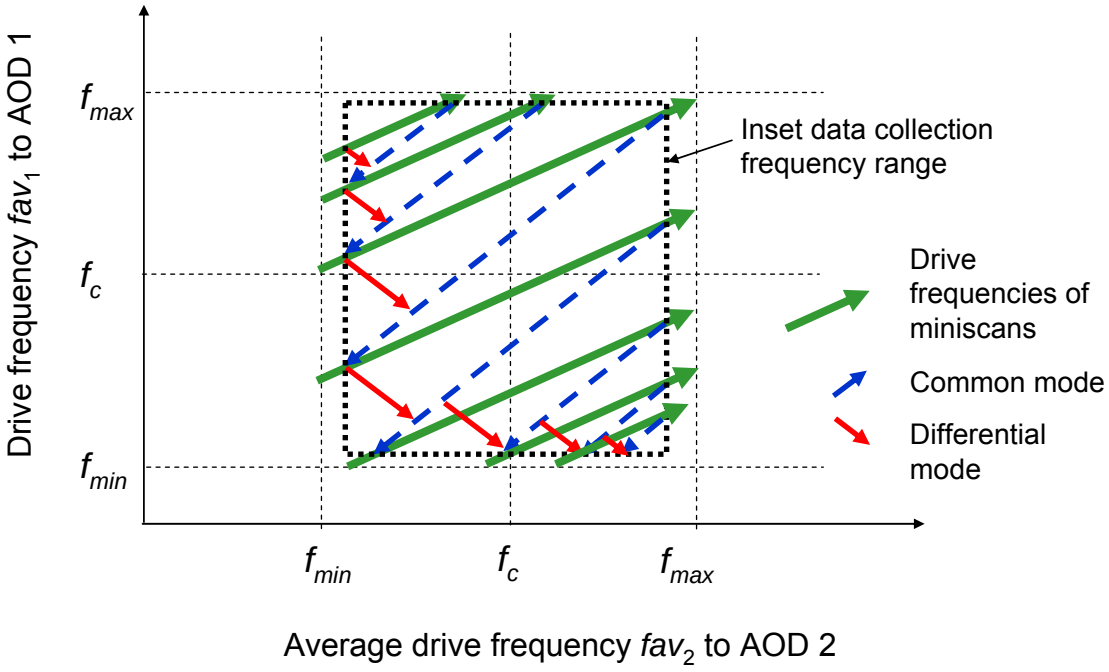

Figure 2.24 Diagram illustrating the full sequence of miniscans making up one full X scan The green arrow correspond to the green pair of drive frequencies shown vs. time on the previous figure. As the green vector has a small differential mode component it is scanning as well as focusing at a particular Z plane. This is shown by the red differential mode lines. The frequency limits for data collection have to be inset with respect to the efficiency limits because data can only be gathered from full AODs. The common mode (blue dashed) fly-back lines ensure that when data gathering starts again in the next miniscan it does so from the same position.

Figure 2.24 illustrates in the fav_2 fav_1 plane how the fastest possible X scan is built up by a sequence of miniscans. The green arrows show the path in this frequency space

of the two drive frequencies at the centre of the AODs. The blue common mode dashed arrows show how the frequencies are reset from the end of one data gathering sequence to the beginning of the next. The start and stop frequencies of the miniscans are then defined by extending these ramps out to the drive frequency limits as shown. Note that as in the pointing mode, the precise direction of the blue common mode unit vector and the red differential mode unit vector are dependent on the chosen focal Z plane according to equations 2.23 and 2.24. It is hoped that these two graphical aids give a good understanding of how the algorithms for computing the precise miniscan drive frequencies work.

It is now a fairly simple extension of the equations already derived to calculate the full equations for each important parameter:

The X scan rate $\delta\theta/\delta t$ is set at a rate so that it takes one dwell time to scan across one voxel. This is done by defining the semiscan angle of the AODs 's', Nvox, the number of voxels in the scan, typically 100 to 500 and the dwell time of the focal spot as it scans across each voxel.

$$\frac{\delta\theta}{\delta t} = \frac{2s}{Nvox \times DwellTime} \qquad \text{equation 2.26}$$

It is also assumed that the Z focal distance of the AOL, $d_2^{'}$ is also predetermined, so that the common mode offset frequency ratio R_{comm} is also fixed. These assumptions give a set of simultaneous equations that can be solved to give the following equations for the precise ramp rates (a_1, a_2) of AOD1 and AOD2 in the desired form:

$$a_1 = \frac{\frac{V}{\lambda}\left(\frac{V}{d_2^{'}} - \frac{\delta\theta}{\delta t}\right)}{\left(2 + \frac{d_1}{d_2^{'}} - \frac{d_1}{V}\frac{\delta\theta}{\delta t}\right)} \qquad \text{equation 2.27}$$

$$a_2 = \frac{V^2}{2\lambda d_2^{'}} + \frac{V}{2\lambda}\frac{\delta\theta}{\delta t} \qquad \text{equation 2.28}$$

These equations apply where there are two AODs for focusing in the X-Z plane or, as shown in Figure 2.19, when there are four AODs. In this case, the

angular scan rate $\delta\theta/\delta t$ is that measured about the AOD2 (which is third in the diagram!). The apparent rate as measured about the last AOD4 can be obtained by multiplying this scan rate by $d_2^{'}/d_4^{'}$.

Referring to Figure 2.19 the appropriate equations for the Y-Z plane are found in a similar manner. Here, ϕ is the angle as measured from the fourth AOD4.

$$a_3 = \frac{V/\lambda\left(V/d_4^{'} - \delta\phi/\delta t\right)}{\left(2 + d_3/d_4^{'} - d_3\delta\phi/V\delta t\right)} \qquad \text{equation 2.29}$$

$$a_4 = \frac{V^2}{2\lambda d_4^{'}} + \frac{V\delta\phi}{2\lambda\delta t} \qquad \text{equation 2.30}$$

This information taken together is the basis for the initial set of algorithms I developed in Matlab to pre-compute the sequence of ramps for all four AODs to either 3D scan or point to a sequence of points of interest chosen from within the scanned 3D volume. We later came to refer to these algorithms as the Absolute Frequency Limit (AFL) algorithms because they are based on the assumption that in order to keep the AOD efficiency high, each AOD must at all times stay within the absolute frequency limits set for the AODs. In chapter 4 we develop new algorithms that scan a larger volume at high efficiency by optimising the frequency limits independently for each miniscan.

Figure 2.25 shows a schematic diagram of the complete prototype with the computer control system that drives the AODs using the Matlab code based on these equations and the compact configuration AODs. With the exception of the prechirper, the other components of the complete 2-photon microscope are generally similar to those of a standard 2-photon microscope although the drive electronics for the AODs and image reconstruction is somewhat more complex than the galvanometer equivalent. The data acquisition from the photomultiplier tubes is precisely synchronised with the drive to the AODs so that for each data gathering timeslot (typically 1 – 4 μs long) the

computer is able to insert into the computer memory the measured light intensity at the 3D coordinates of the voxel that the AOL is pointing to during that time. The prechirper is included to compensate for the effect of the high chromatic dispersion of TeO_2 which otherwise spreads out the Ti-Sapphire laser pulses in time and greatly reduces 2-photon emission efficiency. (Reddy, Kelleher et al. 2008)

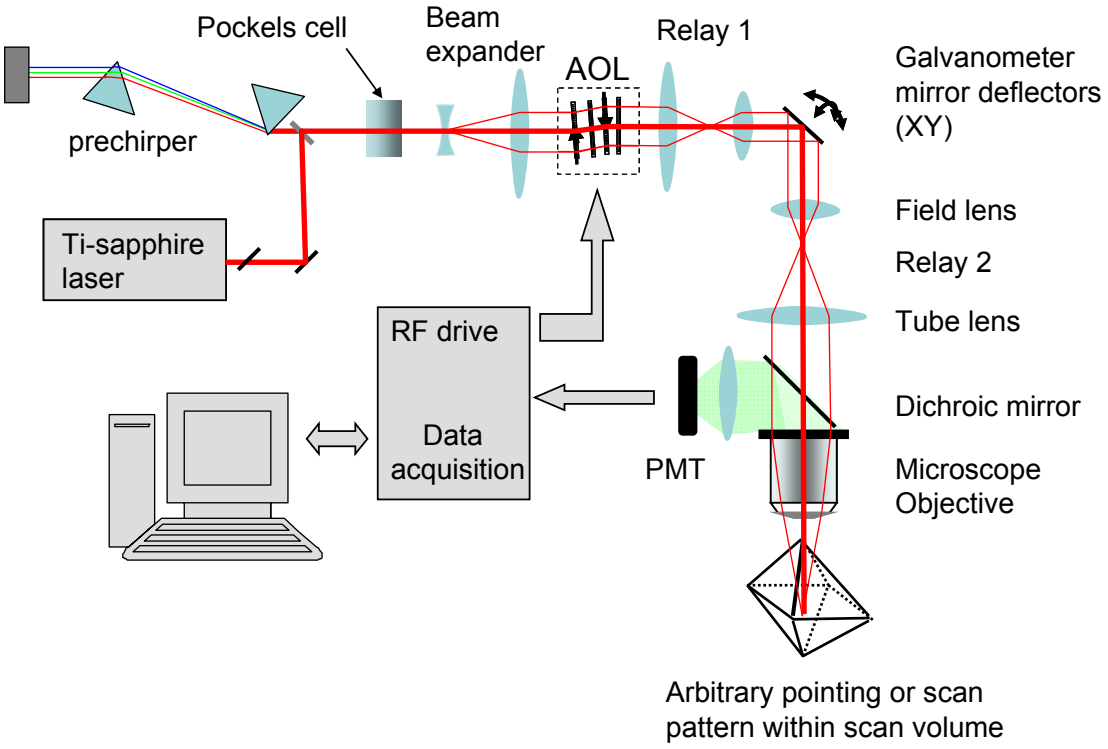

Figure 2.25 Diagram of the complete prototype .system with the compact configuration AOL and computer drive and acquisition electronics

Summary of chapter 2

This chapter starts by developing a clear technical argument justifying the choice of acousto-optic deflectors for the type of high performance optical functional imaging we wish to be able to do. The choice of acousto-optic lens configuration is then discussed and a first design of the overall AOLM described. The equations for the field of view of the microscope are then derived from basic geometrical optics in a form that clarifies the relation ship between the basic AOD performance parameters and the final system performance. The practical problems that would be caused by changing source wavelength using the first AOLM design are then described and a novel ‘compact configuration’ of AOL proposed. This compact configuration requires that new basic radio frequency (RF) drive equations are derived for pointing and scanning. These are derived in the final two sections.

Chapter 3 AOD Design, aberrations and first assembly of AOL

Design of AODs

Acousto–optic device technology is complex but well documented and mature (Goutzoulis, Pape et al. 1994);(Xu and Stroud 1992). It is used today by a relatively small number of specialist manufacturers. At visible and near infra red wavelengths the most widely used material for AODs is Tellurium Dioxide (TeO_2). This is because of its strong interaction between light and sound waves in the crystal and good manufacturablity. The physics of optical and acoustic propagation in this crystal is mathematically very complex because its class 442 crystal symmetry is not only uniaxial birefringent but also optically active(Xu and Stroud 1992) p13. When the electric field of the light wave displaces electrons in the crystal not only do they get displaced linearly, but also they gyrate slightly inducing a magnetic field component as well as the usual electric displacement field. This means that the solution of Maxwells equations for light propagation in the crystal involve tensors of rank 3.

A standard uniaxial birefringent crystal (e.g.calcite) has two refractive indices, ordinary and extraordinary. Light coupled into the crystal will in general couple into both the ‘eigenmodes’ corresponding to these two different refractive indices and propagate separately. ‘Eigenmodes’ or ‘normal modes’ are the natural modes of propagation of light in the crystal. They are the only modes which propagate unchanged: all other modes are made up of a mixture of these two eigenmodes. The polarisation states of the two eigenmodes are orthogonal, and dependent on the precise direction of propagation. The refractive indices are represented on a 3D surface which represents the inverse of the phase velocity of light in the crystal as a function of direction within the crystal Figure 3.1. Ordinary waves, or ‘o-waves’, have the same speed in all directions and therefore the index surface is a sphere. The index surface of the extraordinary ‘e-waves’ is ellipsoidal with the same index as the o-waves only along the crystal axis. In order to explain the design of AODs with greater clarity I have used Matlab 3D graphics to show the index and wave vector surfaces in 3D. The index data is from (Xu and Stroud 1992).

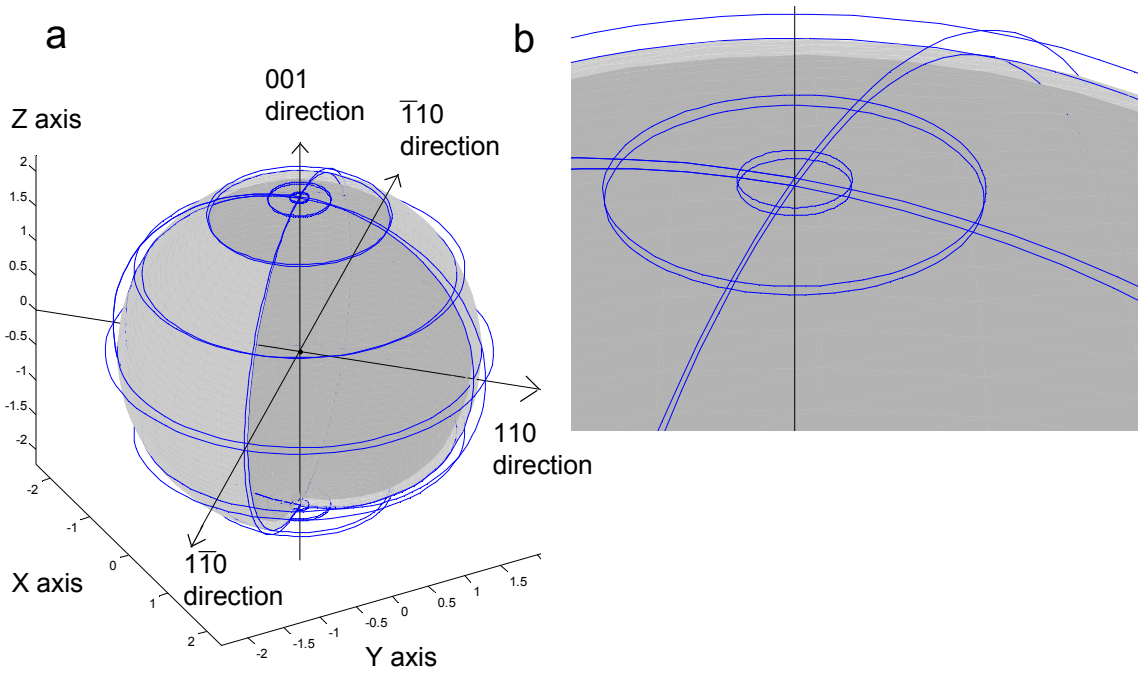

Figure 3.1 The 3D index surface of TeO_2 at a wavelength of 0.8 μm showing refractive index as a function of light propagation direction in 3D space based on data and equations from (Xu and Stroud 1992). Consider a light wave with its phase velocity vector stretching from the origin X,Y,Z =0 (intersection of three black lines) to the index surface. The XY and Z axes are the crystallographic axes. a) View of the complete index sphere showing the optic axis in the Z <001> direction. The pairs of blue latitude and longitude lines show in 3D where the inner 'ordinary' surface and the outer 'extraordinary' surface lie. For clarity ¾ of the inner index sphere has been shaded gray to hide the latitude and longitude lines on the far side of the sphere. The <110> direction is also shown as this is the direction of minimum sound wave velocity and is close to the propagation direction of the usual acoustic wave in the crystal. b) Close up of the latitude and longitude lines around the 'north pole' (optic axis) of the sphere. The upper set of latitude and longitude lines lie in the extraordinary index sphere and the lower set in the ordinary. The inner latitude circle corresponds to all light waves travelling at 3 degrees off the 001 optic axis. The outer circle corresponds to 10 degrees off the optic axis. The index of both surfaces is purely a function of this latitude angle. For clarity the difference between the ordinary and extraordinary indices has been exaggerated at the optic axis. The maximum difference in indices occurs at the equator for light propagating at 90 degrees to the optic axis

As shown in Figure 3.1, for TeO_2 which is a positive uniaxial crystal the extraordinary waves have higher refractive index (slower speed of light) around the equator of the ellipsoid. The additional complication with TeO_2 is that even along the optic axis the e and o index surfaces do not touch. The o-surface is slightly depressed in the Z [001] direction and the e-surface is slightly raised. This is because the crystal structure has a slightly spiral structure (chirality). This causes a problem with operating AODs with

light propagating close to the optic axis. Within about 10 degrees of the axis there is a transition from linear polarisation to circular polarisation on axis and at intermediate angles the eigenmodes are elliptical. This is illustrated in Figure 3.2.

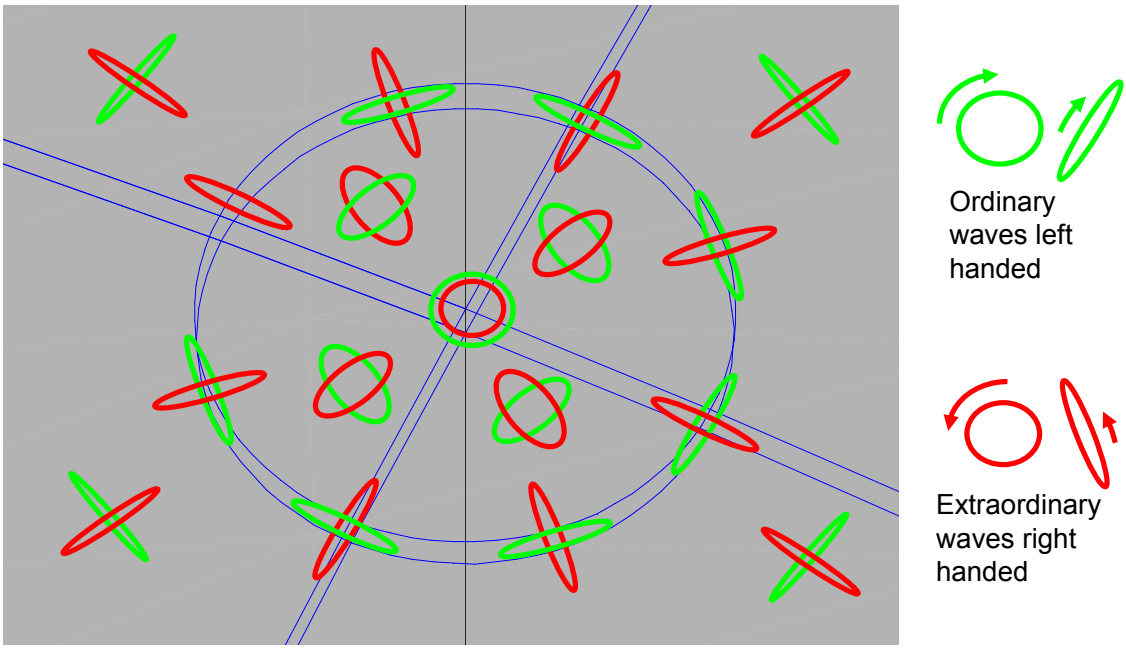

Figure 3.2 Polarisation ellipsoids illustrating the state of polarisation of the two eigenmodes of TeO_2 as propagation direction varies close to the optic axis (vertical black line). The blue lines are the same pairs of latitude and longitude lines showing the two index surfaces as in figure 3.1. The circular blue pair of lines corresponds to the 3 degree off axis latitude line shown in figure 3.1. Ordinary eigenmodes are all left hand polarised (green) and the extraordinary (higher index, or 'slow') waves are all right hand polarised ellipses (red). Exactly on axis the waves are circularly polarised

The e-wave in standard left handed crystal TeO_2 has a slightly higher index (slow wave) than the o-wave. If you launch linearly polarised light along the 001 crystal axis of TeO_2 it splits into two equal intensity propagating circular waves, the right handed e-wave and left handed o-wave (red and green circles on axis in Figure 3.2). At the exit to the crystal these interfere to produce a linearly polarised light wave, but its polarisation has rotated because of the difference in phase velocity of the eigenmodes. At 800 nm this optical activity produces 48.5 degrees of rotation per mm of crystal (Xu and Stroud 1992), p620. As the propagation angle off axis increases so the ellipticity of the eigenmodes increases rapidly so that by 4 degrees off axis at 800nm wavelength the polarisation is nearly linear with only 15% ellipticity. Note that the red extraordinary wave always has the long axis of its polarisation ellipse aligned radially to the optic axis and the ordinary mode is aligned circumferentially.

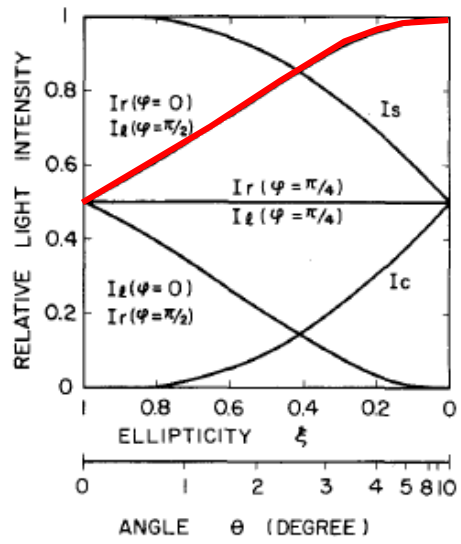

Figure 3.3 The ellipticity varying from 1 (circular polarisation) to 0 (linear polarisation) as wave vector angle off the optic axis θ increases. Also shown is the intensity of an eigenmode when excited by external linear or circularly polarised light as a function of off axis angle θ . Modified from (Yano and Watanabe 1974). The red line shows intensity of light coupled into an eigenmode from linearly polarised incident wave with its long axis of ellipticity parallel to the incident polarisation as a function of off optic axis angle θ.

Figure 3.3 modified from (Yano and Watanabe 1974) plots the ellipticity varying from 1 (circular polarisation) to 0 (linear polarisation) as wave vector angle increases. As shown in the figure, coupling efficiency into the eigenmodes from pure linear or pure circular polarisation waves varies rapidly with ellipticity. Coupling with high efficiency into significantly elliptical or circular polarisation from linear requires careful use of waveplates which increase optical system cost and complexity (Fukumoto, Kawabuchi et al. 1975). The red line shows that coupling from (and to) linearly polarised external waves is better than 95% providing the off axis angle θ is greater than 4 degrees and the linear polarisation is aligned to the long axis of the ellipse. This may require no waveplates if the alignments are fortuitously correct or one half wave plate to adjust the linear polarisation direction.

The remarkably high figure of merit for TeO_2 was found by (Uchida and Ohmachi 1969). It was however (Warner, White et al. 1972) who first pointed out that unusual index surfaces of TeO_2 could be used to make a deflector with a much lower operating power than any previous AOD. These devices operated with incident and

diffracted waves propagating within a few degrees of the optic axis with light close to circular polarisation. This is illustrated in Figure 3.4. This figure is now a wave vector diagram rather than an index surface diagram. Wave vectors diagrams are widely used for AOD design (see Figure 3.10 for definition of wave vectors). The laws of quantum mechanics determine that within a precise amount of uncertainty, the momentum vector (proportional to wave vector) of the incident wave, plus the momentum vector of the acoustic wave equals the momentum vector of the diffracted wave. The additional constraint is that the optical wave vectors must lie on the appropriate index surface. Since wave vector magnitude is proportional to the material index, the index surfaces on a wave vector diagram are the same shape as on an index surface diagram.

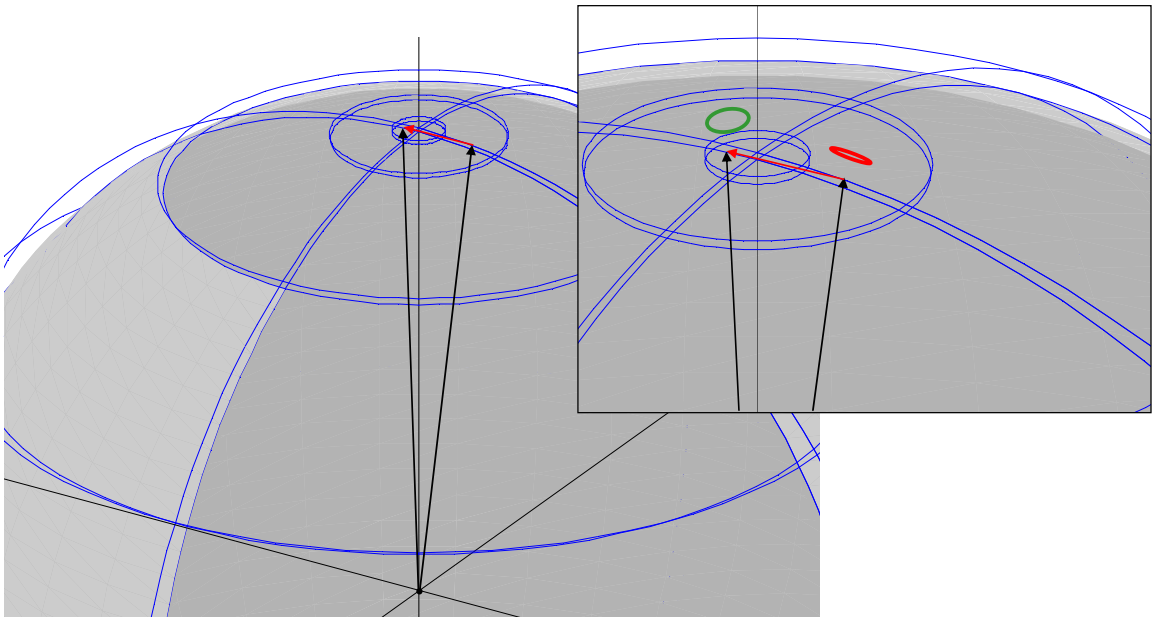

Figure 3.4 Wave vector diagram of an early experimental AOD similar to (Warner, White et al. 1972) showing incident and diffracted optical wave vectors (black arrows) coupled with an acoustic wave vector (red arrow) . The axes (not shown) here represent wave number. (The number of waves/cm in the material . This is proportional to index). The acoustic wave is propagating very close to the <110> direction (see figure 3.1). The insert shows that the right hand incident light wave vector is an extraordinary wave with its polarisation shown as the red ellipse above. The output wave vector is an ordinary wave (green ellipse).

Note that this acoustic vector is closely tangential to the ordinary index wave number surface that the diffracted output wave moves along as drive frequency is varied. This means that even for a fixed direction input optical wave vector and fixed direction acoustic wave, a wide range of output angles can be obtained with only a small error between the sum of the incident and acoustic waves and the diffracted vector which

must be on the ordinary index wave number surface. This is the primary reason that the device has high efficiency over a wide drive frequency range.

There are two problems with this design of AOD however. Firstly, as the acoustic frequency is varied in order to vary the length of the red acoustic wave vector and the direction of the diffracted optical wave vector, the output wave polarisation ellipticity changes rapidly with output angle. Secondly, as shown in Figure 3.5 at high acoustic drive levels there is an unwanted secondary optical coupling.

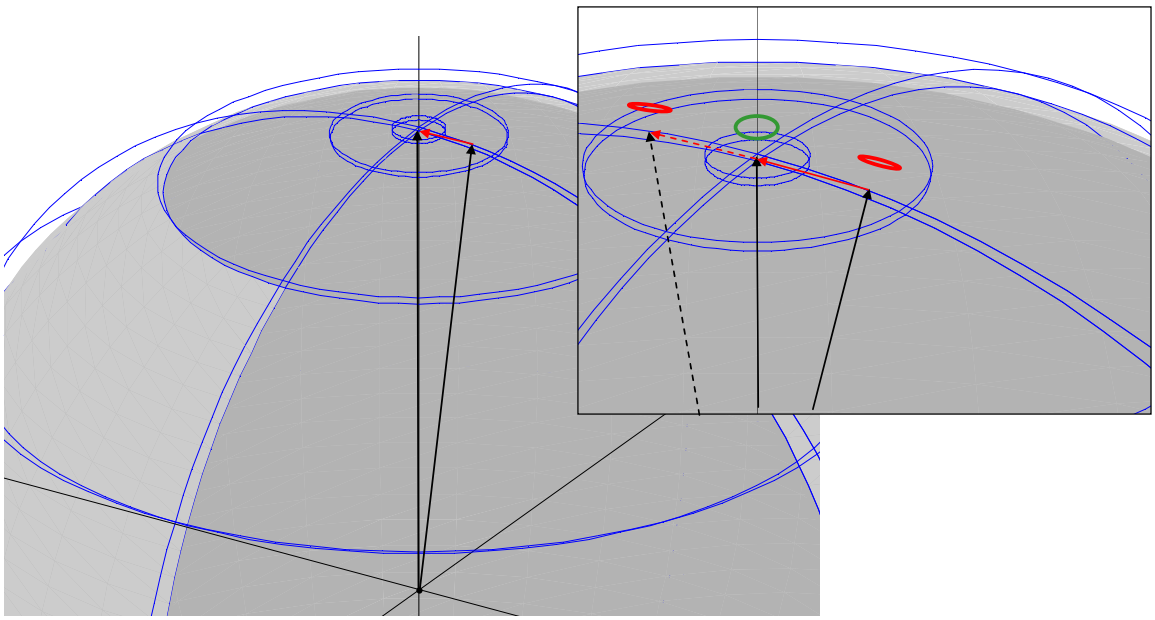

Figure 3.5 Wave vector diagram of an AOD with output wave vector on the optic axis. Insert : At high acoustic drive power a secondary optical coupling occurs to the symmetrically placed extraordinary index surface on the far side of the optic axis via the same acoustic wave (dashed red vector and it produces a wasted secondary output diffracted light wave (dashed black wave vector). This produces a sharp dip in AOD efficiency at the mid band known as the mid band degeneracy dip.

However, the problem reported in Warner is that when the output vector is as shown on axis there is a second order coupling possible between the acoustic wave vector and the extraordinary index surface as shown. At high drive power this second order coupling produces a sharp ‘mid-band degeneracy’ dip in efficiency.

Standard AOD design

It was (Yano, Kawabuchi et al. 1975) who first proposed the 'acoustically rotated' design of TeO_2 deflector widely used today.

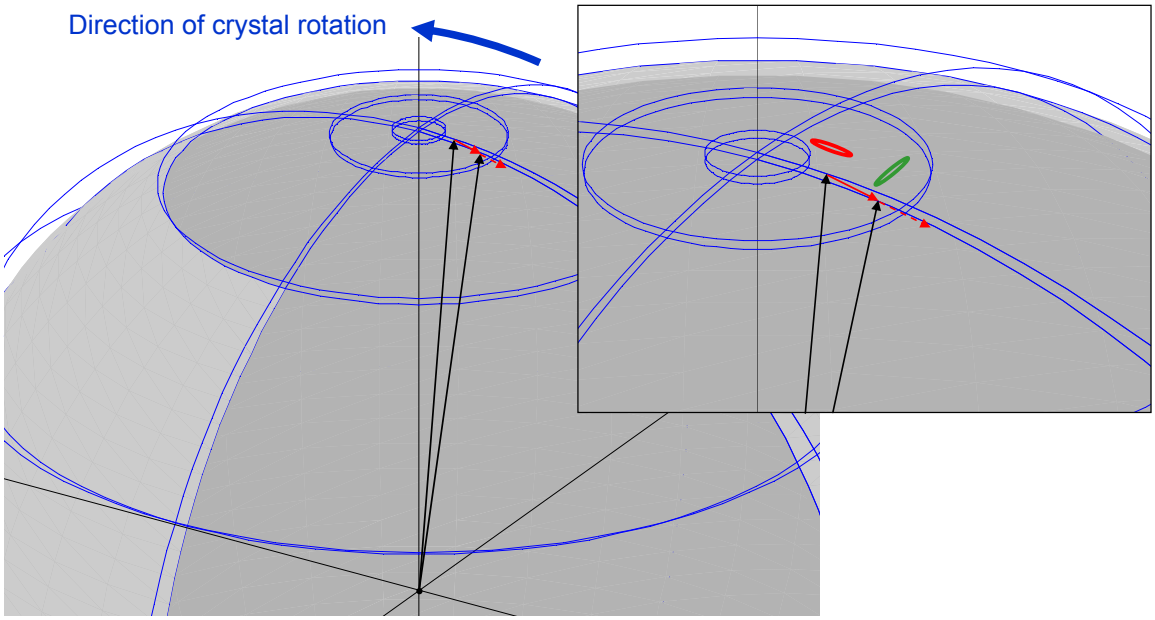

Figure 3.6 Wave vector diagram of an 'acoustically rotated' design of AOD. (Yano, Kawabuchi et al. 1975). It is known as acoustically rotated because, compared to earlier designs, in manufacture, in order to polish the AOD surfaces, the crystal has been rotated in the direction shown by the blue arrow which is in a plane including the acoustic wave vector. In this case the incident extraordinary wave vector is more than 4 degrees off the optic axis and hence is nearly linearly polarised (red ellipse). The output vector is even further off axis (green ellipse). The dashed red arrow shows where secondary acoustic wave vector would couple. Because of the acoustic rotation, this vector is far from intersecting the extraordinary index surface and hence there is a negligible midband dip.

The wave vectors of Yano's acoustically rotated AOD is shown in Figure 3.6. Typically the crystal is rotated by about 5 degrees so that the incident and diffracted polarisations both become nearly linearly polarised (and hence easy to couple to with high efficiency) and the mid band degeneracy does not occur because, as shown by the extended dashed red line, the extraordinary index surface is no longer in the right position to couple to a single added wave vector. For these reasons the acoustically rotated AOD design is the most common form of TeO_2 AOD.

There is however a price to pay. Note in Figure 3.6 that the acoustic wave vector now no longer lies very close to the <110> direction. It too has been rotated by about five degrees with respect to the crystal axes. In order to understand the effect this has on acoustic wave propagation it is necessary to understand the acoustic equivalent of the optical index surface which is known as the acoustic slowness surface.

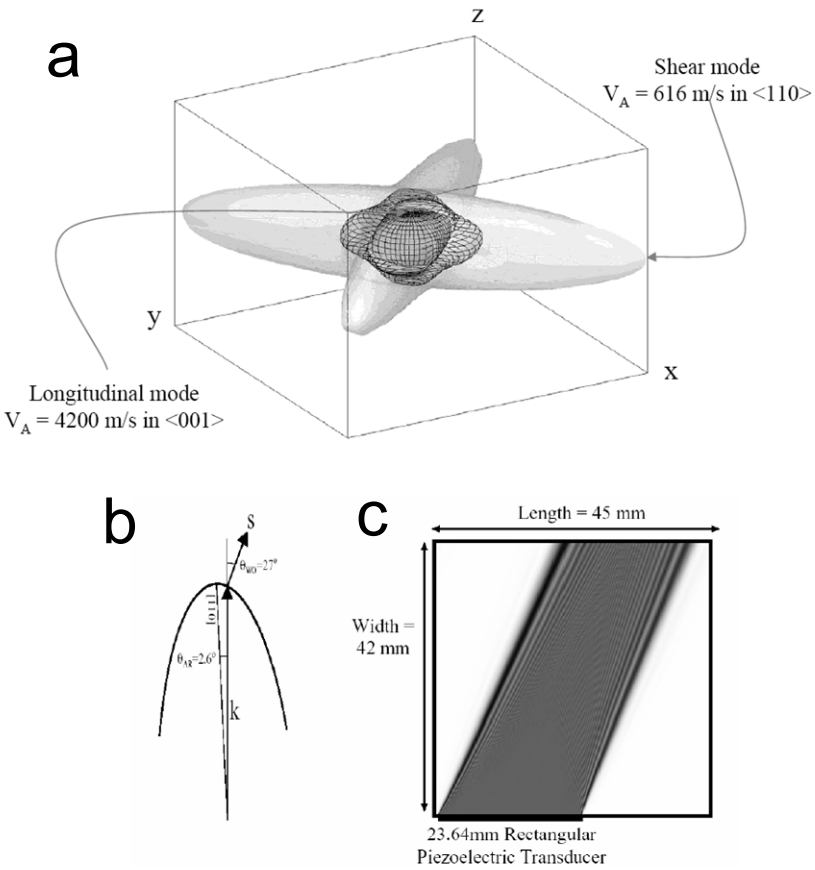

Figure 3.7 Acoustic wave propagation in TeO_2., modified from ((McLoed)) illustrating the remarkable anisotropy of acoustic wave propagation. a) The 3D acoustic wave vector surfaces (slowness surfaces) show that in the shear mode the velocity slows to 616 m/s in the <110> direction but speeds up rapidly for angles away from <110>. As the acoustic vector is tilted off the 110 direction, the energy in the acoustic beam walks off at an angle about 11 times greater than the phase velocity tilt angle. So, as shown in b) and c), a 2.6 degree phase velocity tilt angle produces a walk off angle of 27 degrees. Diffraction is also enhanced remarkably as can be seen by the wide diffraction edge fringes at the edges of the computed acoustic diffraction propagation pattern in diagram c).

Figure 3.7 a) shows the acoustic slowness surfaces for TeO_2. It has three possible acoustic polarisations. The shear mode has a remarkably slow speed of propagation

(616m/s) along the <110> direction. This is largely responsible for the high acousto optic figure of merit of the material. However as tilting the acoustic wave vector causes a rapid increase in propagation speed this results in the unusual anisotropic walk off propagation of acoustic shear waves with wave vectors near the <110> direction b)and c). For the five degree acoustically rotated crystal the walk of angle of the acoustic wave is 55 degrees. This results in the top view of a standard AOD oriented for horizontal deflection as shown in Figure 3.8.

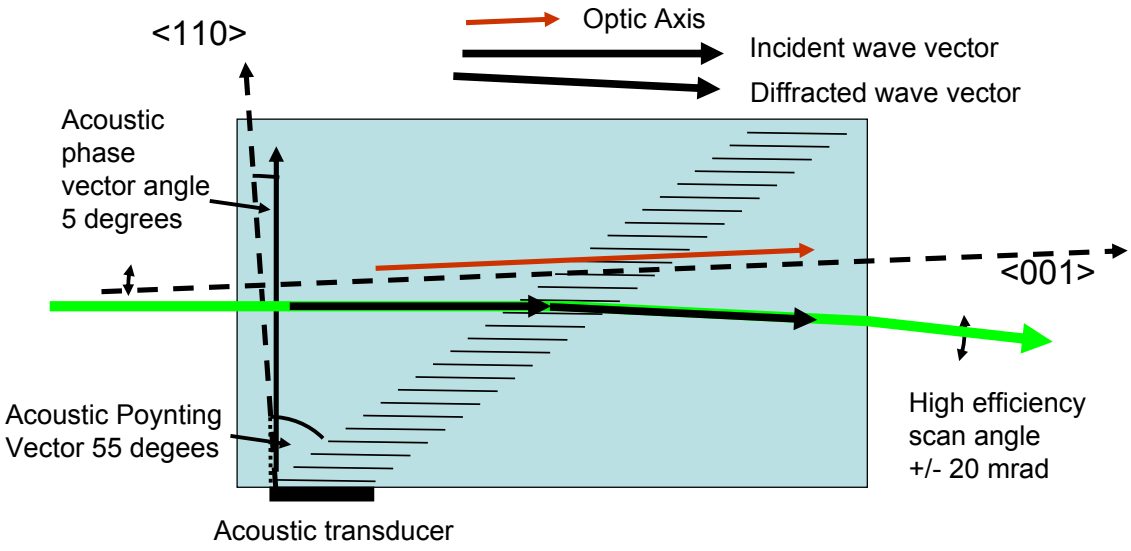

Figure 3.8 Top view of a standard commercial Acousto–Optic Deflector oriented for horizontal deflection showing the typical 5 degree acoustic rotation of the polished crystal faces with respect to the <110> and <001> crystal axes. For the acoustic wave this results in a 55 degree walk-off angle (Poynting Vector). The acoustic wave is shown by the thin black horizontal lines propagating in a very skew (55 degree off axis) direction as it leaves the acoustic transducer at the bottom left of the figure. The thin vertical black arrow shows the direction of the normal to the acoustic transducer (and hence the acoustic wave fronts) and shows that the acoustic wave vector is angled at 5 degrees to the <110> crystal direction. The thick black near horizontal arrows show the typical input optical and diffracted optical output wave directions along with typical output scan angle. The red arrow highlights the <001> direction of the crystal optic axis referred to in later figures.

Figure 3.8 shows a slightly idealised view of the top view of a standard commercial AOD oriented for horizontal deflection. The acoustic and optical wave vectors can be compared to the 3D wave vector diagram in Figure 3.6. The only confusing point is that the acoustic wave vector direction in Figure 3.8 is shown 180 degree rotated and not to scale with the optical wave vectors for compactness and clarity of the figure.

This design of AOD is optimised for maximum high efficiency scan angle often greater than +/- 20mrad.(1 degree = 17mrad). The high walk off angle results in the crystal being approximately 3 times longer than the optical aperture of the crystal (32mm long for 9mm aperture is a widely used commercial design.)

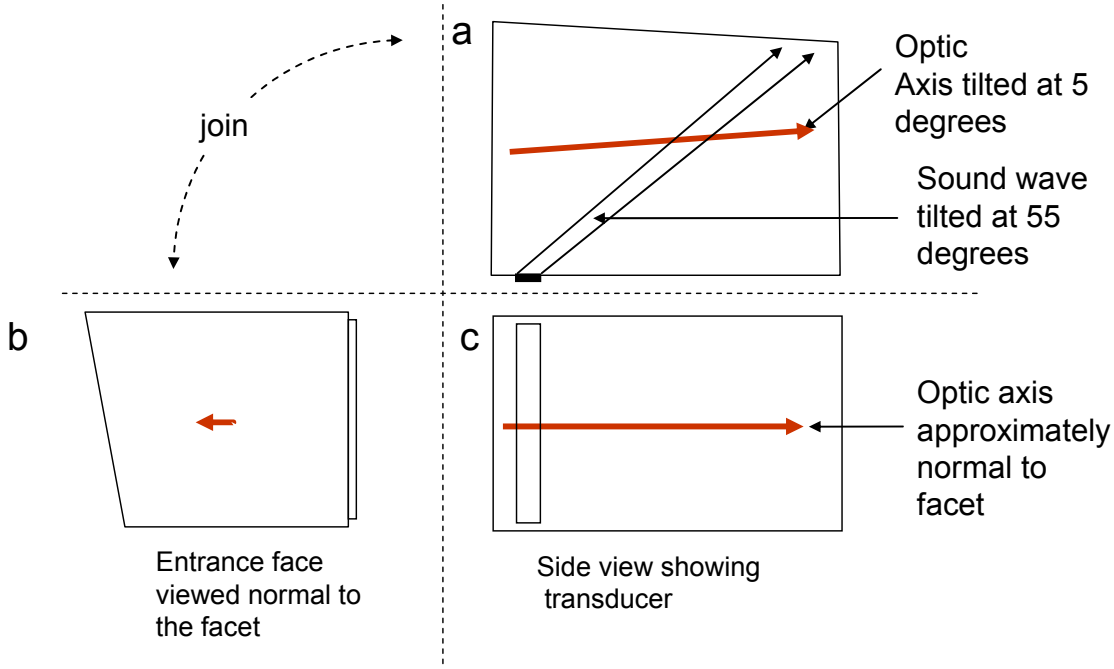

Figure 3.9 3D engineering orthographic projections of a practical commercial AOD. The dashed lines indicate where a 2D paper drawing could be folded around the 3D AOD. The AOD surfaces are a) top surface (for a horizontal plane deflector), b) front entrance surface, c) side view showing the transducer as a rectangle near the front entrance face. The face of the AOD opposite the acoustic transducer is polished at an odd angle and bonded with acoustic absorbing bond to a heat sink. The odd angle of this surface causes any unwanted reflected acoustic wave to bounce around inside the crystal harmlessly until dissipated. The red arrow shows the three projections of the optic axis. For this standard AOD design, viewed from the direction normal to the facet (b), the tilt of the optic axis appears horizontal so the extraordinary incident wave is horizontally polarised and the ordinary diffracted wave is vertically polarised.

In order to understand the input and output polarisations of an AOD, it is useful to be able to picture the direction of the optic axis within the AOD so that polarisation can be related to the polarisation diagram of Figure 3.2. For the standard acoustically rotated AOD, the nearly linear polarisation horizontal polarisation of the input and and nearly linear polarisation of the output optical waves is easy to understand from the 3D orthographic engineering drawing view of Figure 3.9. The orthogonal linear input and output polarisations are convenient and practical as no extra components are needed to make an XY deflector pair. The 90 rotation of the X output polarisation is

ideal to feed into the 90 degree rotated Y deflection crystal. Such pairs are used for 2D scanning laser beam applications such as laser TV projectors and industrial and military laser pointing and scanning systems.

Acceptance angle limitations of AODs

It is apparent from diagrams such Figure 1.12 that for the AOLM application the input acceptance angle of the AOD would ideally be as large as the output scan angle so that it was unlikely that the standard AOD design, highly optimised for a fixed input beam would be the best solution. In my initial contact with manufacturers I found that the details of the AOD design are, as you might expect proprietary, and that getting access to people with sufficient design knowledge to make a custom design is difficult. In order to be able to have knowledgeable discussions with the manufacturers I decided to develop a computer model of the diffraction efficiency of an AOD based on the wave vector model using the equations given in (Goutzoulis, Pape et al. 1994).

Results of modeling of commercially available AODs

Figure 3.10 shows a detailed wave vector diagram of an AOD and the equations for the magnitude of the wave vectors.

Wave vector model of AOD performance

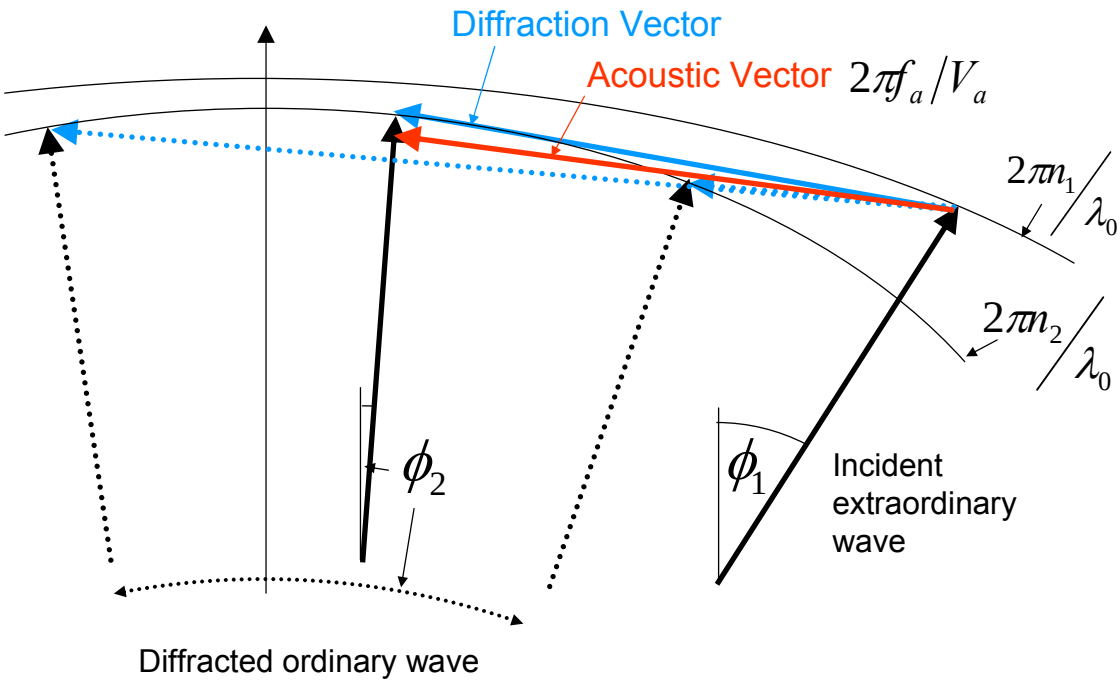

Figure 3.10 Wave vector model of acousto-optic deflector. The black optical incident and diffracted optical waves have indices as defined in the figure. As the acoustic drive frequency is varied so the length of the acoustic wave vector varies (red vector). Its direction is fixed by the angle of the acoustic transducer. The blue optical diffraction vector always meets the output wave vector on the ordinary index surface. As the drive frequency varies so the diffracted output wave angle ϕ_2 varies over the range indicated by the dotted line.

I found that by using the standard design and putting the angular acoustic beam width as an unknown variable I could reproduce the characteristic double peaked efficiency curve given by manufacturers.

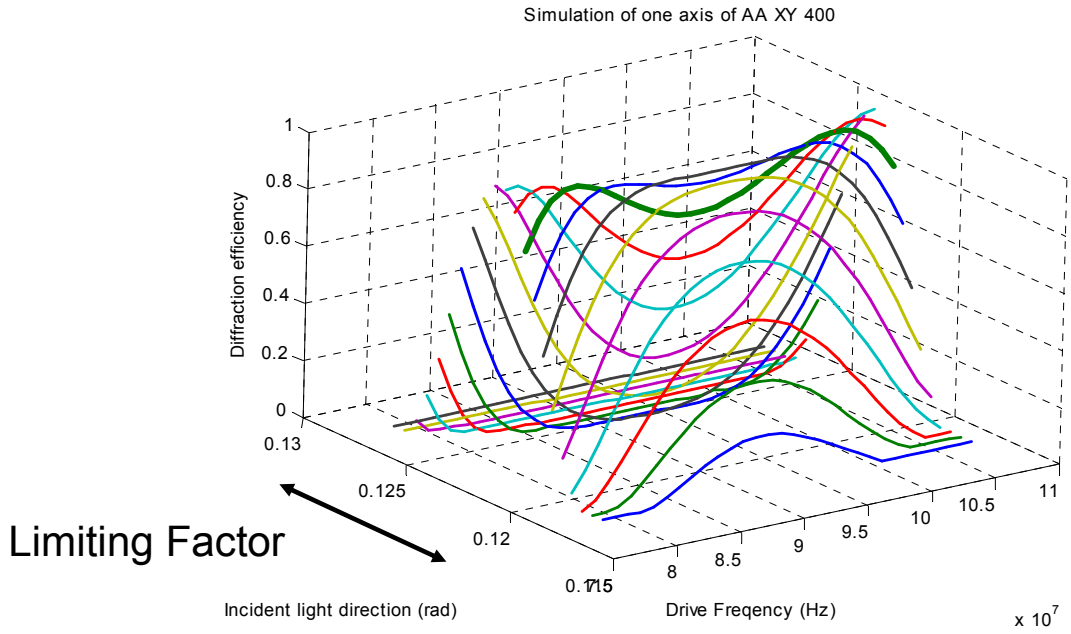

Figure 3.11 Computer model of a standard commercial AOD using equations from (Goutzoulis, Pape et al. 1994). Each different coloured line shows the coupling efficiency vs. drive frequency for a particular angle of incidence of the input light beam. The double headed arrow labelled limiting factor highlights the fact that the narrow range of permissible angles of incidence is a limiting factor in AOLM system design.

This curve of efficiency vs. drive frequency is shown in the 3D plot of Figure 3.11. The bold green curve matched the published efficiency curve of an AA Optoelectronic SA XY400 device. As the acoustic drive frequency in Figure 3.10 is varied the length, but not the direction, of the red acoustic vector changes. It is clear that for the chosen acoustic vector direction there are two drive frequencies where the acoustic vector exactly coincides with the ordinary wave vector surface and results in maximum efficiency. In between those two frequencies the acoustic vector is not exactly matched to the diffracted optical vector in the 001 direction. This produces a dip in efficiency between the two peaks because the larger the mismatch the greater the drop in efficiency. Outside the two maxima the index surface moves away rapidly and coupling efficiency drops rapidly. The overall shape of the curve depends on how rapidly efficiency drops with acoustic angle mismatch; that in turn depends on the angular spectrum of the acoustic wave. That depends on the diffraction pattern of the acoustic wave leaving the transducer. The acoustic angular spectrum is, as you might expect from standard diffraction theory, inversely related to the length of the transducer in the <001> direction. The correct equation allowing for the anisotropic acoustic propagation is given in (Goutzoulis, Pape et al. 1994). When I adjusted the

acoustic angular width to match the efficiency curve (green plot in Figure 3.11) I found that the input acceptance angle shown in Figure 3.12a) was only 3 mrad, much smaller than the desired target of 6-12 mrad. I showed simply by increasing the acoustic angular width that the acceptance angle could be increased to 10mrad as shown in Figure 3.12 b.

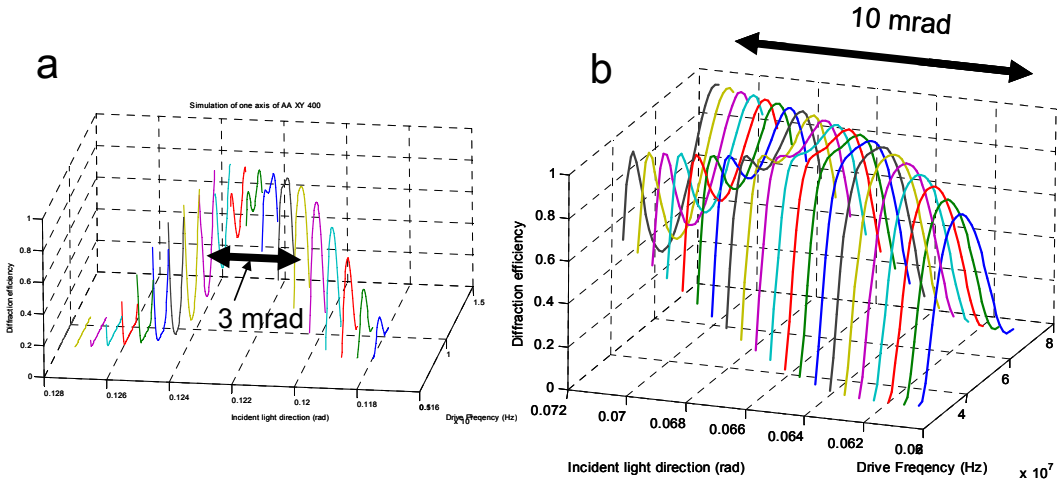

Figure 3.12 Computed efficiency plots showing a) a rotated view of the computed and fitted efficiency plot of the standard commercial AOD from the previous figure. This shows more clearly that the input acceptance angle is only 3 mrad and b) the effect of increasing the angular spread of the acoustic waves in increasing the acceptance angle.

However the problem with doing this is that it would require a 3.3 fold reduction in transducer length in the 001 direction. This would reduce the acoustic to optical interaction length by the same proportion and require that the acoustic power be increased by a large factor to compensate. I found in conversation with the manufacturers that large aperture AODs were already using several Watts of acoustic drive power and that heating and non-linear acoustic effects prevented the increase in acoustic drive by a significant factor. At constant acoustic drive power, the equation for efficiency vs. transducer length is given in (Goutzoulis, Pape et al. 1994). By fitting to commercial data at one point I produced the efficiency curve vs. transducer

length plot of Figure 3.13.

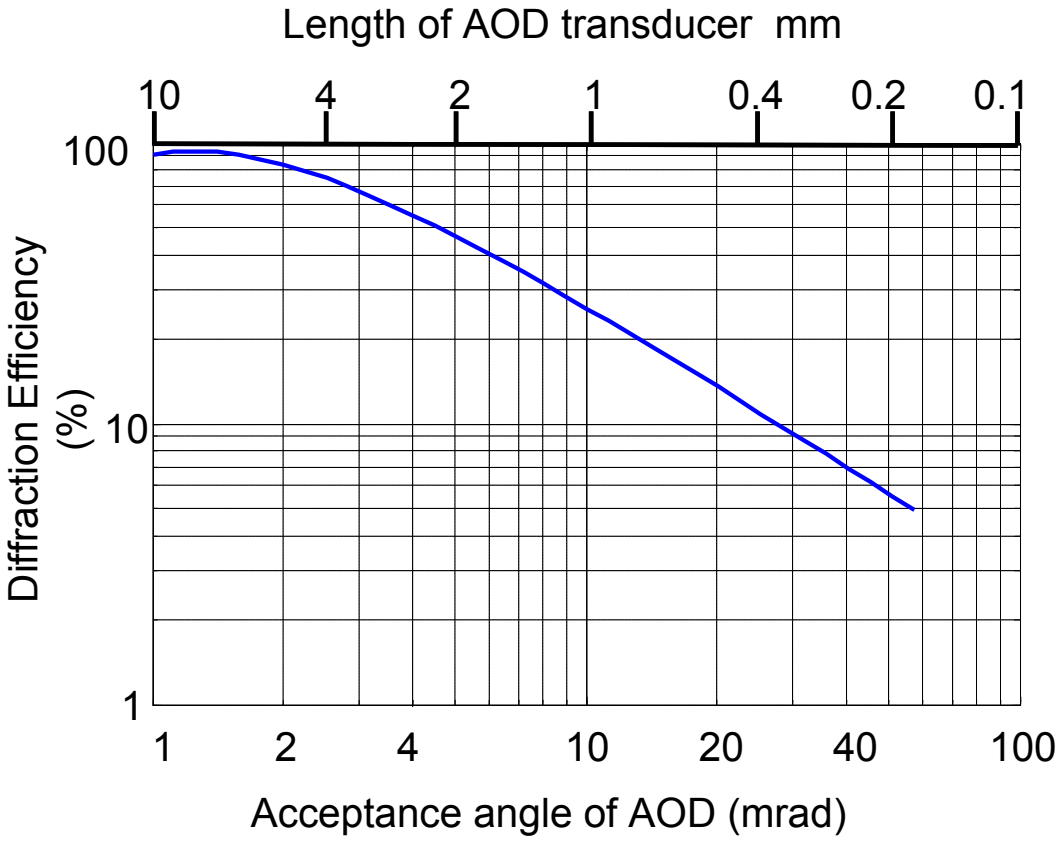

Figure 3.13 Plot of diffraction efficiency for an AOD model with approximately 3W of drive power showing how efficiency drops as the input acceptance angle increases. Increased acceptance angle is achieved by decreasing the length of the acoustic transducer in the direction of propagation of the optical beam. The decreased length reduces the length of the acoustic to optical interaction in proportion so the coupling efficiency drops.

This figure shows that there is strong conflict between high efficiency and large input acceptance angle and that this is one of the most important design trade-offs in the overall system design.

The effect of high acoustic wave walk-off angle on AOD focusing aberration (coma)

Before progressing with designing and procuring AODs I was very concerned about another aspect of the standard AOD design, namely the large walk off angle of the acoustic wave. For the deflection of an input beam into a parallel output beam by a fixed or slowly scanning drive frequency it is clear that the large acoustic walk off

angle has no particularly adverse effect apart from increasing crystal thickness. For the AOL application however where a chirped RF drive causes a lensing effect it is well known that if you tilt the plane of a focusing or defocusing lens it produces the aberration known as coma in the focal spot.

To study this effect I built a series of models using the Zemax (zemax.com) optical design program which is well suited to this type of investigation. In preliminary studies I found that even a 45 degree walk off angle could produce an 8 wavelength path length difference aberration under strongly focusing conditions. Since we would like to form a diffraction limited spot this implies that the target wavefront path length difference across the aperture should be less than a quarter wavelength. I investigated ways to improve the aberration by tilting the output facet of the AOD, but although this greatly reduced the coma, it introduced severe practical difficulties such as unwanted deflection of the beam and a new source of chromatic aberration from the prism shaped AOD crystals. I then studied Zemax models of a 20 degree walk off angle and found that it was a very great improvement and that for scan angles in the range I then studied, (up to AOD semiscan angle of 3 to 5 mrad) that it was quite possible to get diffraction limited imaging of focused spots with 90% Strehl ratio. The Strehl ratio is the ratio of the peak intensity of a point spread function to the maximum theoretical intensity if the optics were perfect diffraction limited optics. I therefore focused attention on discussions with manufacturers aimed at getting an AOD with only a 20 degree acoustic walk off angle. This would mean requiring the acoustic rotation of the crystal to be reduced to 2 degrees.

Design of crystals with reduced acoustic rotation to minimise acoustic walk off angle

This section describes the custom design of an AOD with a 20 degree walk-off angle. (Young, Ho et al. 1990) describe how a low acoustic walk–off angle AOD can be achieved whilst keeping the optical waves sufficiently off axis to have at least 80% linearly polarized eigenmodes. It is achieved by rotating the crystal at right angles to the ‘acoustic rotation’ direction by more than 3 degrees as shown in Figure 3.14.

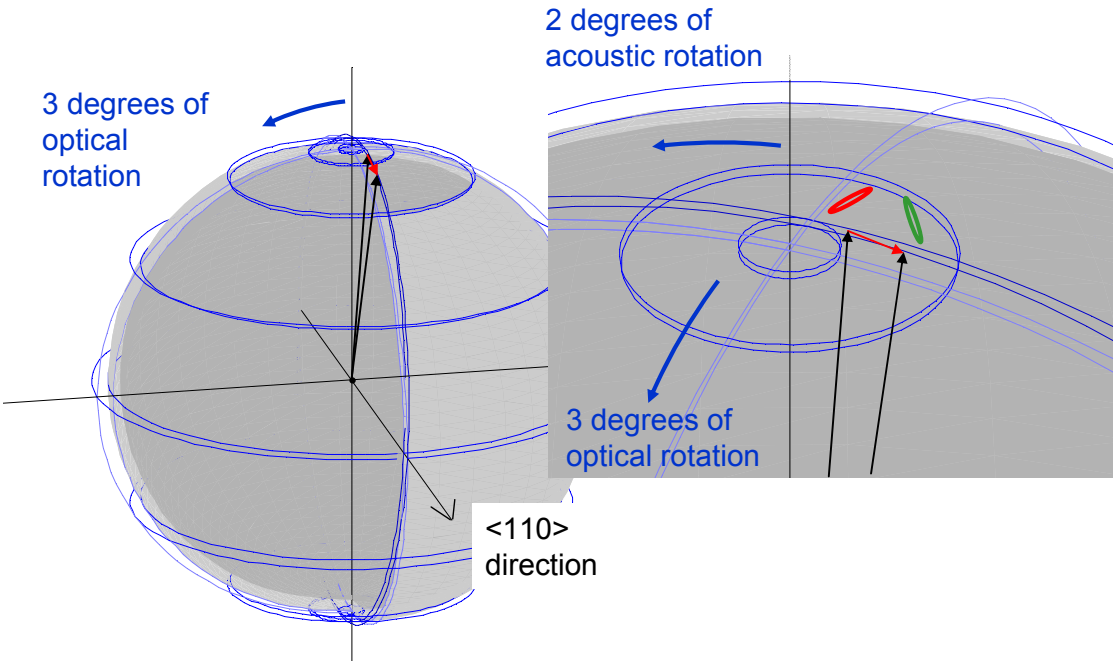

Figure 3.14 3D wave vector diagram for a custom AOD. The main figure is rotated about the vertical optic axis compared to earlier figures so that it is clear that the 3 degree 'optical rotation' of the crystal axis with respect to the wave vectors is rotation about the horizontal <110> axis. It is called optical rotation because, in contrast to acoustic rotation (Figure 3.6) it does not alter the angle of the acoustic wave with respect to the <110> direction. In the inset the upper and lower complete blue latitude circles are, (as in previous figures) in the extraordinary and ordinary wave vector surfaces respectively and are 3 degrees and 10 degrees from the optic axis. The longitude lines have been made semitransparent in order to highlight the new pair of blue 'great circles' that the input and output wave vectors touch. These are also in these wave vector surfaces and are optically rotated 3 degrees about the 110 axis. The incident wave vector has only 2 degrees of 'acoustic rotation' but 3 degrees of 'optical rotation' so that the input and output optical wave vectors are more than 4 degrees to the optic axis and hence predominantly linearly polarised. The red and green ellipses indicate the approximate polarisation states of the incident and diffracted eigenmodes.

For our custom design we chose a 3 degree 'optical rotation' in addition to a 2 degree 'acoustic rotation'. The resulting AOD design is shown in Figure 3.15 and Figure 3.16

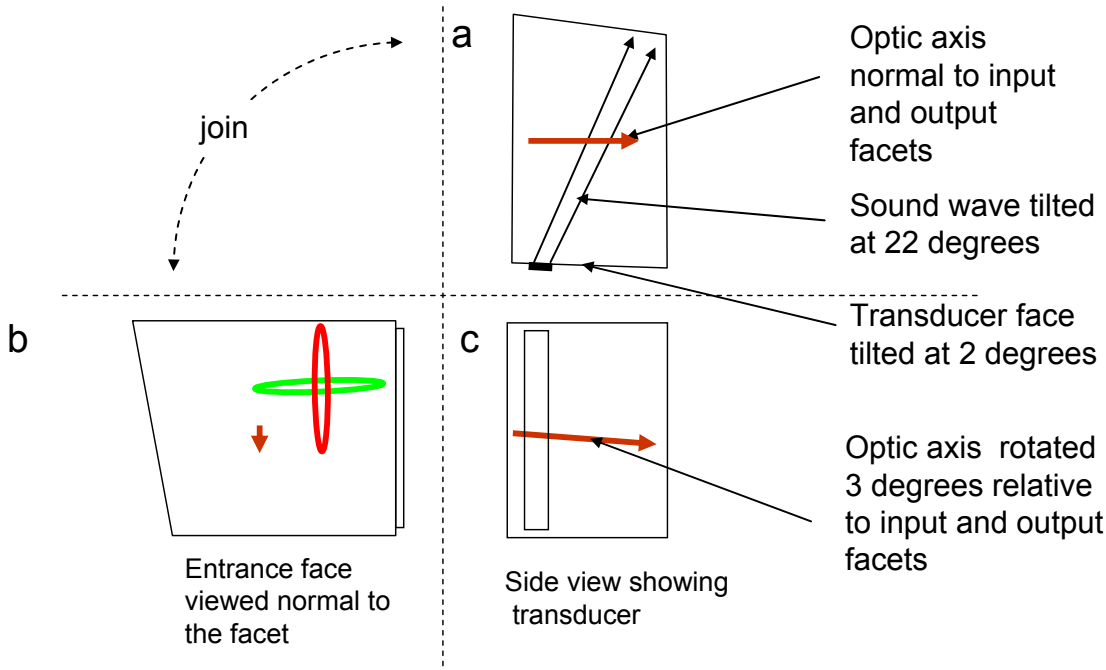

Figure 3.15 3D engineering drawing of the custom designed crystal. The red line is the projection of the optic axis on each view. a) top view of crystal oriented for horizontal deflection. The optic axis is normal to the entrance face. The side face of the crystal with the transducer is polished so that its normal is at 2 degrees to the <110> so that the acoustic wave walks off at 20 degrees as shown b) entrance face showing that in contrast to the standard acoustically rotated crystal (Figure 3.9) projection of the optic axis is vertical not horizontal and so that the input and output polarisations are as shown by the red and green ellipses. c) side view showing transducer and the 3 degree optical rotation.

Figure 3.15 shows the basic optical and acoustic orientations of the crystal. The acoustic wave walks off at 22 degrees whilst the optical rotation results in the input extraordinary wave requiring approximately vertical polarisation as shown.

Figure 3.16.shows that we also varied the transducer length depending on whether the crystal was to be used as the first AOD of the pair, in which case we wanted maximum efficiency irrespective of input acceptance angle, or wider acceptance angle at the expense some loss of efficiency (see Figure 3.13).

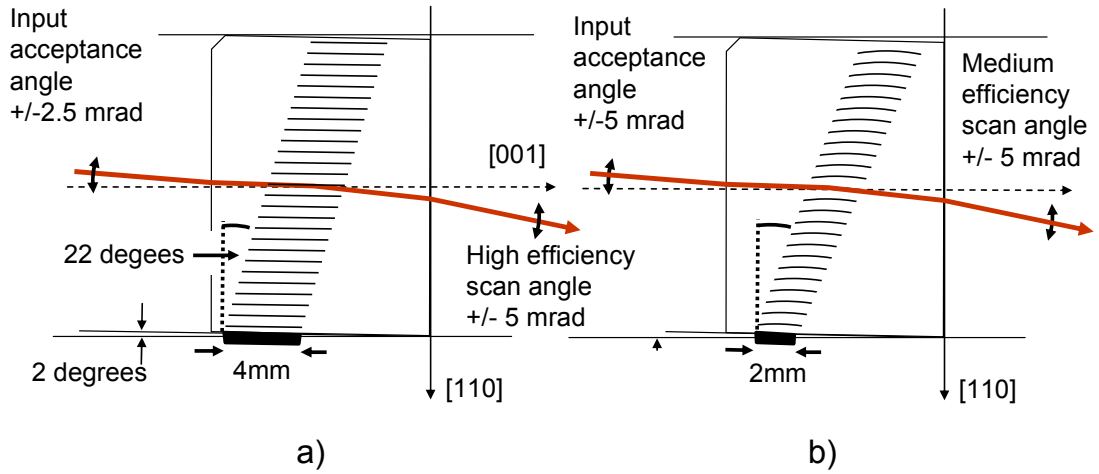

Figure 3.16 Top view of the custom designed AODs using optically rotated crystal alignment. We chose wide (4mm) transducers for the first crystal of each XZ or YZ pair as we wished to maximise efficiency and the input acceptance angle was not relevant. For the second transducer of each pair we chose 1.8 and 2.4 mm transducers adjacent to one another so that we could electrically switch between the two to experimentally determine the optimum trade off between efficiency and acceptance angle. (2mm shown here for simplicity). The input and output acceptance angles and scan angles we expected are shown in the diagram.

Expected performance from computer models

The normalised efficiency of the custom AODs is calculated using the equations for the refractive indices of the ordinary and extraordinary waves as a function of acoustic and optical rotation angle given in (Young, Ho et al. 1990), and a wave vector mismatch model for coupling efficiency (Goutzoulis, Pape et al. 1994). The results are plotted in Figure 3.17

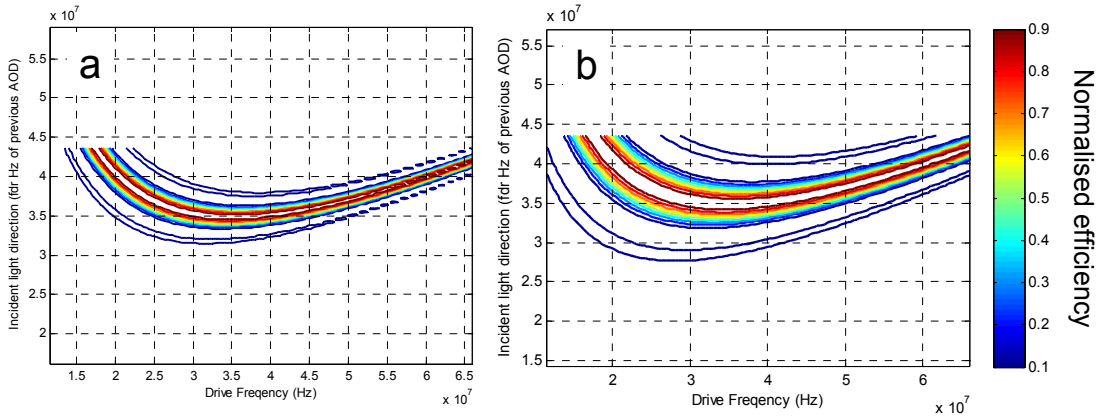

Figure 3.17 predicted efficiency of our custom designed AODs using the equations given in (Young, Ho et al. 1990). The horizontal axis is the AOD drive frequency. The vertical axis is the angle of the incident light. This is plotted it in terms of the drive frequency 'fdr' to a proceeding AOD. The coloured contours are therefore the normalised efficiency expected from the second AOD with the drive to the first AOD at the frequency defined on the vertical axis. a) is modelled assuming a 3.6mm transducer length, b) a 1.8mm transducer length. In both AODs the incident light angle was adjusted to centralise the efficiency plot with a 35MHz centre frequency. Note the normalised efficiency is 1 at maximum irrespective of the absolute efficiency at this drive. The plots do not therefore show the reduced absolute efficiency of the narrower transducer.

In Figure 3.17 the horizontal axis is the AOD drive frequency. These plots are therefore the normalised efficiency expected from the second AOD with the drive to the first AOD at the frequency defined on the vertical axis. The plot is then in the same format as Figure 2.22 and therefore can be used for computing the best miniscan drive parameters for focusing in a particular plane. a) is modelled assuming a 3.6mm transducer length, b) a 1.8mm transducer length. Note that the narrower transducer allows approximately twice the drive frequency range for the first AOD before the efficiency drops to a particular level. This is a direct measure of the increased acceptance angle of the narrower transducer. Design work of this type gave us confidence that the optically rotated design could be a satisfactory basis for the deflectors for the AOLM. It also gave us a basis for a mathematical model of the complete system that we used for overall system design optimisation. This is discussed at the end of this chapter after first discussing the main fundamental limitations and aberrations of the AOD microscope which also needs to be understood to make such a model at least approximately realistic.

Chromatic aberration of AODs, its effect on point spread function and a novel proposed solution

The chromatic aberration caused by AODs and why it is a problem for 2-photon microscopy

Figure 3.18 shows a diagram of an XZ AOD pair in the AOLM. As discussed in Chapter 1, the spectral width of the ultra short pulses from a Ti-Sapphire laser are at best transform limited with a typical spectral width of 10.6nm for 100fs pulse stream at 800nm centre wavelength. The basic equation (1.1) for deflection shows the deflection is proportional to wavelength. The AOD therefore acts as a spectrometer as well as a deflector. Instead of focusing the light to a diffraction limited point, the point spread function (psf) is stretched with the short wavelength components of the light at the inner (less deflected) edge of the psf and the long wavelength components at the outer edge. As illustrated in the figure, the chromatic aberration is a 3D effect with the red component deflected through larger angles than blue and hence for converging light being more strongly focused as well as simply deflected through a larger angle off axis.

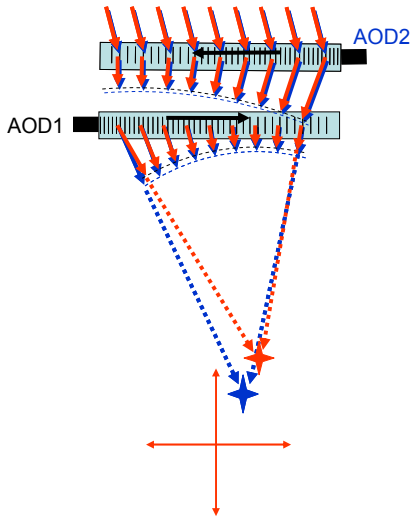

Figure 3.18 Diagram to illustrate the severe chromatic aberration of AOD deflectors. Since the basic equation for the diffraction angle of an AOD is proportional to wavelength, the longer wavelength components of the laser input beam are diffracted through larger angles.

In order to calculate the effect of these and other aberrations on the 2-photon point spread function it is first necessary to understand how the 2-photon point-spread function can be computed and measured.

Derivation of resolution of microscope in terms of the point spread function (psf) of the focal spot across the field of view

The beam waist of the Ti-Sapphire laser light coming to a focus beneath a water immersion objective is illustrated in Figure 3.19.

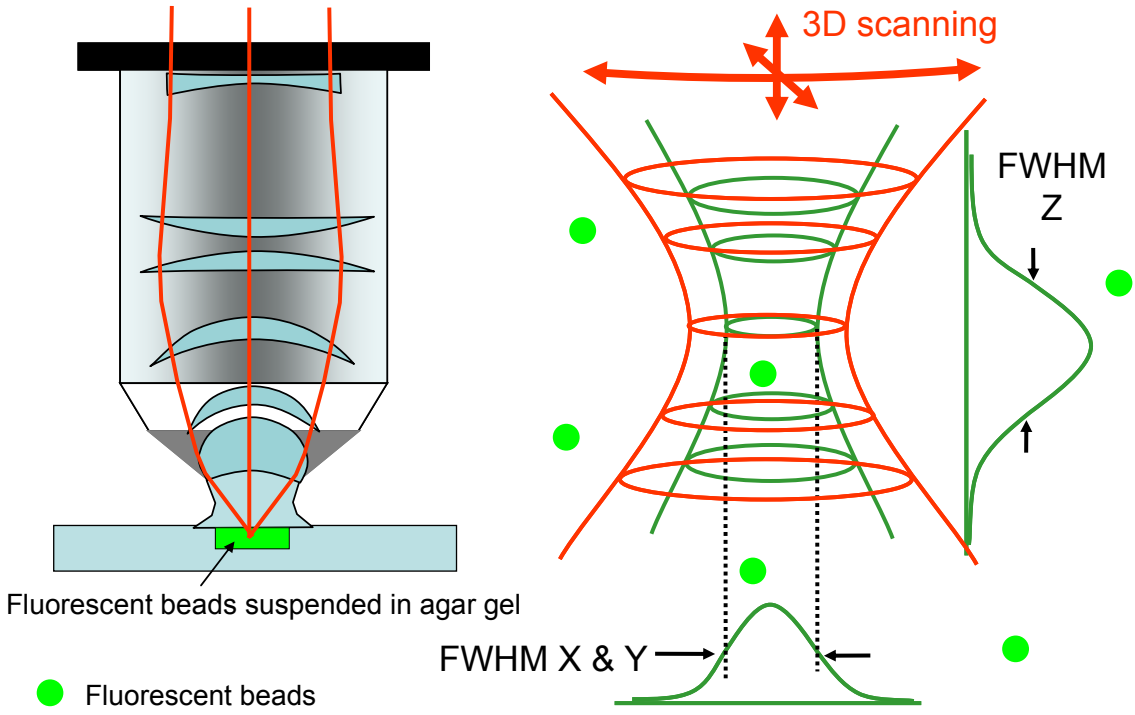

Figure 3.19 Diagram to illustrate the laser beam focusing beneath a water immersion objective lens, how it forms a single photon illumination beam waist (in red) and a two photon beam waist (in green). Also shown are fluorescent beads is randomly scattered in 3D by mixing in an agar gel. Experimental measurements of 2-photon point spread function (psf) are made by scanning the focal spot over the beads. Since the beads are much smaller than the emission or illumination wavelength, (0.2 μm cf 0.5μm or 0.8μm respectively), the experimental psf ,which is the convolution of the real psf with the bead dimensions, is only slightly larger than the real psf.

The total fluorescence is found by integrating this fluorescence over the complete volume near the focus. The 3D shape of the 2-photon point spread function (psf) can be calculated and if saturation effects are ignored, the 2-photon excitation is proportional to the square of the illumination optical intensity at each point in the volume. As shown in green in Figure 3.19, this beam waist is therefore appreciably smaller in dimensions than the Ti-Sapphire single photon beam waist (shown in red). The detailed theory for such calculations is complex ((Higdon, Torok et al. 1999)), however for the present purposes a sufficiently accurate model can be obtained by

using the approximations given by (Zipfel, Williams et al. 2003) who give equations for the dimensions of Gaussian approximations to the 2-photon excitation point spread function. These are given in terms of the Full Width Half Maximum (FWHM) dimensions in the XY plane and parallel to the Z axis. The 3D dimensions are inversely related to NA in a similar manner to the way 3D FOV is related to NA. At NA= 0.8 at 800nm wavelength, the theoretical psf in the XY plane is 0.37 μm FWHM and in the axial, Z direction the Gaussian fit to the 2 photon psf is 1.89 μm FWHM. In order to measure the psf of a 2-photon microscope it is standard practice to use sub wavelength fluorescent beads. As we wanted to measure this resolution not in one 2D plane, but across the whole volume of the field of view we dissolved beads in an agar gel as shown diagrammatically in Figure 3.19. The microscope is then driven to scan focal spot across the beads in 3D as indicated. The collected fluorescence data is then used to reconstruct the image which is the convolution of the actual psf with the intensity profile of the bead concerned. In the XY plane, at Z=0, I have assumed that the simplified equation for the radial length of the measured psf is then given by the convolution of the Gaussian approximation to 2-photon diffraction spot intensity distribution, the Gaussian approximation to the chromatic aberration intensity distribution, and the Gaussian approximation to the bead dimensions.:-

$$l = \sqrt{\left(w^2 + \left(\frac{r\Delta\lambda}{\sqrt{2}\lambda} \right)^2 + b^2 \right)} \qquad \text{equation 3.1}$$

Where w is the FWHM of the 2-photon psf as given in (Zipfel, Williams et al. 2003), λ is the laser wavelength, $\Delta\lambda$ is the FWHM of the spectral width of the laser, r is the radius of the psf from the centre of the field of view and b the Gaussian equivalent FWHM of the bead . The middle term in this expression $\left(\frac{r\Delta\lambda}{\sqrt{2}\lambda} \right)$ is the chromatic aberration component of the convolution. It is proportional to the radius of the psf from the centre of the field of view because at the centre there is no chromatic aberration and proportional to the FWHM of the spectral width divided by the absolute wavelength because the AOD is acting as a spectrometer with deflection linearly propotional to wavelength . The factor of $\sqrt{2}$ reduction in chromatic aberration width takes into account the squaring of the Gaussian intensity distribution by the 2-photon luminescence non-linearity. At very large chromatic aberration, so

that the diffraction spot width w and bead dimension b are negligible equation 3.1 approximates to $\left(\frac{r\Delta\lambda}{\sqrt{2}\lambda}\right)$ which is, as expected, a Gaussian with a FWHM $1/\sqrt{2}$ times the proportional spectral width of the laser spectrum times the radius of the psf from the perfect compensation point . The use of convolution for adding optical aberrations, rather than linear addition is standard optics (Salome, Kremer et al. 2006; Otsu, Bormuth et al. 2008). The effect of this chromatic aberration in the Z=0 plane is illustrated in Figure 3.20.

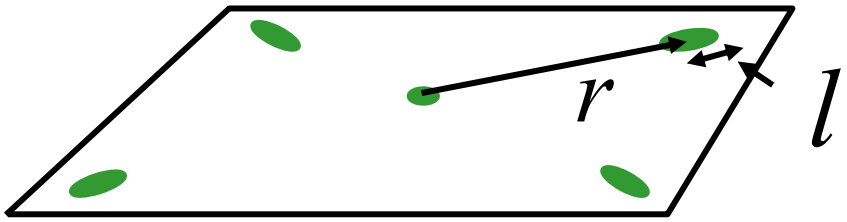

Figure 3.20 The effect of chromatic aberration on the psf across the Z= 0 (natural focal plane) of the microscope according to equation 3.1. r is the radial distance from the centre of the field of view and l the FWHM Gaussian fit to the long axis of the elliptical point spread function. The long axis is always aligned radially.

In the Z axial direction a similar argument results in the equation of the effect of chromatic aberration on the width *d* of the Z psf predicted by (Zipfel, Williams et al. 2003) of :-

$$dz = \sqrt{\left(d^2 + \left(\frac{z\Delta\lambda}{\sqrt{2}\lambda}\right)^2 + SA^2 + b^2\right)} \qquad \text{equation 3.2}$$

Where z is the axial displacement of the psf from the centre of the field of view. In this equation I have included the effect of spherical aberration *SA* which is expected to dominate over chromatic aberration for large NA microscope objectives (Keller 1995)

Note that these equations predict that both the Z and XY components of chromatic aberration are simply proportional to the distance from the centre of the field of view where chromatic aberration is cancelled out to zero. The chromatic aberration is therefore radial in 3D space with the chromatic elongation a maximum along the 3D radial direction. It is a 3D form of 'magnification chromatic aberration', that is to say the aberration can be simply characterised by saying that the long wavelength image

is larger than the short wavelength image. This type of magnification chromatic aberration is well known in 2D as it produces coloured fringes around high contrast objects in cheap binoculars (Hecht 2001). It is obvious to consider if there are any optical means to correct for this aberration. I initially considered a wide variety of schemes based on single dispersive lenses that counteracted the chromatic aberration of the Acousto-optic lens. I found with all these schemes however that it might be possible to compensate the XY chromatic aberration in one particular 2D plane, but because the additional dispersive lens itself produced a large axial chromatic dispersion, it was impossible to compensate the field of view centred on zero axial chromatic aberration at the natural focal plane of the objective.

Novel proposed solution using diffractive optical elements in a telecentric relay

I eventually discovered a solution to the chromatic aberration problem, whilst the solution is not perfect, it goes a long way to solve the problem.

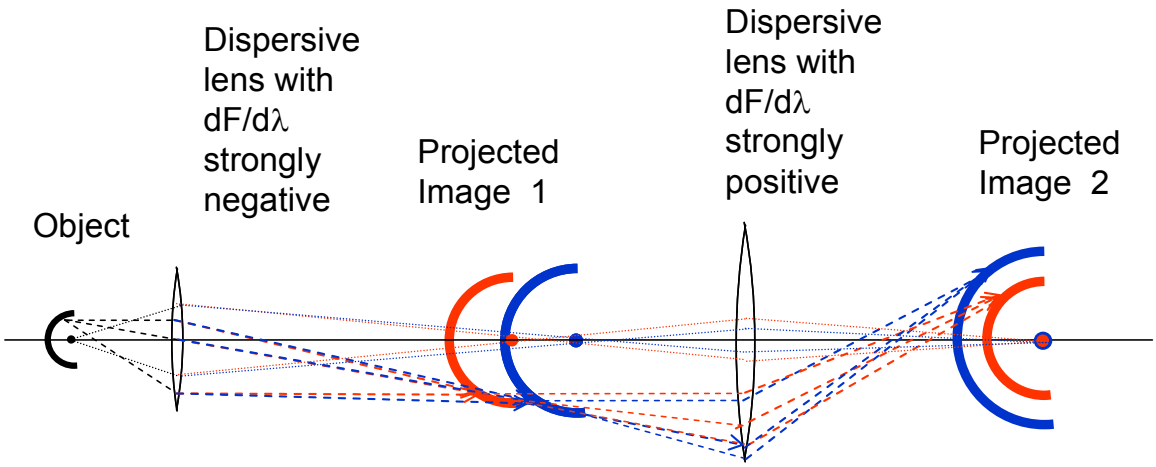

Figure 3.21 Concept of chromatic aberration correction in 3D using highly dispersive lenses in a telecentric relay configuration. Consider a hemispherical object with a point object at is centre of curvature as shown on the left. The lens projects an image of this object as shown. If the lens has a high negative dispersion of focal length with wavelength the longer wavelength components shown in red produces a smaller image closer to the lens than the shorter wavelength components (i.e. the red image is less magnified and nearer than the blue). If you then place a second dispersive lens, this time with a positive dispersion of focal length with wavelength, this magnifies the blue image less than the red. Because of the positioning of the red and blue projected images 1, it is clear with the correct magnitude of dispersion for lens two , the red and blue hemispheres of image 2 can become concentric again. Overall the dispersive telecentric relay formed by the pair of lenses magnifies the longer wavelengths less than the shorter wavelengths, but produces no linear axial chromatic dispersion at the centre of the field of view. This is the opposite of the chromatic aberration beneath the objective of the AOLM with no compensation and therefore a promising candidate for correcting the inherent aberration of the AOLM. Note that for clarity this diagram does not show the extra stretching in Z that the image would experience if it were actually magnified as shown here.

Consider Figure 3.21 . In order to compensate for the chromatic aberration produced by the AOLM it is necessary for the compensating optics to project the aberrated field of view with a lower 3D magnification for the long wavelength light than the short wavelength light. In addition there must be no introduced chromatic aberration at the centre of the field of view. The solution I came up with involves the use of two highly dispersive lenses forming a telecentric relay. The first lens has a negative dispersion

of focal length vs. wavelength so that the long wavelength component of the image is closer to the lens and less magnified than the short wavelength component. Thus although it is starting to correct the magnification aberration, it has introduced a large axial aberration. This is evident from considering the shape of a 3D projected image of a hemisphere and central point in red (long wavelength) and blue (short wavelength). The large axial displacement of both images at projected image 1 is typical of the problem caused by single dispersive lens correction. The second telecentric relay lens continues to magnify the longer wavelengths by less than the short, but this is despite its positive dispersion of focal length with wavelength. This is because the longer wavelength image 1 is further away from the second lens than the short wavelength image. The positive dispersion is chosen to exactly compensate the axial dispersion at the centre of the field of view so that, at all wavelengths, the centre of the sphere is imaged onto the same point in projected image 2. The compensator then has magnified the long wavelength component less than the short wavelength and the magnification chromatic aberration is centred on the natural focal point representing the centre of the field of view. To a first approximation therefore this compensator has the opposite chromatic aberration to the AOL and can be used as a compensator.

Models of 3D aberration field

To evaluate the performance of this new proposed method of correcting the magnification chromatic aberration of diffractive optical elements such as the AOL, I developed a Matlab model based on geometric optics that calculates the projected field of view at two wavelengths representing the upper and lower wavelengths of the FWHM Gaussian fit to the spectral width of the laser. This gave a direct measure of the chromatic aberration in XY and Z. The model also calculates the field of view for given fixed scan angle limits and computes the total number of resolvable voxels (NRV) the microscope can image in 3D. This number of resolvable voxels is based on voxels of dimensions equal to the XY and Z FWHM dimensions of the psf at that point in 3D space calculated from equations 3.1 and 3.2. The voxels are only counted as part of the NRV if the energy density at the voxel is above a preset 2-photon threshold (1 MW/cm^2 in these calculations). The NRV is thus a useful overall figure of merit for such a 3D microscope. The dimensions of each resolvable volume in the

field of view are computed using the equations above. The model however does not include the effect of spherical aberration which for a high NA final objective would almost certainly mask the chromatic effects calculated here at large values of Z (Higdon, Torok et al. 1999) . The computed number of resolvable voxels is then plotted as a function of the strength of the chromatic aberration correction as shown in Figure 3.22. The parameter C is a dimensionless parameter which is a common multiplier to the dispersion of each lens as defined in the figure.

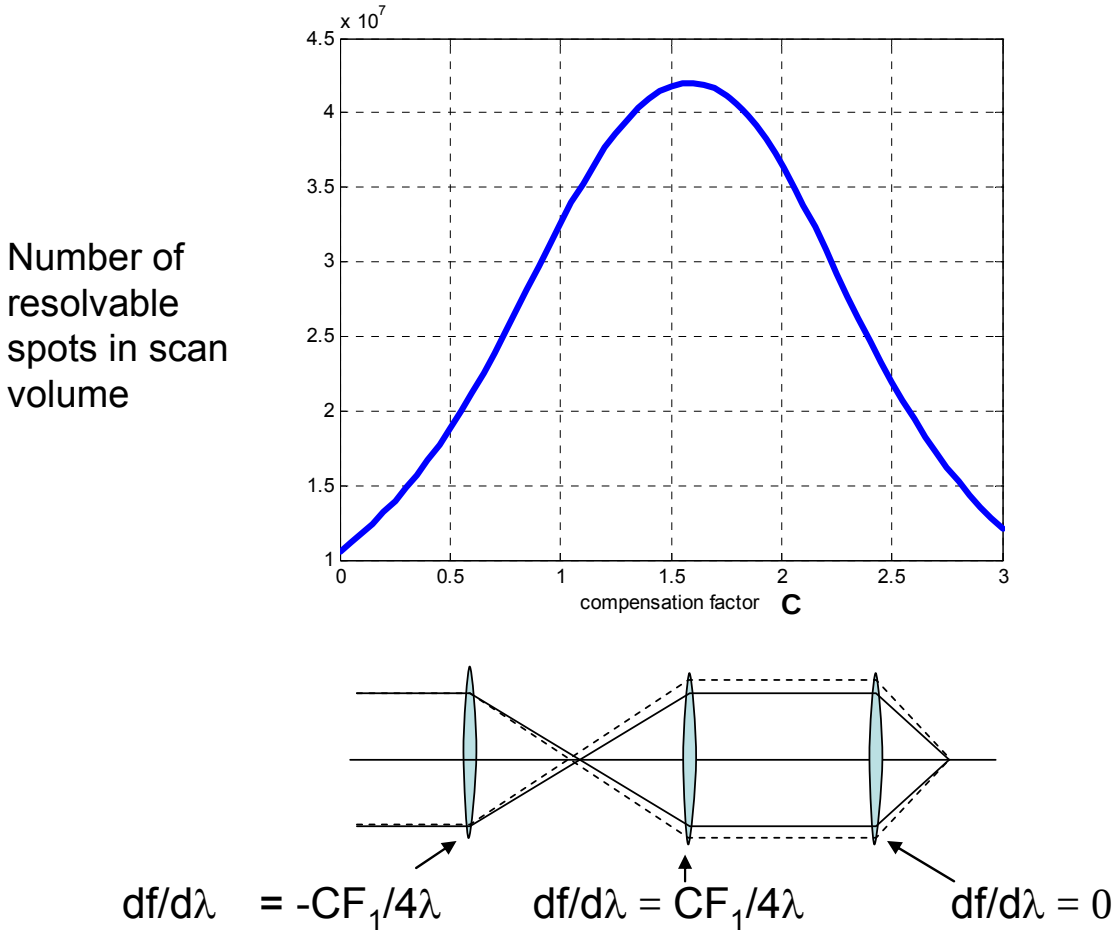

Figure 3.22 Diagram to define and illustrate the effect that varying the compensation factor C has on the number of resolvable voxels (NRV) it is possible to scan in 3D. The model computes the size of the psf and the power density for certain assumed laser power and optical train losses. It sets a threshold below which it assumed the power density is too low for two photon excitation. As the dispersion compensation improves so the psfs get smaller over a larger scan volume and the total number of resolvable points increases.

The results show that the best compensation factor lies between 1 and 2 and that a four fold increase in the number of resolvable volumes is achievable. Note that this model assumes that irrespective of the scan angle the optical power out of the objective is constant (20mW in this case). The model does not take into account the

fact that large scan angles will reduce the power because wider acceptance angle lower efficiency AODs will be required. Nevertheless, the model can be used to understand the physics of the compensator by plotting how power density at the focal spot, which is reduced by chromatic aberration, varies across the 3D field of view. It is also possible to visually plot the direction in 3D space of the chromatic aberration. The results for C varying from 0-2 are shown in the next 4 figures.

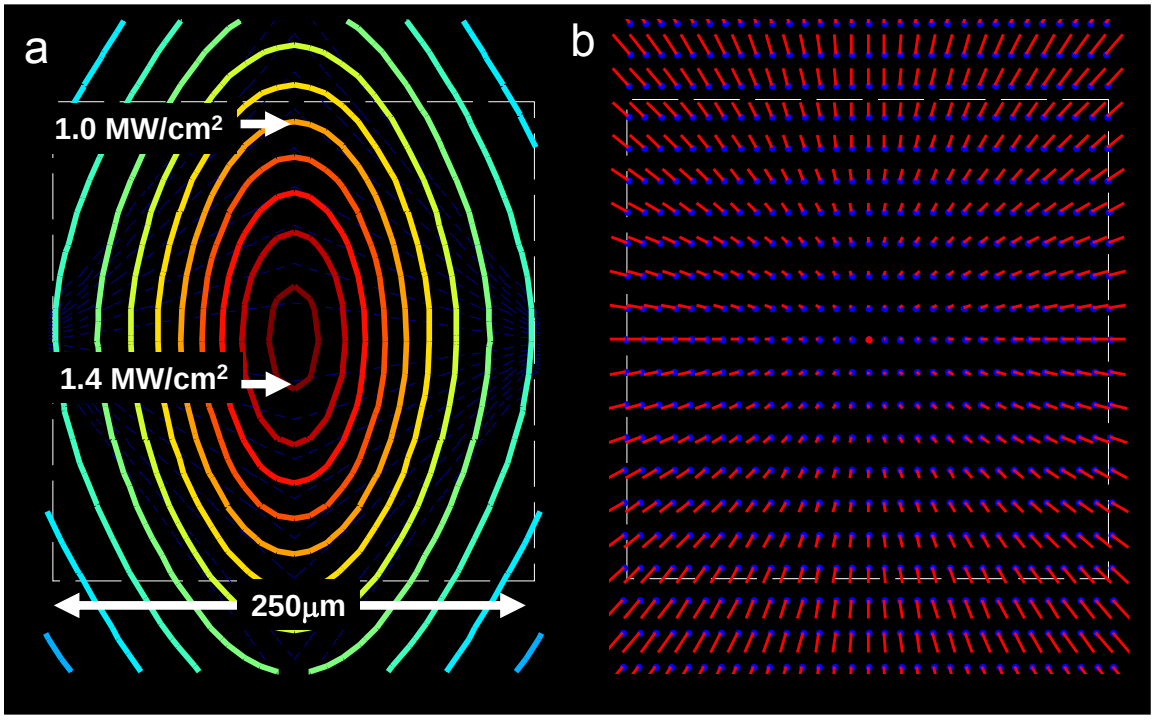

Figure 3.23 Calculated chromatic aberration vector field and its effect on optical energy density for the case of no chromatic aberration compensation (C=0). The figure is a vertical cross section through a volume of just over 250 μm cubed representing the scan volume beneath an NA =0.8 lens with 6mrad AOD semiscan angle. The dashed white line represents the sides of the cubic scan volume. The effect on a) the power density of the point spread function assuming a fixed total power after the objective, but power density varying because of the effect of chromatic aberration on the psf area at the focus. Note the size of the 1MW/cm^2 orange power density contour is much smaller than the scan volume. If this is the two photon threshold the machine will only be useable inside this contour. In b) the blue points indicate the position of the focus for an array of scan positions at the short wavelength end of the Ti-Sapphire laser spectrum and the red tails the relative length and direction on the XZ plane of the chromatic aberration. Note that the chromatic aberration vector is always pointing radially away from the centre of the FOV. The number of resolvable detection volumes (NRV) is 11 million in this case.

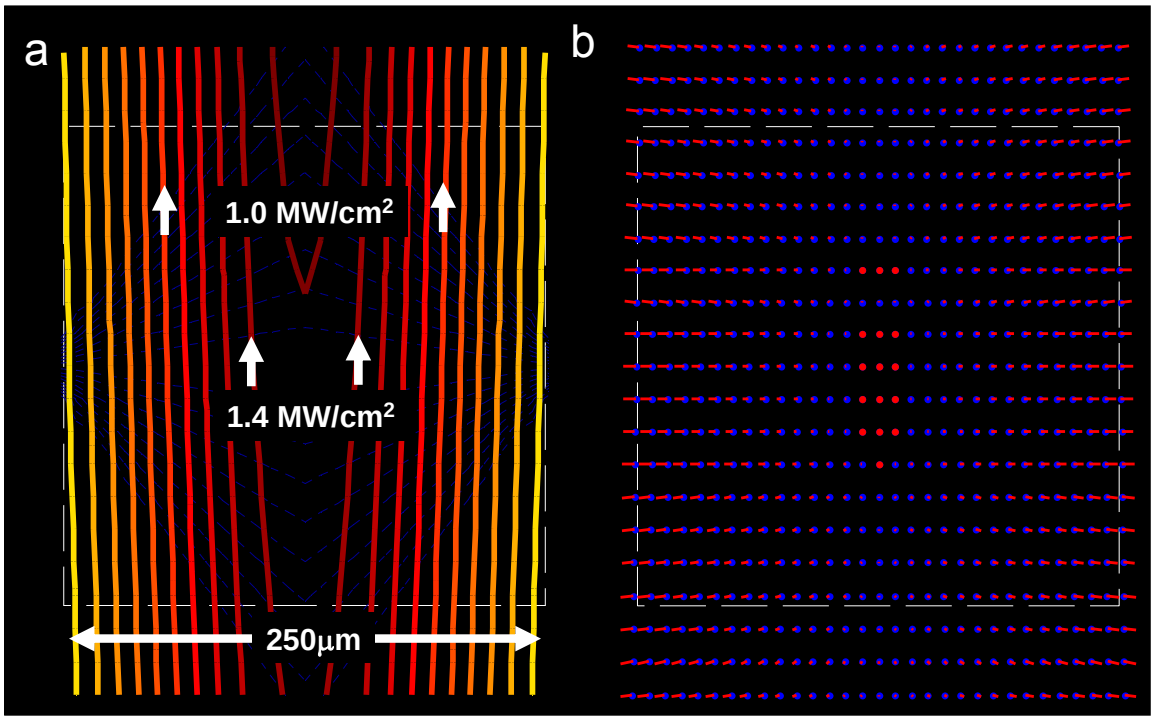

Figure 3.24 The same plot as the previous figure but with a compensation factor set to C=1. Note the much shorter 'quiver tails' on the plot of chromatic aberration relative magnitude and direction. Note also that for this compensation factor there is perfect compensation of the axial (Z) chromatic aberration across the whole field of view, but the XY plane aberration is only half compensated. This results in vertical power density contour lines in a). Note however that 1MW/cm² contour lines include a much larger percentage of the volume and therefore the NRV is much larger at 32.5 million.

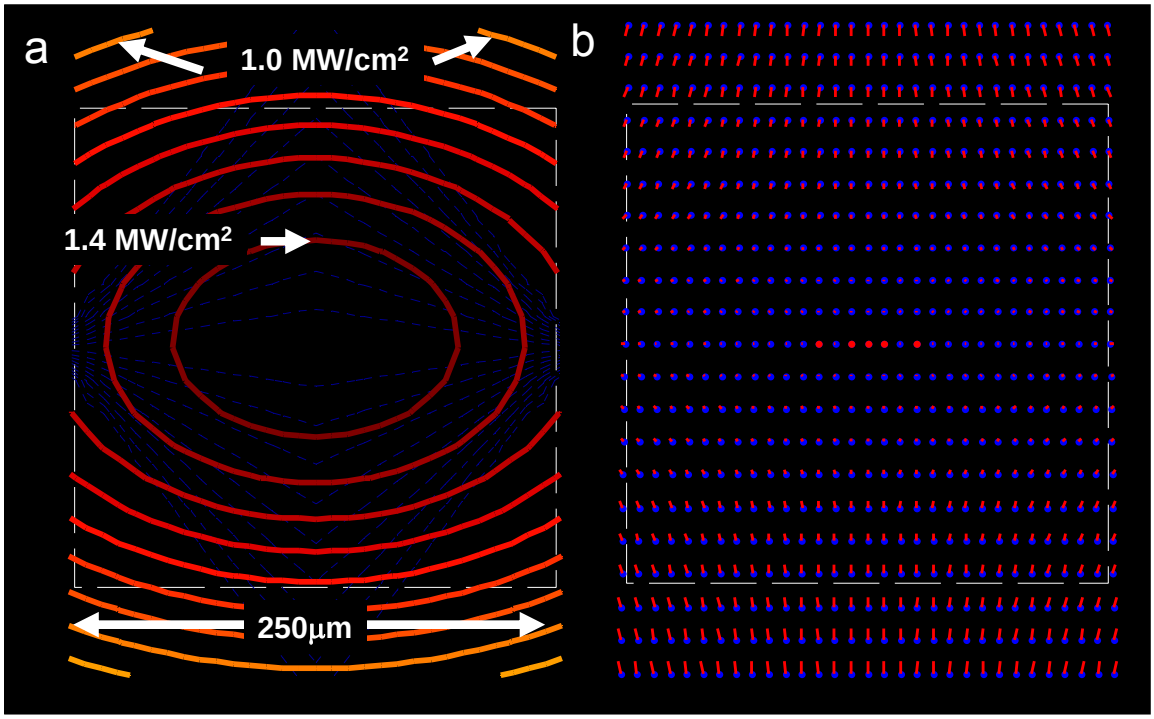

Figure 3.25 a) contour and b) chromatic aberration quiver plot for C=1.7. Note that the quiver plot shows slight over compensation in Z, (quiver tails pointing inward) and under compensation in the XY plane (small quiver tails pointing out at the very edge of the FOV). This compensation factor is however close to optimal. Note that the 1MW/cm^2 contour lines are completely outside the 250 μm cube and this results in maximising the number of resolvable voxels (NRV= 42 million) .

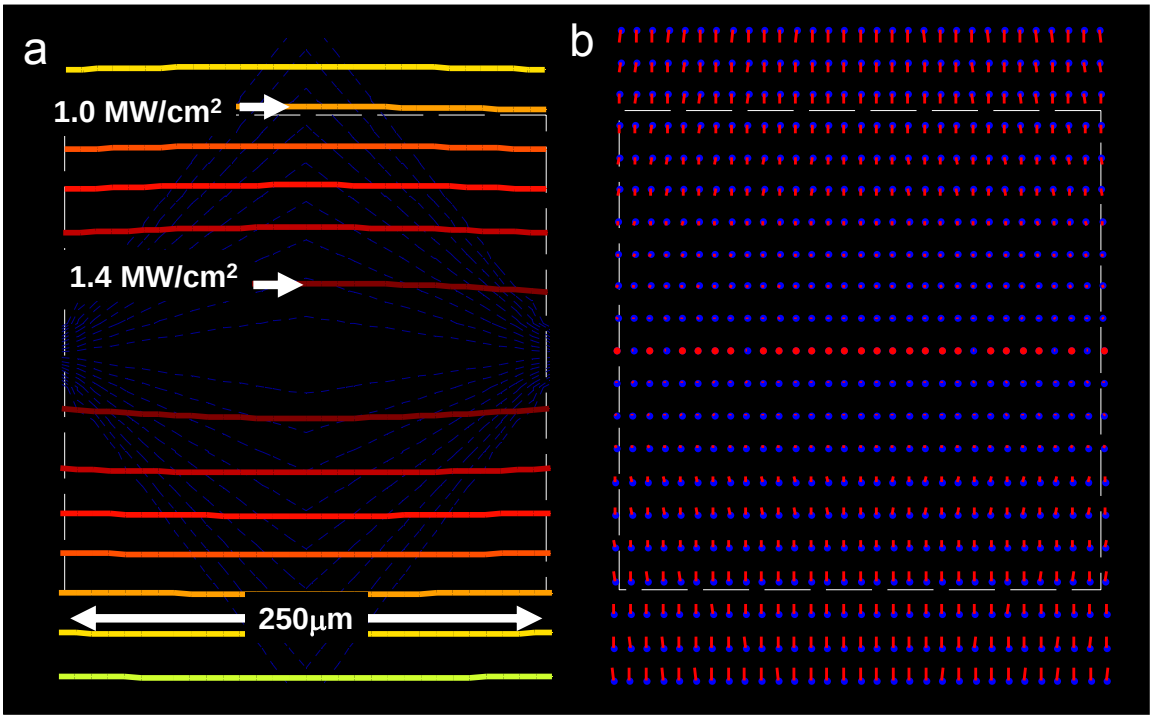

Figure 3.26 a) power density contour and b) chromatic aberration quiver plot for C=2. Note that the quiver plot shows over compensation in Z, (quiver tails pointing inward) but perfect compensation in the XY plane. The compensation factor is however slightly larger than optimal. Note that the 1MW/cm^2 contour lines are just on the edge of the 250 μm cube and this results in the number of resolvable voxels (NRV= 37 million) .

To understand the effect of this chromatic aberration correction in more detail, consider Figure 3.23 to Figure 3.26. These show vertical 2D XZ sections through the 3D field of view using the Matlab model to generate a) power density plots and b) 'quiver diagrams' that show the direction and relative magnitude of the chromatic aberration for an array of points covering the whole field of view. The blue points are the centres of the psfs at the short wavelength end of the FWHM of the laser spectrum. The end of the red lines represent the chromatic aberration to the long wavelength end of the spectrum. Note that the graphics exaggerate the absolute length of the aberration for clarity; however across each figure the relative length of the quiver vectors is accurate. Note that in Figure 3.23 which shows the case of zero

compensation, the aberration is, as expected, radial away from the centre of the field of view and gets larger in proportion to the distance from the centre.

Figure 3.24 shows the same plot but the compensation factor C=1. This shows perfect axial (Z) compensation but under compensates in the X (and Y) plane. Figure 3.25 shows the case of using a compensation factor C=1.7 to compensate the AOL induced chromatic aberration. The quiver diagram shows that there is slight over compensation of the chromatic aberration in Z that causes the longer wavelength (red) quiver tails to point inwards at large absolute values of Z focus, and that in the X (and Y) direction there is slight under compensation with the red quivers still pointing away from the centre of the field of view at large absolute values of X. Overall however the shorter quiver tails in the compensated case shows that there is substantially less chromatic aberration over the whole field of view so the volume of each psf is smaller and the power density higher. There are therefore a greater number of resolvable points.

Figure 3.26 for C=2 shows perfect compensation in the X (and Y) planes but over compensates in the axial direction. The conclusion from these results is therefore that the new design of chromatic aberration compensator can increase the number of resolvable volumes by a large factor (around four for this field of view and 2-photon energy threshold setting). However it is not perfect, being able to produce perfect axial correction for C=1 or perfect XY plane compensation for C=2 and with an intermediate optimum that maximises the NRV. The reason for these results is not difficult to understand. The corrector works by varying the magnification of the projected image rapidly with wavelength. For any lens system the axial magnification is the square of the linear magnification therefore the proportionate rate of change of axial magnification with wavelength is twice the value of its proportionate rate of change of tangential magnification. However, the aberration we are correcting from the AOL system has equal proportionate change of magnification in all 3D radial directions. It is tempting to deduce from this that is impossible to perfectly correct the chromatic aberration of the AOL in all three directions. (I would like to be proved wrong on this).

As it appears impossible to get perfect chromatic aberration compensation it seems very likely that any practical compensator will need to have adjustable compensation for instance for imaging fields of view with different shapes. Deep columnar objects would prefer C=1 and wide shallow objects would prefer C=2, generally in between, intermediate C would be optimum. A practical compensator must also be able to compensate despite the laser wavelength varying over its whole operating range say 700-900 nm or 1000nm. This puts quite strong constraints on the design of practical optics.

Design of a practical chromatic aberration corrector

This section describes how an aberration corrector based on these principles can be designed given the constraints that it is necessary to operate over a wide wavelength range, (at least 700-900nm) and that it is desirable to be able to adjust the compensation factor C over the range 1-2.

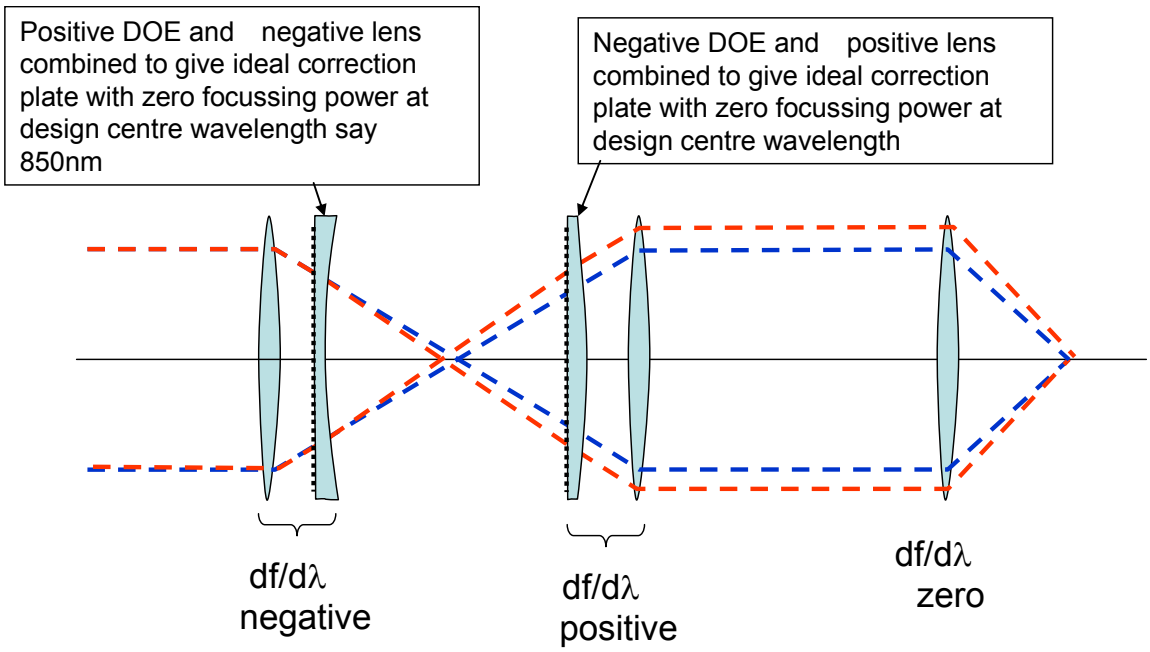

Figure 3.27 First design of a practical compensator using diffractive optical elements (DOEs) combined with plano-convex or concave lenses of opposite sign and strength so the correction plate has no focusing power and can therefore be moved along the Z axis to vary the value of compensation factor C without affecting the image relay effect of the rest of the compensator optics. This however only works well at one wavelength

The first design I considered is shown in Figure 3.27. This splits up the function of the telecentric relay into two non dispersive standard relay lenses and introduces the

compensating chromatic aberrations by the use of separate compensation plates. These plates are designed so that at the central operating wavelength, e.g.850nm, the diffractive optical lens element (DOE) of which it is formed is exactly compensated by a conventional non dispersive lens so that it has no optical power. The first compensator plate has a positive (converging) DOE and a negative (concave) conventional lens. The second plate is the opposite way round as shown. The path of longer and shorter wavelength components of the laser light is indicated by the red and blue dotted lines in the figure. The higher NA and hence smaller magnification of the longer wavelength components is apparent after the final lens.

The advantage of the compensator plates is that the compensation factor C can be varied over a wide range simply by adjusting the separation of the compensator plates, without needing to adjust the position of any of the other optical components. This is fine, but what if you wish to alter the centre wavelength? If you change nothing else, the magnification of the output beam diameter over the input beam diameter increases rapidly with increasing wavelength (and vice versa). To compensate for this at different centre wavelengths, it is necessary to make the outside converging telecentric relay lenses either replaceable, with a different focal length for each wavelength, or to use telephoto lenses with adjustable focal length as shown in Figure 3.28.

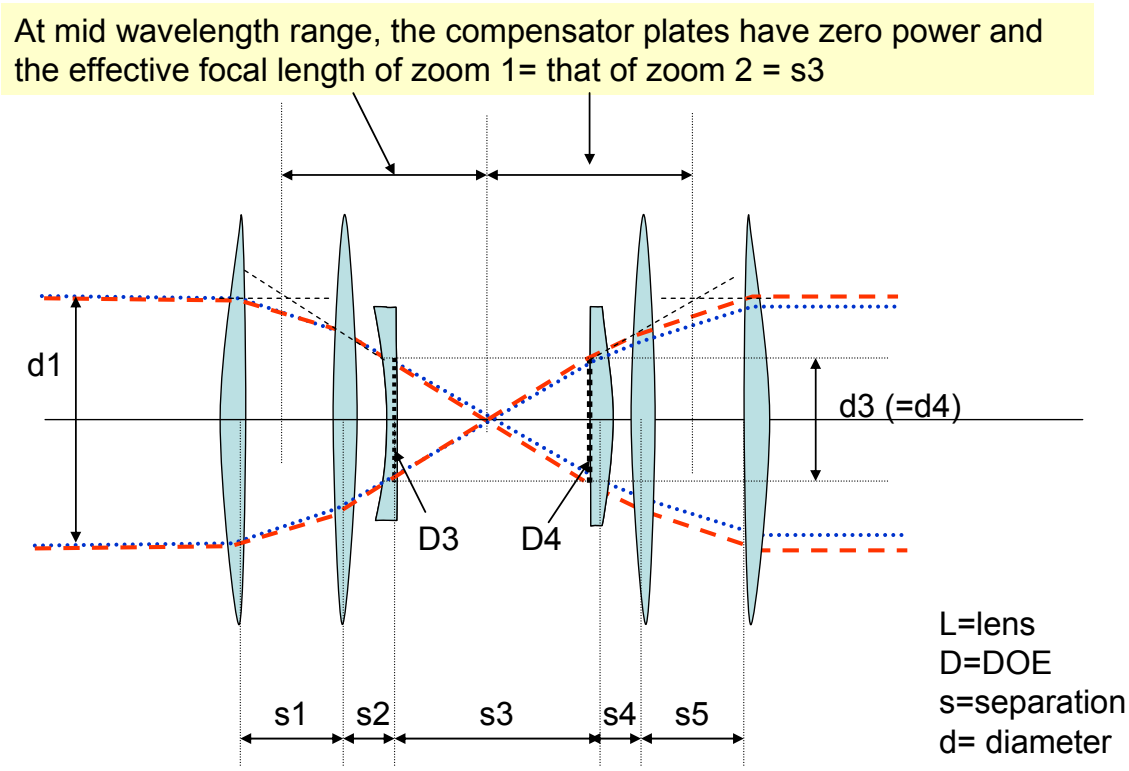

Figure 3.28 Diagram of the final design of zoom compensator which replaces each of the outside telecentric relay lenses with a pair of weaker telephoto lenses which by adjusting their separation and position with respect to the compensator plates can compensate for the changes in strength of the diffractive optical elements DOEs as the centre wavelength of the laser is adjusted over the 700-900nm range

Using straight forward equations derived from a geometric optics model of the system it is possible to design a system that will operate over 700-900nm wavelength range and a compensation factor range of 1-2, at constant output /input beam diameter magnification of 1, simply by adjusting the axial separations of the lenses s1 to s5. The detailed equations can be found in our patent ((Kirkby, Silver et al. 20.03.2008)) and are summarised by the MatLab plots of Figure 3.29.

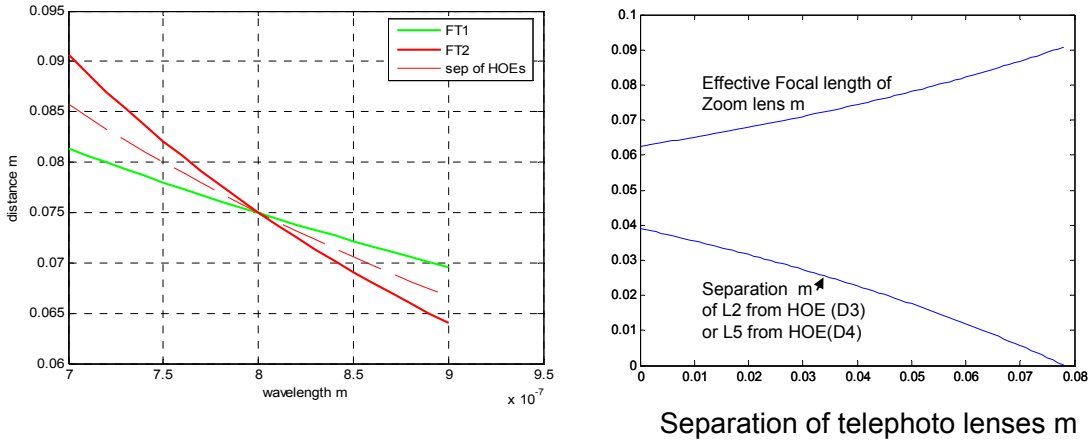

Figure 3.29 Plots for calculating a) the required effective focal length of telescopic lens 1 and 2 and the required separation of the DOEs in the previous figure as a function of wavelength and b) the focal length and distance to the first lens of a telephoto lens as a function of the separation of the telephoto lens pair (each 125mm focal length).

These designs formed the basis of the DOEs and lenses we bought in order to test the benefit of this kind of chromatic aberration correction. The key issue to determine experimentally is whether the chromatic aberration correction components give sufficient benefit to 2-photon efficiency to overcome the optical losses introduced by the additional optical components. The diffractive optical elements (DOEs) we purchased from Silios (silios.com) have about 80% transmission efficiency each so there is a 36% loss from these two elements alone.

Temporal dispersion of AODs

Magnitude of temporal dispersion in TeO_2 and why it is a severe problem for 2-photon microscopes

The large thickness of AODs has been a significant disincentive for the use of AODs in 2-photon microscopy because it causes a large chromatic dispersion effect on the pulse width of the pulses from the Ti-Sapphire lasers. Chromatic dispersion is measured in units of fs^2/m. The effect of all the lenses in a typical 2-photon microscope is to produce about 13,000 fs^2/m dispersion which spreads the 100fs pulses of the laser to about 300fs width. This is not too much problem as there is

usually plenty of laser power spare so that reduction in 2-photon fluorescence intensity can easily be compensated by increased laser power.

Each centimetre of thickness of TeO_2 produces 6300fs^2/m of dispersion at 700nm wavelength. Four conventional 9mm aperture, 30mm long AODs (Figure 3.30a) therefore produce 76,000 fs^2/m of dispersion that broadens Ti-Sapphire laser pulses well into the picosecond pulse width range and increases the laser power required for 2-photon luminescence by a large factor (3-10 times depending on initial pulse width). Even the thinner custom designed AODs (Figure 3.30 b) that we have chosen for this application have 38,000 fs^2/m dispersion, enough to spread the 100fs laser pulses to 1.5 ps pulse width as shown in Figure 3.31a . As the power budget for our 3D microscope is marginal anyway, we decided that it was important to compensate for the AOD dispersion (and if possible the remaining microscope dispersion) so that pulse length at the specimen can be kept as short as possible and 2-photon sensitivity maximised.

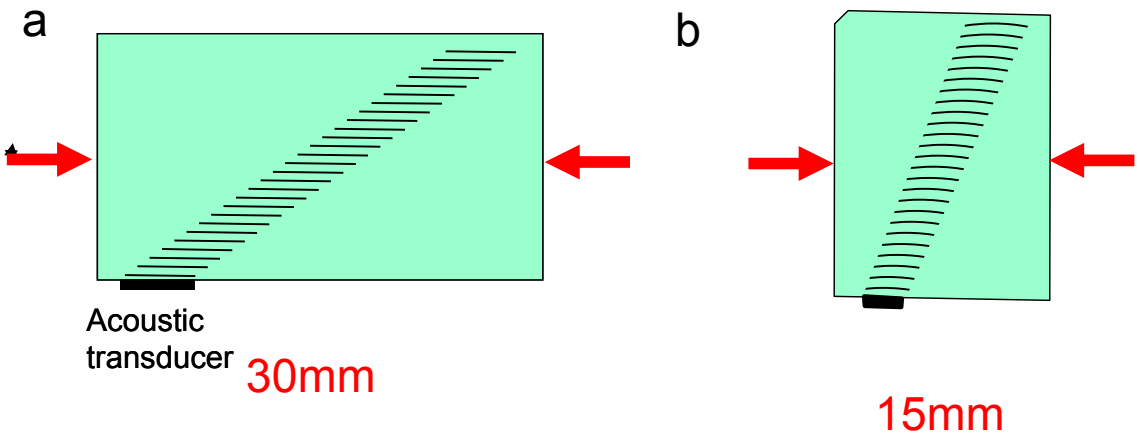

Figure 3.30 Comparison of thickness of a) a typical standard commercial AOD for deflection (typically 9mm aperture) and b) the optically rotated design used here only 15mm thick for a 15mm aperture.

Compensation for temporal pulse dispersion using a prechirper

The way in which a prism based prechirper precompensates the pulse leaving the prechirper so that after traversing the AODs the pulse is restored to close to its original pulse length is explained in Figure 3.31b.

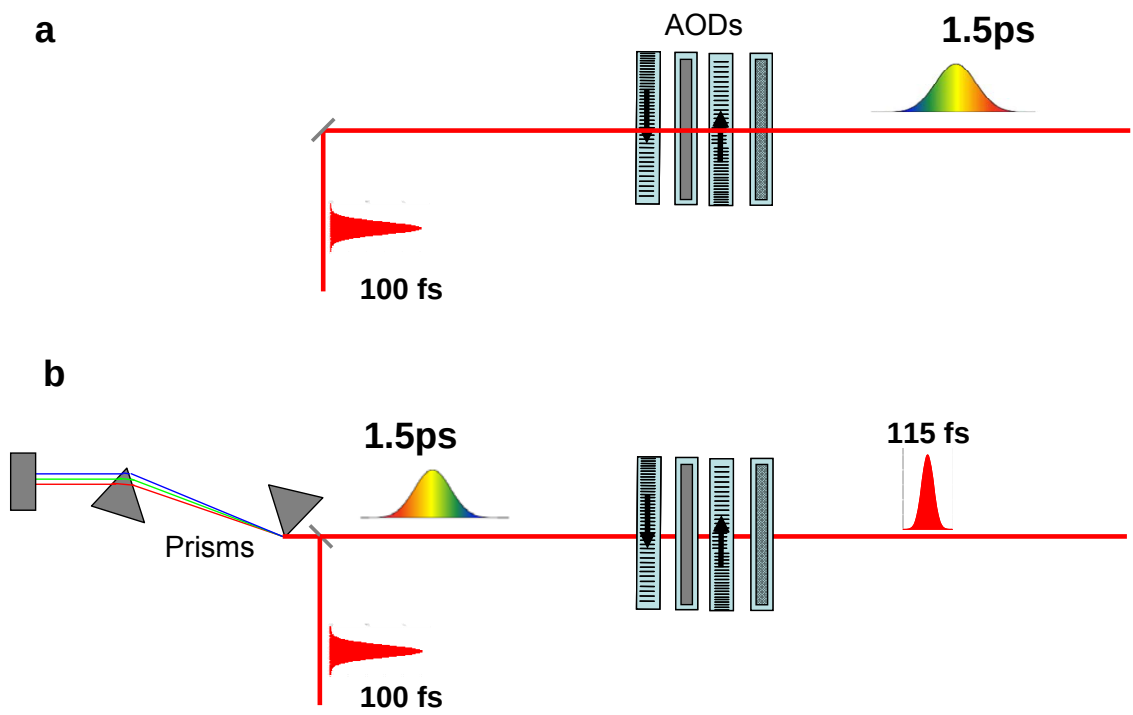

Figure 3.31 The effect of chromatic temporal dispersion on a 100fs pulse of light at 800nm wavelength with and without precompensation. In a) there is no compensation for the high dispersion caused by the total thickness of the 4 AODs (60mm in our prototype system). As the pulse has a transform limited spectral width of 10.6nm, the different wavelengths travel at different speeds through the highly dispersive TeO_2 of the crystals. The longer wavelength components travel faster and arrive first, spreading the overall pulse width to 1.5 ps, (fifteen times longer). The prism based prechirper b) uses prisms made of fused quartz and polished at the Brewster angle for minimal reflection of correctly polarised light. The prism pair has anomalous (negative) dispersion to refract the short (blue) components of the spectrum along a shorter optical path than the longer wavelength (red) components. Although on the diagram it appears that the red light goes through a shorter path, this is its physical path length. The optical path length of the red light is actually longer because it passes through a much larger length of the high refractive index prism material. The pulse length of the pulse exiting the prechirper is 1.5ps, but it has its short wavelength (blue) components first. When this pulse traverses the four AODs the AOD dispersion is balanced by the pre-compensation and the pulse width of the emerging pulse is returned to a figure close to the original 100fs.

Few commercially available prechirpers exceed 15,000 fs^2/m compensation. My colleague[3]negotiated with APE Berlin (http://www.ape-berlin.de/index_engl.html) and bought a customised prism based prechirper with folded optics that is capable of up to 56,000 fs^2/m compensation, enough to pre-compensate for our four customised AODs and the microscope optics. Today it would be impractical or at least

[3] Srinivas Nadella carried out the design and choice of manufacturer for the prechirper.

uneconomic to obtain a pre-chirper that would precompensate for the much longer standard AODs so that the ability to prechirp is dependent on using the custom design AODs with a small walk off angle and much reduced thickness. Thus the practicality of incorporating a prechirper into the AOLM is an important second benefit of the custom AOD design.

Models of overall system design and resulting Target Specification for AODs sent to prospective manufacturers

This section discusses how the design information given in this chapter was combined together in a model of the overall system and used to make a choice of the key aspects of the specifications of the AODs.

Model of overall system

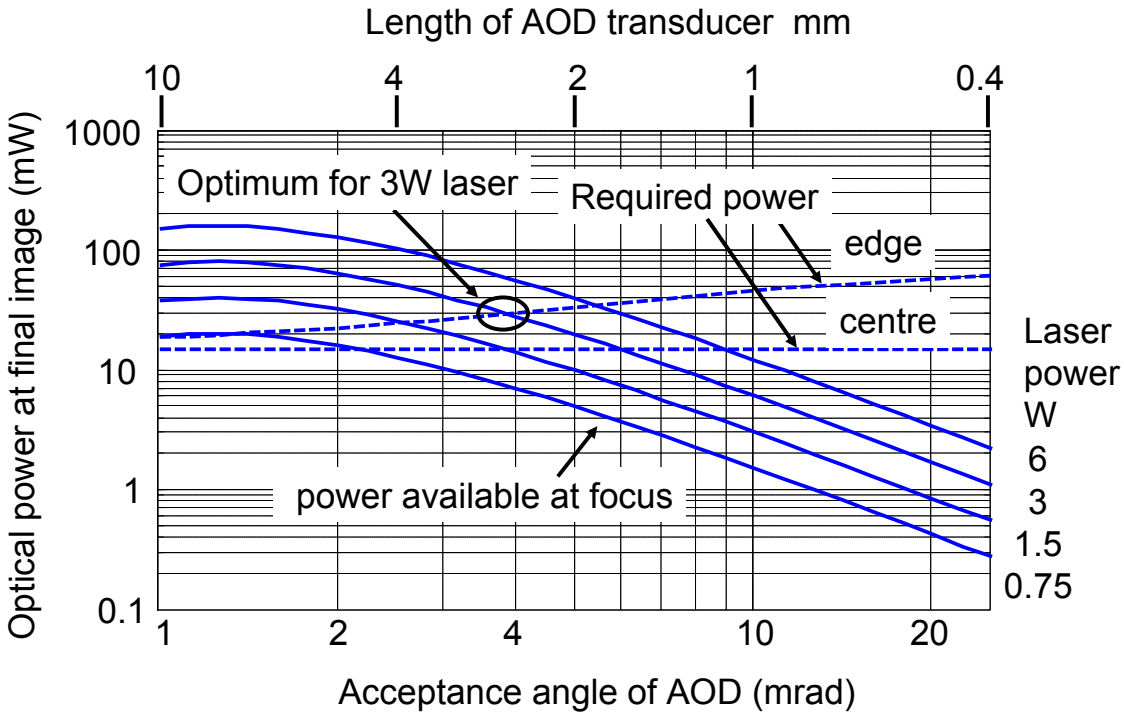

Figure 3.32 A nomogram aimed at enabling the optimum design of AOD transducer length to be chosen for the second AOD in each XZ and YZ pair. This is computed by a Matlab model of the power losses in the complete optical train. Starting with the a range of laser output powers listed on the left and estimating the losses for each optical element, the power available at the focus can be estimated and plotted in the solid lines. The required power can be estimated from existing experimental data, we estimated 15mW for optical functional imaging at the centre of the FOV. At the edges, more power will be required because of aberrations.

Based on the models of the AODs and expected point spread functions described earlier in the chapter, I was able to make models of the complete system that could be used to help with choice of the AOD design. A nomogram to help with such choice is shown in Figure 3.32.

This plots the expected optical power at the focus of the objective as a function of the semi-scan acceptance angle of the second AOD in each pair for a range of laser output powers. The model works by first assuming the total losses of all the other components in the system. This is quite problematic as there are a large number of optical components in series and by varying the assumptions made about the losses of each component it was possible to vary the overall transmission of the system from less than 1% to 10%. In this figure I have assumed 3% overall transmission excluding the loss of the 2 AODs whose efficiency alters as the acceptance angle is varied. The dashed lines on the plot then show the required power at the focus for sufficient two photon fluorescence for optical functional imaging. This is also quite problematic to estimate. As there is heavy scattering in brain tissue the depth that the laser beam can penetrate is dependent on the power available, so in that sense the more power available the better as it will allow imaging to a greater depth. Based on the power levels found to be required for 2D optical functional imaging (Koester, Baur et al. 1999; Hopt and Neher 2001; Oheim, Beaurepaire et al. 2001) and personal communication with my colleagues[4] we decided that a reasonable target would be 15 mW at the centre of the field of view. This power level would have to increase at the edge of the field of view to allow for the effect of aberrations on psf size.
This plot shows that it is reasonable to aim for an acceptance angle from the second AOD of each pair in the range 3-5mrad. It also shows that if you increase the acceptance angle even slightly beyond this figure the power falls off rapidly and there is the danger that there will be too little power for 2-photon fluorescence anywhere in the field of view. A second way of plotting the results from this model is shown in Figure 3.33 which shows the predicted number of resolvable volumes (NRV) as a function of the designed acceptance angle.

[4] Emanuelle Chaigneau and Tomas Fernandez-Alfonso

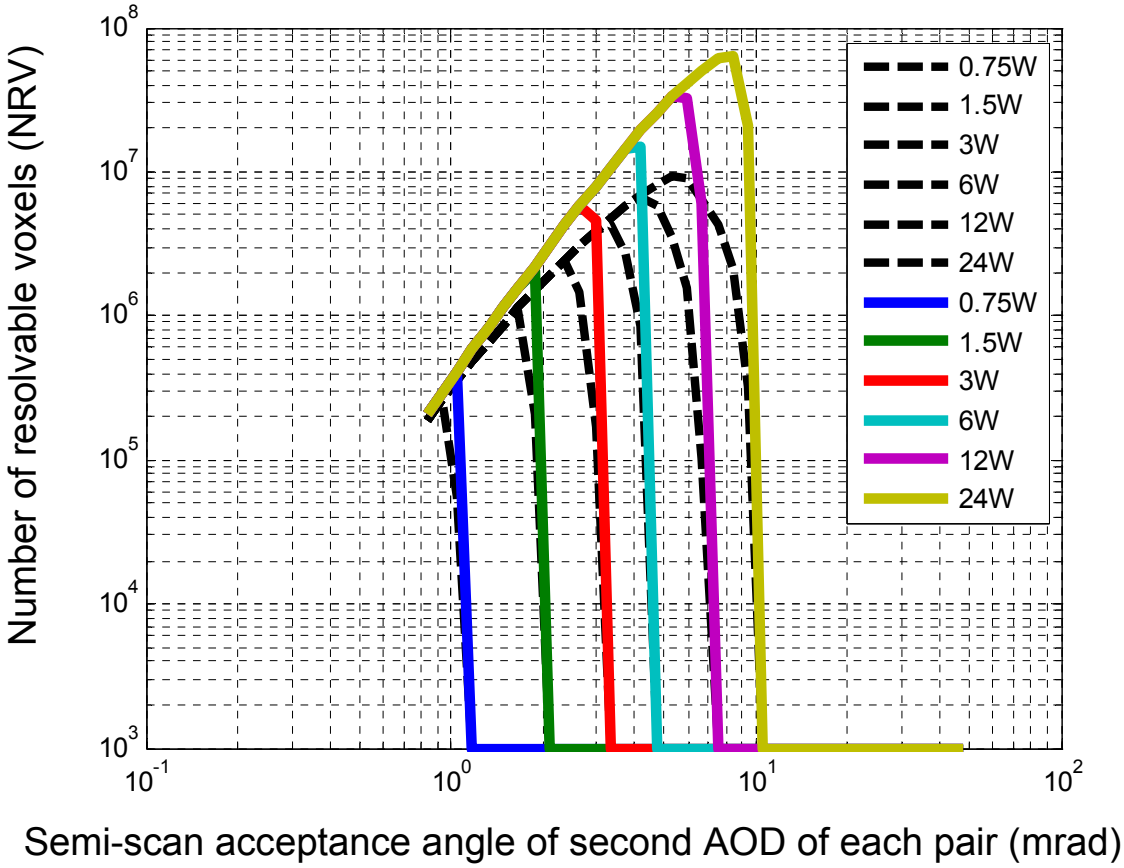

Figure 3.33 Predicted performance of the complete system in terms of the total number of resolvable voxels (NRV) as a function of the semiscan angle chosen for the second AOD of each pair. The 'threshold intensity' for two photon emission is taken as 1MW/cm^2. The dashed black lines are with compensation factor C=0 and the coloured lines are with C=1.7. Each plot represents a different optical power available from the laser. Today's commercial lasers deliver about 3W of power, but the level is increasing with time.

The figure plots the number of resolvable voxels for a range of laser output powers both with and without chromatic aberration compensation. This shows very clearly the precipitous drop in NRV if the AOD is designed with too large an acceptance angle. This is slightly artificial as it is based on the assumption of a sharp threshold optical intensity below which there is no 2-photon emission. A more correct model would take into account that 2-photon efficiency is dependent on the square of optical intensity, so what would actually happen is that the speed of gathering photons would drop as the square of intensity, not quite such a precipitous cliff as shown.

Discussion: Model of design trade-offs affecting system power budget shows achieving full target specification difficult

These results showed fairly early in the project that achieving the desired overall performance was going to be difficult. The field of view calculations showed that with the initial assumptions about the frequency drive limits of AODs we needed at least a semi-scan acceptance angle of 6mrad from the second AOD of each pair in order to achieve a 250μm cube scan volume beneath an NA=0.8 objective. The power budget nomogram, Figure 3.32, showed that with a 3W laser and reasonable estimates of optical system losses that it was risky to order AODs with more than 3-5 mrad acceptance angle. On the other hand the NRV plot of Figure 3.33 shows that providing the chromatic aberration correction is implemented it is possible to reach 6 mrad scan angles with laser powers up to 12W or alternatively by paying careful attention to minimize the optical losses of every component in the system. (The best commercially available lasers have 3-4 W output powers today, but these figures are increasing slowly year by year.)

For our first AODs we decided to hedge out bets and order AODs for the second of each pair with two different transducer widths so that we could switch electrically between the two and choose the optimum experimentally. We prepared the specifications as shown in Table 3.1 and Table 3.2. We were cautious on acceptance angle and specified a minimum of 3 mrad semi-scan acceptance angle for the narrower of the two transducers on the second AOD of each pair and 1.5 mrad for the first transducer. The AOD s that were delivered had acoustic transducer lengths of approximately 3.6mm on the first AOD of each pair and 2.4 and 1.8mm for the two transducers on each of the second AODs of each pair.

Requirement Specification for AOD X1 and AOD Y1

Model No: 45035-15-2/3DEG-.8 See G&H quotation 7th June 2006 No 20060607/01

Device/Parameter	Minimum	Comment
Acousto–optic Deflector		
Configuration of use	Two deflectors, one for for each X & Y axis	
Aperture size	15 × 15mm	
Depth of AOD crystal (light path physical length)	15mm max expected	
Centre frequency	35 MHz	Must be same as AODs X2 & Y2
Deflection angle range[5]	+/- 2.9 mrad	More preferred but not critical
Frequency Range	35 +/- 2.11 MHz	More preferred but not critical
Resolution/time-BW prod	100	
Wavelength Range	750-880nm	
Transmission	95%	
Incident angle range	+/- 1.5 mrad	Not critical
Diffraction Efficiency 750nm[6]	90%	
Diffraction efficiency 850nm	85% worst case	
Polarisation	Lin/Parallel/perp	
Material	TeO_2	
Speed of sound determining deflection angle at a particular frequency	619 m/s	Must be same as AODs X2 & Y2
Acoustic walk off angle	20 degrees	
Acoustic Drive power	3W	
Reliability	> 2000hrs at full power	

Table 3.1 Requirement specification for the first AOD of each pair

[5] With respect to incident beam measured in air for one AOD
[6] Over full range on incidence and deflection angles for one AOD

Requirement Specification for AOD X2 and AOD Y2

Model No: 45035-15-2/3DEG-.8-2TR See G&H quotation 7th June 2006 No 20060607/01

Device/Parameter	**Minimum with transducer 1 operating**	**Minimum with transducer 2 operating**
Acousto–optic Deflector with 2 transducers for selectable acceptance angle		
Configuration of use	Two deflectors for each X & Y axis	
Aperture size	15mm x 15mm	15mm x 15mm
Depth of AOD crystal (light path physical length)	16mm max	16 mm max
Centre Frequency and bandwidth	35MHz	35MHz
Resolution/time-BW prod	100	50
Wavelength Range	750-880nm	750-880nm
Transmission	95%	95%
Deflection angle range[7]	+/- 2.9 mrad minimum	+/-1.5mrad
Incident angle range	+/- 2.9 mrad minimum	+/-1.5mrad
Diffraction Efficiency 750nm[8]	75% worst case	90%
Diffraction efficiency 850nm	65% worst case	85%
Polarisation	Lin/Parallel/perp	Lin/Parallel/perp
Drive frequency and range	35 +/-2.11 MHz	35 +/-1.05 MHz
Material	TeO_2	TeO_2
Speed of sound determining deflection angle at a particular frequency	619 m/s	619 m/s
Acoustic walk off angle	20 degrees	20 degrees
Acoustic Drive power	8W	4W?
Reliability	>2000hrs at full power	>2000hrs at full power

Table 3.2 Requirement Specification for the second AODs of each pair

[7] With respect to incident beam measured in air for one AOD
[8] Over full range of incidence and deflection angles for one AOD

Evaluation of the AODs

This final section of the chapter describes some of the problems we experienced in assembling the AOL and how we solved them to assemble our first working AOL.

Once we had received delivery of the four custom designed AODs we tried to evaluate their performance compared to the specification. At this stage we had not appreciated the fact discussed earlier in the chapter, that the input polarisation for the extraordinary wave is approximately vertical rather than horizontal as in nearly all standard AODs. As a result, we repeatedly kept exciting the wrong input and output modes with unsatisfactory efficiency vs. drive frequency functions. We were concerned that perhaps the crystals were not oriented properly in the correct 2 degrees acoustic rotation and 3 degrees optical rotation. After helpful discussion with the manufacturer Gouch and Housego (www.goochandhousego.com) we made detailed measurements of the AOD crystal orientation which confirmed that the crystals were indeed correctly oriented and gave us a clear experimentally based understanding of both the orientation of the long axis of the input wave polarisation ellipsoid and the long axis of the output polarisation ellipsoid. The next section discusses these measurements.

Measurements of AOD crystal orientation

Figure 3.34 to Figure 3.38 shows the main results of a set of experiments we did to test whether the AODs were correctly oriented and to understand the optimum input and output polarisations. To date we have not purchased quarter wave plates so our experiments have all used linearly polarised input laser light and (Thorlabs) linear polarisation analysers for measuring polarisation. This means that there are some losses in coupling to the elliptically polarised eigenmodes. Since the ellipticity is expected to be 23% for the input wave and 19% for the output wave corresponding to approximately 88% and 94% coupling respectively to linear polarisation at centre frequency we judged that this loss could be ignored in the early stages of development. (Estimation based on Figure 3.3). Note therefore that the linear polarisation directions shown in the next four figures are actually the direction of the long axis of the polarisation ellipsoid.

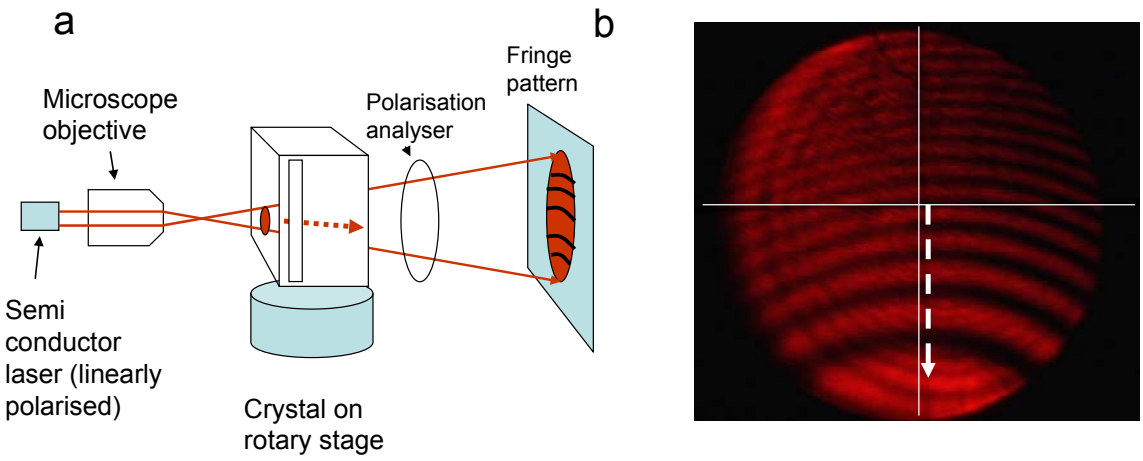

Figure 3.34 a) Apparatus for measuring the orientation of the optic axis in an AOD. b) photograph of the screen showing the polarisation fringes. The white solid line cross shows the normal to the facet whilst the dashed arrow show the expected theoretical direction of missorientation of the optic axis with respect to that facet. The fact that the fringes are normal to this dashed arrow confirms that the crystal axis is misoriented in the correct direction. Other measurements (not shown) confirmed that the tilt of the optic axis within the crystal was indeed the required 3 degrees within the measurement accuracy (0.2 degrees)

Figure 3.34 shows the apparatus we set up to measure the orientation of the crystal axes of the AODs. A diverging linearly polarised visible light beam is made by transmitting the collimated red light beam from a semiconductor laser pointer into a 10x microscope objective. This diverging beam was passed into the front face of the

AOD crystal and a polarisation analyser placed after the crystal. A pattern of fringes was then projected onto a paper screen. We carefully marked on this screen the position of the normal to the facets (using reflections off the facet). The diverging beam monitors a range of propagation directions in the crystal. Within the crystal the light is propagating in the two eigenmodes whos index difference increases with increasing angular radius from the optic axis. The dark fringes correspond to angular directions of equal path length difference between the two eigenmodes. These therefore form circles around the direction of the optic axis.

Figure 3.34 to Figure 3.38 show results for AOD X1 which deflects light horizontally. A top view of this crystal showing the computed direction of the maximum efficiency input and output beams at 35MHz drive frequency is shown in Figure 3.35.

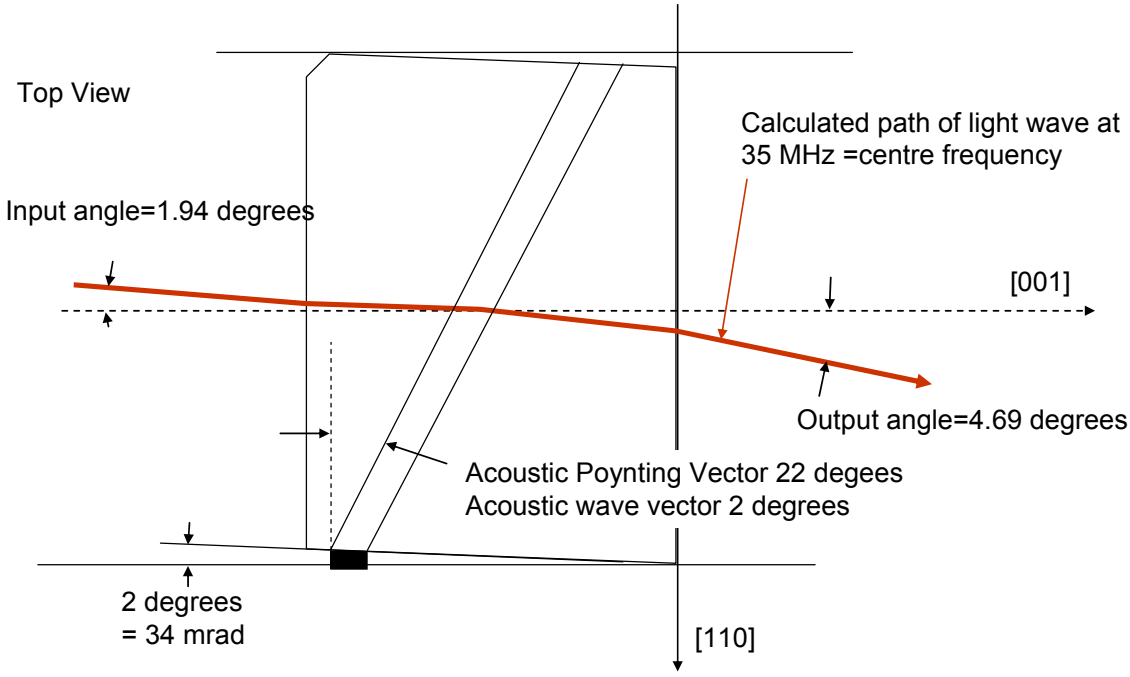

Figure 3.35 Top view of the custom AOD showing the precise angles of incidence and diffraction at its 35MHz centre frequency, (from manufacturer and confirmed by the wave vector model illustrated in Figure 3.10)

The input beam is orientated at 1.94 degrees to the optical axis and the output beam at 4.8 degrees, the orientation within the crystal is reduced by a factor n, where n is the refractive index. Figure 3.36 shows why the vertical misorientation of the foreshortened view of optic axis rotates clockwise as the crystal is rotated to view exactly along the input or output directions.

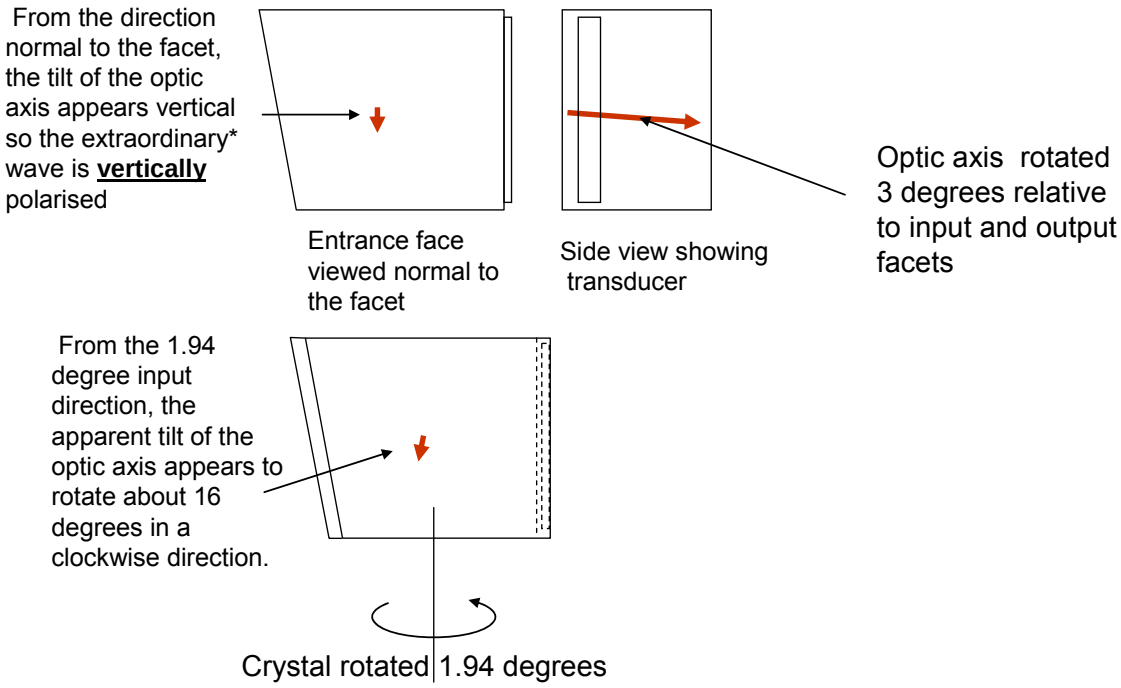

Figure 3.36 illustration of how the foreshortened projection of the crystal axis viewed from normal to the entrance facet appears to rotate by 16 degrees clockwise as the viewing angle is rotated by 1.94 degrees to align with precise direction of the maximum efficiency input beam. Thus the extraordinary wave is polarised in this 16 degree rotated direction. This is found to be the input linear polarisation that gives the highest efficiency from the AOD.

The equation for the angle of rotation based on small angle geometry is:- $\theta = arctan(\phi_h / n\phi_v)$ where ϕ_h = external horizontal misorientation and ϕ_v is the internal optical rotation which in this case is vertical. Using this equation we expect 16 degrees and 35 degrees respectively for the rotation of the apparent misorientation of the crystal axis viewed along the 1.94 degree input and 4.8 degree output directions respectively. Figure 3.37 and Figure 3.38 show how this calculation is nicely confirmed by the observation of the fringes with the crystal rotated about the vertical axis to correspond to the 1.94 degree input direction and 4.8 degree output direction respectively.

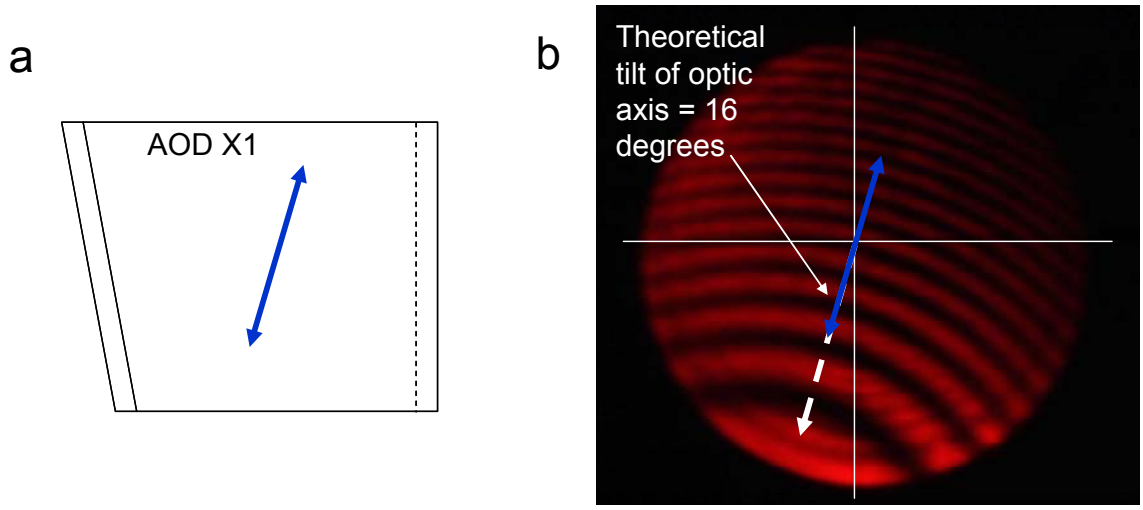

Figure 3.37 a) Approximate angle of input linear polarisation for maximum efficiency, b) Fringe pattern with the viewing angle rotated horizontally 1.94 degrees, parallel to the input beam direction for the wanted highest efficiency input mode. In theory the input polarisation is tilted by 16 degrees clockwise (dashed white line). The fact that this line is close to normal to the fringes shows a good match to experiment. This direction corresponds to the long axis of the elliptical extraordinary wave eigenmode.

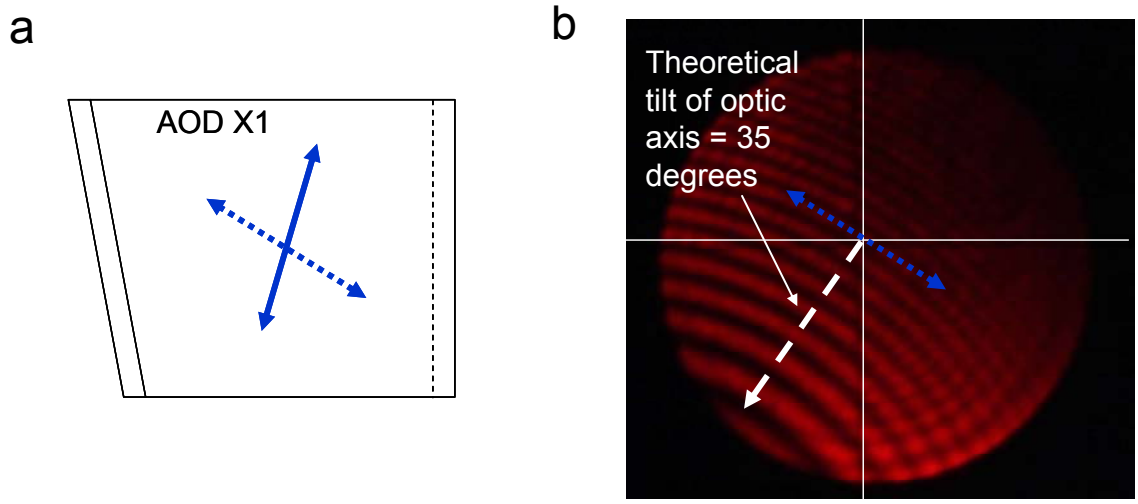

Figure 3.38 a) approximate directions of the long axes of the input(solid blue) and output (dashed blue) linear polarisations of the input and output beams for maximimum efficiency at 35 MHz drive frequency. b) polarisation fringes viewed from 4.8 degrees to the normal (parallel to the output beam), showing that they are rotated by the theoretically expected 35 degrees.

The fact that the fringes are always at right angles to the calculated apparent external misorientation of the axis confirms that the theory and the construction of the crystal is correct in this respect. As we expect the input polarisation to be in the extraordinary mode, the highest efficiency linear input polarisation is expected to be parallel to the

solid blue arrows shown on Figure 3.37 a) and Figure 3.38 a) and the output polarisation in the ordinary mode parallel to the dashed blue arrows in Figure 3.38 a). We found that understanding the optimum input and out put polarisations of the AODs is essential in order to assemble the compact configuration of AODs with all four AODs operating in the correct mode. After each AOD we placed a polariser orientated as expected to maximise output from this 4.8 degree ordinary index eigenmode. Half wave plates (Thorlabs) were placed before each AOD so that the input polarisation can be adjusted to correspond to that required for the 1.94 degree input extraordinary eigenmode.

Building and aligning the compact configuration

Photographs of the first design of the compact configuration are shown in Figure 3.39 and Figure 3.40.

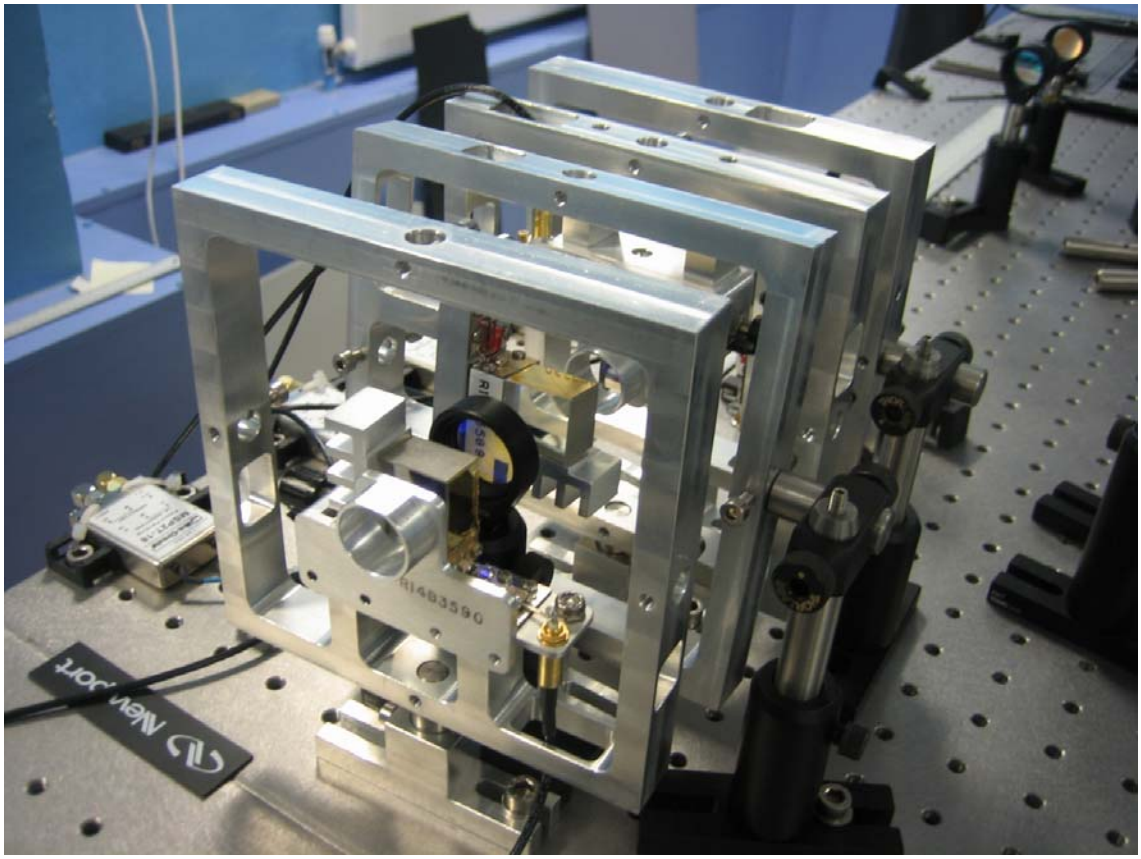

Figure 3.39 Photograph of the first design of mounts for the four AODs of the compact configuration[9]. The gold metallic transducer contacts can be seen on the side and top of AODs X1 and Y1 respectively

[9] Mechanics by Alan Hogben and Duncan Farqueharson of the UCL Biociences workshop.

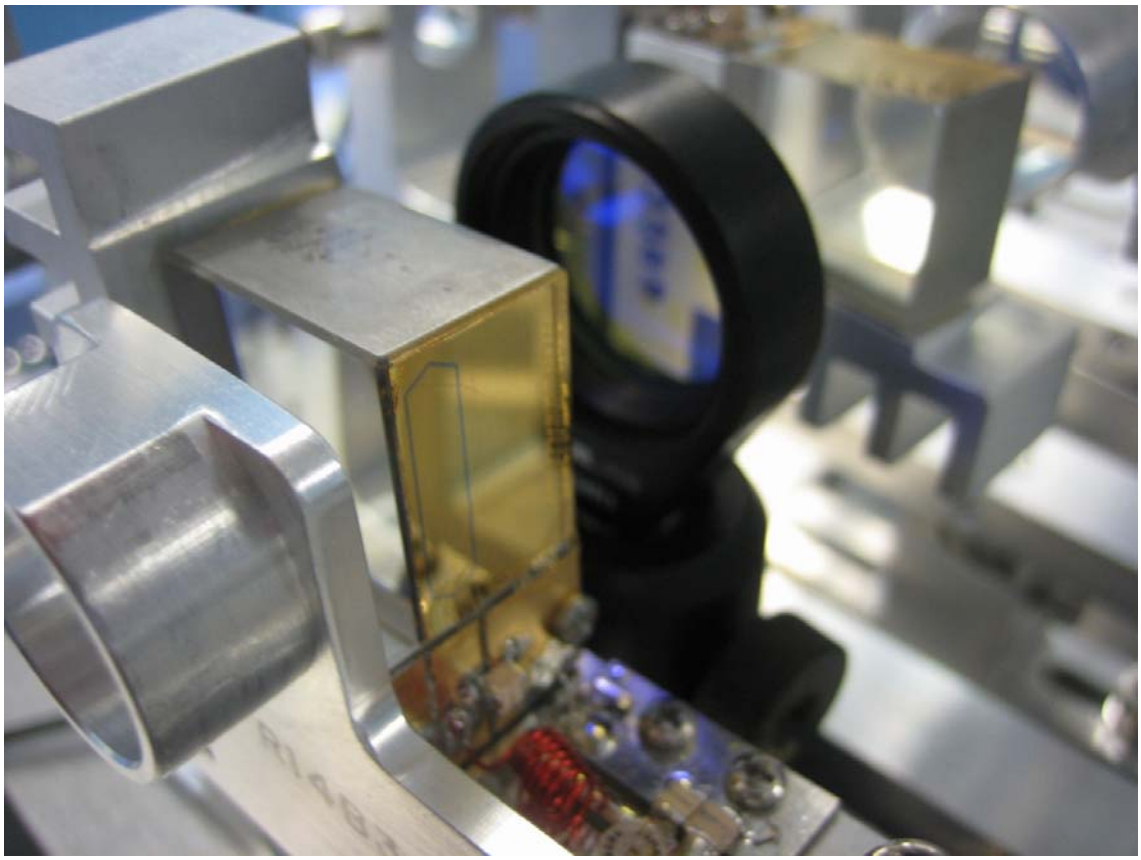

Figure 3.40 Close up photograph of AOD X1 showing the transducer more clearly. In the lower part of the picture the RF impedance matching coils can be seen.

The length of the whole AOL is appreciably less than 30cm. The figures show how it is quite practical to place the AODs within 50 -60 mm grating to grating spacing as required to avoid large lateral movement when changing wavelength. This is still true in later design which include semi circular supports for a rotatable polariser and half wave plate (HWP) after each AOD. We have found that using the correct input and output polariser and half wave plate positions it is straight forward to align all four AODs in a few hours work. Initially, for each AOD in turn the preceding HWP is adjusted to give the correct input polarisation, and a polariser after the AOD set to the correct output angle. The Bragg angle is then adjusted for maximum output power at 35 MHz drive. The input and output polarisations are then fine tuned (usually only a few degrees) to maximise efficiency.

Summary of chapter 3

In this chapter I have explained the design principles of conventional commercially available acousto-optic deflectors and the reasons this design is unsuitable for our application. The design of an ‘optically rotated’ AOD is explained which enables the

acoustic walk off angle to be reduced from 55 to 20 degrees. Its performance is modelled. The problems caused by the large chromatic aberration of AOD deflectors are explained and a novel method of minimising this aberration across the 3D field of view is proposed and its performance modelled. Models of the overall AOLM system are used to choose the optimum design parameters for the customised AODs we purchased. The problems we encountered in first assembling the four AODs into the acousto optic lens are explained and experiments to confirm that the AODs crystals are correctly aligned and polished are described.

Chapter 4 Drive electronics, control systems and development of new drive algorithms

This chapter starts with a system level description of the complete AOLM and its control system and drive electronics. The chapter then discusses the drive algorithms, measurements of XY efficiencies of the 4 AODs and the derivation of the new 'Optimised Frequency Limits' (OFL) drive algorithms. These OFL algorithms reduce the variation in diffraction efficiency with drive frequency and allow a much larger volume to be imaged.

System architecture

As described in chapter 1, the purpose of developing the AOLM, is not just to develop and prove the principle of operation of the microscope, but also to develop a good user interface. The microscope can then be used by a neuroscientist who's expertise and first aim is studying new brain physiology, not sorting out arcane problems with microscope control software or the user interface. This is a very challenging task. Many person-years of effort go into developing testing and debugging the control systems of commercial microscopes.

In order to construct a prototype AOLM we needed to define an overall control system and choose both the software and hardware components of the system. A simplified view of the overall system architecture is shown in Figure 4.1. This diagram is in the usual system engineer's format in which the architecture is broken up into a set of functional modules. The first part of the system design is then to define the interfaces between the modules so that each module can be developed and, if necessary, modified internally without affecting the rest of the system. The Integrated Microscope Control System (ICMS) is a software control system running on a high performance PC (Dell Precision 690 www.dell.com). The PC controls and interfaces with a set of National Instruments (www.ni.com) driver and data acquisition boards (two boards NI PCI 6115 and NI PCI 6713 are sufficient for the basic instrument). These in turn communicate with the peripherals such as the galvanometers, the optical shutters and Pockel's cell for laser intensity control (not shown), the photomultiplier tube (PMT) detectors and preamplifiers. Figure 4.1 shows

the interfaces between each functional module labelled with the initials of the adjoining units.

We initially tried to use Matlab (www.mathworks.com) software to control the system hardware, but found that the Labview (www.ni.com) graphical language developed by National Instruments for controlling its specialised driver and data acquisition boards to be faster and easier. Matlab (www.mathworks.com) on the other hand is very well suited for the development of algorithms using a C like programming language that is particularly optimised for rapid processing of large multi-dimensional matrices and it has an excellent graphics user interface.

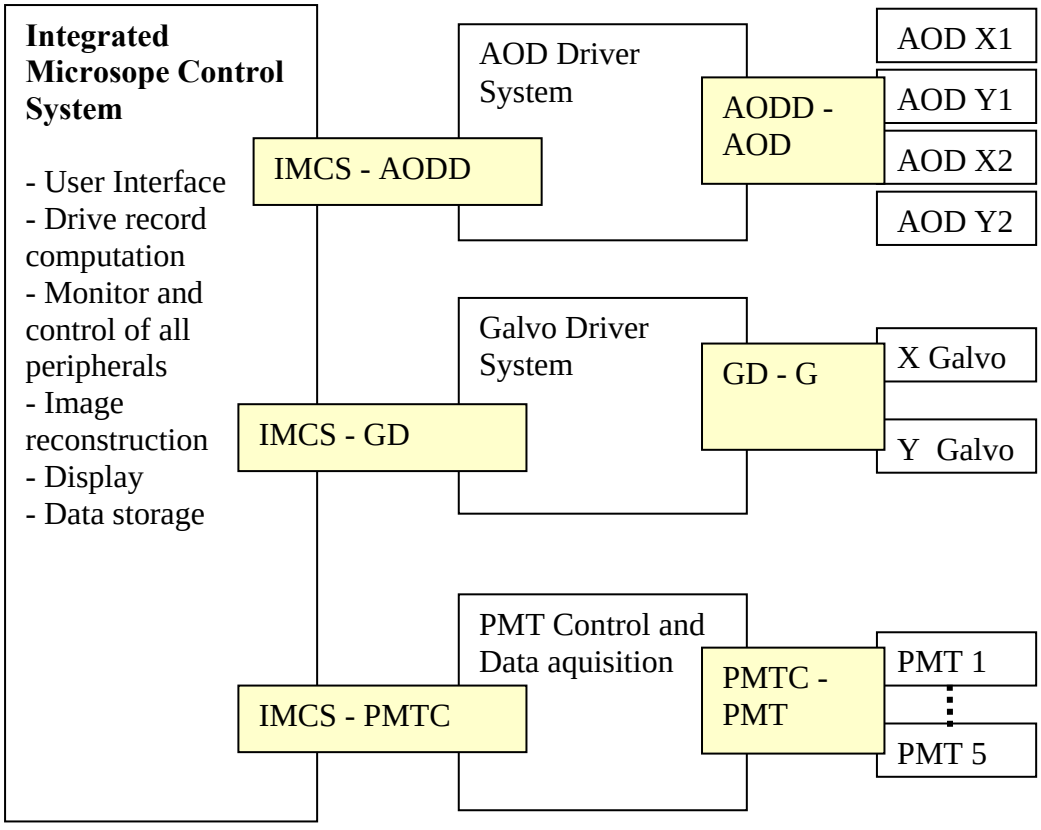

Figure 4.1. The overall system configuration. The functional blocks of the system are on a white background whilst the interfaces, labelled with the initials of the functional blocks they interface between, are highlighted in yellow. The peripherals, the Acousto-optic deflectors (AODs), the XY galvanometers (Galvos) and photomultiplier tubes (PMTs) on the right hand column are each controlled via separate sub units in the middle column. The master control system is the Integrated Microscope control System that uses a PC.

The heart of the system is the AOD control and driver functional units. The user interface and computation of the necessary AOD drive records takes place in the IMCS and interfaces to the AOD driver electronics via the IMCS-AODD interface. In the first prototype, this was physically a set of four RS232 links that link the PC to the AOD Driver unit. The AOD driver unit synthesises and amplifies the radio frequency (RF) waveforms used to drive the four AODs via the AODD-AOD interface. This is physically a set of 50 ohm RF cables with separate cables to control the RF switches that control which of the transducers are being used on the second of each pair of AODs. The next section describes how these subsystems work together functionally.

AOD drive using intelligent Direct Digital Synthesis (iDDS) of RF waveform

A search for driver electronics suited to AODs led to the early choice of the Isomet (www.isomet.com) intelligent Direct Digital Synthesiser (iDDS) for driving the AODs with linearly ramped RF drive. We ruled out the use of analogue driver systems because we wanted to be able to randomly jump from one ramp rate to another in a couple of microseconds and needed very high precision of start frequency and ramp rate so that the pointing was accurate. The analogue alternative of Voltage Controlled Oscillators (VCOs) are difficult to specify to such high precision if the frequency modulation waveform is wide bandwidth and not repetitive. A top level view of how the IMCS controls the iDDS in order to drive the AODs to produce a particular pointing or scanning sequence is shown in Figure 4.2.

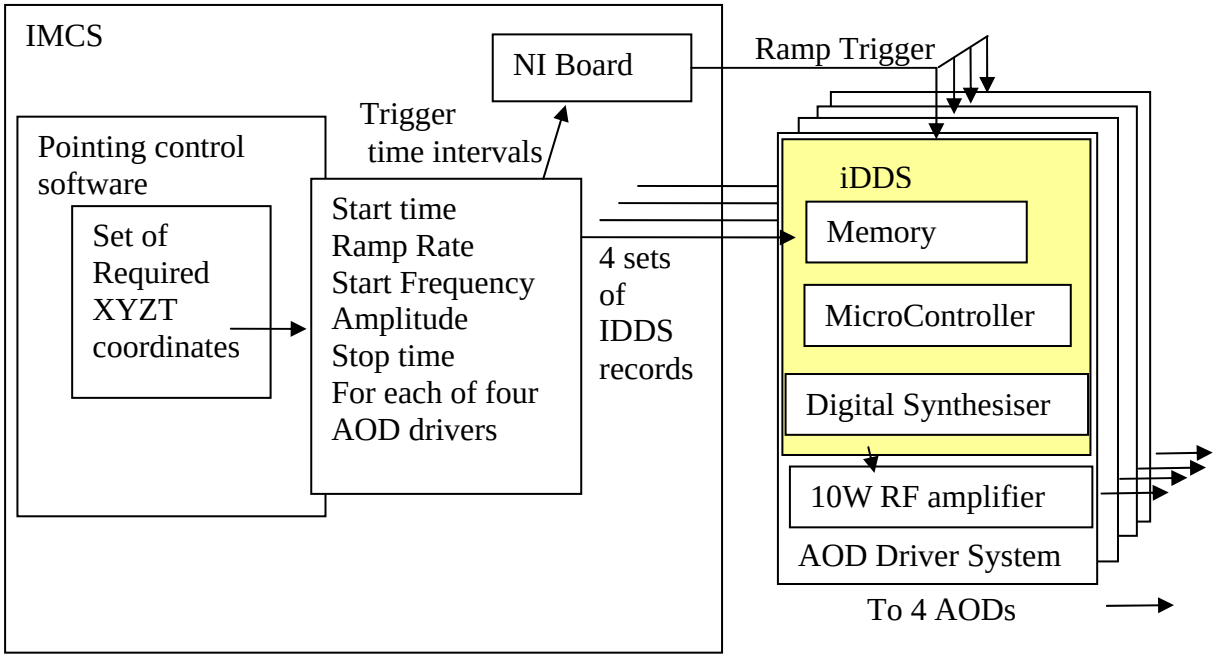

Figure 4.2. How the ICMS controls the iDDS to deflect the laser beam in a particular pointing mode sequence. Using the user interface software, the user specifies the pointing mode, the pointing position sequence and duration of each dwell in the region of interest. The Matlab and NI sofware converts this into a set of instruction records and transmits the data to the AOD driver system. This uses an Isomet (www.isomet.com) intelligient Digital Synthesiser (iDDS - yellow background) that generates the radio frequency waves in a ramp sequence from the sets of sequential records loaded into its memory. At the users command the ramp sequences are triggered by a trigger sequence from the NI driver board.

It uses a direct digital synthesis (DDS) RF driver chip set (Analogue Devices Inc. http://www.analog.com) that performs the synthesis of the RF waveforms. Originally the Isomet iDDS system combined the DDS chip with a memory and trigger system so that either a single frequency could be produced or an arbitrary sequence of RF tones could be produced in rapid sequence. This could be used to generate linear ramps if each frequency step and time interval was constant. This 'Image' mode was however very memory intensive so that it was only possible to load up a few ramps into memory before the memory was full and would require reloading. We needed a new mode of operation that was much more efficient on memory and triggering. In consultation with us, Isomet developed a new mode of operation that only loaded in the start frequency, stop frequency, ramp rate and amplitude for each ramp. This enabled just over 4,000 ramps to be stored in the initial version (20,000 in the latest

version). The waveform is in fact still made up of a sequence of equal small changes in RF frequency at equal time intervals so that an approximation to a linear frequency ramp can be obtained. Note, however, that once triggered, and in the ramp of a particular miniscan (see Figure 2.23 for description of a miniscan), no changes to ramp rate or drive amplitude can be made.

In the pointing mode the IMCS computes and sends a set of iDDS records from the PC to each of the iDDS units via an RS232 link (the latest version with 20,000 records uses a higher speed USB link). Once loaded into memory, these records can be triggered as often as is wished using the trigger sequence generated and stored at the same time as the iDDS records. This is controlled by the Labview user interface.

Algorithms for pre-computing RF drives to produce the required laser focus and scan patterns

In order to develop the Matlab algorithms and code for controlling the microscope I first developed a simplified simulation of the entire system.

Pointing mode algorithms

I developed algorithms for the pointing mode based on the assumption that the drive frequency limits to the AODs were simply the drive frequencies at the centre of the AOD range +/- the frequency required for one semiscan angle ‘s’. Working from the equations 2.17 to 2.30 that I had derived for the ramp rate and centre frequency of each ramp and the specifications for the iDDS I first specified the various terms that were needed for the computation:

Dwell voxel	*DV(p)* a voxel where the laser is to dwell
Voxel number in a sequence	*p* (as in Dwell Voxel (p), DV(p))
3D Coordinates of *DV(p)*	*X(p), Y(p), Z(p)*
Data clock time period	*Tdc*
Data clock number	*n* (*time into ramp* = $n \times Tdc$)
Dwell Time	*Td(p)* (must be an integral multiple of Tdc)
AOD filltime	*Tft* (integral number of data clock times)
Start frequency of Ramp for AOD X1 etc.	*fsx1(p), fsx2(p), fsy1(p)* and *fsy2(p)*
Ramp rate for AOD X1 etc.	*ax1(p), ax2(p), ay1(p),* and *ay2(p)*

Given a chosen sequence of points in 3D space as shown in Figure 4.3. the drive frequencies vs. time of each AOD can be calculated as plotted in Figure 4.4.

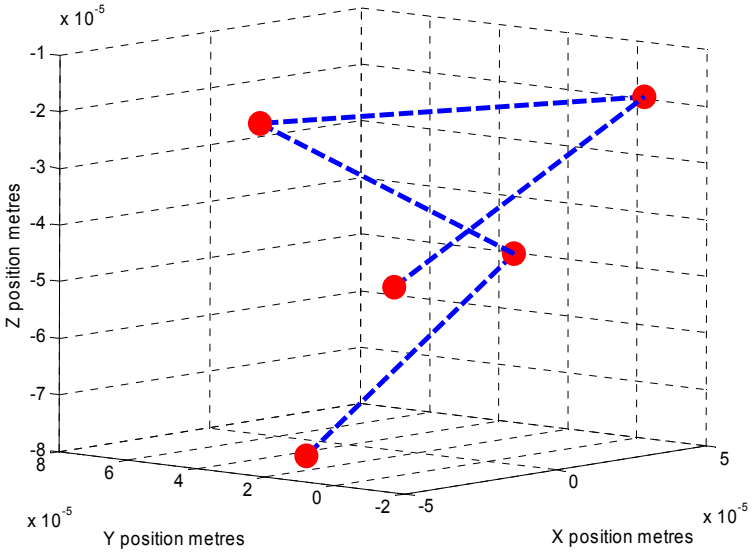

Figure 4.3 chosen points in 3D space of dwell voxels DV(1:5) in a five point pointing mode cycle (PMC). The pointing mode cycle is the sequence of regions of interest that are monitored repetitively to build up the luminescence intensity vs. time for each point.

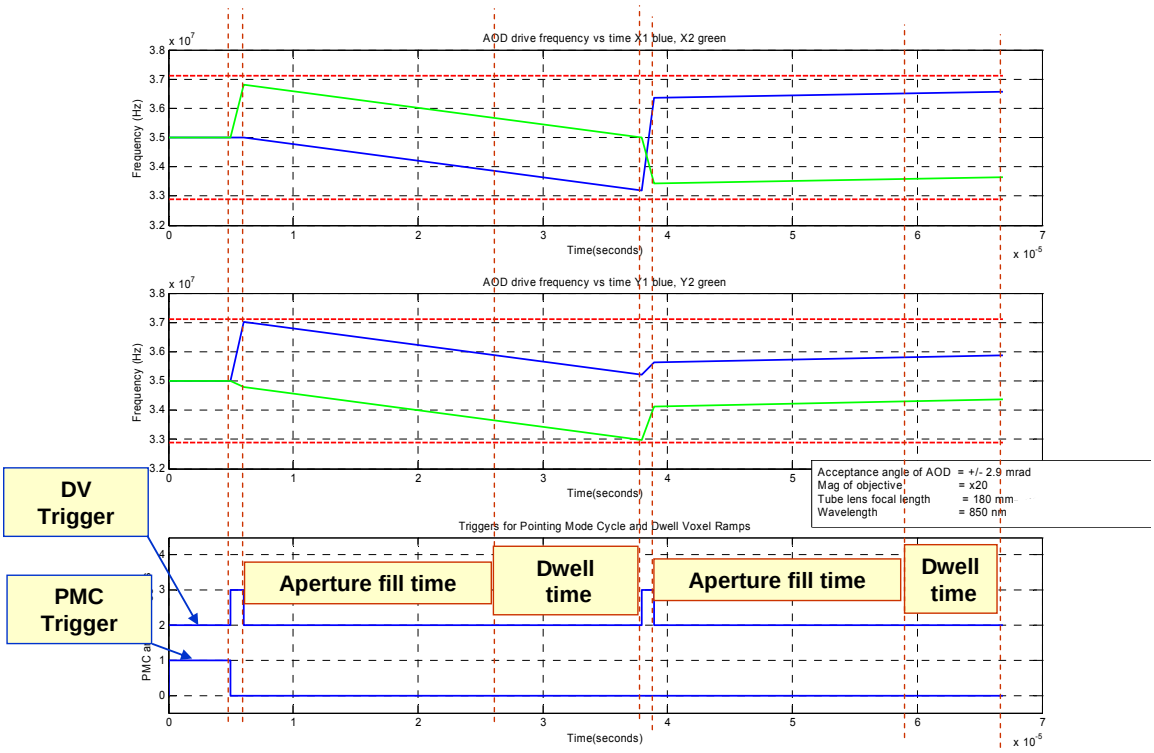

Figure 4.4 The RF drive for the first two Dwell Voxels of a Pointing mode cycle (PMC). a) Drive frequency vs. time for AODs X1(blue) and X2(green) showing limits to AOD drive frequency range (red dashed lines). b) Drive frequency vs. time for AODs Y1(blue) and Y2(green) showing limits to AOD drive frequency range (red dashed lines). c) Trigger pulses; lower trace the PMC trigger, upper trace the Dwell Voxel ramp trigger. Note the Dwell time on a voxel can vary, in this case programmed to increase dwell time with z depth. The first voxel has a large negative value of the chirp rate and focuses at large negative value of Z. The separation between the X1

and X2 ramps and the Y1 and Y2 ramps determines the X and Y coordinates of the voxel respectively.

The trigger voltage vs. time is also calculated in a data file prepared for each dataclock time of the pointing mode cycle. Two cycles of a five point pointing mode cycle are shown in Figure 4.4. A separate file is prepared that lists for each time slot n whether the photomultiplier tube output should be stored and if yes, which voxel in 3D space the output represents. In operation this data is passed onto the Labview code for control of time sequence reconstruction for each point that the laser addresses during the Pointing Mode Cycle.

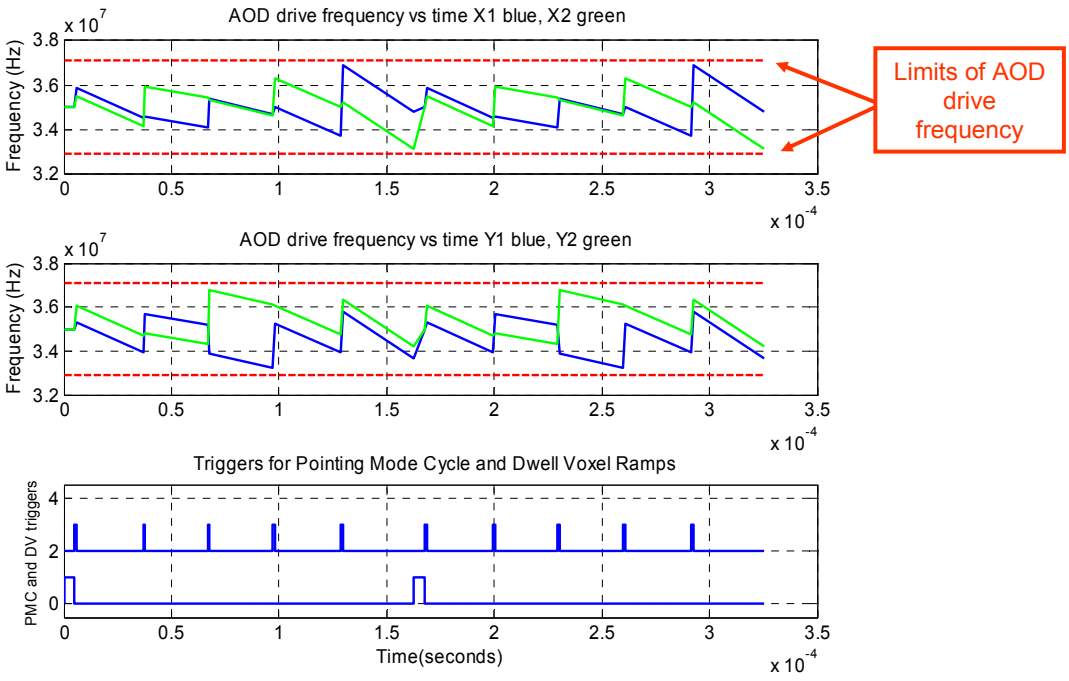

Figure 4.5 Drive frequency vs. time for two of the AODs showing the triggers for two pointing mode cycles.

Figure 4.5 shows RF drive frequency vs. time for two pointing mode cycles over a total time of 350 μs. In practice, for optical functional imaging over longer time periods, the pointing mode cycle is simply repeated as many times as necessary and the fluorescence intensity data from the dwell time of each ramp is independently plotted against time for each of the five Dwell Voxels.

Algorithms for scanning

The first algorithm I developed for scanning is illustrated in Figure 4.6 to Figure 4.9. First the operator chooses the Z plane to be scanned. In this case the normalised Zn = 0.3 (where Zn varies from -1 to +1 from lower to upper point of the octahedral scan volume (See description of Figure 2.9 for explanation of octahedral field of view)) It is possible to scan a small area of the Z plane by specifying zoom and centre of zoom coordinates. In this case at zoom =1 the maximum area that can be scanned without exceeding the specified drive frequency limits is first computed as indicated by the blue octahedral limits shown in Figure 4.6.

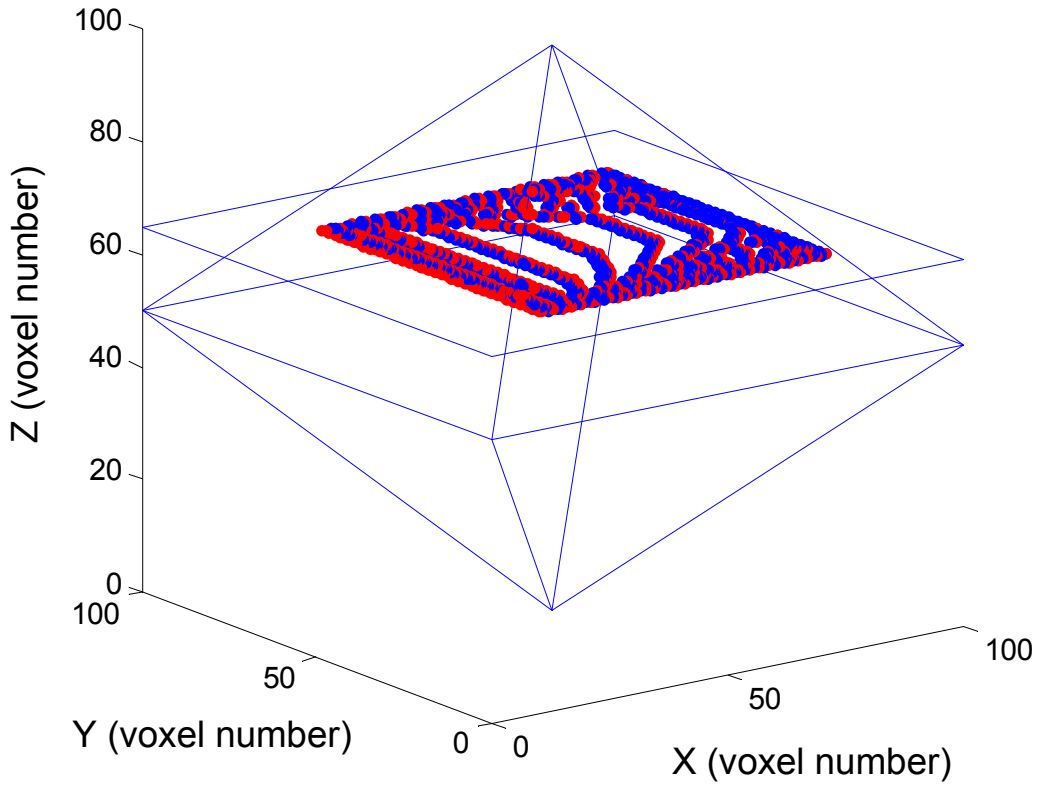

Figure 4.6 A 3D view of the way in which the AODs scan an XY plane in this case at Z=+0.3. The blue octahedron represents the theoretical limits of the pointing ability of the laser spot (based on the assumption of fixed frequency limits for the AODs). Red voxels are the start of miniscan. Blue voxels are the end. The Matlab computer program that generated this plot is based on the equations derived in the last section of chapter 2. It calculates each miniscan so that the number of voxels it scans in each miniscan is maximised without any of the AOD start or stop frequencies going out of the assumed AOD high efficiency drive frequency range (The Absolute Frequency Limit Algorithm). This is why the miniscans nearer the middle of the field of view are longer than those at the edges and this distinctive miniscan pattern is produced.

A set of miniscans is then computed to carry out the fastest possible overall scan at the specified dwell time per voxel, (typically 0.1 to 4 μs). The number of voxels in each miniscan is much larger nearer the centre of the field of view than at the edges because of the frequency limits. This leads to the distinctive miniscan pattern shown in Figure 4.6 by the red and blue dots.

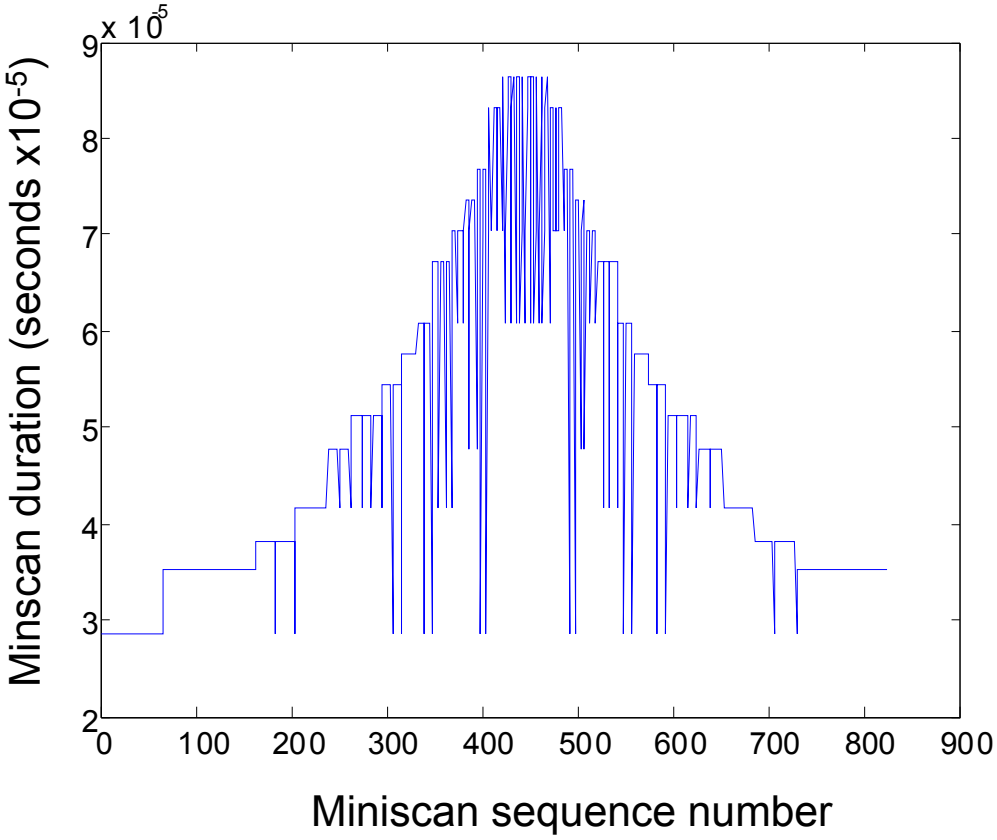

Figure 4.7 Ramp time of each of the 824 miniscans plotted against miniscan sequence number for the same Z plane (Z voxel number 66) shown in the previous figure. The minimum ramp time is 28 μs corresponds to the AOD fill time (24 μs)plus one voxel dwell time (4μs). This minimum ramp time only occurs for miniscans around the edges of the image, the maximum ramp time (88 μs) occurs in the middle of the image where the full AOD bandwidth can be used for ramping to produce Z displacement rather than static separation of ramps for X or Y deflection. The intermittent short ramps near the middle of the frame of view correspond to short miniscans at the beginning or end of X scans.

Figure 4.7 shows how, for this Absolute Frequency Limit (AFL) scanning algorithm, the 824 miniscans forming the overall sequence are longer in the middle of the overall scanning time than at the edges.

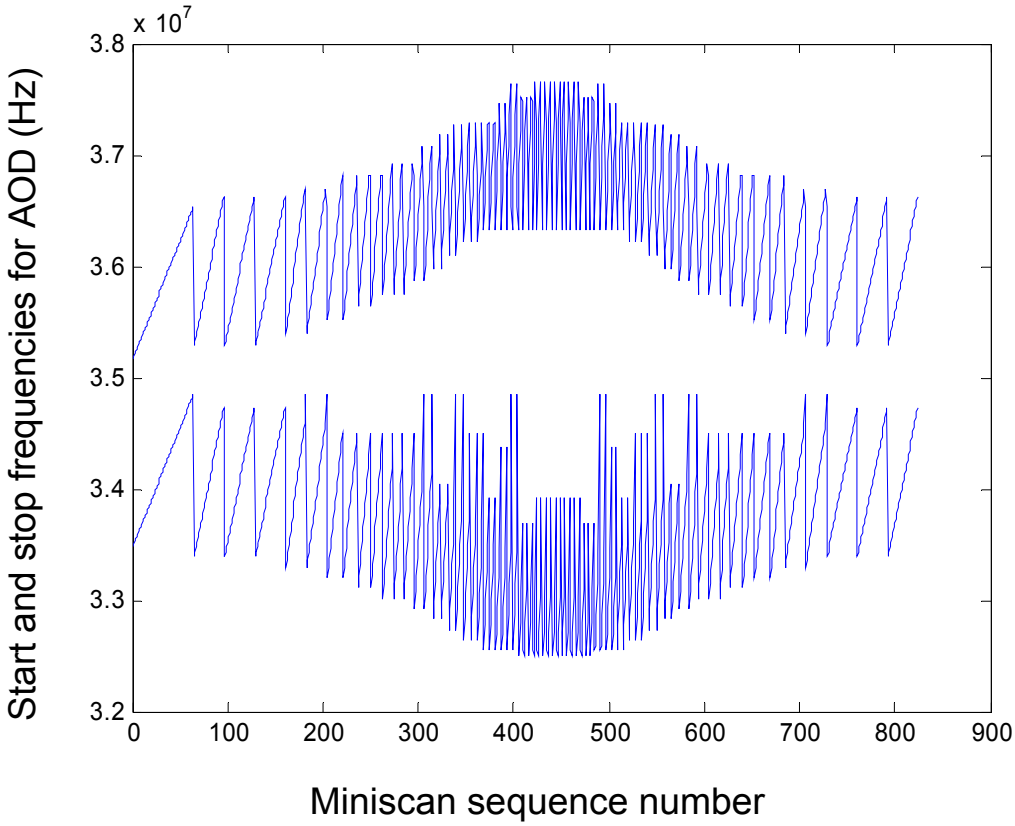

Figure 4.8 Start and stop frequencies of AOD X1 vs. miniscan sequence number showing in this case that the frequencies are all within the absolute frequency limits of 32.5 to 37.5 MHz.

The start and stop frequencies for each miniscan for the drive to the X1 AOD are shown in Figure 4.8. This diagram shows that close to the middle of the field of view the long miniscans each use up nearly the whole bandwidth between the frequency limits, but that near the edges the scans are much shorter because one of the other AODs (not shown) hits its limits.

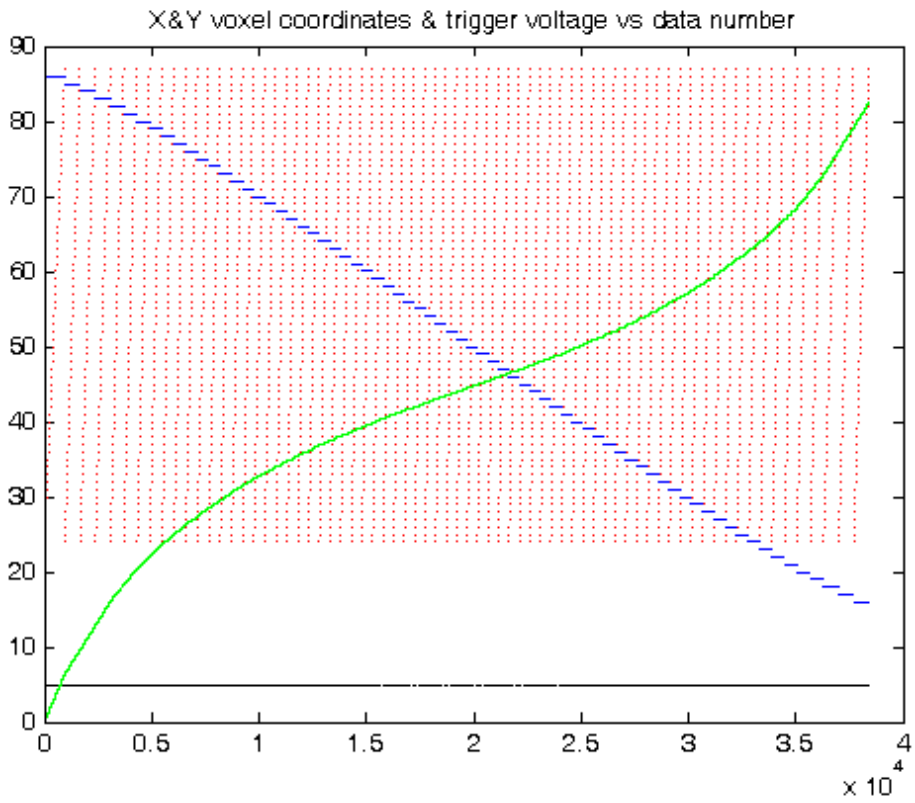

Figure 4.9 shows the X voxel number(red), Y voxel number (blue) and minscan number/10 (green) for each of the 824 miniscans. The X axis is the data acquisition time slot number, each time slot is 4 microseconds. This data is used to assign the concurrently acquired light intensity data to the appropriate X Y and Z coordinates of the Voxel.

Figure 4.9 shows the pre-computed voxel X and Y coordinates vs. data time slot number. Without recalculating or reloading the miniscan record data, the LabView code can use the trigger file and XY coordinate data of this figure to scan repetitively in 'Livescan' mode to semi continuously image the same set of voxels and present the image in real time on screen. The repetitions are usually averaged over multiple frames to improve signal to noise ratio.

Once this pointing and scanning software was completed we were able to make the initial evaluation of the microscope performance reported at the beginning of chapter five. The algorithm just described in this section was the absolute frequency limit (AFL) algorithm which produces an octahedral field of view and variable length miniscans. However more recently we have developed an improved understanding of the real limits to the drive frequencies of the AODs and developed a new algorithm, the optimised frequency limit (OFL) algorithm, that scans a larger volume using the

same AODs. The experimental and conceptual basis of this is described in the next two sections.

Measurements of X1 -X2 and Y1-Y2 diffraction efficiency plots

Whilst we were gaining understanding of the way in which the complete acousto-optic lens (AOL) system operates we made many measurements of the individual AOD efficiency vs. drive frequency. They showed high efficiency over at least the 30 to 40MHz drive frequencies corresponding to 6.5 mrad semiscan deflection angles for a fixed input angle. These plots are however not sufficient to model the complete AOL performance as it is the input acceptance angle of the second AOD in each pair that is actually the main limitation of the system. It is in practice quite difficult to make accurate high speed measurements of the input acceptance angle of an AOD without using another AOD in front of it to make accurate fine deflections of the input beam. In order to solve this difficulty, we have found it most useful in practice to measure the performance of the complete AOL and use this information to deduce the performance of each AOD. The only difficulty with this approach is that it is impractical to measure the optical power levels in between the AODs because there is insufficient space to place a large area detector there. The measurement obtained of overall AOL efficiency is the product of the efficiency of all four AODs in series. This potentially introduces uncertainty as to the root cause of any particular behaviour. However from a system perspective this is the performance that it is most important to understand. The measurement we have recently found most useful is to plot efficiency vs. X1 and X2 drive frequencies for fixed Y1 and Y2 drive frequencies (and vice versa). We have automated the data collection procedure for this information using LabVIEW code.

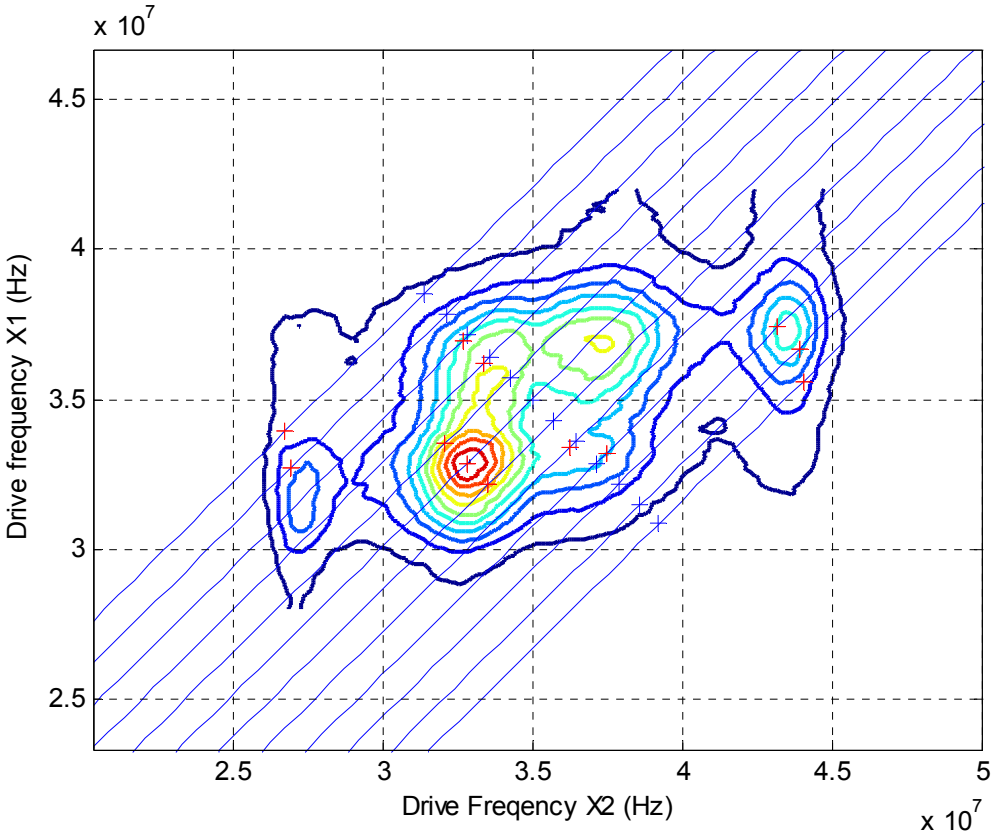

Figure 4.10 contour plot of efficiency of complete Acousto–Optic Lens (AOL) as a function of the drive frequencies to AODs X1 and X2 whilst AODs Y1 and Y2 are driven at 35MHz fixed frequencies. The contours are normalised 2 photon efficiency measured by scanning the focused spot through a fluorescent plastic slide (Chroma Technology Corp http://www.chroma.com/). The peak normalised intensity is 1 at the centre of the red contour, each contour is a step of 0.1. Super imposed on the plot is a diagram to illustrate the computation the a new miniscan algorithm (the Optimised Frequency Limit (OFL) Algorithm) does to maximise efficiency for each miniscan. The blue crosses represent the pair of differential mode drive frequencies (see Figure 2.21 for theory) required to give the required X deflection at the centre of the miniscan (12 miniscans are computed here). The blue diagonal lines through each blue cross are the common mode drive frequencies that give the same X deflection in the Z=0 plane. The red crosses represent the point on each common mode line where the miniscan centre will have the highest efficiency. This pair of drive frequencies is chosen for the centre voxel of the miniscan.

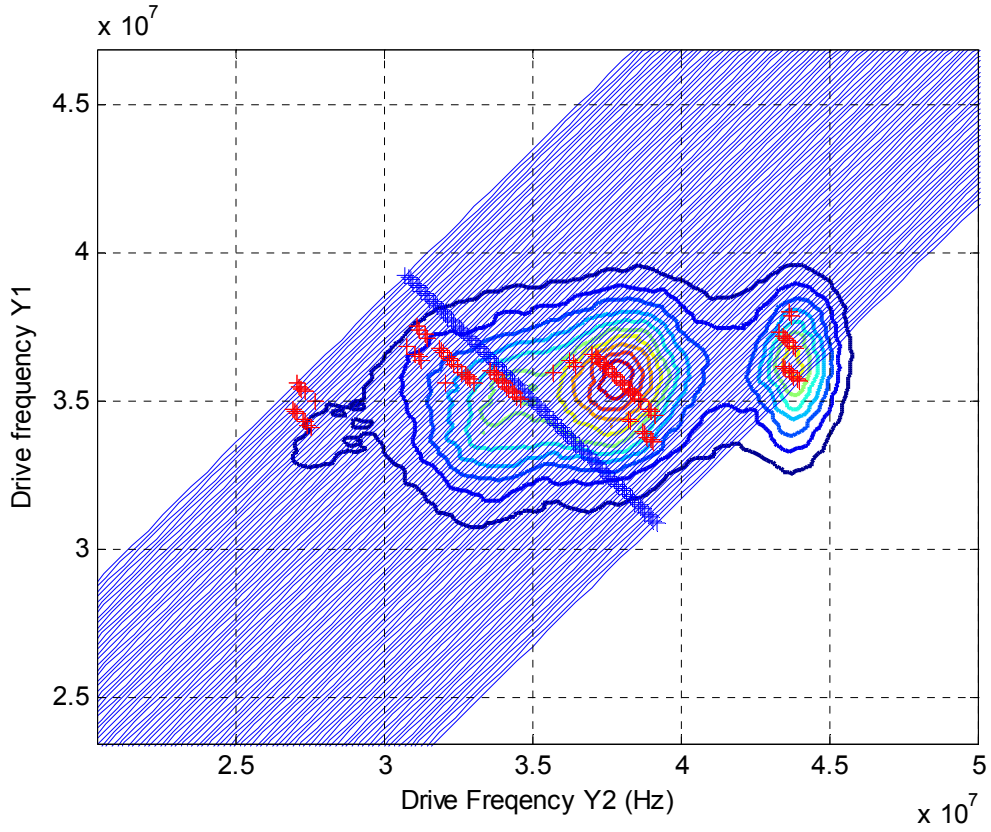

Figure 4.11 contour plot of efficiency of complete Acousto–Optic Lens (AOL) as a function of the drive frequencies to AODs Y1 and Y2 whilst AODs X1 and X2 are driven at 35MHz fixed frequencies. The contours are normalised 2 photon efficiency measured by scanning the focused spot through a fluorescent plastic slide (Chroma Technology Corp http://www.chroma.com/). The peak normalised intensity is 1 at the centre of the red contour, each contour is a step of 0.1. Super imposed on the plot is a diagram to illustrate the computation the new (OFL) miniscan algorithm does to maximise efficiency for each miniscan. The blue crosses represent the pair of differential mode drive frequencies (see Figure 2.21 for theory) required to give the required Y deflection at the centre of the miniscan (100 independent deflections are computed here, one for each line of the vertical scanning and used repeatedly for each miniscan making up a particular Y full scan). The blue diagonal lines through each plotted blue cross are the common mode drive frequencies that give the same Y deflection. The red crosses represent the point on each common mode line where the miniscan centre will have the highest efficiency. This pair of drive frequencies is chosen for the centre voxel of that Y full scan.

The contour plots of 2-photon efficiency, measured right through the completed microscope are shown for X1, X2 drive frequency parameters in Figure 4.10. These are measured at high speed by scanning the X2 drive frequency over the full plotted range, and dividing the range into 100 pixels at 4 μs/pixel and stepping X1 by one hundredth of its full range after each line. There is a small correction on plotting the X2 frequency against its drive frequency data point to allow for the fact that the

frequency at the centre of the AOD lags behind the frequency at the transducer by half the AOD fill time times the X2 ramp rate.

Note that this contour plot shows that useful 2-photon efficiency (to the blue 0.2 normalised 2-photon efficiency contour) can be obtained for X2 drive frequencies varying from 27 to 44 MHz corresponding to 11 mrad semiscan angle, whereas the frequency range for AOD X1 is only 31 to 38MHz corresponding to a semiscan angle of 4.5 mrad. Since we know that the high efficiency deflection angle of AOD X1 is much larger than 4.5 mrad semiscan angle we can surmise (but not prove from this plot) that the reason for the limited range of high efficiency X1 frequencies is the limited acceptance angle of AOD X2. Figure 4.11 shows the same type of plot for the 2-photon efficiency of AODs Y1 and Y2, with X1 and X2 at fixed frequency. This shows similar results but not such high efficiency at the lower end of the Y2 frequency range. This may be caused by non optimal Y2 alignment.

Both these plots can be compared with the theoretical plots for AOD1, and AOD2 efficiency in Figure 3.17 b. It is not surprising that the 2-photon efficiency falls off at high and low frequencies compared to theory because 1) the theoretical model does not include the limited bandwidth of the RF transducer and 2) chromatic aberration causes 2-photon efficiency to fall off as the net deflection (differential drive frequency) increases. However it is clear that the experimental results include a cyclic component to efficiency vs. frequency plots that is not present in the theoretical model. The expected single ridge of high efficiency is split into a series of rounded hills separated by dips. Peaks and dips are separated by 4 MHz in X1, X2, Y1, but not apparent in Y2. As the peaks and dips are all separated by approximately equal frequency differences, it suggests that there is some form of cyclic interference effect causing this. The reason for this is not yet certain. A possible explanation is that the theoretical model used for Figure 3.17 is inadequate in ignoring the fact that the linearly polarised light entering the AODs will excite not only the wanted extraordinary mode (94% efficiency; see discussion concerning Figure 3.38) but also the unwanted ordinary mode (6%). At the grating these will interfere in an optical path length dependent manner that depends on the angle of incidence of the propagating wave because the differential optical path length is dependent on the refractive index difference between ordinary and extraordinary waves. This will

produce peaks and troughs in AOD efficiency caused by the same effects that cause the interference effect in Figure 3.34 to Figure 3.38. This theory is consistent with the apparent lack of any 'cyclic interference' on efficiency vs. AOD Y2 drive frequency as the output from that AOD does not couple into any more AODs. More experimental work is needed to confirm or refute this theory. However, these cyclic interference effects are relatively small, the most significant aspect of the results is that it points the way to scanning much larger volumes using new drive algorithms, as explained in the next section.

Derivation of new drive algorithms

These measurements, together with the understanding of common mode and differential mode frequency drive which we had derived in chapter 2, Figure 2.20 to Figure 2.24 showed us how we could develop new drive algorithms. These can overcome the limitations of the fixed drive frequency limits we based our first pointing and scanning algorithms upon. The original algorithm we now refer to as the Absolute Frequency Limit (AFL) algorithm as it operates by simply initially specifying the maximum and minimum drive frequencies it is permissible to drive any of the four AODs. The new Optimised Frequency Limit (OFL) algorithm uses the algorithm described graphically and in the captions to Figure 4.10 and Figure 4.11 to maximise the overall diffraction efficiency at the centre of each miniscan. This also minimises the variation in efficiency from voxel to voxel within each miniscan. It is clear in both these plots that it is possible to drive the second AOD of each pair over a much wider range of frequencies than the first AOD and still find combinations of drive frequencies that give high efficiency. As will be shown in the results of chapter 5, this enables the scan volume to change from the octahedral shape described so far to a cuboid of more than three times the volume.

Summary of chapter 4

This chapter describes the drive electronics, control systems and system architecture of our prototype system. It describes how the concepts and equations for pointing and scanning developed in chapter 3 are converted into Matlab and labVIEW software, and how this software is used by the overall PC based integrated microscope control system. It then describes how intelligent digital synthesizers are used to drive the AODs and the software and hardware necessary to control the timing of the RF drive signals, the photomultiplier tube data collection and reconstruction of images. The final two sections describe how high speed measurements were made of the overall AOL diffraction efficiency vs. the X1,X2 and Y1,Y2 AOD drive frequency pairs for XZ and YZ deflection. Based on this data, and the theory developed in chapter 2, a new algorithm to optimize the AOD frequency limits for each miniscan is explained.

Chapter 5 Experimental results: AOL and AOLM

In this chapter I summarise the main experimental results we have obtained at various key stages of the development of the complete AOLM. The results are approximately in chronological order, except the results of point spread function measurements which are presented after the latest field of view and imaging experiments. This is so that the comparison of the field of view between the old AFL and the new OFL algorithms is clearer.

Measurement of speed of refocusing of the AOL

The first measurement we made on first assembling the AOL was to measure the speed at which the dynamic lens could focus. Figure 5.1 shows a view of the AOL followed by a 500mm lens and a single silicon detector 3mm diameter (Thorlabs model PDA36-EC) ,http://www.thorlabs.de/ shielded by a pinhole 30 μm in diameter. The detector has 1- 10MHz bandwidth depending inversely on the gain of the built in preamplifier. As there is plenty of signal we used low gain and thus had 5-10 MHz bandwidth.

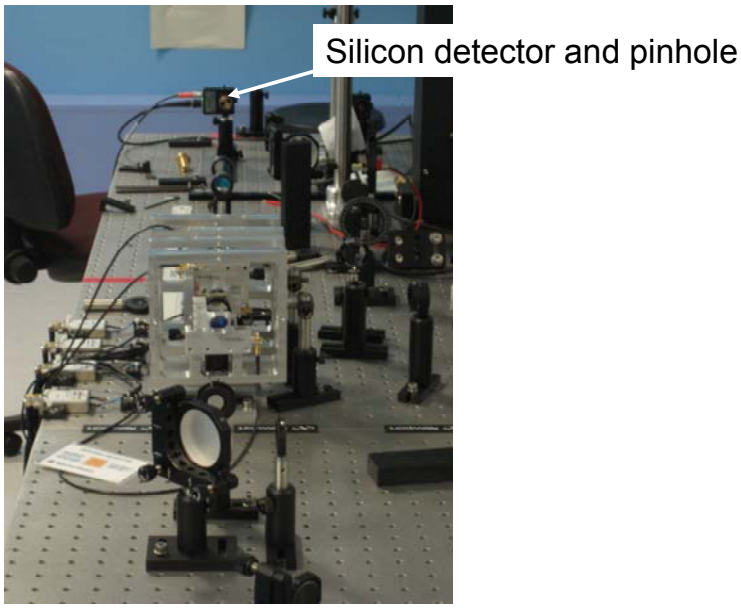

Figure 5.1 Photograph of the first assembled compact configuration of the AOL showing a silicon detector and pinhole in the distance following a f = 500mm lens.

To test random access pointing of the AOL across the field of view we needed a minimum of 3 detectors and used pellicle beam splitter to project the focused spot onto one or other of the pinholes without the detector interfering with the light to the other detectors. This is illustrated in Figure 5.2a. The pinholes were axially separated by -40, 0 and 40mm from the natural focal plane of the lens and positioned arbitrarily in the XY plane.

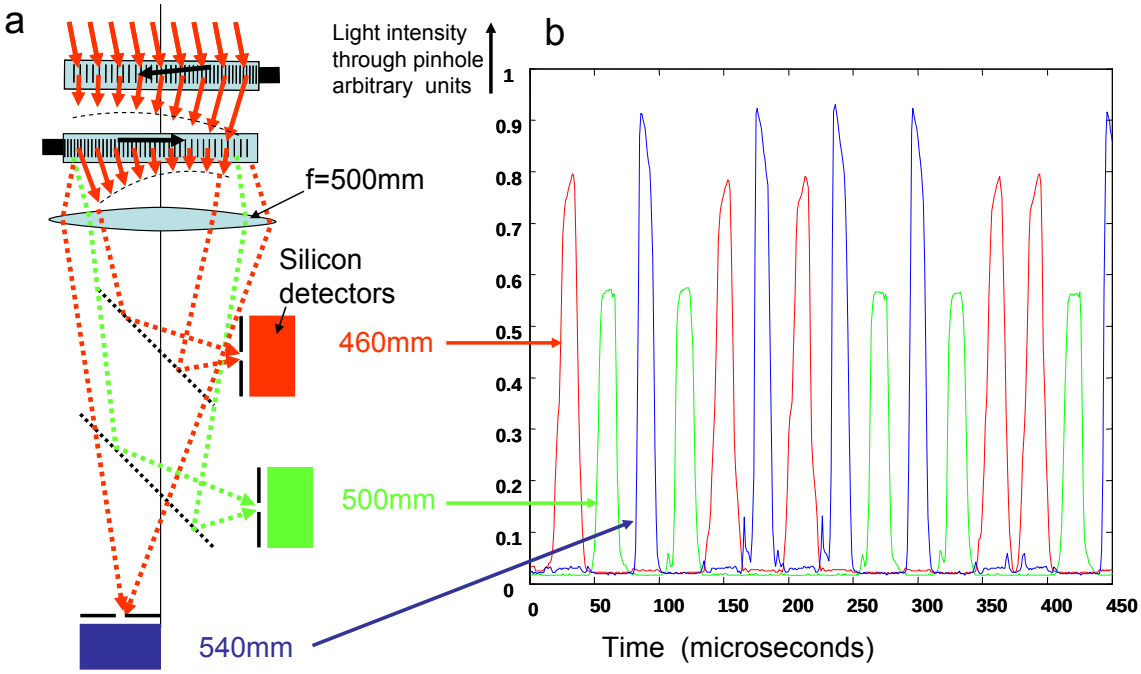

Figure 5.2 a)Experimental set up and b) results from initial 'pointing mode' tests showing it possible to randomly focus on any one of the three pinhole detectors and jump from pinhole to pinhole at 30kHz. The pinhole size of 30 μm is designed to match the diffraction limited spot size of the beam. The black dotted lines in the set up diagram represent beam splitters. The pinholes are separated by up to 80mm axially and are positioned arbitrarily in the XY plane. All are within the field of view of the AOL with following 500mm lens.

The correct 'ramp' drive frequencies for the pointing mode for each position in the field of view were formed by using a grid pointing algorithm I had developed to point sequentially an array of points in 3D space. The brightest pointing voxel was then chosen for each pinhole detector for 'random access' pointing testing. We found that using the grid pointing algorithm we could distinguish from the time sequences of pointing in say a 5x5 grid of miniscans whether there was any residual unwanted movement of the spot with time. I had incorporated parameters '*movex*', '*movey*' and '*astig*' into the program which fine tuned the ratios of X1:X2 drive frequency ramp rate, Y1:Y2 drive frequency ramp rate and mean X:Y drive frequency ramp rate respectively. Adjusting these eliminated drift of the spot in X and Y and corrected any

astigmatism respectively. These parameters did not have to be adjusted outside the range 0.98 to 1.02.

Figure 5.2b shows the results colour coded red, blue and green so that the detector signal can be seen for all three detectors in parallel. The sequence of pointing mode 'ramps' was then programmed to cycle round the three detectors in a range of 'random' orders and then repeat the original miniscan to check that there were no hysteresis or memory effect problems. The results show, that random access pointing and focusing in 3D was possible at 30 kHz total sample rate.

Since the time for any new acoustic waveform to fill the 15 mm aperture AOD is *AODfill* = 24 μs and we expected to gather data from the region of interest (ROI) for approximately a further T_{ROI} =9 μs, we expected that in use it would be feasible to jump from ROI to ROI at 1/33 μs= 30 kHz. Demonstrating this experimentally was an important first feasibility demonstration.

Examination of the blue and red traces (Z= +40mm and -40mm respectively) show that there is a sloping top to the light pulses into the detectors not apparent at Z=0 (green) trace. The apparent higher amplitude of the red and blue traces is a result of turning up the preamplifier gain more on these traces as there was less light and only step changes in gain were possible. Note the slope of the top of the blue and red traces is opposite in direction. After careful checking of the responses of adjacent voxels to check that there was no significant movement of the spot during this time, we concluded that these slopes resulted from changes in the overall efficiency of the AOL as the frequencies of all four AODs are scanned rapidly down in frequency (Z=+40mm) or up in frequency(Z=-40mm). This was the first measurement of the effect we now refer to as 'patternation' because it causes a patterning artefact on images using scanning mode. This effect is discussed further in this chapter and the next.

Correction of temporal dispersion

After confirming that the AOL was operating as expected we[10] aligned the necessary telecentric relays and mirrors to project the image of the last AOD onto the back

[10] The work in this section was carried out by K M N Srinivas Nadella.

aperture of the objective lens of the microscope so as to form the complete optical path of the AOLM system as shown in Figure 2.17 . The next step was to adjust the temporal dispersion compensation system described at the end of chapter 3 (Figure 3.31). In order to do this we used the Femtocontrol (http://www.ape-berlin.de) and Carpe Autocorrelator multipath unit inserted in the laser beam just after the laser itself and an autocorrelation monitoring head after the final objective. We then adjusted the prechirper to minimise the measured pulse length after the objective. The results are shown in Figure 5.3.

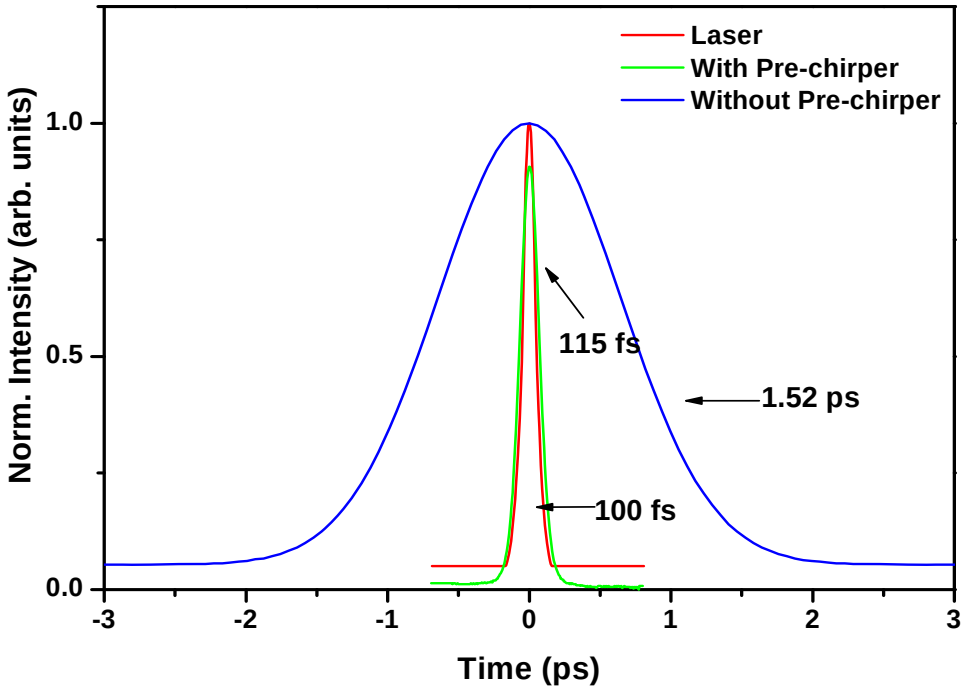

Figure 5.3 Experimental measurements of the laser pulse width at various positions through the system. The laser itself emits a stream of 100fs pulses (red). If this is passed through the complete system without the use of the prechirper the pulse width increases to 1.52 ps as measured beneath the final objective lens (blue). When the prechirper is introduced it stretches the pulse first in a negative direction so that when it subsequently propagates through the microscope it emerges after the final objective with only 115fs pulse width (green).

The results were very satisfactory. The pulse length on leaving the laser is 100fs, without any prechirper the large dispersion of the AODs and microscope optics spreads the pulse with to 1.52ps. The prechirper compensates well and reduces the pulse length back to 115fs after the objective.

Early 3D Imaging results using the AOLM

This section describes the main results we obtained when we first tested the complete AOLM, the 'pattternation' effects of variation of AOD efficiency on the image quality, and how we found that the field of view could be increased considerably and patternation reduced by changing from the absolute frequency limit (AFL) algorithm to the new optimised frequency limit (OFL) drive algorithm.

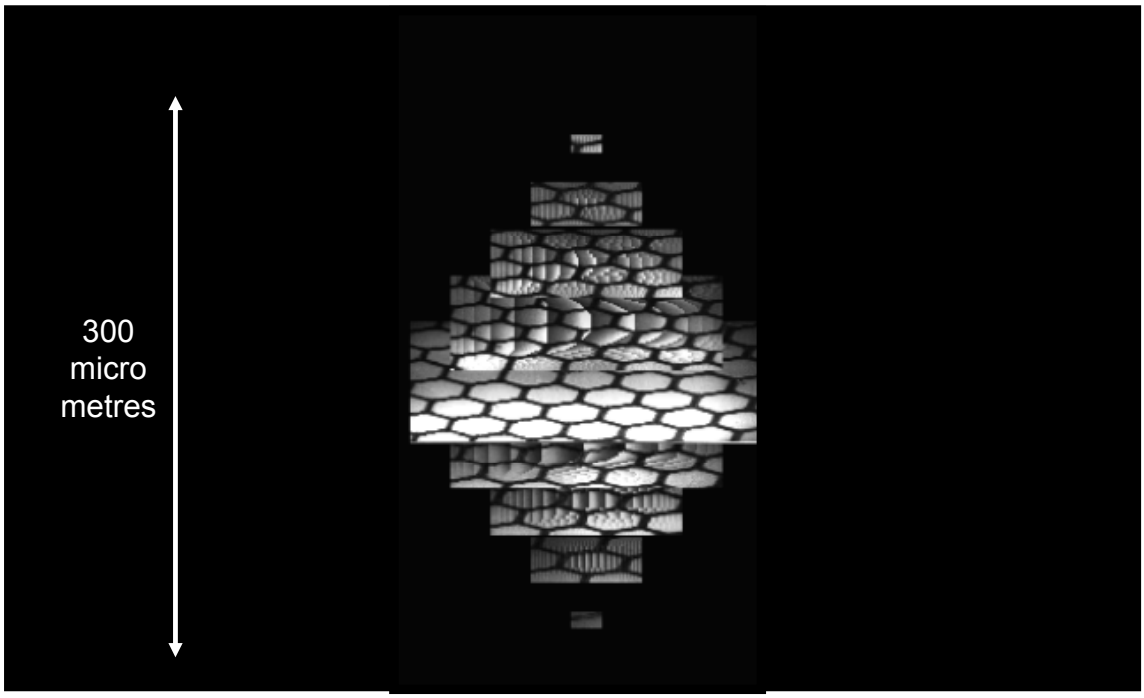

Figure 5.4 The complete field of view beneath an NA=0.47, 20X objective for the normalised Z range from -0.8 to +0.8 in steps of 0.2 and a semiscan angle s=4.3. The image is formed by 2-photon imaging with the beam scanning across a plastic luminescent slide (Chroma Technologies), above which has been placed a 42 μm pitch hexagonal electron microscope grid made of copper. This forms the hexagonal shadow pattern on the luminous background and allows the field of view to be measured accurately. The original AFL (absolute frequency limit) scanning program was used. For each 2D image plane the stage was moved mechanically to bring the image into focus at the Z focal plane defined by the AOD focal setting (Z axis).

One way of viewing the field of view and scan uniformity for the microscope driven by the AFL (absolute frequency limit) algorithm is shown in Figure 5.4 which shows the complete field of view beneath a 20X objective with an under-filled back aperture that resulted in an effective NA of 0.47. The measurements are for the normalised Z range from -0.8 to +0.8 in steps of 0.2. The overall pyramid shape and the large field of view are apparent beneath this 20X objective. Note that in the non Zn = 0 scan planes the miniscan pattern is very visible. We refer to this artefact as patternation. It is caused by variations in the 2-photon luminescence during the individual miniscans and is caused by changes in AOD efficiency with scan angle. It is most obvious in the

Zn = +0.2 plane where it can be seen in the wide miniscans near the centre of the field of view. The fluorescence is brightest at the right hand (trailing edge) of each miniscan. We have tried several approaches to solving the patternation problem. The most successful without altering the drive frequency algorithms was to monitor the light intensity variation of the particular miniscan pattern using an optical tap[11] on the scanned laser beam and large area silicon detector, and then use this monitored signal, suitably amplified and inverted, to modulate the Pockels cell of the microscope in anti-phase with the intensity variations. By adjusting the details of the transfer function of the amplifier, gain, offset, non-linearity etc, it was possible to minimise the observed patternation when the same scan pattern was reused. This produced our best early images of pollen grains at a variety of focal planes as shown in Figure 5.5. This figure is arguably showing clear images of pollen grains using AOD focusing at larger axial displacement than any others published to date. Nevertheless, careful examination of the images away from the Z=0 plane shows that there is still significant evidence of the miniscan pattern. It was very difficult to find one set of modulation parameters that compensated the patternation accurately over the whole field of view. However, before refining the techniques for compensating for patternation we decided that it was important to implement the Optimised Frequency Limit (OFL) algorithm so that for each miniscan we had chosen the drive frequency combination that gave the peak AOL diffraction efficiency and that that the peak efficiency would occur at the centre of each miniscan thus minimising the overall change in efficiency along the length of the miniscan.

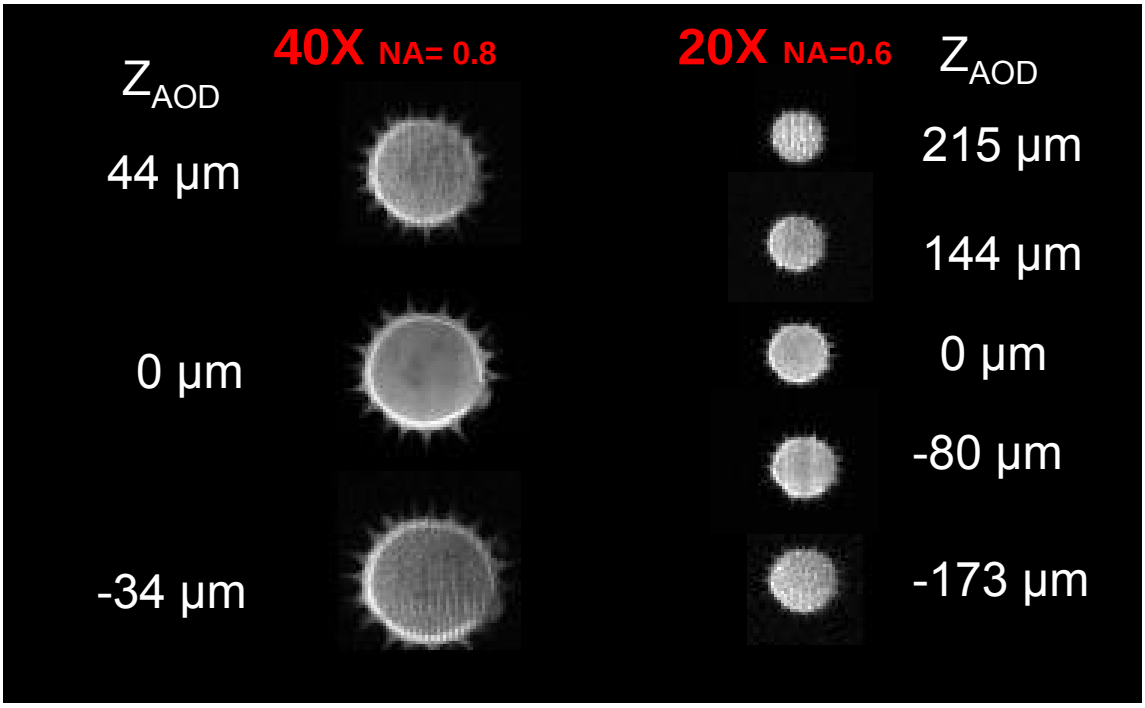

[11] The optical tap is formed by an 8% reflection 92% transmission pellicle set with its normal at 8 degrees to the main light path

Figure 5.5 Images of pollen grains using Pockels Cell modulation of the laser intensity to minimise patternation effects. The Z_{AOD} is the measured displacement of the focal plane of the objective by the AOL. This has been compensated by moving the equator of the pollen grain into clear focus by adjusting the height of the objective lens. These images used the original AFL dive algorithm and modulated Pockel's cell patternation compensation. The change in XY plane magnification with Z position results from imperfect adjustment of the telecentric relays connecting the AOL to the microscope. When the relay lens spacing is not perfect the relay is not exactly telecentric and this effect occurs.

Progress towards solving the patternation problem and extending the usable field of view

The progress we have recently made towards solving the patternation problem and towards significantly increasing the field of view is illustrated in Figure 5.6 and Figure 5.7.

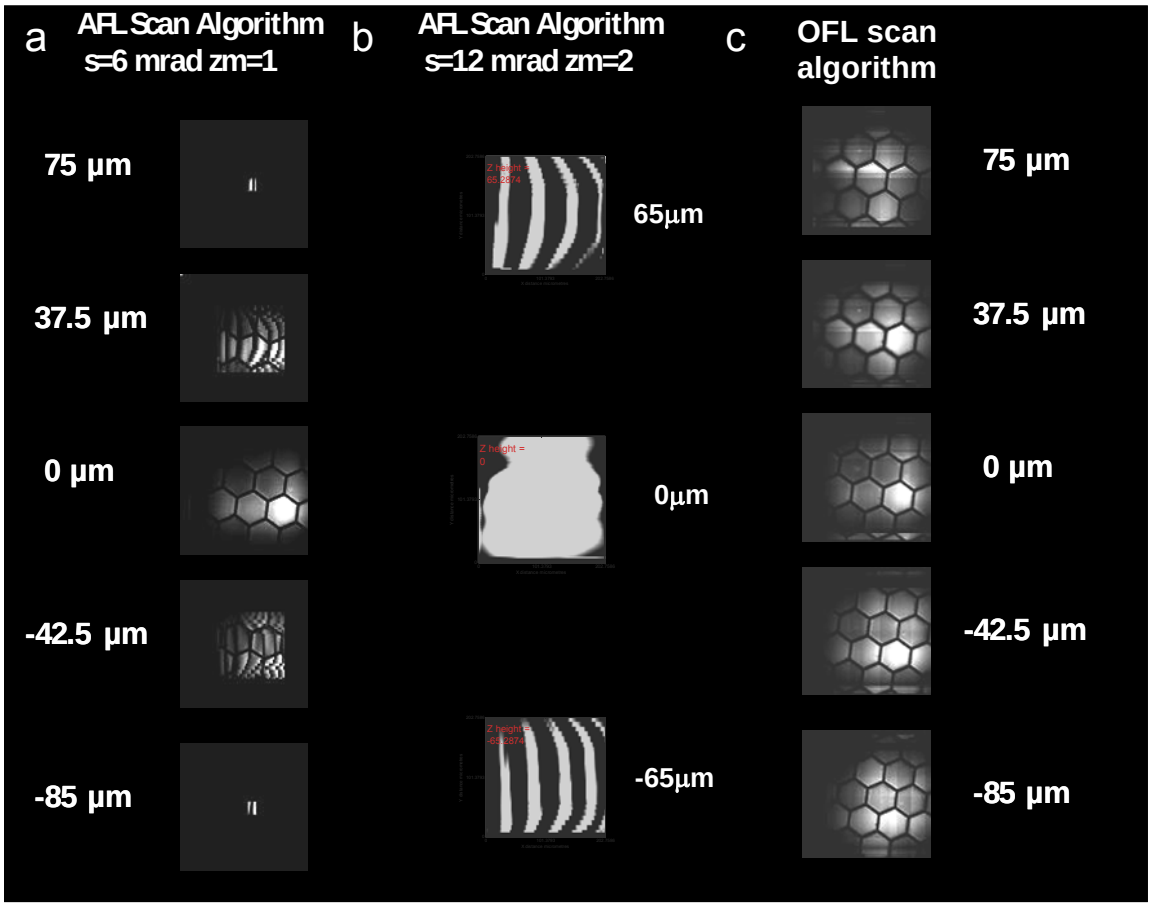

Figure 5.6 Comparisons of field of view beneath a 40X NA=0.8 objective using a) AFL (absolute frequency limit) scan algorithm with s= 6 mrad, b) AFL scan algorithm with s=12 mrad but zoom=2. c) OFL (optimised frequency limit) scan algorithm described in chapter 4, with a programmed semiscan angle of 6mrad. The field of view in each image 180µm (the electron microscope grid is 42 µm pitch).

Figure 5.6a) shows what happens if the semiscan angle, s, is increased to 6 mrad in order to increase the field of view beneath an NA=0.8, 40X objective using the old AFL algorithm. The characteristic programmed octahedral shape can be seen with very small scan area at large Z displacements in order to avoid the AODs going beyond their frequency limits. Note that the patternation in this image is much more pronounced than in Figure 5.4 because s = 6 rather than 4.3 mrad so the AODs in each miniscan are allowed to scan a larger frequency range. At both ends of each miniscan for Z= +37.5μm and -42.5μm the intensity of the 2-photon image drops significantly.

The image set in Figure 5.6b shows how the old AFL algorithm can be used to overcome the field of view (FOV) limits by doubling the scan angle limits and specifying *zoom*=2. This doubles the size of the octahedral FOV, but truncates the XY dimensions to the same 180 μm. It was this measurement that first showed that us high efficiency could be obtained over a large scan area at large axial displacements. The patternation with these conditions is however very severe because at the beginning and end of each miniscan the AOD frequency deviations are very large and the AODs are in very low efficiency regions. This produces the severe patternation shown at Zn = +/- 65 μm (There is no em grid on this set of images).

The results of the new OFL (Optimised frequency limit) algorithm set for the same XY scan coverage are shown in c). Note that the OFL scan algorithm is showing approximately constant scan area and clear images of the em grid over a 160μm axial range. The fading of intensity at the edges of the field of view is presumably caused by the severe chromatic aberration at these large XY deflections as well as reductions in the AOL efficiency.

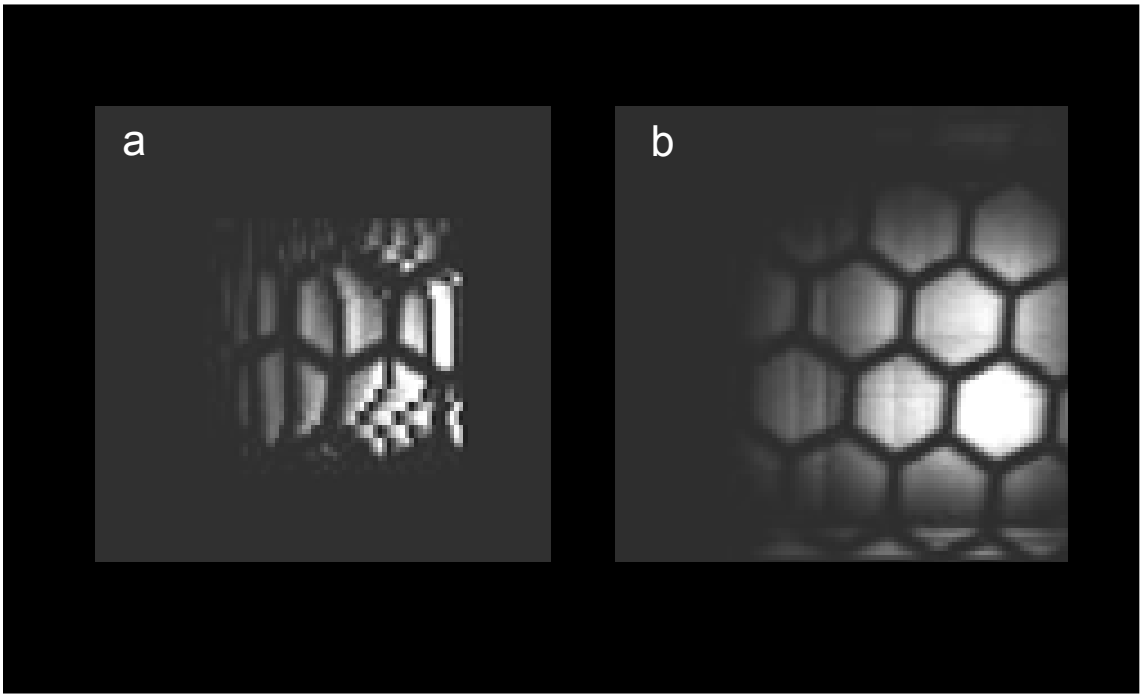

Figure 5.7 Magnified comparison of images from the previous figure, a) using the old absolute frequency limits (AFL) algorithm and b) using the new optimised frequency limits (OFL) scan algorithm. Both images measured at Z=-42.5 μm

A magnified view comparing images from the AFL and OFL algorithm at Z=-42.5 μm are shown in Figure 5.7. It is clear that good progress has been made in both extending field of view and in reducing patternation. However the OFL algorithm here is in its very first version (only just completed at the time of writing). The length of each miniscan is the same across the whole scan area and is a preset variable. These images have been set with individual voxels being the miniscan length which gives the slowest but least patternated images.

The slight tartan pattern on the image is caused by the fact that we used no drive amplitude or Pockel's cell compensation to the change in efficiency which occurs when the algorithm jumps from one high efficiency maximum to another as seen in Figures 4.10 and 4.11. Similarly we have made no attempt to compensate for change in efficiency across the field of view caused by variation in peak efficiency of each miniscan.

The field of view for the OFL algorithm compared to the AFL algorithm, for the same scan dimensions at Z = 0 is cuboid rather than octahedral and thus has approximately

3 times larger scan volume depending precisely on the limits to Z scan caused for instance by loss of resolution. This larger cubic field of view and reduced patternation is clearly a very useful basis for adding further improvements in the near future.

Latest Results with OFL algorithm for extending field of view

In order to test the limits of field of view and to obtain a first view of the image quality across the whole field of view with the new OFL algorithm a series of measurements were made on electron microscope (em) grids that had been coated with dye by immersion and drying three times in fluoroscein solution (Abbey Color). Fluoroscein is a fluorescent dye that works well with 2-photon excitation. The field of view was measured beneath 20X, 40X and 60X objectives. Note that these measurements were taken after the improvements to the precision of the AOD mounts described in the following section on point spread function measurements.

Experimental results using a Fluorescent Grid

The next three figures, Figure 5.8 to Figure 5.10 show the results for these three objectives with the OFL algorithm set for 3,6 and 9mrad.

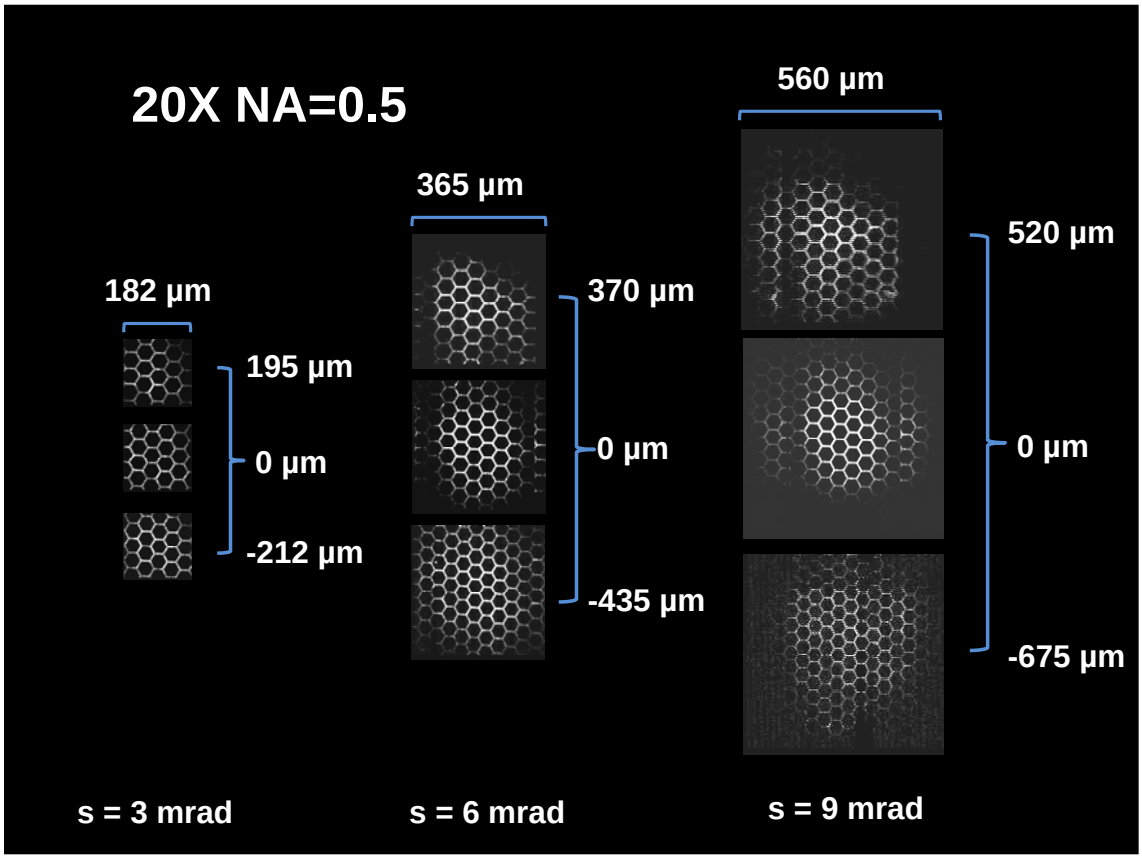

Figure 5.8 Images of a fluoroscein (AbbeyColor) coated electron microscope grid beneath a 20X objective with a nominal effective NA of 0.5. This uses the new OFL algorithm at semiscan angles s = 3, 6 and 9 mrad. Before taking each image, the grid is brought into focus by moving the grid with respect to the objective and noting the axial displacement required. The full image width and axial (Z) focal plane displacements shown are the experimental measurements for each image. The variations in background black density in these images is a result of manual contrast adjustments to individual images prior to combining them in this figure and has no great technical significance.

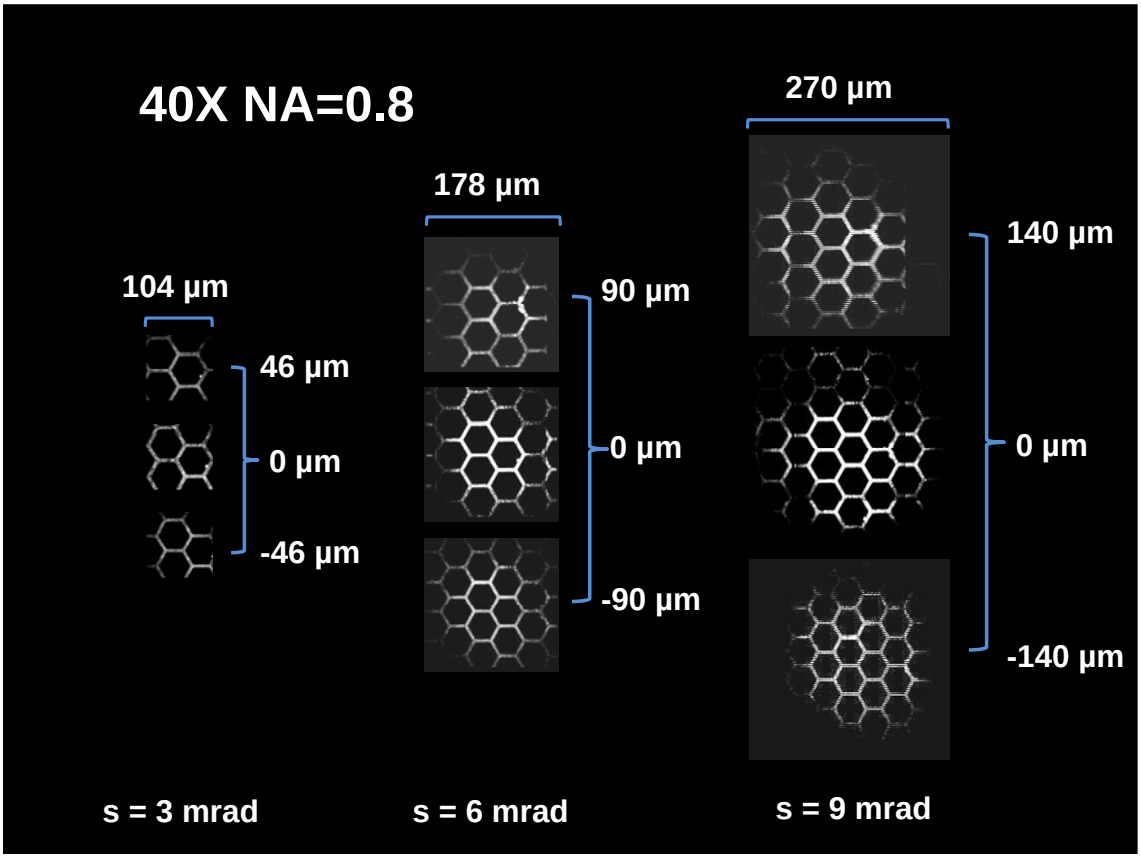

Figure 5.9 Images of a fluoroscein (AbbeyColor) coated electron microscope grid beneath a 40X objective with a nominal effective NA of 0.8. This uses the new OFL algorithm at semiscan angles s = 3, 6 and 9 mrad. Before taking each image, the grid is brought into focus by moving the grid with respect to the objective and noting the axial displacement required. The full image width and axial (Z) focal plane displacements shown are the experimental measurements for each image. The variations in background black density in these images is a result of manual contrast adjustments to individual images prior to combining them in this figure and has no great technical significance except, as you might at expect at higher NA where spherical aberration effects become more significant, the extreme displacement images are inherently lower contrast to start with.

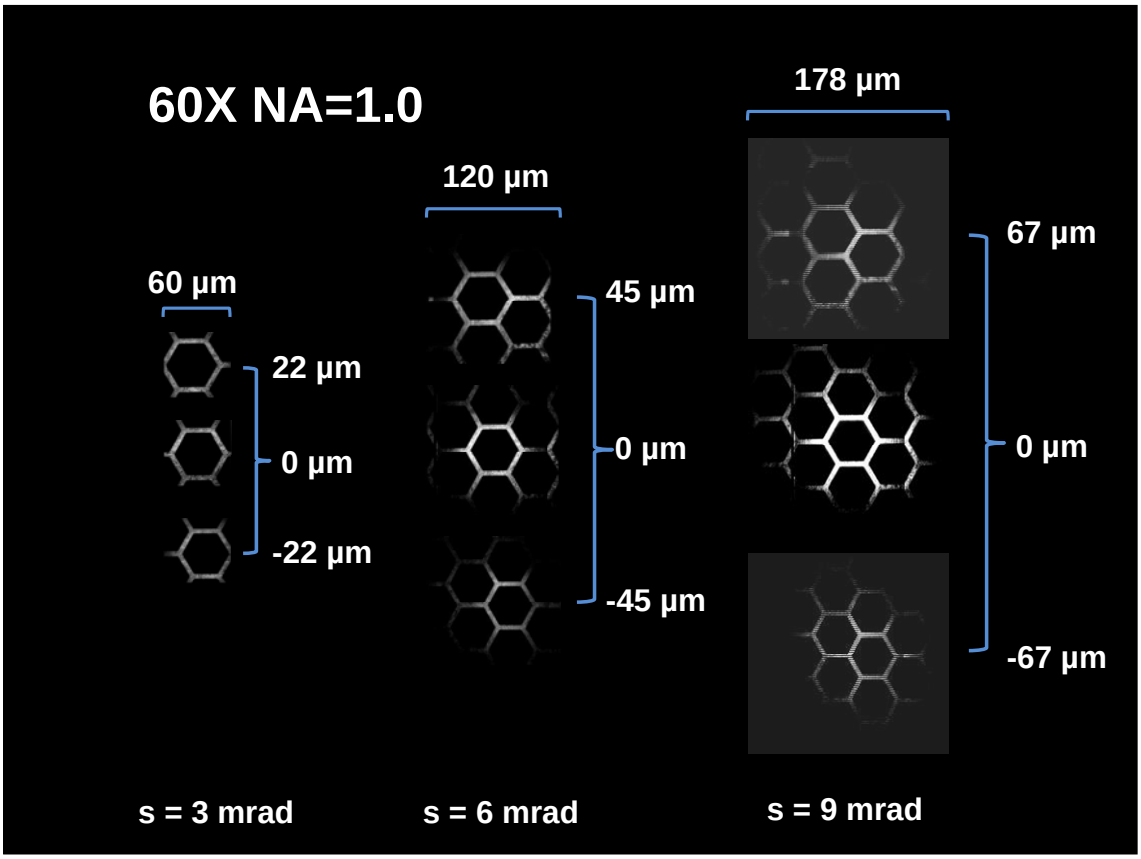

Figure 5.10 Images of a fluoroscein (AbbeyColor) coated electron microscope grid beneath a 60X objective with a nominal effective NA of 1. This uses the new OFL algorithm at semiscan angles s = 3,6 and 9 mrad. Before taking each image, the grid is brought into focus by moving the grid with respect to the objective and noting the axial displacement required. The full image width and axial (Z) focal plane displacements shown are the experimental measurements for each image. The variations in background black density in these images is a result of manual contrast adjustments to individual images prior to combining them in this figure and has no great technical significance except, as you might at expect at higher NA where spherical aberration effects become more significant, the extreme displacement images are inherently lower contrast to start with.

The results shown in Figure 5.8 to Figure 5.10 are all at a number of voxels of *Nvox* = 200 covering the whole field of view in each case. At this resolution it appears to the eye that the imaging quality is not varying very significantly over the whole field of view for all three semiscan angles s = 3, 6, 9 mrad. At s = 9 mrad, it is interesting to note that for the 40X NA= 0.8 lens the field of view comes close to covering the target field of view of 250×250×250µm.

Close examination of the figures shows additional points. In all cases the brightness of the images fades towards the edges of the field of view particularly for s = 9mrad. The fading is least for the 20X objective and most for the 60X objective. This is presumably because of the effect of chromatic (and maybe other types of) aberration increasing at the edges of the FOV in each XY plane in addition to any drop off in AOL efficiency. It will be very interesting to repeat these measurements with the chromatic aberration correction in place. It is noteworthy that the image quality is not dramatically reducing at least at this voxel density (200 x 200 voxels in this image) with the large axial range tested. It is perhaps surprising that spherical aberration has not degraded the high axial displacement images much more significantly. More detailed high resolution images and point spread function measurements are needed to clarify this issue.

Another point worth noting is that there is a small increase in XY plane magnification as the axial focus is changed from maximum negative to maximum positive. The lateral magnification is 9% greater at normalised Z = +1 compared to Zn=0 and 9% smaller at Zn = -1. This is a small effect compared to that visible in Figure 5.5. This shows that there is still a lack of exact telecentricity that can be corrected by further adjustment of the position of lenses in the telecentric relays between the AOL and the objective. Prior to this measurement we adjusted telecentricity using the AFL algorithm and we had insufficient FOV at large axial displacement to give sufficient accuracy of the magnification to notice this small residual degree of lack of telecentricity.

Comparison of measured 3D field of view (FOV) with theory

These measurements on fluorescent grids included measurements of FOV and axial displacement for all values of normalised axial displacement Zn = -1,-0.8..., step = +0.2, ..., 1.0 for all semiscan angles s = 3,6,9 mrad.

It is useful to compare these experimental measurements of field of view with the theoretical derivation of Chapter 2. The theory shows that in the idealised perfectly telecentric model the XY plane and axial ‘Z’ field of view are dependent on the AOD width ‘W’ and semiscan angle ‘s’ and the effective NA of the AODs viewed from the final focus. If the telecentric relays linking the AOD to the objective are not perfectly

adjusted then NA varies with Z focal plane and a more elaborate theoretical model is needed to correctly fit the nonlinearity of Z displacement vs. 'Zn' (the normalised Z displacement used for calculating the AOD drive parameters.)

We first measured the width of the projected image of the final AOD on the back aperture of the objective lens. Within the accuracy of our measurement, the telecentric relay chain magnifed the 15mm AOD aperture by 0.6 to 0.66 times giving a projected back aperture width of 9-10mm. If the exact focal length of the water immersion objective is known, this back aperture width can be used with the basic equation NA=$n \sin(\theta)$ to calculate the effective NA of the objective relevant for calculating FOV.

The three water immersion objectives we used in these tests were Olympus 20X, NA=0.95, 40X, NA=0.8, and 60X, NA= 0.9. The Olympus Website (http://www.olympusmicro.com) states that the focal length of the objective is their standard microscope tube length, 180mm, divided by the objective magnification. Using this information with the projected width of the AODs at the objective back aperture allows the effective NA of the AOLM to be calculated for each objective. Assuming W = 9mm, the calculated figures are 20X, NA=0.47, 40X, NA=0.80, 60X, NA=1.0. The fact that the effective NA of the AOLM at 60X is larger than the actual NA (1.0 cf. 0.9) simply means that the physical back aperture of the 60X objective will cut off the outer edge of the projected AOD aperture. That is to say the objective is slightly over filled. This was confirmed by checking the actual physical back aperture of the lens was 7.3 mm as calculated for NA=0.9. Note that it is the effective NA calculation that is relevant to FOV calculations as the physical aperture will not change the angles of the incoming rays, just cut off rays at the outer edge of the cone and thus reduce image brightness and resolution.

In Figure 5.11.The theoretical plot of XY field of view (blue lines) at semiscan angles of 3, 6 and 9 mrad of Figure 2.13 is compared to the actual field of view measurements at these calculated values of effective NA (red dots).

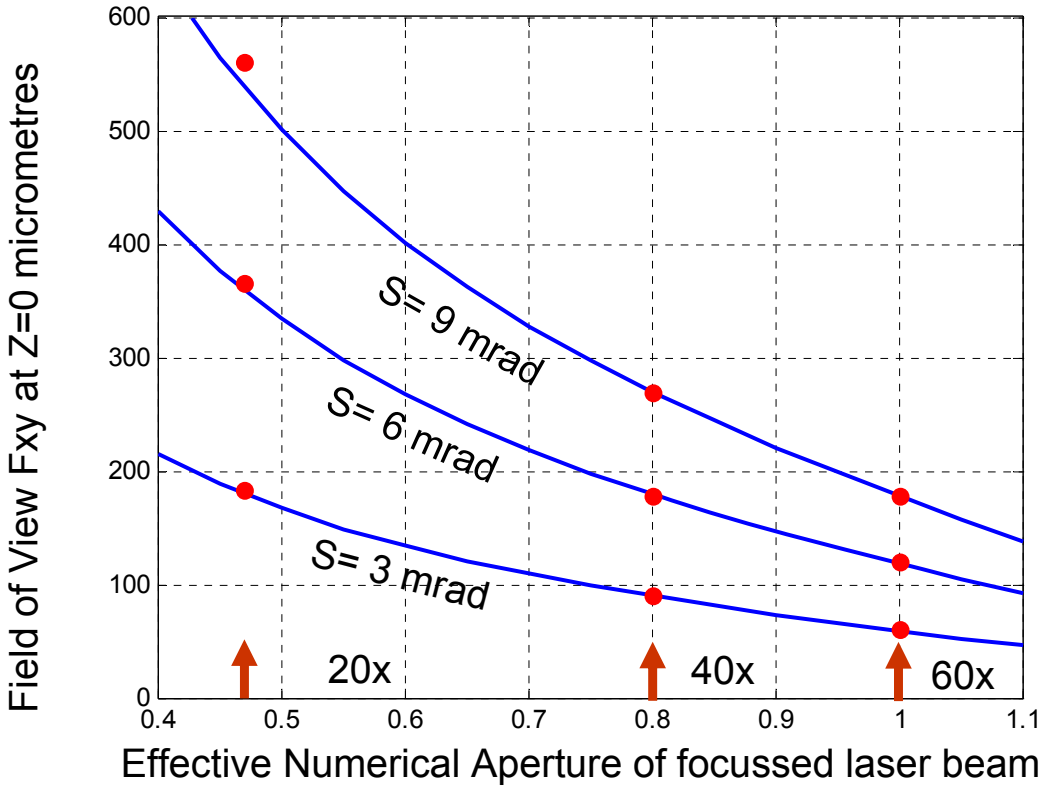

Figure 5.11 Experimental measurements of X (and Y) field of view (red dots) plotted for comparison with the theory of equation 2.8 and Figure 2.13. (solid blue lines) the theoretical plot shows that the FOV for a particular scan angle is inversely related to the objective NA. W= 15mm. Also shown on the diagram is the magnification of the Olympus objective lenses we evaluated. Data points have been added at NA =0.47, NA=0.8 and NA=1.0 as these are the values of effective NA of the AOLM that give the best fit and are also consistent with a projected width of the AOD image on the back aperture of the objective of 9.0 mm.

It is clear from these results that assuming W = 9mm, there is very good agreement between the theoretical and experimental XY plane field of view at Z=0 using all three objectives at all three semiscan angles.

The results for axial displacement are plotted in Figure 5.12 and compared to the theory from equation 2.10. In this case, using the same set of effective NA values for plotting the comparison of theory with experiment, the fit was not so good. The fit is much better assuming W = 9.8mm which results in NA = 0.50, 0.84 and 1.03 for the 20X, 40X and 60X objectives respectively.

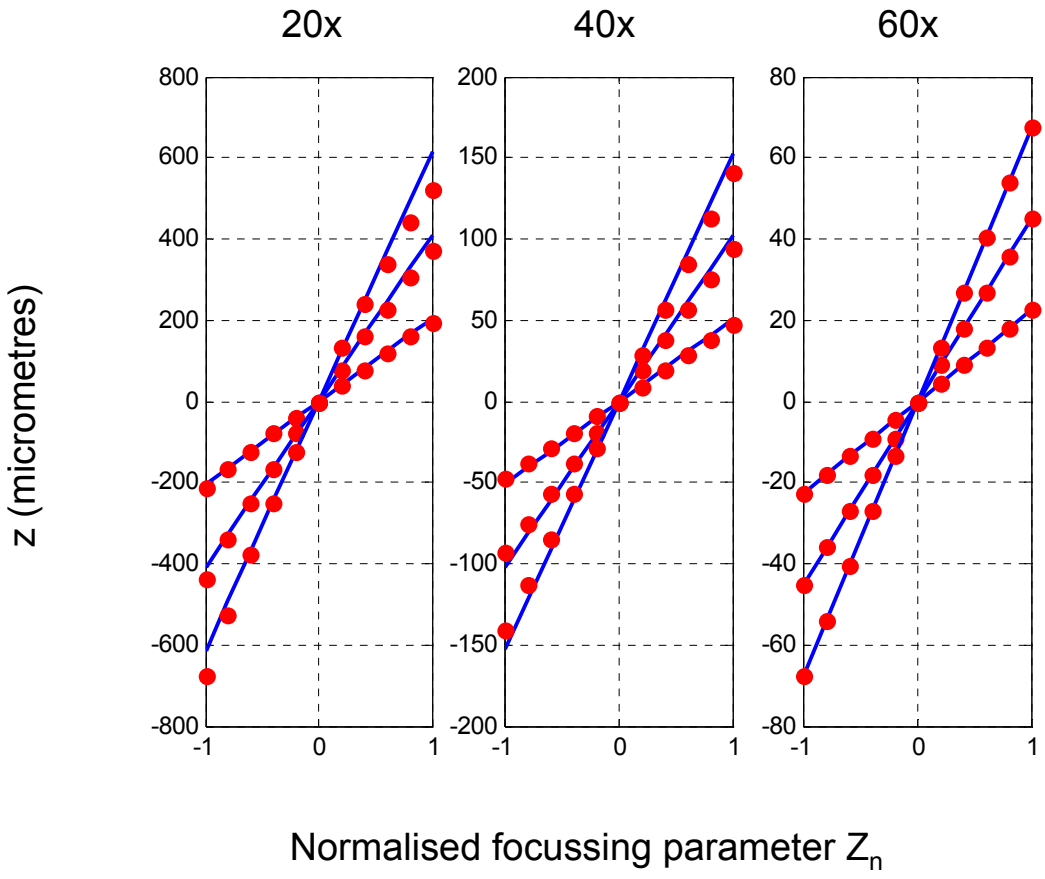

Figure 5.12 Experimental measurements (red dots) of the Z axis displacement as a function of normalised focusing parameter Zn for three final objectives. The solid black line is the theoretical displacement calculated by equation 2.10 for the NA= 0.50, 0.84 and 1.03 for 20X, 40X and 60X objectives respectively. These values of NA are consistent with a projected width of the AOD image on the back aperture of the objective of 9.8mm. For each objective the displacement is calculated and experimental results plotted for semiscan angles, 3, 6 and 9 mrad.

So the comparison between theory and experiment of Figure 5.11 and Figure 5.12 both show good fit of theory to experiment assuming that the width of the projected image of the AOD on the back aperture lies in the range 9-10mm consistent with the limited accuracy of our experimental measurement.

However the best fit is found assuming W= 9.0mm for the XY plane field of view and W = 9.8mm for the axial field of view. This is a 9% discrepancy. I am confident that this discrepancy is simply caused by the imperfect telecentricity of the relays linking the AODs to the back aperture. The 9% increase in magnification when the normalised Z parameter Zn is increased by 1 apparent in Figure 5.8 to Figure 5.10 is obviously caused by a diverging field of view; the magnification of the final image produced by the microscope reduces as the focal plane of the AOLM moves away

from the objective lens. This divergence will also cause the field of view at Zn = 0 to be greater than it should be and a nonlinearity in Z displacement vs. Zn. This divergence would certainly cause discrepancies in the best fit values of W between XY plane and axial Z measurements using the telecentric equations that are similar to those observed here.

It is clear that the next stage of work in this area is to repeat the experiment with more accurate adjustment of the exact telecentricity and perhaps to derive the precise field of view equations under conditions of non exact telecentricity and refit the data presented here.

From the perspective of the overall project however these results nevertheless confirm that the theory is accurate within 9%, and that the new OFL algorithm scans the beam over a field of view that is close to the target 250×250×250 μm for semiscan angle s = 9 mrad beneath an objective with approximately 0.8 effective NA. As expected from the chromatic aberration theory, there is significant fading of 2 photon imaging brightness at the edges of the field of view.

Latest results of OFL algorithm for pollen grain imaging over a large axial range

To get a first view of the image quality at higher zoom over the much larger axial ranges possible with the OFL algorithm we took images of pollen grains with the AOLM focusing covering the range of normalised Zn = -0.8, 0, 0.8. The results are shown in Figure 5.13 and Figure 5.14 for semiscan angles of s = 6 and 9 mrad respectively.

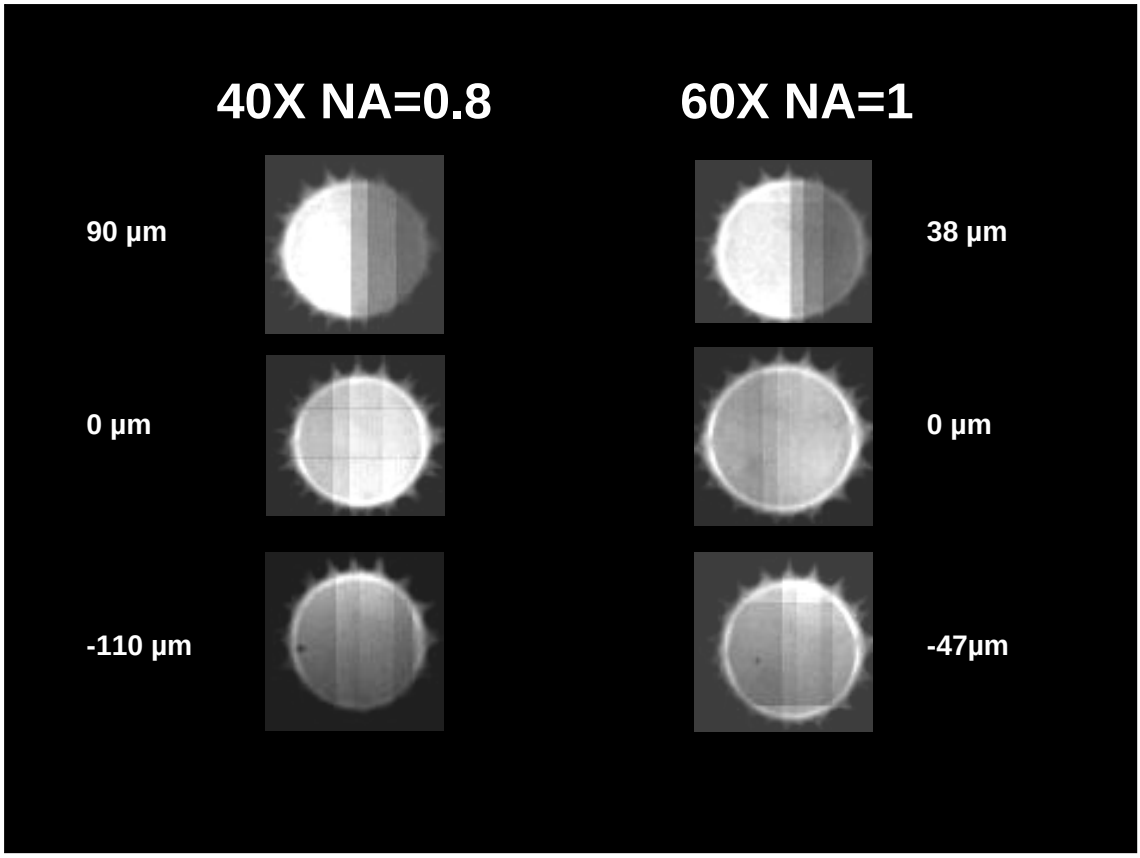

Figure 5.13 Images of pollen grains with the new OFL algorithm for 40X and 60X lenses. Pollen grain axial position adjusted so that an equatorial section is taken in each case. Figures correspond to the axial displacement of the focus of the AOLM from the natural (Zn=0) plane. Semiscan angle s = 6 mrad, *Nvox* = 100, No. of frames = 16, Zn = 0.8, 0, -0.8. Zoom adjusted to give 40-45 µm square image size.

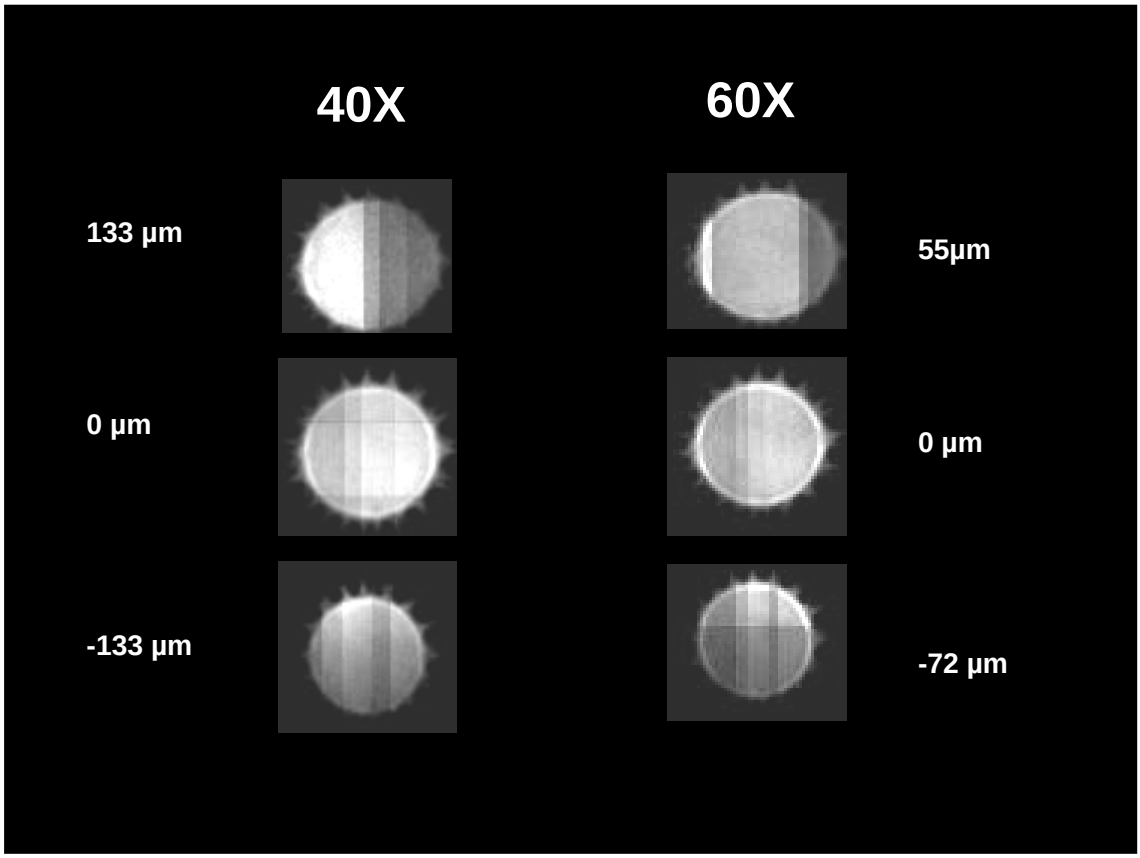

Figure 5.14 Images of pollen grains with the new OFL algorithm for 40X and 60X lenses. Pollen grain axial position adjusted so that an equatorial section is taken in each case. Figures correspond to the axial displacement of the focus of the AOLM from the natural (Zn=0) plane. Semiscan angle s = 9 mrad, *Nvox* = 100, No. of frames = 16, Zn = 0.8, 0, -0.8. Zoom adjusted to give 40-45 µm square image size.

These results show the spines of the pollen grains moderately clearly over more than a 250 µm axial range beneath the 40X NA=0.8 lens and more than 120 µm axial range beneath the 60X NA=1.0 lens.

This is very encouraging as it implies that the XY plane psf is probably sub micron in dimensions over this large axial range even at NA=0.8. If confirmed by bead measurements this is an important aspect of meeting the target specification. The tartan patternation is again caused by jumps between high efficiency regions using the OFL algorithm. So, although there is further work to do to minimize patternation, the OFL algorithm with no correction or compensation appears to be successfully optimizing the frequencies for all four AODs so the miniscan reaches maximum brightness possible at the centre voxel of each miniscan.

The OFL algorithm is therefore a good basis to start controlling spot intensity to minimize patternation. It is also clearly worth while to now carry out detailed point spread function measurements with this arrangement. We have not been able to do this prior to PhD thesis submission so the psf data in the next section is earlier data using the old AFL algorithm.

Measurements of point spread functions (psfs) – comparison with theory and the development of new crystal mounts

This section describes the experimental measurements we have made on the point spread function of the microscope. The results of this section were obtained before we developed the OFL algorithms and for Figure 5.15 to Figure 5.19 before we upgraded the precision of the crystal mounts. The results in this section are considered chronologically in order to explain how we understood the main aberrations we observed in our first point spread function measurements. It explains why we introduced the new crystal mounts, reports first psf measurements with the new mounts, and finally, why these measurements showed even more strongly the necessity of developing the OFL algorithm.

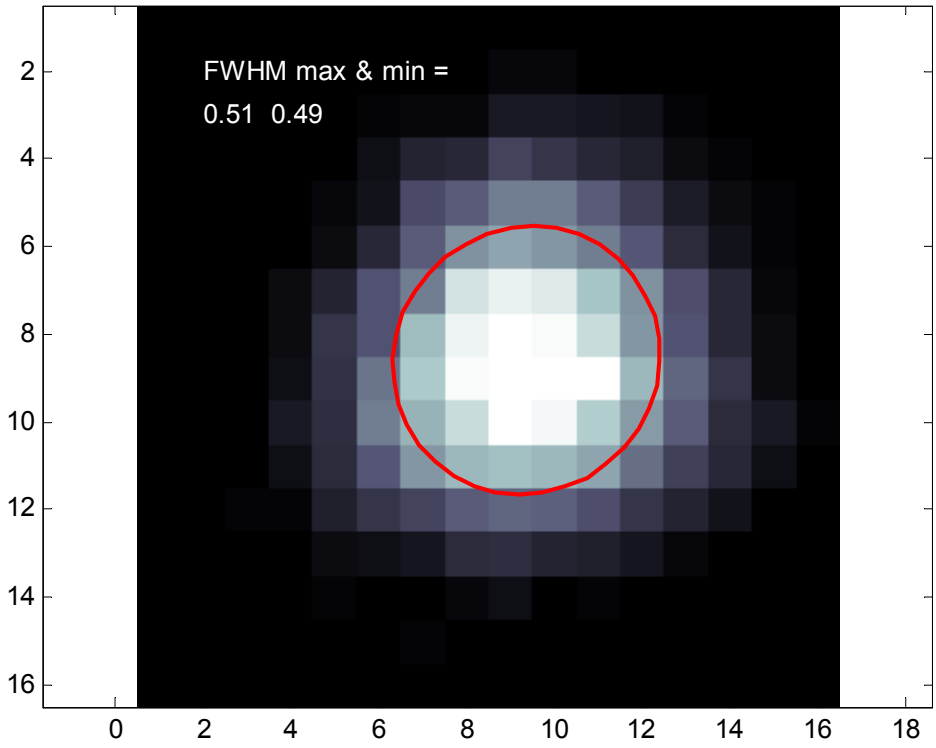

Figure 5.15 An example of an experimentally measured XY plane section through the beam waist of the 2-photon point spread function (psf) beneath a NA=0.8 40X lens. The red line is the full width half maximum (FWHM) of an elliptical Gaussian intensity distribution that is a least squared error fitted to the experimental distribution. This psf was measured close to the centre of the field of view at Zn=0 using 0.2 µm fluorescent beads. The full width half maximum of the psf is 0.49 by 0.51 µm. This compares to the theoretical value of 0.42 µm using equation 3.1 and assuming the bead had a Gaussian profile of FWHM 0.2µm.

In order to measure the point spread function (psf) of the microscope and compare the results with theory, we used the techniques and equations described in Chapter 3 'Derivation of resolution of microscope...'.

Fluorescent beads were dissolved in agar so that beads could be found at sufficient density all over the field of view. Each bead was measured by imaging at high zoom factor over a stack of Z planes usually at least 30 Z planes deep covering about 2-3 times the depth of an individual axial point spread function. We empirically adjusted the agar bead density so that there were between two to five beads visible in any XY plane at sufficiently high zoom to get eight or more voxels between the FWHM points

of the approximately Gaussian intensity distribution. This is to get sufficiently high number of good quality single beads to be able to unambiguously measure their psf dimensions and to ensure that the measurements are above the Nyquist sampling limit and not subject to sampling errors. All psf measurements to date have been done with the old AFL algorithms.

At high zoom and strongly focusing or defocusing Z planes there are still many miniscans in the field of view, so it is important to carefully adjust the fine tuning parameters '*movex*', *movey*' and '*astig*' to minimise any psf astigmatism and ensure that the miniscans line up precisely and a good quality image of the cross section of the experimental psf can be reconstructed.

It is also important to be able to accurately measure the dimensions of the psfs. We started using commercially available curve fitting routines, but soon found that they were slow and did not quite measure what we were interested in. I have therefore developed MatLab code that measures the key parameters. I made this code progressively more and more automated as the labour involved in analysing large volumes of data became more and more apparent to me.

Figure 5.15 shows the experimentally measured psf of a 0.2 μm fluorescent bead close to the centre of the field of view of a 0.8NA, 40X objective. The red line is the full width half maximum (FWHM) of a Gaussian elliptical function least squared fitted to the experimentally measured data. It is important to fit with an elliptical rather than circular Gaussian function so that psfs suffering from astigmatism and chromatic aberration can be measured. In this case the psf is very nearly circular and close to 0.5 μm in diameter. This is slightly larger than the theoretically expected (equation 3.1) experimental value of 0.42 μm for this NA (0.8) and bead size (0.2μm).

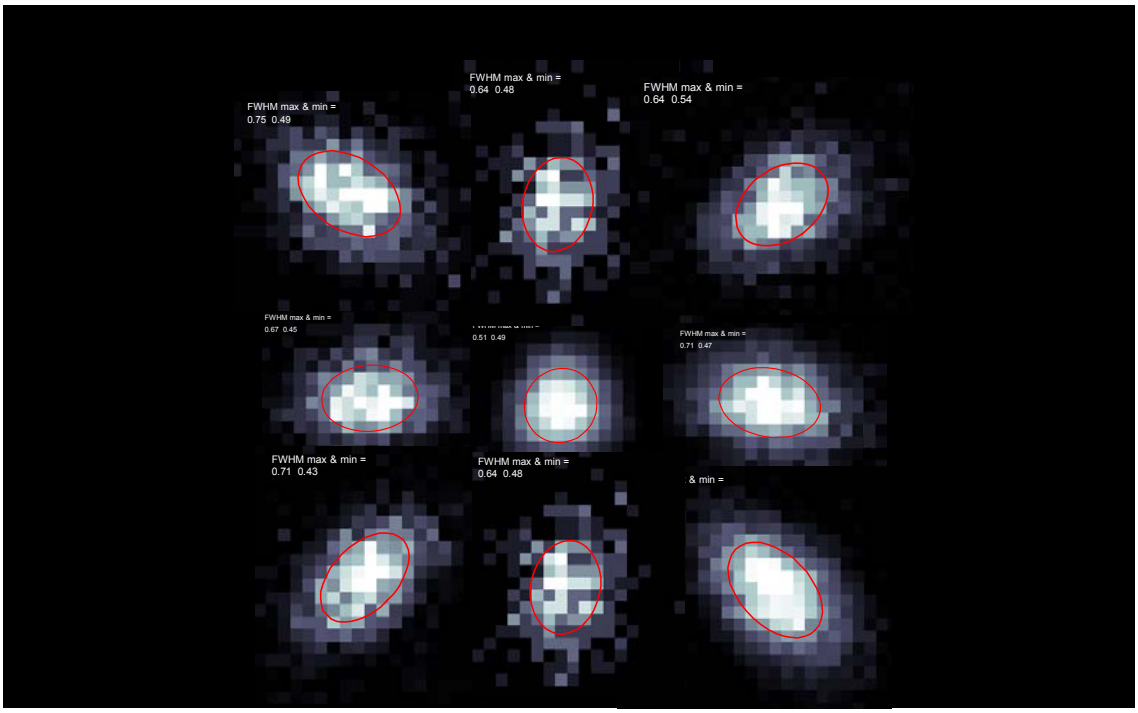

Figure 5.16 A composite image of nine psfs distributed across the XY plane at Z=0 on a grid of pitch 52μm centred at X = Y = 0. Note that as expected the chromatic aberration is approximately radial and centred on X = Y = 0. The minimum psf width for these is in the range 0.43 to 0.59 micrometres, the maximum for the psfs on the X and Y axes away from X = Y = 0 is in the range 0.58 to 0.71 μm (c.f. 0.59 μm in theory from equation 3.1) whilst the diagonal corner psfs have maximum FWHM in the range 0.64 to 0.78 μm (c.f. 0.74 μm in theory from equation 3.1).

The next measurements we made were of the psfs in the XY plane at Z = 0. Figure 5.16 shows that the experimental results have approximately the theoretically predicted shape and orientation of chromatic aberration induced lengthening of the psfs as radius from the centre of the FOV is increased. These measurements were on the standard microscope with no chromatic aberration correction. The theory used for the comparisons described in the caption is from chapter 3, Figure 3.20, equation 3.1.

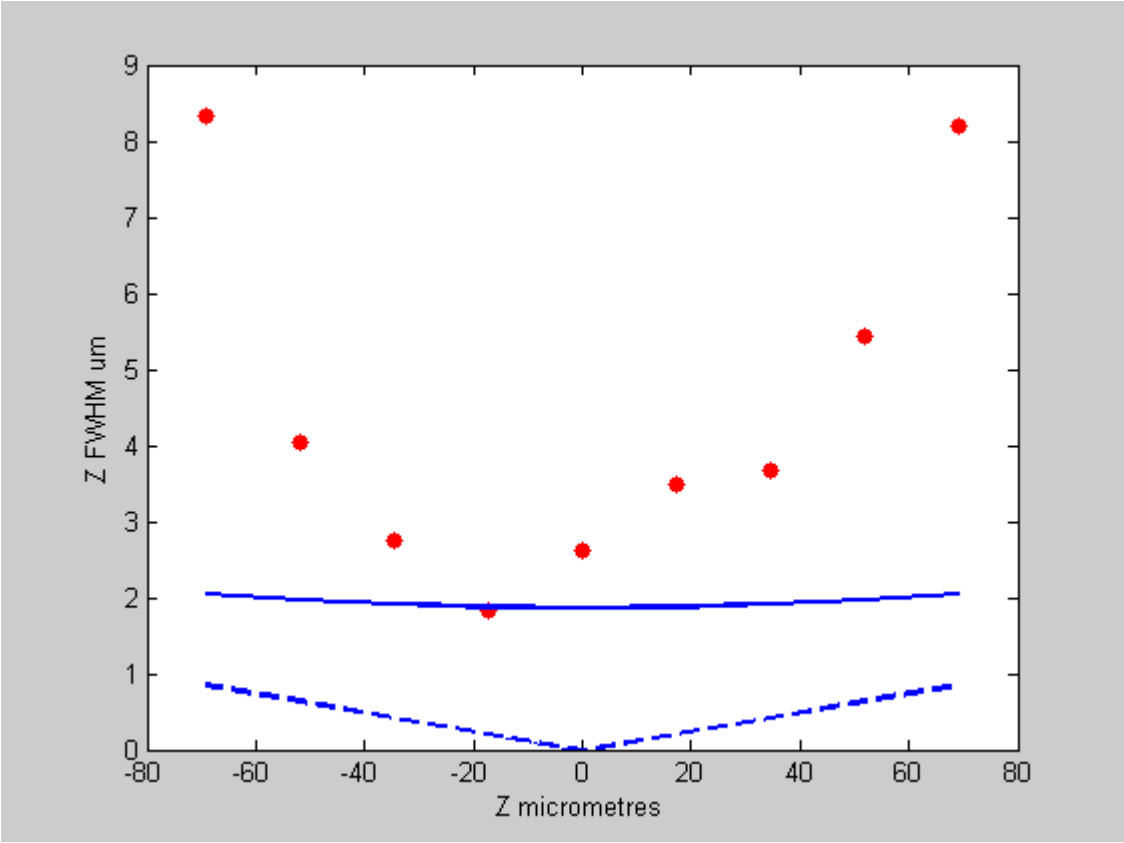

Figure 5.17 First experimental measurements (red dots) of the Z psf as a function of Z displacement from the natural focal plane of the lens. The results are for a 40X lens at NA=0.8 with semiscan angle s= 4.3 mrad using the AFL algorithm for scanning. The solid blue line is the calculated Z psf according to equation 3.2 assuming there is chromatic aberration but no spherical aberration. The dashed blue line is the theoretical axial chromatic aberration alone with FWHM spectral width of 10.6 nm for the laser spectrum.

The first axial (Z) direction psf measurements we made are shown in Figure 5.17. The laser was scanned using the AFL algorithm which has an octahedral field of view with the greatest Z depth along the X,Y= (0,0). The red dots are the experimental results from least squares fitting to the Z profile of the average intensity across an XY region of interest of approximately 0.7 x 0.7 μm centred on the highest intensity point of the distribution. The Z-stack bead images were chosen visually from those recorded as representative and artefact free.

The results show less than 4 μm Z psf over a Z depth of about 80 μm. The comparison of the results with the theory show only one of the points, a Z= -20 μm is on the theoretical line, with the Z psf increasing rapidly over the +/- 40 μm from the minimum. The increasing Z psf with focusing away from the minimum, in this case,

cannot be explained by chromatic aberration. The theoretical Z psf depth, plotted as the solid blue line is the convolution of the psf at the centre of the field of view with the theoretical chromatic aberration plotted by itself as the dashed line below.

Initially we assumed the discrepancy must be the spherical aberration from the objective. However careful examination of the Z stacks showed that the psfs in fact had the classic symptoms of astigmatism. That is to say, as the XY plane cross section of the focal spot is scanned through the focus, although there is a minimum circular radius at the focus, there are axially displaced elliptical foci that have narrower short axis radii equally spaced in Z on either side of the circular focus. The ellipses are orthogonal to one another in the XY plane. This residual astigmatism, after electronically correcting for any astigmatism perpendicular and parallel to the X axis using the '*astig*' fine tuning parameter, was at 45 degrees to the X and Y axes. The astigmatism increased approximately linearly with distance of the AOL Z focal plane from the natural focal plane at Z = 0, and changed sign at Z = 0.

We spent several months identifying the cause of this astigmatism and eliminating it. I will summarise the main steps here, but not show all the details as we eventually proved experimentally that the astigmatism could be reduced below our current experimental measurement capability simply by much more precise orthogonal alignment of the deflection axes of each AOD crystal.

Briefly I found by modelling the system in Zemax that I could reproduce these details of the astigmatism by simply assuming that the crystals were axially misaligned by spiral rotation about the Z axis of each AOD in turn by angles of up to a couple of degrees or so. Initially I had several potential theories as to the cause of the experimentally observed astigmatism, including potential subtle effects caused by different optical path lengths for light taking left hand as opposed to right hand spiral paths through the AOD crystal. (Zemax does not have the capability to model optical activity). I 'invented' and tested in Zemax, a way of compensating for the varying astigmatism with Z focus position. Using Zemax modelling I proved that a pair of optician's astigmatic test lenses could compensate the AOD twist induced astigmatism for all AOL Z focal planes. I ordered suitable lenses and inserted them in one of the existing telecentric relays and remeasured the Z psfs. After carefully

aligning the weak astigmatic lenses we could minimise, but not completely eliminate the astigmatism for all Z focal planes of the AOL. The resulting psfs are shown in Figure 5.18. They are measured both in the XY plane and along the Z axis as a function of position along the Z axis at X,Y= (0,0).

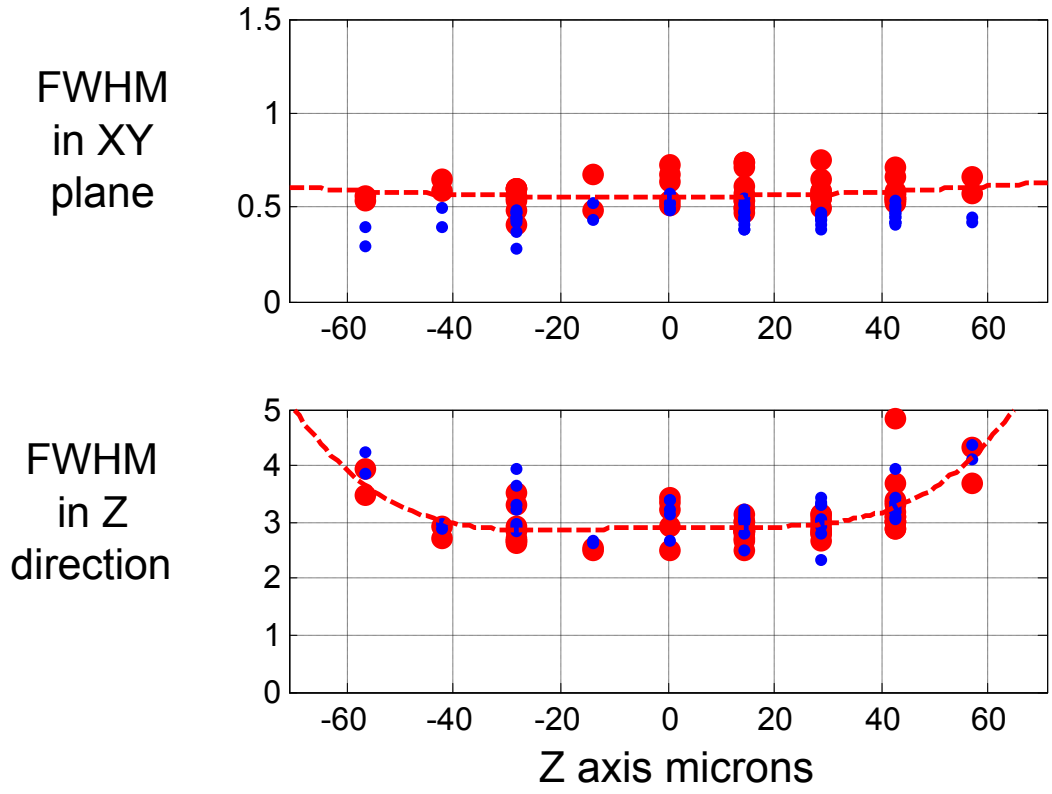

Figure 5.18 First automated measurement of XY and Z psf FWHM dimensions beneath a 40X NA=0.8 lens. Units are all μm . All measurements are made close to the Z axis X,Y=(0,0). The upper trace is long (red) and short (blue) axis of the 2-photon beam waist ellipse plotted against the Z axis coordinate of the bead concerned. For the Z axis the red dots are Z psf FWHM averaged over a region of interest of 10×10 pixels centred on the bead, the blue dots are averaged over the central 2×2 pixel region. The semiscan angle is 4.3mrad using the old AFL scan algorithm. These results show less than 0.6×0.6×3.5 μm psf over the central 100μm depth of field. The AODs were not perfectly axially aligned and the dominant astigmatic aberration limiting Z psf in the previous figure had been compensated to some extent by weak astigmatic correction lenses.

These results were encouraging as they showed it was possible to get less than 0.6×0.6×3.5 μm psf resolution over 100 μm of Z depth beneath an NA=0.8 lens and that the residual astigmatism of the AOL could be at least approximately post compensated.

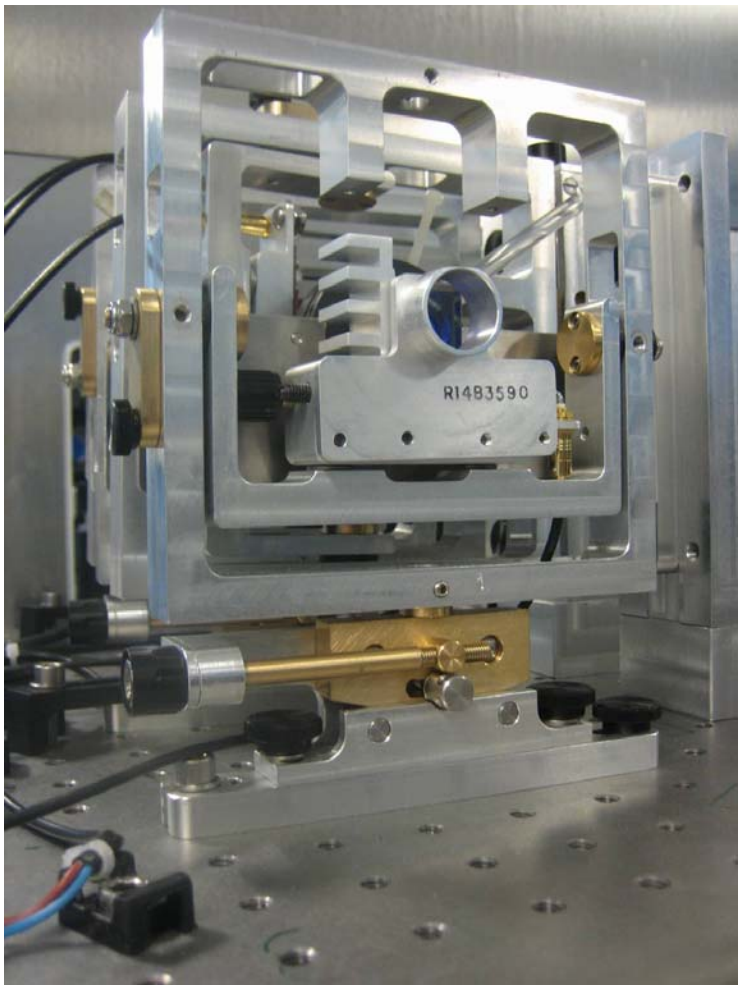

Figure 5.19 New mounts for the AODs with independent fine control of axial (Z axis) rotation about the centre of the crystal using the brass lead screw visible underneath the main frame. Rotation about the horizontal X axis uses the next half frame in whilst rotation about the Y axis to control the Bragg angle has a course manual setting about the clamped support mount just above the brass lead screw, and a fine lead screw control close to the crystal and not visible here[12].

We had, however, also set in motion the alternative improvement to the AOL design which was to introduce a fine axial angle control to each AOD. This is mechanically quite difficult to do, because we wanted the rotation about all three axes centred on the crystal. A photograph of the new mounts with independent lead screw controlled axial (Z axis) rotation about the centre of the crystals is shown in Figure 5.19. Each AOD can be rotated by up to +/- 4.5 degrees about the Z axis and clamped into the chosen position. Fine angle adjustment about the X and Y axes is also straight forward.

[12] Mechanics by Alan Hogben and Duncan Farqueharson of the UCL Biosciences Engineering model shop.

We re-assembled the compact configuration of the AOL using an additional stage added to the protocol for aligning each AOD. After optimising the Bragg angle, a lens is used to project the zero order (undeflected) and -1 order (wanted deflected) mode spots onto a screen with precision radial angle alignment marks. The axial angle of the AOD is fine tuned so that these two spots are either exactly horizontal (for X deflectors) or vertical (for Y deflectors).

With these new mounts and this new protocol in place we find that the residual astigmatism is below the limits we can observe or measure. No astigmatic corrector lenses are now necessary to get non astigmatic point spread functions throughout the field of view.

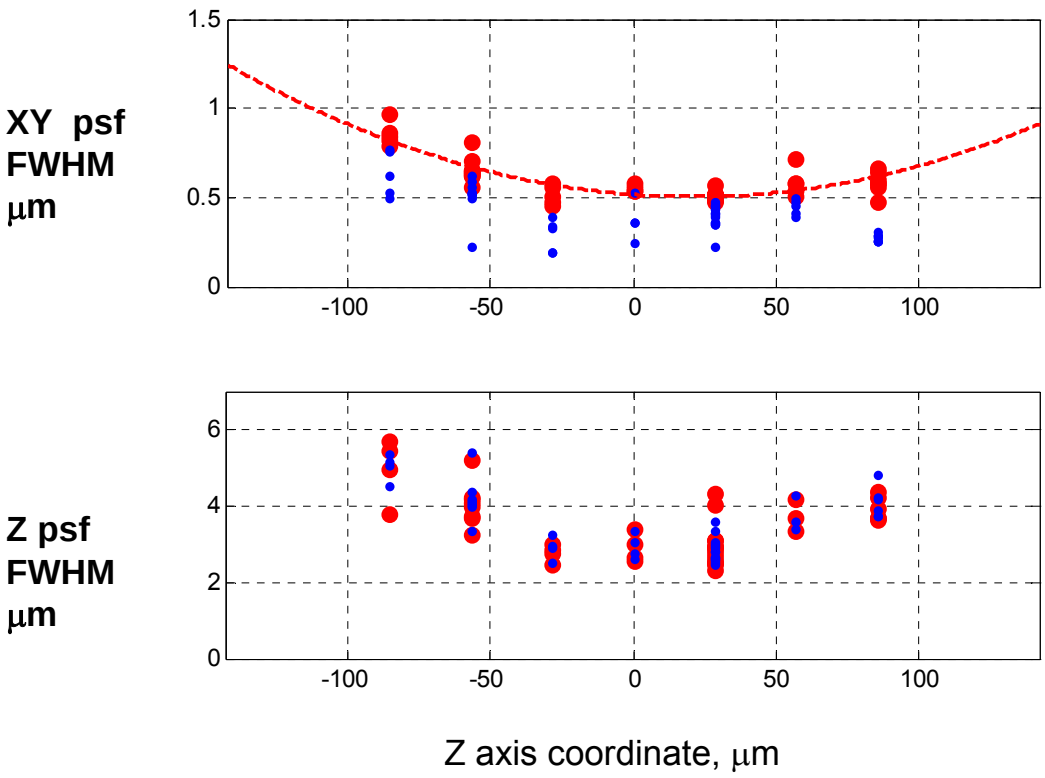

Figure 5.20 Automated psf measurements of the AOL with improved axial alignment of each AOD to minimise astigmatism. All beads lie close to the Z axis X,Y=(0,0). These data were taken with the old AFL scan algorithm at s=8.7 mrad and zoom 32. In the upper plot the red points are the maxima of the fitted ellipses and the blue points the minima. Note that several of these points are unrealistically narrow and have fitted to narrow patternation induced artefacts in the images. In the lower plot, the red points are Zpsf averaged over 10×10 voxels in the XY plane and the blue points Zpsf averaged over 2×2 voxels

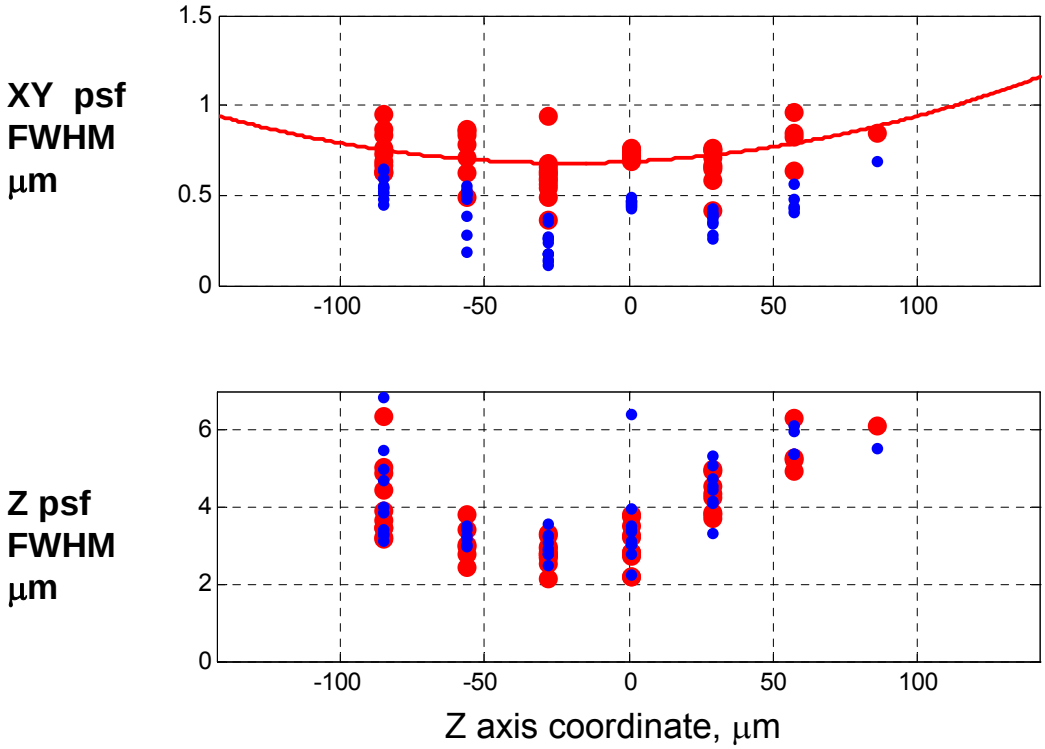

Figure 5.21 Automated psf measurements of the AOL with improved axial alignment of each AOD to minimise astigmatism. This set of data was one of four sets of data taken at the corners of a 100 µm XY square, this one at XY coordinates (-50 µm, 50 µm). In the upper plot the red points are the maxima of the fitted ellipses and the blue points the minima. Note that several of these points are unrealistically narrow and have fitted to narrow patternation induced artefacts in the images. In the lower plot, the red points are Z psf averaged over 10x10 voxels in the XY plane and the blue points Zpsf averaged ove 2×2 voxels

Automated point spread function measurements from across a larger field of view than previously possible were made using the new AOL with this improved precision axial alignment of the AODs. The results are shown in Figure 5.20 and Figure 5.21. The bead psf image results were taken with the old AFL algorithm at semiscan angle s = 8.7 mrad and zoom 32. As in Figure 5.6b), the combination of large scan angle and the AFL algorithm caused very strong patternation effects similar to those in Figure 5.6b). I could nevertheless use the automated psf analysis program to give an approximate idea of the true psf dimensions, this time over a cuboid , rather than an octahedron shaped volume of dimensions of greater than XYZ= 100×100×180µm. The results along the Z axis close to X,Y= (0,0) are shown in Figure 5.20 and close to the X,Y = (52 µm,52 µm) in Figure 5.21. Taken together the data suggested that the

psfs, which are without any chromatic aberration correction, are less than 1x1x4 μm over a cubic region of approximately XYZ=100×100×100 μm.

There are however some caveats. The automated psf data analysis was not as reliable as in the first set of automated measurements shown (Figure 5.18) due to difficulties with the automatic filtering of the data at the higher zoom factors used and with the patternation effects from the old AFL scan algorithm. This is obvious in XY plane data on both figures which show anomalously small minimum psf widths (blue points). These were caused by the interfering patternation rather than being of any real physical significance. Nevertheless, the apparent shift of the minimum Z psf width at the edge of the cube to Z = -30 to -40 μm was approximately reproduced at the other 3 corners of the XY square but not at the centre (X,Y= (0,0)) as shown in the previous figure. This may be a real physical effect, and clearly more accurate measurements are needed in order to understand such effects. These will be carried out shortly with the new OFL algorithms.

Prior to carrying out further measurements on the psfs of beads, my colleagues have carried out the biological tests of the microscope reported in the next sections. These are aimed at determining whether the performance in real biological tissue is as expected from the microscope design.

First images of neurons

Together with my colleagues Tomas Fernandez –Alfonso and Srinivas I have chosen the data available that best summarises the performance of the prototype in the application for which it is intended. The data was gathered during 2008/2009 in brief periods between the various measurements and modifications to the microscope and software described in the previous parts of this results Chapter. All the results in this section are from before the introduction of the OFL algorithm.

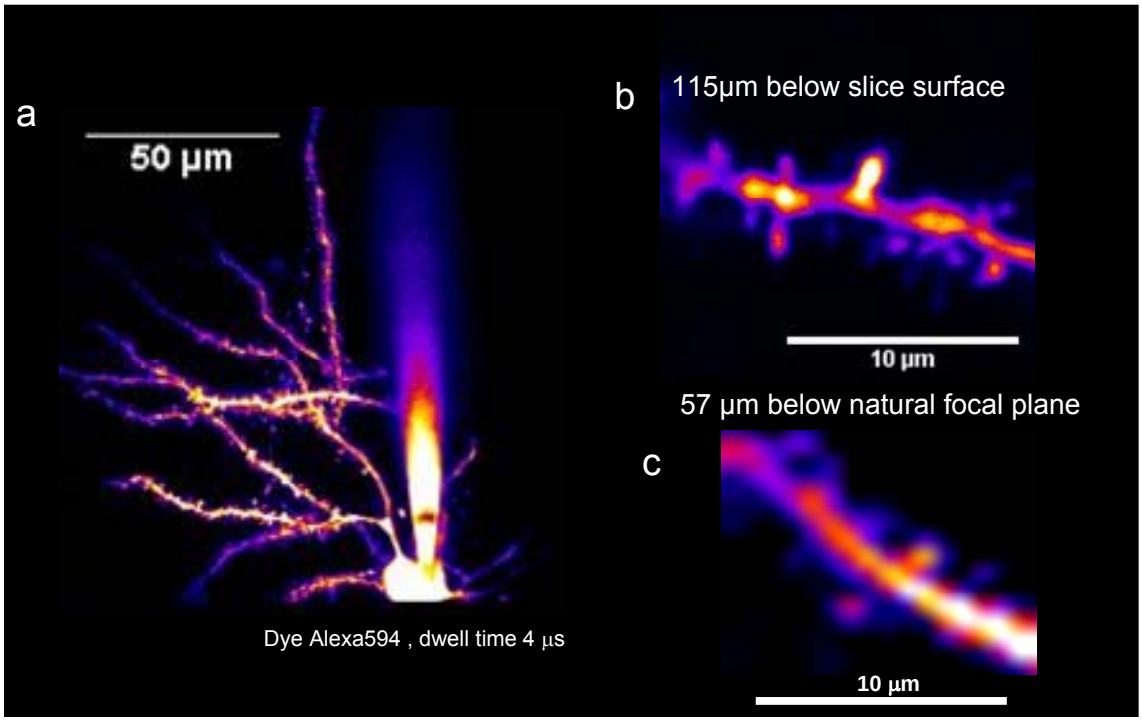

Figure 5.22 a) Z projection of a pyramid cell from a 3D stack of 50 images spanning 10-135 µm deep in layer 2/3 of the cortex of a mouse. Scan parameter s=4.3mrad. The cell is patch clamped and filled with intracellular solution that includes 200µM Alexa594 and 0.1mM EGTA. b) image to show that the microscope has sufficient power and resolution to image individual spines on one of the dendrites at a tissue depth of 115 µm. c) Image demonstrating it is possible to image individual spines even with the AOL focusing set at 57 µm below the natural focal plane of the lens.

The striking image of a patch clamped layer 2/3 pyramid cell from the cortex of a mouse shown in Figure 5.22 was the first to prove that the microscope had sufficient optical power transmission and resolution to image through a slice of brain tissue up to 135 µm thick and show enough resolution, even with 57 µm of AOLM focusing to pick out individual spines on the dendritic arbour.

First measurements of action potentials

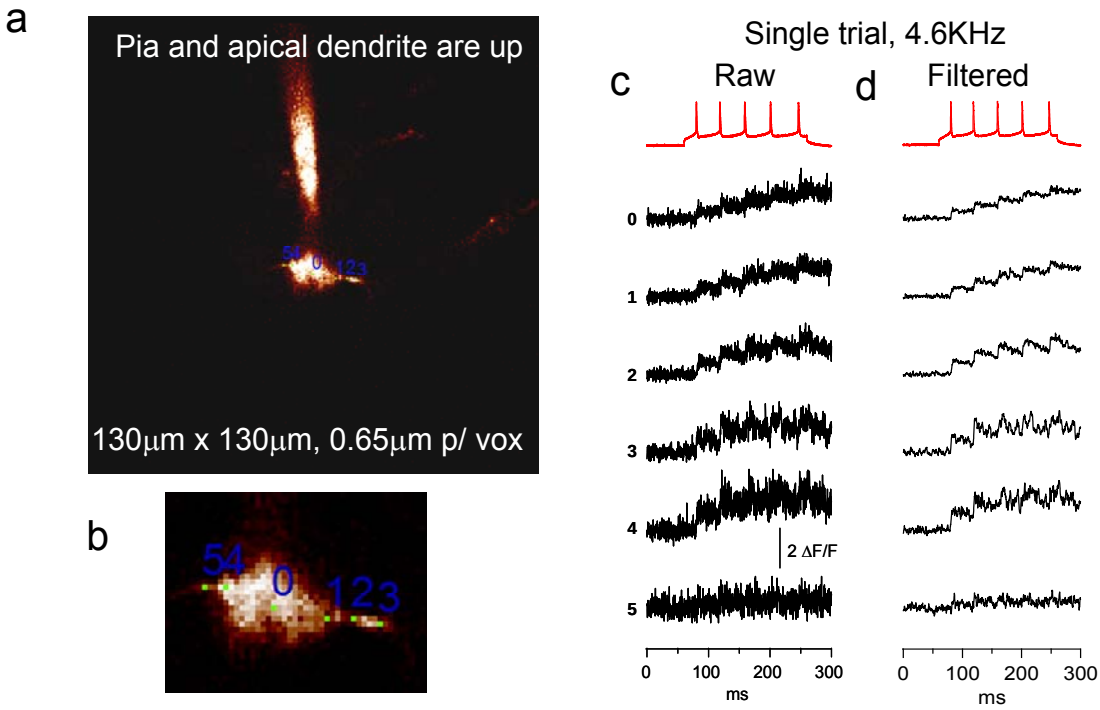

Figure 5.23 Action potential detection from 6 positions on a layer 2/3 pyramidal neuron cell body 50μm deep in a 400 μm thick slice of brain tissue taken from the barrel cortex of a mouse. a) full field of view of cell body with patch clamp containing 0.1μM EGTA, 200μM Fluo4, 40μM Alexa 594 in solution. b) Magnified view of cell body showing the 6 different regions of interest (ROIs) selected for optical functional imaging. c) Electrical patch clamp measurements of action potential train (red) and raw data from six optical functional imaging traces from the six ROIs. Data collection time per ROI T_{ROI}= 4μs AOD cycle time T_C= 36μs. Data collection rate per ROI = 4.6kHz. d) Raw data trace averaged over 6 data collection points with a sliding window. Experimental work by (Fernandez-Alfonso) and (Srinivas)

Figure 5.23 shows one of our first tests of optical functional imaging carried out on a layer 2/3 pyramid neuron in an acute slice from the cortex of a mouse. On this occasion the dye that perfuses the cell from the patch clamp includes Fluo 4 which is a calcium sensitive dye. After imaging, Figure 5.23a, the patched cell body, six separate regions of interest (ROIs) were chosen Figure 5.23b. The cell was then briefly electrically depolarised using the patch clamp in order to drive its membrane above the threshold necessary for it to start generating action potentials spontaneously. As can be seen from the red trace Figure 5.23c, a sequence of 5 electrically measured action potentials resulted, separated by 40ms from one another (25Hz). In the cell body the action potentials allowed short bursts of opening of the voltage gated calcium channels and the resulting rapid rise in calcium concentration

was picked up by the sudden step up in number of fluorescent photons collected in each data collection time T_{ROI}= 4μs. The sampling rate at each ROI is 4.6 kHz or one sample every 216 μs. The fluorescence plots represent relative fluorescence compared to the background fluorescence and are plotted in terms of ΔF/F, the relative change in fluorescence compared to the average background. The calcium ion influx is much faster than its removal from the cytoplasm (Kerr and Denk 2008), so the calcium concentration decays much more slowly than it rises. In fact it only decays a few tens of percent before the next action potential arrives and boosts the calcium concentration again. The step rises in calcium concentration are clearly visible even in the raw data shown in grey. The detailed sawtooth waveform is much clearer Figure 5.23d when this data is averaged by a 6 data point sliding window. Note that there are significant variations in the magnitude of the calcium response in different monitoring positions in the cell body.

A major aim of these experiments was to determine whether it was possible to obtain millisecond accuracy of the timing of the action potentials from the calcium fluorescence data. Figure 5.24 shows an analysis of fluorescence data from 3 of the ROIs on a similar experiment.

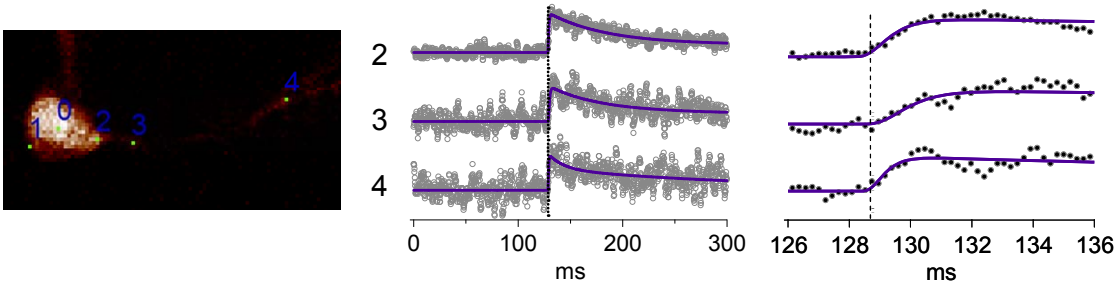

Position	ΔF/F peak	RT10-90% ms	ΔAP time ms	τ1 ms	τ2 ms
2	0.82	1.59	-0.1	55	5113
3	0.72	2.03	0.33	48	766
4	0.74	1.05	-0.05	14	213

Figure 5.24 Rise times of calcium fluorescence at three different positions in a layer 2/3 cell. Rise times estimated by curve fitting to fluorescence data from ROI 2 near apical dendrite in tapered part of cell body about 3 µm wide, ROI 3 in dendrite 3 µm from cell body, ROI 4 in dendrite 35 µm from cell body. Experimental work and data analysis by

On this occasion the ROIs were distributed more widely, not only in the cell body, but also along the dendrite. To most accurately deduce the start of the action potential Tomas has found that fitting the data to a single exponential rise with double exponential decay works well.

The data in the table show the 10-90 rise times varying in the range 1-2ms. Despite this variation Tomas has found that the 10% rise point on average matches the electrical transient of the action potential best. (Note the early rise of the theoretical exponential line has a small curvature added for improved matching). The ΔAP time is the error between the electrical and optical action potential time measured in this way. This data and other data he collected show that sub millisecond action potential timing can be routinely measured in this way. The experiments in Figure 5.24 were all carried out in the natural focal plane of the lens at Zn =0.

In order to test whether the AOLM operated equally well over a range of focal distances the experiment was repeated on a single cell measuring the electrical and optical action potential timing in three different focal planes. This was done by

moving the cell axially between measurements and keeping the monitoring spot position constant as close as practically possible`. The results are shown in Figure 5.25

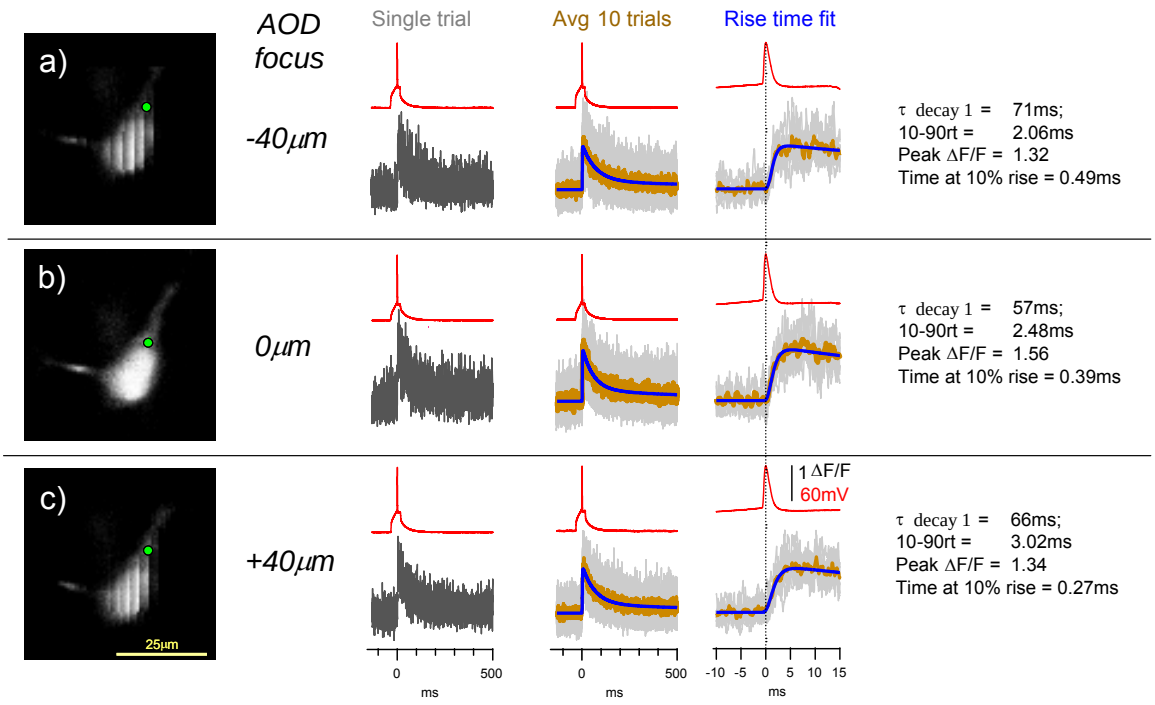

Figure 5.25 Test to determine if action potentials can be monitored equally well at different AOL axial Z focus settings. a) AOLM focused at -40µm, b) focused at the natural focal plane, c) AOLM focused 40 µm above it s natural focal plane. In each case the cell body was moved axially so that the same region of the soma near the apical dendrite was used for monitoring Calcium fluorescence. The red trace is the electrical membrane potential measured with the patch clamp, the grey data is the Calcium fluorescence data, the orange data is the same measurement with data averaged over 10 trials, and blue fitted to an exponential rise and exponential fall equation.

The results show remarkable consistency of signal levels, signal to noise ratio and a variation of action potential timing of less than a quarter of a millisecond over a focal range of 80 µm (albeit for only 3 samples).

Taken together these first optical functional imaging results show that the AOLM is capable of optically monitoring calcium levels in ROIs at close to 30kHz whilst either random access sampling in the XY plane or changing the focus of the AOL in the

axial direction over an 80 μm range . It has sufficient signal to noise ratio to monitor action potential timing from neurons with sub-millisecond precision. Note however that since the Z focusing experiment was on the same ROI on the same neuron in order to check consistency of signal to noise with change of focus, the depth of tissue that the beam was focusing through was not changing with the AOL focus. The next biological experiments (yet to be carried out) will be aimed at combining these capabilities to determine the volume (and particularly the depth range) over which it is possible to maintain sufficiently high signal to noise ratio whilst carrying out true 3D random access monitoring of ROIs.

Summary of chapter 5

This chapter describes the main experimental results to date of the complete AOLM. It starts by showing that the AOL can randomly refocus in 3D at 30kHz and that the prechirper pre-compensates for the AOL and microscope temporal dispersion sufficiently well that the pulse width is only increased from 100fs at the laser to 115 fs at the specimen. 3D imaging results are shown for the AOLM using the original absolute frequency limit scan algorithm. The problem of patternation is described and progress towards solving it with the optimized frequency limits (OFL) algorithm reported. It is shown that the OFL enables high efficiency scanning over more than a 200 μm cube at 0.8 NA. Measurements of the microscope point spread function show better than 1x1x4 μm resolution over a cubic region of approximately XYZ=100×100×100 μm. These measurements are without the proposed chromatic aberration correction. Finally we report on our first images of neurons, and functional imaging of multiple regions of interest on individual neurons which we stimulated to fire action potentials. The signal to noise ratio is sufficiently high to enable millisecond time resolution of action potentials to be achieved whilst changing the AOL focus over an 80μm range.

Chapter 6 Conclusions and Discussion

Summary of main achievements

This thesis outlines the theoretical and experimental work that I have carried out during the development of a prototype high speed 3D 2-photon microscope based on AODs. This development arose from initial proposal that 4 AODs could be used to form a high speed dynamic lens (Kaplan, Friedman et al. 2001) and the target specifications that my supervisor proposed for high speed 3D optical functional imaging in neuroscience.

I have analysed deflection bandwidth requirements for the type of 3D 'pointing mode' system we require and the results show that AODs have a large advantage over other existing technologies. I have studied the limitations of AODs that have largely prevented their widespread use in 2-photon microscopy to date. I have invented solutions to several of the key problems and proposed a detailed design for a prototype microscope. A key design advance was to use customised AODs with a low acoustic walk off angle. A novel compact configuration for the 4 AODs will substantially reduce the practical difficulties of changing operating wavelength. I have modeled the AOL design and derived the new RF drive frequency control algorithms necessary for the compact configuration. I have proposed and analysed a novel solution for minimizing the serious chromatic aberration inherent to the use of diffractive devices such as AODs.

We have built a prototype machine and demonstrated many of the key aspects of the target performance. Experimental clues from the prototype and deeper understanding of the complex multidimensional optical physics determining the relationship between the RF drive parameters and the overall acousto-optic lens diffraction efficiency has led to the extension of the RF drive frequency control algorithms to give a substantial increase the field of view and improvement of the uniformity of light transmission during scanning. These enable the laser beam to be scanned over a volume close to the 250μm cube of the target specification at a numerical aperture NA = 0.8. We have demonstrated that the prototype AOLM can achieve 30 kHz random access sampling of multiple regions of interest on neurons in live tissue. Moreover, the SNR is

sufficiently good to detect individual action potential-evoked calcium transients with fluorescent dyes and to determine their timing with millisecond resolution. These specifications and results represent a significant improvement over current technologies for functional optical imaging.

Comparison of AOLM with other recent approaches for optical functional imaging

There have been several interesting papers published during the development of this AOLM. I have divided them up for discussion into those using AOD technology and those using different technology to achieve similar aims.

AOD-based imaging approaches

The first proof-of-principle demonstration of high speed 3D 2-photon optical functional imaging using AODs was published by Peter Saggau's group (Reddy and Saggau 2007; Reddy, Kelleher et al. 2008) They describe both what they call 'structural imaging' and 'random access' imaging of individual neurons over volumes of tissue of XYZ= 200×200×25μm beneath a nominal NA=1, 60X objective. They describe imaging pollen grains and measuring psfs over a focusing range of up to 50μm, but report substantial drop off in 2-photon power for Z displacement greater than ±25 μm. This compares to our results of 150×150×130 μm scan volume shown in Figure 5.10 for a very similar[13] NA=1, 60X lens and very similar back aperture fill diameter. They attribute their limited depth of scan to the use of conventional narrow input acceptance angle commercial AODs and advocate the use of customized wide acceptance angle AODs in future. There are, however, other substantial differences in the system they describe and the system we have developed. In particular their use of commercial AODs means that the walk off angle of the AODs they were using was of the order of 55 degrees rather than the 20 degrees of our customized design. It seems possible that coma arising from this large walk off angle limited their ability to image at more than ±25 μm from the natural focal plane.

[13] The back aperture fill 'W' for the Reddy microscope is 9 mm AOD aperture (from manufacturer) divided by 1.2 :1 telecentric relay = 7.5mm., Our microscope has 15mm x 0.6= 9mm back aperture fill from data in chapter 5, 'Comparison of measured field of view with theory' This is then apertured by the 7.3mm physical back aperture of the 60x microscope.

The fact that (Reddy, Kelleher et al. 2008) could scan laterally over XY=200×200 μm beneath a NA=1, 60X objective compared to our 130×130 μm is perhaps because they used a narrower spectrum (Mira,HP Coherent) laser with 200fs pulse length. In principle this should have a transform limited spectral width of 5nm spectral width, half the spectral width of ours. In the paper they said it had ~10nm spectral width, if so then the pulses were not transform limited. The long pulse length and possibly narrower spectrum minimised the temporal dispersion of their system. This was important because they decided that the large temporal dispersion of their standard commercial AODs which were each 30mm long was so large that it was impractical to compensate with a prechirper. As a result, their 200fs laser input pulses were stretched to 1.8 ps length in passing through the microscope. This pushes up the power required for 2-photon imaging substantially (a factor of 3 in theory) and necessitated the use of optical powers at the back aperture of the objective of 40-100mW compared to about 4- 20 mW for scanned imaging in our microscope or other conventional 2-photon microscopes with normal 200-300 fs pulse length at the specimen.

At no point in any of their published papers do Reddy and Saggau explain their control algorithms. It is not clear whether they have developed the miniscan concept, indeed it might well be that doing so would be very difficult with the less precisely controlled analogue voltage controlled oscillators they used to control drive frequency of the AODs. It is possible therefore that their 'structural imaging' mode is actually the same as the pointing mode and that they spend 14 μs of AOD fill time (for their 9mm aperture AODs) for every approximately 4 μs of data collection dwell time. If true, this would make structural imaging with their microscope much slower than ours in the miniscan mode. Another difference between the Reddy and Saggau system and ours is that they do not use the compact configuration of AODs, they have not discussed either the impracticality of changing wavelength with the long telecentric relays they use to relay the image of one AOD to the grating of the next.

Examination of the methods section reveals that the recordings of action potential evoked calcium transients (Reddy, Kelleher et al. 2008) were low pass filtered at 50Hz to achieve a good SNR. This is somewhat surprising as the noise in their traces is comparable to our traces, which were only filtered at 1kHz (Figure 5.23 etc.).

Comparing the Reddy and Saggau results with those reported in this thesis gives us confidence that although we did not publish first, our design is a significant advance on their publication and much closer to a useable high speed 3D 2-photon microscope for optical functional imaging.

During the course of the work reported in this thesis there was one other 3D 2-photon AOD based microscope paper published (Vucinic and Sejnowski 2007) This, as discussed in (Reddy, Kelleher et al. 2008) is a fast 3D scanning scheme using 2 AODs that only changes focus in the Z direction as a result of fast X or Y scanning. It is not a pointing mode system and, as acknowledged by the author, suffers from poor duty cycle at high sparsity as I described in more detail in the first section of chapter 2, 'Choice of deflection system'. Lastly, (Kremer, Leger et al. 2008) report on a high performance 2D AOD system for optical functional imaging. They report a large aperture (13mmAOD) that is capable of scanning over more than 40 mrad scan angle. This compares to the 36 mrad = 4 x 9 mrad semiscan angle for our system (Figure 5.9). They also report on the detailed space time frequency measurements of the point spread functions of this system using a measurement system known as 'FROG'. It would be very interesting to carry out similar measurements on the psfs of our system in order to understand combination of spherical and chromatic aberrations that presumably limit the psfs of our system at large AOL Z focusing.

Other Technologies

Liquid crystal phase modulator technology has also been applied to diffractive imaging applications. One of these technologies developed by Holoeye (www.holoeye.com) has been used for an interesting approach to optical functional imaging of many neurons in parallel. At present the results reported are for two dimensional imaging only, although programmable diffractive elements such as the Holoeye system can focus in the third dimension as well. Nikolenko (Nikolenko, Watson et al. 2008) reported on a 2D system that used a Holoeye SLM based phase modulator to focus or 'beam shape' its total diffracted power onto the bodies of many 10s of neurons in cortical tissue in parallel. They then used a CCD camera to monitor all the cells in parallel at 60Hz. They were able detect the changes in calcium concentration in individual cells following individual action potentials. They do not

say the time precision they could achieve but it looks in the order of 100ms from the data they present.

A separate paper (Brendon, Volodymyr et al. 2009) from the same group reports on speeding up conventional raster scanning by using diffractive optical elements to form an array of beamlets for 2D 2-photon imaging with a parallel array detector such as CCD or photomultiplier tube array. As most conventional 2-photon microscopes have plenty of laser power to spare, this is clearly a simple way of speeding up data acquisition. This is related to the TriM Scope from LaVision Biotec which uses up to 64 2-photon laser beams to parallelise and speed up scanning, and the emitted fluorescence is imaged onto a fast CCD camera, which can run at 100Hz. This has been used extensively for imaging network activity in slices (Crépel, Aronov et al. 2007). As the authors acknowledge, it will not be suitable for deep tissue 3D imaging as scattering will cause crosstalk between data acquisition channels and there is much less power spare in deep tissue in the microscope because of laser scattering losses. The results they report demonstrate the expected speed up in data acquisition but also appear limited to about 100ms time resolution for action potential detection.

An interesting recently reported mechanical system with the potential for much more rapid refocusing in Z than any previous mechanical focusing system is the piston mirror system (Botcherby, Juskaitis et al. 2007). It has the potential for operation at speeds up to around 1kHz cycle time as it uses a light weight piston mirror that sits in air at the focus of an auxiliary objective. There is thus no need to move the objective. By matching the angular convergence of the auxiliary objective so that it matches both the sine and Hershel conditions with the main water immersion objective, a high degree of correction of the spherical aberration that would otherwise limit the Z displacement of a high NA remotely focused objective has been demonstrated. Clearly this system will only operate in the scanning mode in the Z direction, its deflection bandwidth is not high enough to be considered for the pointing mode. However, if for instance, it was hybridised with XY deflectors operated in the pointing mode, then providing half the ROIs in each Z plane are monitored before moving down to the next Z plane and the other half on the cyclic return of the Z plane in the return direction, then, assuming a fairly uniform distribution of neurons in the Z direction, it is possible in principle to obtain a duty cycle close to that of a full

3D pointing mode system up to a sparsity in the Z direction $S_S = 1/2T_{ROI}R_S$. This corresponds to a sparsity of 50 for R_S=1 kHz Z scan rate and T_{ROI} = 10µs. This means that the focal spot would on average move 5µm in the data collection time T_{ROI} if the Z scan depth was 250µm. For 100 Hz rates the sparsity would be 500 and the laser spot would only move 0.5 µm in T_{ROI} = 10 µs. This is probably sufficiently small not to matter in comparison to a Z psf of 2 µm.

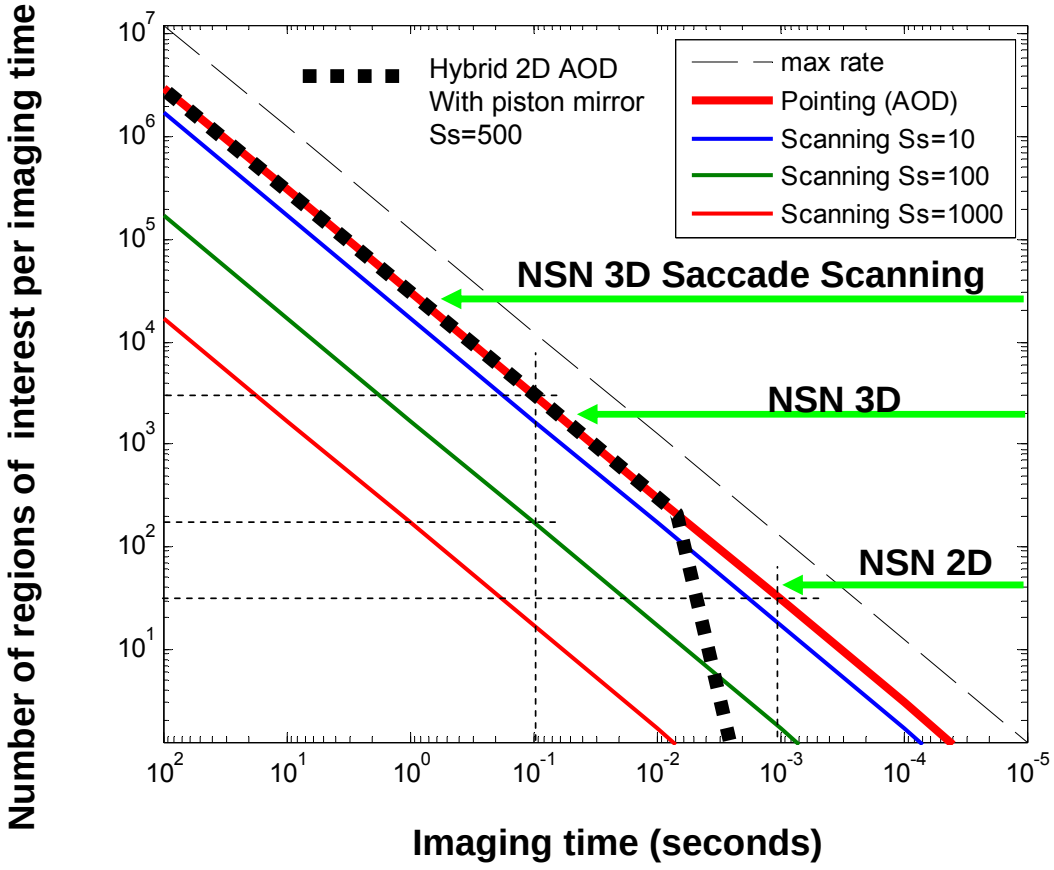

Figure 6.1 The relationship between number of regions of interest and imaging time for pointing mode and scanning mode. Black dashed line shows the expected relationship for a hybrid 2D AOD – piston mirror system. In all cases the total dwell time in each region of interest T_{ROI} is 8µs. The pointing mode transit time is 25µs. The sloping black dashed line shows the maximum number of ROIs that could be monitored with infinite deflection bandwidth (zero transit time between ROIs). The vertical and horizontal black lines pick out particular imaging rates for comparison. For the scanning mode results are for 3 different spatial sparsities *Ss*. The horizontal green arrows indicate the approximate number of selectable neurons (NSN) for high speed imaging in a volume of rat cortex 250×250×250µm (3D) and 250×250µm (2D). (Ohki, Chung et al. 2005) and 500×500×500µm for Saccade scanning in 3D (our extrapolation).

Figure 6.1 shows the expected relationship between the number of regions of interest that the Hybrid 2D AOD – piston mirror system can monitor and the imaging speed Rs superimposed on the pointing mode scanning mode relationship plot presented earlier in Figure 2.6. This plot shows that the combination of a pointing XY deflector mode (e.g. 2D AOD scanner) and the piston mirror is well worth considering as a competitor to the AOLM system described in this thesis. If, for instance, it was possible to design such a system so that it delivered higher optical power to the back aperture of the objective and it gave smaller axial psfs over a larger field of view and the end user was happy to trade off faster cycle time and random access ability in Z that the AOLM system offers, then it may be a good option. For example, if the system is monitoring 1000 neurons or more, then for $T_{ROI} = 10\mu s$, the sampling rate of individual neurons is more than 10ms with either system. In this case, if it does not matter what order the neurons are scanned in the Z direction, and, if the neurons are distributed fairly uniformly in Z, then the performance of the AOLM would be similar to a hybrid piston and 2D AOD scanner. The decision of which choice was best would then be made in terms of comparison of Z psf dimension and field of view which may be better for the piston mirror solution.

It is clear from this analysis however that if high sparsity is wanted at kHz sampling rates, the region above 100Hz imaging rate where the AOLM and hybrid 2D – piston mirror solution deviate in Figure 6.1, then, the hybrid 2D AOD- piston mirror solution will not be able to compete with the AOLM solution.

Status of results to date

The results presented in chapter five are very much work in progress as our priorities have been driven in various phases between improving understanding, improving performance and obtaining preliminary results for demonstrating the progress to date. At each stage of these development cycles, there have been dramatic improvements in performance. We are still far from reaching the full potential of the acousto-optic lens microscope (AOLM). In particular, it was only at the beginning of 2009 that we realised the potential for new drive algorithms to significantly improve the size and shape of the high efficiency field of view from octahedral to the enclosing cuboid. At the time of writing, the new optimized frequency limits (OFL) algorithms have only

been working in their initial form for a few weeks and have been used to demonstrate the improvements to field of view described in chapter 5, Figure 5.6 to Figure 5.11. We have postponed re-measuring the point spread functions (psfs) across the full field of view and measuring the chromatic aberration correction whilst we completed the biological test results reported in Chapter 5.

Performance of the prototype AOLM

In chapter 5, Figure 5.6 to Figure 5.11, I presented results showing that the prototype AOLM is capable of scanning and pointing with sufficient power and resolution for 2-photon imaging of test grids that covers approximately a 200μm cube. The field of view matches that predicted theoretically to within 7%. There is however noticeable fading at the edges of the field of view (Figure 5.7) which is likely to be at least in part caused by the theoretically expected chromatic aberrations. The new OFL drive algorithm is essential to achieving this large scan volume without the serious patternation problems of the Absolute Frequency Limits (AFL) algorithm. The results of point spread function (psf) measurements of beads indicate, but do not prove, that the present microscope is capable of imaging with better than an XYZ resolution of 1×1×4 μm over a 3D cube of 100×100×100 μm. This is without chromatic aberration correction and is therefore approximately as expected from the theory in chapter 3, 'Derivation of resolution of microscope..'. The results also show that the AOLM is capable of imaging the structure of neurons in live acute slices of mouse brain cortex to a depth of over 100 μm. Moreover, spines on dendrites, which are of the order of 1 μm in size, can be resolved even with over 50 μm of AOL focusing.

Experiments using the AOLM for optical functional imaging of a single neuron at 4.6 kHz sampling rate per region of interest (ROI) and 4 μs sample collection time shows that individual action potential-evoked calcium transients can be detected clearly with a high signal to noise ratio (SNR). This was maintained when the AOL focus was varied over an 80 μm range. These recordings allowed the timing of individual action potentials to be inferred from the rising phase of the calcium transients with a precision of approximately 1ms. These results show that the performance of the prototype AOLM is sufficient for high spatio-temporal optical functional imaging and this can be improved further given that the dwell time can be increased to 8 or 16 μs.

It should, however, be noted that despite altering the AOL focus by over 80μm, the optical functional imaging results reported here were all carried out at about 40-50 μm tissue depth. The signal to noise ratio will reduce exponentially with tissue depth as a result of optical scattering. The next (yet to be carried out) optical functional imaging experiments will be the first time we have tested true 3D random access optical functional imaging and it will be very interesting to see how performance varies with tissue depth.

Further Work: improving image patternation and aberration of the psf

Throughout the project the problems caused by the variation of efficiency of AODs with scan angle have been amongst the most difficult to understand and correct. I have developed increasingly sophisticated MatLab models of individual AODs and modeled what should happen when four AODs are concatenated to form the AOL. Each AOD needs a three dimension plot to map its efficiency vs. drive frequency and input incident angle, four dimensional if, as I have recently done, you calculate using the large signal efficiency rather than the usual low acoustic drive model known as the Born approximation (Xu and Stroud 1992). Calculating the overall efficiency of the AOL thus becomes at least a 12 or 16 dimensional problem.

The variations of efficiency with drive angle cause problems by introducing unwanted variations in 2-photon efficiency, for instance when scanning during a miniscan. This causes patternation. In principle, this could be corrected for either by independently controlling the incident laser power to the AOL or by post processing the image. Since post processing the image would cause variations in noise level with position, we prefer to find a solution to the problems of controlling the laser power so that the spot intensity does not vary along a miniscan or between miniscans.

Comparison of Figure 3.17, the theoretical efficiency plot of an X1,X2 AOD pair over the f1,f2 drive frequency space with the experimental plot of Figure 4.10 and Figure 4.11 shows that the experimental plots have peaks and troughs of efficiency every 4 MHz in a cyclic manner. This cyclic efficiency variation with frequency is not shown by my model and therefore must be caused by a physical effect that I have not included. As discussed in Chapter 4, it is plausible that this could be an effect of

variation of the eigenmode polarization with propagation angle in the crystal analogous to the cyclic interference fringes we utilized to precisely measure the crystal orientation in Figure 3.34 to Figure 3.38. If this is correct then we may be able to minimise the effect by more accurately adjusting the state of polarization between the crystals so that light is launched into the crystal with the optimum polarization to couple into the correct elliptical extraordinary eigenmode. There will then be no optical power in the orthogonal mode to cause the cyclic interference effect. Such an optimisation would require the use of additional quarter wave plates between each crystal.

Even with this improvement it is clear that during each miniscan there will be significant variation of intensity of the 2-photon focused spot with time along the scan. The new OFL algorithm has successfully enabled each miniscan to find maximum efficiency possible for the middle voxel of each miniscan (data not shown). I now need to develop algorithms that not only compensate for the change in efficiency when the OFL algorithm jumps from one peak efficiency in f1,f2 frequency space to another, but also modulates either an external Pockel's Cell or the acoustic drive intensity during a miniscan to give constant efficiency equal to the maximum possible at the ends of each miniscan. Unfortunately, it is of course necessary to level down the peaks of intensity to match the troughs, this makes it particularly important to find ways to minimize the troughs in *f1, f2* frequency space, perhaps by the use of additional quarter wave plates.

We have experimented with three ways to implement such laser spot intensity control in the scanning mode:

1. Scan a uniformly fluorescent sample and measure the intensity variation vs. time during the scan, then implement a separate intensity control via a Pockels Cell that inverts the measured intensity modulation and hence compensates the AOD induced variation. This method was used for the pollen grain images in Figure 5.5. This method is, however, very tedious as it requires measurement of the 2-photon intensity in a uniform fluorescent medium for every different scan frame you might wish to use.

2. Measuring the transmission efficiency, inverting the signal and using a Pockels cell to correct for intensity variations. This was achieved by tapping off ~8% of the diffracted light in the AOL output with a pellicle set with its normal at 8 degrees to the beam (to avoid polarization effects) and monitoring its intensity with a large area (3 mm diameter) high speed silicon photo diode. This signal is then used to form a 'single photon' brightness image of the particular scan frame, and by comparing the local single photon intensity to the average intensity, a correction signal was generated for modulating the Pockel's Cell in antiphase with the local intensity variation. This method worked well on occasions but it was very difficult to identify the cause when it failed to work well.
3. Develop a mathematical model of efficiency vs. drive frequencies for the AOL, so that the compensation drive can be computed at the same time as the scan drive parameters are calculated. We have tried this method with the old absolute frequency limit (AFL) algorithm, but our mathematical model of the complete system was too inaccurate to be satisfactory.

Part of the problem was that with the old AFL drive algorithm, the variations in intensity that the compensation mechanism was trying to correct for were too large. I hope that the fact that the middle voxel of any miniscan is always the brightest will make the minor parabolic correction to intensity vs. time much more tractable with the new OFL algorithm. The fact that the algorithm has independent external control of the length of each miniscan makes the prospects of success much higher. As stated in the figures concerned, the images presented in this thesis using the new OFL algorithm are all with only one voxel miniscan length to minimize patternation effects.

The second major problem that requires further work involves optimising the point spread function across the field of view, by minimizing chromatic and spherical aberration. The measurements of the psf we have made show that, at least in the XY plane at Z=0 chromatic aberration causes the psf to be lengthened in a radial direction centred on the centre of the field of view (See Chapter 3, ' Derivation of resolution of microscope'). The chromatic aberration itself increases in proportion to the spectral width of the laser and the radial distance from the centre of the field of view. My

Matlab models (Figure 3.23) show that in 3D the chromatic aberration remains radial with the aberration vector pointing out radially from the centre of a sphere. The magnitude of the chromatic aberration is equal to the FWHM of the laser spectral width divided by its wavelength times the radial distance to the centre of the FOV. For our current laser (Spectra physics Mai Tai, www.newport.com) the spectral width is 10.6nm causing chromatic aberration of 1/80 of the deflection of the focus from the centre of the FOV resulting 1 μm of chromatic aberration at 80 μm radius from the centre of the field of view. Our experimental measurements at 52 μm and 75 μm radius were consistent with the expected aberration (Figure 5.21). It is not therefore surprising that the 2-photon imaging brightness falls off rapidly towards the edges of the 200 μm cube imaged using the fluorescent grids in Figure 5.9.

There are two potential ways to minimize chromatic aberration, reduce the spectral width of the laser, or implement the magnification chromatic aberration compensation described in Chapter 3 'Designing a practical chromatic aberration corrector'. There are two leading brands of Ti-Sapphire laser the Spectra Physics 'MaiTai' (www.newport.com) that we have used here and the Coherent 'Chameleon' (www.coherent.com). The Spectra physics laser has a pulse width of 100fs and the Coherent 140fs. The spectral widths are inversely related to the pulse length at 10-13nm and 5-6nm respectively. Since 2-photon efficiency reduces with increasing pulse length it is not obvious which laser is the better for 2-photon imaging. In view of the strong effect of chromatic aberration limiting the FOV in the AOLM we have developed it is obviously worth while to experiment with the narrower laser spectrum Coherent laser and find out whether it gives the approximate doubling of the linear dimensions of FOV in the XY plane that might be expected for the predicted reduction in chromatic aberration.

We have purchased the lenses and diffractive optical elements (DOE)s for the chromatic aberration compensator (DOEs from www.silios.com) shown in Figure 3.28. We have checked that the DOEs have better than 80% transmission efficiency. Even so, the loss of the compensator will be at least 40%. The questions we need to determine experimentally are whether the chromatic aberration compensator works as designed, and if so whether the benefits of improved field of view are out weighed by

the insertion loss of the compensator. This latter point depends on whether there is spare laser power for the measurements that are being made.

Once the chromatic aberration is minimized with one or both of the strategies above, the dominant form of aberration is likely to be spherical. Spherical aberration will increase with distance from the natural focal plane and with the NA lens. For functional imaging applications where a large axial range of focus is required, we intend to restrict the NA of the system to 0.7-0.8. This will be achieved by under filling high NA objectives, allowing the full NA to be used for light collection.

We have very little evidence of what the spherical aberration will be at large Z displacements when using the new OFL algorithms. The XY plane images of pollen grains Z displaced by +/- 133mm beneath an NA=0.8 40X lens in figure 5.14 seem remarkably clear and crisp. It is difficult to believe that there is enormous axial spherical aberration, but proof is required from direct psf measurements

Prospects for meeting or exceeding target specification with the current design

Implementation of the improved patternation control, a narrow spectrum 2-photon laser and the chromatic aberration compensator, is predicted to increase the effective X-Y field of view to at least 200x200 μm and perhaps in excess of the target 250×250 μm whilst maintaining the lateral PSF dimension below 1μm. I am much less confident about meeting the target of a 2 μm axial psf over a 250 μm focusing range. It seems likely from results to date that it will only be possible to achieve a <4 μm axial psf over this range. This is important because the functional imaging signal can be contaminated by signals arising from surrounding extracellular tissue collectively known as the neuropil[14], reducing the SNR (Gobel, Kampa et al. 2007). Nevertheless, the first experimental optical functional imaging signals we have from the 80 μm Z depth range are encouraging in this respect (Figure 5.25). These results show that signals with the largest SNR arise from the large proximal dendrite close to the soma

[14] Neuropil is made up of a high density of axons and dendrites from other neurons.

of pyramidal neurons in mouse cortex. This region, where the soma tapers into the dendrite, is about 10 μm wide, large enough to completely surround even a 4 μm axial psf. These results suggest that we can get results with the present psf without contamination from the neuropil.

Our priorities now are to complete biological test results for publication, introduce patternation control into the OFL algorithm, re-measure and fine tune the psf without chromatic aberration compensation and then make first measurements of whether the chromatic aberration compensation works as designed and improves the overall microscope performance. Finally we will test the system, with and without chromatic aberration control but with a narrower spectrum laser.

Patents, proposed new hybrid '3D Saccade scanning' microscope and prospects for commercial exploitation

During the course of the work described in this thesis we have filed two patents (Kirkby, Silver et al. 20.03.2008; Silver, Kirkby et al. 2009) The first, which has 60 diagrams, covers all the key ideas described in chapter 2 and 3 on the compact configuration, AOD design and compensating for the chromatic aberration of AODs, The second covers a concept we name as saccade scanning. It is worth outlining here as it is aimed at combining the benefits of mechanical scanning with AOD pointing. The idea is simply to combine a 3D AOD pointing mode system in series with galvanometer and/or piston mirror mechanical scanning. The idea is to not just use the AOD system to point in a steady direction but in each region of interest to control the AOD 3D scan velocity to exactly compensate the movement of the mechanical system for the duration of the data gathering time period T_{ROI} . Thus in each ROI the 3D AOD motion briefly cancels the 3D mechanical movement. In this way, a high spatial sparsity S_S can be achieved whilst benefitting from the larger low aberration field of view of mechanical scan systems. We refer to such systems as saccade scanning systems as they move from region of interest to region of interest in a series of small jumps in a similar way to the way the eye saccade scans a scene. It is possible that a high performance 'Rolls Royce' optical functional imaging system based on the concepts of this Thesis would thus combine all the benefits of mechanical scanning systems with those of the AOLM. In principle, assuming that the piston mirror system could indeed be made to work with low losses and low

aberrations at 100Hz or higher, then such a saccade scanned system might well be able to cover a volume of 500×500×500 μm and thus achieve high sparsity optical functional imaging of up to 24000 neurons as indicated by the maximum number of selectable neurons (NSN) for 3D saccade scanning on Figure 6.1. Unlike the hybrid piston mirror 2D AOD system described in the previous section, the performance would not drop off at high frame rate, but equal that of the AOLM up to the highest speeds (i.e. follow the thick solid red line of Figure 6.1).

The filing of the Patents was funded by UCL business and there are plans to invite selected commercial manufactures to demonstrate the system as soon as we are confident that such a demonstration would properly represent the capabilities of the technology. The technology we have developed still appears to have fundamental advantages over all other known technologies for high speed 3D optical functional imaging at high spatial sparsity, (see Chapter 1, 'Temporal and spatial sparseness of action potentials...'). If the target specification can be met, then there is every reason to believe that there will be high demand for a 2-photon microscope with these capabilities from the neuroscience community. We have already demonstrated many of the key aspects of the design and the particular technologies we have chosen to develop all seem reliable, reproducible and hence manufacturable. There are, therefore, good prospects that the right company could make a success of developing an optical functional imaging instrument based on this technology.

Potential for improving AOLM performance through the further development of control electronics and algorithms

As described in chapter 4, the current prototype microscope pre-computes the scanning and pointing mode data up to 20,000 miniscans before loading the data records into the memory of the iDDS digital synthesiser that drives the AODs with the correct radio frequency (RF) signals. At present these signals are limited to a sequence of linear ramps with defined start frequency, duration and RF ramp rate. Each AOD pair can therefore only act as a dynamic cylindrical lens. There are several reasons why an upgrade to the control system will improve AOLM performance. These include the following:

1. Increasing the bandwidth for uploading data between the computer and iDDS memory will speed up use. If the computation and loading time can be made

shorter than an individual miniscan, then a system that adapts the scan parameters in response to the image in real time can be made. This would open up many new applications including automated tracking of active neuronal signals and compensation for movement of live tissue etc. This latter capability is likely to be very important at high spatial sparsity for in-vivo imaging as pulsating blood vessels and breathing cause significant tissue movement in live animals.

2. If the mathematical function describing RF frequency vs. time during a miniscan can not only include the first order linear ramp rate term as today, but also higher order, parabolic, cubic and sinusoidal etc. terms, then this introduces the possibility of not only correcting lens and tissue induced aberrations but also of making the spot scan in any direction in 3D, including the axial direction. With linear ramps imaging in Z requires refocusing between miniscans because the Z plane is fixed during any miniscan.

During 2008, two final year undergraduates, under the supervision of Dr John Mitchell of UCL Electrical Engineering Department carried out a very successful project to develop and demonstrate such a system based on Field Programmable Gate Array (FPGA) technology. From October 2009 it is planned for a PhD project to extend this work.

In conclusion, this thesis describes the design and development of an Acousto-Optic Lens Microscope (AOLM) for optical functional imaging of live brain tissue from initial conception through several stages of development. Each stage has involved understanding key problems, inventing and implementing the solutions in a prototype microscope, and evaluating the results. The performance of the microscope has improved at each stage and is confidently expected to improve still further. The results are promising, both in terms of 3D field of view, resolution of the point spread functions across the field of view, and from the sub millisecond temporal resolution for monitoring action potentials in our first optical functional imaging tests on mouse cortex. Indeed, we are now not too far from our initial target performance of kHz optical functional imaging over a 250μm cube of brain tissue and are significantly ahead in several important respects of any published data. These results suggest that our AOLM technology will be suitable for widespread use in the neurosciences and that it will soon be time to seek partners for commercial exploitation.

References

Amos, W. B. and J. G. White (2003). "How the confocal laser scanning microscope entered biological research." Biol Cell **95**(6): 335-42.

Antic, S. and D. Zecevic (1995). " Optical signals from neurons with internally applied voltage-sensitive dyes." Journal of Neuroscience **15**: 1392–1405.

Attwell, D. and S. B. Laughlin (2001). "An energy budget for signaling in the grey matter of the brain." J Cereb Blood Flow Metab **21**(10): 1133-45.

Botcherby, E. J., R. Juskaitis, M. J. Booth and T. Wilson (2007). "Aberration-free optical refocusing in high numerical aperture microscopy." Opt Lett **32**(14): 2007-9.

Brecht, M., A. Roth and B. Sakmann (2003). "Dynamic receptive fields of reconstructed pyramidal cells in layers 3 and 2 of rat somatosensory barrel cortex." J Physiol **553**(Pt 1): 243-65.

Brendon, O. W., N. Volodymyr and Y. Rafael (2009). "Two-photon imaging with diffractive optical elements." Frontiers in Neural Circuits **3**.

Brown, D. (2008). "Cambridge Technology Inc - Resonant scanners."

Brown, D. (2009). "OPTICS FOR SCANNING: Rapid scanning applications drive mirror design." Laser Focus World Retrieved March, from http://www.laserfocusworld.com/display_article/355405/12/none/none/Feat/OPTICS-FOR-SCANNING.

Buzsaki, G. (2004). "Large-scale recording of neuronal ensembles." Nat Neurosci **7**(5): 446-51.

Buzsaki, G. (2006). Rhythms of the Brain, Oxford University Press.

Cajal, R. (1911). Histologie du système nerveux de l'homme et des vertebrés. Paris, Maloine.

Color, A. (2009). "Fluoroscein dyes." from http://www.abbeycolor.com/fluorescein.php.

Crépel, V., D. Aronov, I. Jorquera, A. Represa, Y. Ben-Ari and R. Cossart (2007). "A Parturition-Associated Nonsynaptic Coherent Activity Pattern in the Developing Hippocampus." Neuron **54**(1): 105-120.

Daw, N. D. and K. Doya (2006). "The computational neurobiology of learning and reward." Curr Opin Neurobiol **16**(2): 199-204.

Denk, W., D. W. Piston and W. W. Webb (1995). Two photon molecular excitation in laser-scannning microscopy. Handbook of confocal microscopy. J. B. Pawley, Plenum**:** 445-458.

Denk, W., J. H. Strickler and W. W. Webb (1990). "Two-photon laser scanning fluorescence microscopy." Science **248**(4951): 73-6.

DiGregorio, D. A., O. Negrete, A. Jeromin, H. B. Peng and J. L. Vergara (2000). "Localization of action potentiual-induced presynaptic calcium domains to active zones of a cultured neuromuscular junction." J Physiol (Lond) **In Press**.

DiGregorio, D. A. and R. A. Silver (2001). "High spatial and temporal resolution measurements of action potential-induced presynaptic calcium transients in central axon varicosities." IUPS Abstracts.

Edwards, F. A., A. Konnerth, B. Sakmann and T. Takahashi (1989). "A thin slice preparation for patch clamp recordings from neurones of the mammalian central nervous system." Pflugers Arch **414**(5): 600-12.

Ferezou, I., S. Bolea and C. C. Petersen (2006). "Visualizing the cortical representation of whisker touch: voltage-sensitive dye imaging in freely moving mice." Neuron **50**(4): 617-29.

Fukumoto, A., M. Kawabuchi and H. Hayami (1975). "Polarization Considerations in the Operation of a Two-Dimensional TeO2 Abnormal Bragg Deflector." Appl. Opt. **14**(4): 812-813.

Gobel, W., B. M. Kampa and F. Helmchen (2007). "Imaging cellular network dynamics in three dimensions using fast 3D laser scanning." Nat Methods **4**(1): 73-9.

Gollisch, T. and M. Meister (2008). "Rapid neural coding in the retina with relative spike latencies." Science **319**(5866): 1108-11.

Goutzoulis, A. P., D. R. Pape and S. V. Kulakov (1994). Design and Fabrication of Acousto Optic Devices, Marcel Dekker.

Hamill, O. P., A. Marty, E. Neher, B. Sakmann and F. J. Sigworth (1981). "Improved patch-clamp techniques for high-resolution current recording from cells and cell-free membrane patches." Pflugers Archiv. European Journal of Physiology **391**(2): 85-100.

Hecht, E. (2001). Optics, Addison-Wesley.

Helmchen, F. and W. Denk (2005). "Deep tissue two-photon microscopy." Nat Methods **2**(12): 932-40.

Higdon, P. D., P. Torok and T. Wilson (1999). "Imaging properties of high aperture multiphoton fluorescence scanning optical microscopes." Journal of Microscopy **193 Pt2**: 127–141.

Higley, M. J. and B. L. Sabatini (2008). "Calcium signaling in dendrites and spines: practical and functional considerations." Neuron **59**(6): 902-13.

Hille, B. (2001). Ion channels of excitable membranes, Sinauer Associates,Inc.

Hopt, A. and E. Neher (2001). "Highly nonlinear photodamage in two-photon fluorescence microscopy." Biophys J **80**(4): 2029-36.

Huxter, J., N. Burgess and J. O'Keefe (2003). "Independent rate and temporal coding in hippocampal pyramidal cells." Nature **425**(6960): 828-32.

Iyer, V., T. M. Hoogland and P. Saggau (2006). "Fast functional imaging of single neurons using random-access multiphoton (RAMP) microscopy." J Neurophysiol **95**(1): 535-45.

Iyer, V., B. E. Losavio and P. Saggau (2003). "Compensation of spatial and temporal dispersion for acousto-optic multiphoton laser-scanning microscopy." J Biomed Opt **8**(3): 460-71.

Jeffery, K. J. (2007). "Integration of the sensory inputs to place cells: what, where, why, and how?" Hippocampus **17**(9): 775-85.

Jezzard, P. (2001). Functional MRI:an introduction to methods, Oxford University Press.

Kaplan, A., N. Friedman and N. Davidson (2001). "Acousto-optic lens with very fast focus scanning." Optics Letters **26**(14): 1078-1080.

Keller, H. E. (1995). Objective lenses for confocal microscopy.
. Handbook of Biological Confocal Microscopy, Plenum Press, New York.**:** 111–126.

Kerr, J. N., C. P. de Kock, D. S. Greenberg, R. M. Bruno, B. Sakmann and F. Helmchen (2007). "Spatial organization of neuronal population responses in layer 2/3 of rat barrel cortex." J Neurosci **27**(48): 13316-28.

Kerr, J. N. and W. Denk (2008). "Imaging in vivo: watching the brain in action." Nat Rev Neurosci **9**(3): 195-205.

Kerr, J. N., D. Greenberg and F. Helmchen (2005). "Imaging input and output of neocortical networks in vivo." Proc Natl Acad Sci U S A **102**(39): 14063-8.

Kirkby, P. A., R. A. Silver and K. M. N. S. Nadella. (20.03.2008). "IMAGING APPARATUS AND METHODS." from http://www.wipo.int.

Koester, H. J., D. Baur, R. Uhl and S. W. Hell (1999). "Ca2+ fluorescence imaging with pico- and femtosecond two-photon excitation: signal and photodamage." Biophys J **77**(4): 2226-36.

Kremer, Y., J. F. Leger, R. Lapole, N. Honnorat, Y. Candela, S. Dieudonne and L. Bourdieu (2008). "A spatio-temporally compensated acousto-optic scanner for two-photon microscopy providing large field of view." Opt Express **16**(14): 10066-76.

Landau, H. J. (1967). "Sampling, data transmission, and the Nyquist rate " Proceedings of the IEEE **55**(10): 1701-1706.

Lev-Ram, V., H. Miyakawa, N. Lasser-Ross and W. N. Ross (1992). "Calcium transients in cerebellar Purkinje neurons evoked by intracellular stimulation." Journal of Neurophysiology **68**: 1167-1177.

Levy, W. B. and R. A. Baxter (1996). "Energy efficient neural codes." Neural Comput **8**(3): 531-43.

Margrie, T. W., M. Brecht and B. Sakmann (2002). "In vivo, low-resistance, whole-cell recordings from neurons in the anaesthetized and awake mammalian brain." Pflugers Arch **444**(4): 491-8.

McLoed, R. "University of Colarado at Boulder." ECE5606 advanced Optics Lab Tutorial, from http://ecee.colorado.edu/~ecen5606/Lectures/Acoustooptics.pdf.

Montemurro, M. A., M. J. Rasch, Y. Murayama, N. K. Logothetis and S. Panzeri (2008). "Phase-of-firing coding of natural visual stimuli in primary visual cortex." Curr Biol **18**(5): 375-80.

Nelson, D. A. and L. C. Katz (1995). "Emergence of functional circuits in ferret visual cortex visualized by optical imaging." Neuron **15**(1): 23-34.

Nicholls, J. G. (2001). From Neuron to Brain, Sinauer.

Nikolenko, V., B. O. Watson, R. Araya, A. Woodruff, D. S. Peterka and R. Yuste (2008). "SLM microscopy: scanless two-photon imaging and photostimulation using spatial light modulators." Frontiers in Neural Circuits **2**.

Oheim, M., E. Beaurepaire, E. Chaigneau, J. Mertz and S. Charpak (2001). "Two-photon microscopy in brain tissue: parameters influencing the imaging depth." J Neurosci Methods **111**(1): 29-37.

Ohki, K., S. Chung, Y. H. Ch'ng, P. Kara and R. C. Reid (2005). "Functional imaging with cellular resolution reveals precise micro-architecture in visual cortex." Nature **433**(7026): 597-603.

Oku, H., K. Hashimoto and M. Ishikawa (2004). "Variable-focus lens with 1-kHz bandwidth." Optics Express **12**: 2138 - 2149.

Olshausen, B. A. and D. J. Field (2004). "Sparse coding of sensory inputs." Curr Opin Neurobiol **14**(4): 481-7.

Otsu, Y., V. Bormuth, J. Wong, B. Mathieu, G. P. Dugue, A. Feltz and S. Dieudonne (2008). "Optical monitoring of neuronal activity at high frame rate with a digital random-access multiphoton (RAMP) microscope." J Neurosci Methods **173**(2): 259-70.

Petersen, C. C., T. T. Hahn, M. Mehta, A. Grinvald and B. Sakmann (2003). "Interaction of sensory responses with spontaneous depolarization in layer 2/3 barrel cortex." Proc Natl Acad Sci U S A **100**(23): 13638-43.

Reddy, G., K. Kelleher, R. Fink and P. Saggau (2008). "Three-dimensional random access multiphoton microscopy for functional imaging of neuronal activity." Nat Neurosci **11**(6): 713-720.

Reddy, G. D. and P. Saggau (2005). "Fast three-dimensional laser scanning scheme using acousto-optic deflectors." J Biomed Opt **10**(6): 064038.

Reddy, G. D. and P. Saggau (2007). "Development of a Random Access Multi-photon Microscope for
Fast Three-Dimensional Functional Recording of Neuronal Activity." Proceedings of SPIE 64430U-1 **6443**: 64430U-1 - 64430U-8

Rózsa, B., G. Katona, E. S. Vizi, Z. Várallyay, A. Sághy, L. Valenta, P. Maák, J. Fekete, Á. Bányász and R. Szip?cs (2007). "Random access three-dimensional two-photon microscopy." Appl. Opt. **46**(10): 1860-1865.

Sabatini, B. L. and W. G. Regehr (1996). "Timing of neurotransmission at fast synapses in the mammalian brain." Nature **384**(6605): 170-2.

Sabatini, B. L. and W. G. Regehr (1999). "Timing of synaptic transmission." Annu Rev Physiol **61**: 521-42.

Salome, R., Y. Kremer, S. Dieudonne, J. F. Leger, O. Krichevsky, C. Wyart, D. Chatenay and L. Bourdieu (2006). "Ultrafast random-access scanning in two-photon microscopy using acousto-optic deflectors." J Neurosci Methods **154**(1-2): 161-74.

Sato, T. R., N. W. Gray, Z. F. Mainen and K. Svoboda (2007). "The Functional Microarchitecture of the Mouse Barrel Cortex." PLoS Biol **5**(7): e189.

Silver, R. A. (2004). Proposal to EPSRC to develop high speed 3D 2- photon microscope. from http://gow.epsrc.ac.uk/ViewGrant.aspx?GrantRef=EP/D501199/1

Silver, R. A., P. A. Kirkby, K. NADELLA, M., N, Srinivas and M. SZULCZEWSKI. (2009). "Optical Beam methods and apparatus." from http://www.wipo.int.

Stosiek, C., O. Garaschuk, K. Holthoff and A. Konnerth (2003). "In vivo two-photon calcium imaging of neuronal networks." Proc Natl Acad Sci U S A **100**(12): 7319-24.

Tsutsui, H., S. Karasawa, Y. Okamura and A. Miyawaki (2008). " Improving membrane voltage measurements using FRET with new fluorescent proteins." Nature Methods **8**: 683-5.

Uchida, N. and Y. Ohmachi (1969). "Elastic and Photoelastic Properties of TeO[sub 2] Single Crystal." Journal of Applied Physics **40**(12): 4692-4695.

Vinje, W. E. and J. L. Gallant (2000). "Sparse coding and decorrelation in primary visual cortex during natural vision." Science **287**(5456): 1273-6.

Vucinic, D. and T. J. Sejnowski (2007). "A compact multiphoton 3D imaging system for recording fast neuronal activity." PLoS ONE **2**(1): e699.

Warner, A. W., D. L. White and W. A. Bonner (1972). "Acousto-optic light deflectors using optical activity in paratellurite." Journal of Applied Physics **43**(11): 4489-4495.

White, J. G., W. B. Amos and M. Fordham (1987). "An evaluation of confocal versus conventional imaging of biological structures by fluorescence light microscopy." J Cell Biol **105**(1): 41-8.

Wilson, T. (1990). Confocal Microscopy, Academic Press.

Wilson, T. and A. R. Carlini (1984). "Three-dimensional imaging in confocal imaging systems with finite sized detectors." Journal of microscopy

Wilson, T. and A. R. Carlini (1987). Optics Letters **12**: 227.

Xu, J. and R. Stroud (1992). Acousto-Optic Devices, Principles, Design and Applications, John Wiley and Sons Inc.

Yaksi, E. and R. W. Friedrich (2006). "Reconstruction of firing rate changes across neuronal populations by temporally deconvolved Ca2+ imaging." Nat Methods **3**(5): 377-83.

Yano, T., M. Kawabuchi, A. Fukumoto and A. Watanabe (1975). "TeO[sub 2] anisotropic Bragg light deflector without midband degeneracy." Applied Physics Letters **26**(12): 689-691.

Yano, T. and A. Watanabe (1974). "Acousto-optic figure of merit of TeO[sub 2] for circularly polarized light." Journal of Applied Physics **45**(3): 1243-1245.

Young, E. H., H. C. Ho and L. J. Harrison (1990). "Optically rotated long time aperture TeO2 Bragg cell " SPIE Proceedings **1296**(Advances in Optical Information Processing IV): 304-315.

Zhu, L., P. C. Sun and Y. Fainman (1999). "Aberration-free dynamic focusing with a multichannel micromachined membrane deformable mirror." Appl Opt **38**(25): 5350-4.

Zipfel, W. R., R. M. Williams and W. W. Webb (2003). "Nonlinear magic: multiphoton microscopy in the biosciences." Nat Biotechnol **21**(11): 1369-77.